Observatório Nacional

DOCTORAL THESIS

DETERMINATION OF PHYSICAL PROPERTIES AND TOPOGRAPHY OF TNOS FROM STELLAR OCCULTATIONS AND ROTATIONAL LIGHT CURVES: THE CASE OF 2002 MS_4 OBJECT

FLAVIA LUANE ROMMEL

RIO DE JANEIRO
2022

Ministério da Ciência, Tecnologia, Inovações e Comunicações
Observatório Nacional
Programa de Pós-Graduação

Doctoral Thesis

DETERMINATION OF PHYSICAL PROPERTIES AND TOPOGRAPHY OF TNOS FROM STELLAR OCCULTATIONS AND ROTATIONAL LIGHT CURVES: THE CASE OF 2002 MS_4 OBJECT

by

Flavia Luane Rommel

A Thesis submitted to the faculty of the Astronomy Ph.D program from Observatório Nacional in fullfilment of the requirements for the degree of Doctor of Philosophy in Astronomy.

Advisor: Dr. Felipe Braga Ribas

Co-advisor: Dr. Julio I. B. Camargo

Rio de Janeiro, RJ – Brazil
December 2022

R766 Rommel, Flavia Luane

Determination of physical properties and topography of TNOs from stellar occultations and rotational light curves: the case of 2002 MS_4 object [Rio de Janeiro] 2022.

xxxiv, 161 p. 29,7 cm: graf. il. tab.

Thesis (doctoral) - Observatório Nacional - Rio de Janeiro, 2022.

1. Stellar occultations. 2. Trans-Neptunian Objects. 3. 2002 MS_4. 4. 2004 XR_{190}. I. Observatório Nacional. II. Título.

CDU 000.000.000

“DETERMINATION OF PHYSICAL PROPERTIES AND TOPOGRAPHY OF TNOS FROM STELLAR OCCULTATIONS AND ROTATIONAL LIGHT CURVES: THE CASE OF 2002 MS_4 OBJECT”

FLAVIA LUANE ROMMEL

THESIS SUBMITTED TO THE FACULTY OF THE ASTRONOMY Ph.D. PROGRAM FROM OBSERVATÓRIO NACIONAL IN FULLFILMENT OF THE REQUIREMENTS FOR THE DEGREE OF DOCTOR IN ASTRONOMY.

Approved by:

Dr. Felipe Braga Ribas – Universidade Tecnológica Federal do Paraná (UTFPR-Curitiba)
(Advisor)

Dr. Julio I. B. Camargo – Observatório Nacional (ON)
(Co-advisor)

Dr. Jorge Marcio Ferreira Carvano – Observatório Nacional (ON)

Dr. Alvaro Augusto Alvarez Candal – Observatório Nacional (ON)

Dr. Gonzalo Tancredi – Universidad de la República (UDELAR)

Dr. Othon Cabo Winter – Universidade Estadual Paulista Júlio de Mesquita Filho (UNESP)

RIO DE JANEIRO, RJ – BRAZIL
19 DECEMBER 2022

To Ana and Astor,
my loved parents.

Acknowledgments

It isn't easy to acknowledge all people who made this Ph.D. thesis feasible with only a few words. However, I will do my best to communicate my appreciation to everyone who supported me scientifically and emotionally throughout these years. First, I would like to thank my parents, Ana and Astor, who taught me to fight for my dreams and supported me since the beginning of this long journey. It was not easy to be available from a distance every time I thought this dream was impossible for me. However, they were there and helped me stand up and continue fighting. Mom, dad, this work is the result of our efforts to achieve the dream of the small me, a public school student living in the countryside of Brazil who dared to dream a big dream.

I want to thank my advisors, Dr. Felipe Braga Ribas and Dr. Julio I. B. Camargo, who made this study possible and trusted in my capabilities since day one. Thank you for your patience and dedication to teaching me how to do high-level research. Thanks to the Coordenação de Aperfeiçoamento de Pessoal de Nível Superior (CAPES) for the financial support during these years, and also to the Observatório Nacional for providing the opportunity to course the Ph.D. I would like to thank the Laboratório Interinstitucional de e-Astronomia (LIneA) for supporting me financially and by providing the hardware/software tools needed to develop many steps of this study.

I am grateful to all members of the Rio Group, our research group, for all their support during these years. Many thanks to Dr. Roberto Vieira Martins for being an example to be followed and for all the financial/scientific support during the entire course. Also, I am thankful to Dr. Rodrigo Boufleur, Dr. Bruno Morgado, Dr. Gustavo Benedetti Rossi, and Dr. Altair Gomes Júnior for their support in many activities of this study, for bringing me into the SORA project, for teaching me how to manipulate large telescopes, for carefully reading this manuscript, for their advice, and for being my friends.

I would like to thank Dr. José Luis Ortiz for receiving me in Granada and providing many opportunities to improve this study. I am grateful for meeting the Spanish team, who helped me learn different subjects. Especially Dr. Rafael Morales and Dr. Nicolás Morales, who patiently supported the massive analysis of the TNOs images made in this study. Also, I am grateful to the Instituto de Astrofísica de Andalucía (IAA) for receiving me for three months and allowing such amazing interaction.

Last but not least, I will be forever grateful to my girlfriend and brothers, Shayene

Cardoso, Fabio J. Rommel, and Alan A. Rommel, for being by my side daily and supporting me unconditionally through this challenging journey. Also, thank to all my friends for the support, especially Msc. Jessica Pauletti, Msc. Jeraldi Hiroki, Maria Eduarda Colaço, and Marcos G. Weippert for their support in good and hard times. These people are not astronomers, but made my days more colorful, are worried about my well-being, and celebrate with me every achievement, even in difficult times like the pandemic. I am very happy to have them in my life.

Muito obrigada a todos!

Flavia Luane Rommel

DETERMINATION OF PHYSICAL PROPERTIES AND TOPOGRAPHY OF TNOS FROM STELLAR OCCULTATIONS AND ROTATIONAL LIGHT CURVES: THE CASE OF 2002 MS_4 OBJECT

ABSTRACT

Forty-five years had elapsed since the discovery of Chiron, three decades since the first observation of a trans-Neptunian object (except Pluto), and currently, thousands of small objects have been discovered in the outer solar system. Due to the significant distances from the Sun, it is thought that their global physical-chemical composition has been unaffected since their formation. Therefore, studies about these objects may reveal valuable information about the solar system's formation and dynamical evolution. However, mainly due to the faintness and small angular sizes on the sky plane, the knowledge about Centaurs and trans-Neptunian objects is still scarce and fragmented.

Direct images of these distant objects acquired from Earth are possible only for a few dozen of them, and space-based telescopes also detected a few hundred objects in the thermal band. Therefore, the physical properties of most objects remain entirely unknown. However, the current stellar catalogs' accuracy brings to light one of the most accurate technique to determine an object's size and shape from Earth, the stellar occultations. It consists of acquiring photometric images of a star while a small object passes in front of it (at the sky plane), blocking its flux for a given observer. Occultations have been used successfully in the last ten years for small bodies' size and shape derivations, but also to discover surrounding structures like rings and jets.

This work analyzes nine stellar occultations by 2002 MS_4 and one by 2004 XR_{190}. The images were acquired between 2019 and 2022 from telescopes worldwide and came from various instruments. Therefore, standardization was needed before submitting them to the aperture photometry. The aperture photometry provided the stellar flux as a function of time for each observational station, the occultation light curves. Each positive detection of the occultation is a measurement of the object's limb, and by analyzing all the positive chords at the sky plane, the object's projected limb is derived with sub-km accuracy. Unlike the expected for large objects, the 2002 MS_4 did not present a perfectly rounded limb. Thus a topography search and characterization methodology is developed to measure it adequately. This is the first time that a multichord occultation detected significant topography in a trans-Neptunian object.

Direct images of trans-Neptunian objects from public and private repositories are also analyzed through different approaches. Due to the diversity of formats and header keys, they are submitted to a pre-processing step before the aperture photometry. In these images, the aperture photometry gives the object's flux as a function of time, and the light curves do not provide a limb measurement. However, the variation of the object's flux as a function of the phase angle may provide the absolute magnitude and some superficial information. A rotational light curve also may be derived if data are precise enough. This work presents estimates of the object's absolute magnitude and the rotational period from absolute photometry.

Keywords: Stellar occultations. Trans-Neptunian Objects. 2002 MS_4. 2004 XR_{190}.

Flavia Luane Rommel

DETERMINAÇÃO DE PROPRIEDADES FÍSICAS E TOPOGRAFIA DE TNOS A PARTIR DE OCULTAÇÕES ESTELARES E CURVAS DE LUZ ROTACIONAIS: O CASO DO OBJETO 2002 MS_4

RESUMO

Quarenta e cinco anos se passaram desde a descoberta de Chiron, três décadas desde a primeira observação de um objeto trans-netuniano (exceto Plutão) e atualmente milhares de pequenos corpos foram descobertos no sistema solar exterior. Devido a sua distância ao Sol, acredita-se que sua composição físico-química global foi pouco afetada desde sua formação. Portanto, estudos sobre esses corpos podem revelar informações valiosas sobre a formação e evolução dinâmica do sistema solar. No entanto, devido principalmente ao seu baixo brilho e pequeno tamanho angular no plano do céu, o conhecimento a respeito dos centauros e objetos trans-netunianos ainda é escasso e fragmentado.

Observações diretas destes objetos distantes a partir da Terra são possíveis apenas para algumas dezenas deles e telescópios espaciais também detectaram algumas centenas de objetos na banda do térmico. Portanto, as propriedades físicas da maioria destes corpos permanece completamente desconhecidas. No entanto, a acurácia dos catálogos estelares atuais trouxe a tona uma das mais acuradas técnicas para determinação de tamanho e forma de pequenos corpos, as ocultações estelares. Ela consiste em adquirir imagens fotométricas de uma estrela enquanto um pequeno corpo transita em frente a ela no plano do céu, bloqueado seu fluxo para um dado observador. Elas tem sido utilizadas com sucesso nos últimos dez anos para derivações de forma e tamanho de pequenos corpos, mas também para descobrir estruturas circundantes como anéis e jatos.

Este trabalho analisa nove ocultações estelares por 2002 MS_4 e uma por 2004 XR_{190}. As imagens foram adquiridas entre 2019 e 2022 em telescópios do mundo todo e vieram de vários instrumentos diferentes. Portanto precisaram ser padronizadas antes de serem submetidas à fotometria de abertura. A fotometria de abertura forneceu o fluxo estelar em função do tempo para cada estação observacional, as curvas de luz de ocultação. Cada detecção positiva de ocultação é uma medida do perfil do corpo e, analisando todas as cordas positivas no plano do céu, o limbo projetado do objeto é obtido com acurácia sub-quilométrica. Diferente do esperado para objetos grandes, 2002 MS_4 não apresentou um limbo perfeitamente arredondado. Assim uma metodologia de busca e caracterização de topografia é desenvolvida para medi-lo adequadamente. Esta é a primeira vez que uma ocultação multi-cordas detecta topografia significativa em um objeto trans-netuniano.

Imagens diretas dos objetos trans-netunianos oriundos de repositórios públicos e privados também foram analisadas através de abordagens distintas. Devido à diversidade de formatos e chaves no cabeçalho das imagens, elas foram submetidas à uma etapa de pré-processamento antes da fotometria de abertura. A partir destas imagens, a fotometria de abertura fornece o fluxo do objeto em função do tempo e as curvas de luz não oferecem uma medida do limbo do corpo. No entanto, a variação de fluxo do objeto em função do ângulo de fase pode fornecer sua magnitude absoluta e alguma informação sobre sua superfície. Uma curva de rotação também pode ser obtida se os dados forem precisos o suficiente. Este trabalho apresenta estimativas de magnitude absoluta e períodos de rotação para os objetos estudados.

Palavras-chave: Ocultações estelares. Objetos trans-netunianos. 2002 MS_4. 2004 XR_{190}.

List of Figures

List of Tables

List of Abbreviations

VATT Advanced Technology Telescope

DZA Algeria

ADU Analogical Digital Unit

ARG Argentina

BRA Brazil

CAN Canada

CFEPS Canada–France Ecliptic Plane Survey

CFHT Canada France Hawaii Telescope

CPU Central Processing Unit

CTIO Cerro Tololo Inter-American Observatory

CCD Charge Coupled Device

CHL Chile

C/A Closest Approach

CMOS Complementary Metal Oxide Semiconductor

HRV Croatia

DES Dark Energy Survey

DEC Declination

DBF Delta Basis Function

DIA Difference Image Analysis

DE Differential Evolution

ERC European Research Council

ESO European Southern Observatory

ELT Extremely Large Telescope

FOV Field of View

FITS Flexible Image Transport System

FRA France

FWHM Full-Width at Half Maximum

***Gaia* DR2** *Gaia* Data Release 2

***Gaia* DR3** *Gaia* Data Release 3

CAHA German-Spanish Astronomical Center at Calar Alto

GPS Global Positioning System

HSO Herschel Space Observatory

HST Hubble Space Telescope

HUN Hungary

IRAF Image Reduction and Analysis Facility

IAA-CSIC Instituto de Astrofísica de Andalucía - Consejo Superior de Investigaciones Científicas

IDL Interactive Data Language®

IAU International Astronomical Union

ICRS International Celestial Reference System

ITA Italy

JWST James Webb Space Telescope

JPL Jet Propulsion Laboratory

JD Julian Date

JFC Jupiter Family Comet

LSST Legacy Survey of Space and Time

LST Local Solar Time

LS Lomb-Scargle

M2 Massive prOcessing Of aStronomical imagEs (Moose) - version 2

MPI Max Planck Institute for Astronomy

MCMC Maximum likelihood via Monte-Carlo Markov Chain

MMR Mean Motion Resonance

MPC Minor Planet Center

MPEC Minor Planet Electronic Circular

NAM Namibia

NOIRLab National Optical-Infrared Astronomy Research Laboratory

NEAT Near-Earth Asteroid Tracking

NTP Network Time Protocol

NTT New Technology Telescope

NIMA Numerical Integration of the Motion of an Asteroid

OM Observing Manager

OLC Occultation Light Curve

OP Occultation Portal

OIS Optimal Image Subtraction

OSSOS Outer Solar System Origins Survey

Pan-STARRS 1 Panoramic Survey Telescope and Rapid Response System 1

PDM Phase Dispersion Method

OPD Pico dos Dias Observatory - Brazil

PRAIA Platform for Reduction of Astronomical Images Automatically

PSF Point Spread Function

PA Position Angle

RAM Random Access Memory

RA Right Ascension

RMS Root Mean Square

RLC Rotational Light Curve

SFFT Sacadic Fast Fourier Transformation

SDO Scattered Disc Object

OSN Sierra Nevada Observatory - Spain

SNR Signal-to-Noise Ratio

SS Solar System

SSOIS Solar System Object Image Search

ZAF South Africa

SOAR Southern Astrophysical Research Telescope

ESP Spain

SST Spitzer Space Telescope

SKA Square Kilometre Array

SORA Stellar Occultation Reduction and Analysis

SOFIA Stratospheric Observatory for Infrared Astronomy

TNG Telescopio Nazionale Galileo

TMT Thirty Meter Telescope

TNO Trans-Neptunian Object

TUR Turkey

2MASS Two Micron All Sky Survey

UKR Ukraine

USA United States of America

UT Universal Time

VEN Venezuela

VLT Very Large Telescope

VTI Video Time Inserter

WFI Wield Field Imager

WCS World Coordinate System

ZTF Zwicky Transient Facility

List of Symbols

χ^2_{pdf}	χ^2 per degree of freedom
$\mathbf{H}_{\text{R}}$	absolute magnitude in R-band
$\mathbf{H}_{\text{V}}$	absolute magnitude in V-band
$\mathbf{L}$	angular momentum
ΔO_{if}	angular separation between object's initial and final positions
ω	angular velocity
$\mathbf{AP}_{\text{source}}$	aperture that measures the source's flux
a'	apparent semi-major axis
b'	apparent semi-minor axis
ϵ'	apparent oblateness
f', g'	apparent object's center
$\mathbf{PA}'$	apparent position angle of the semi-minor axis
ζ	aspect angle
au	astronomical units
σ_{calc}	calculated uncertainty
$\mathbf{F}_{\text{cal}}$	calibration flux
cm	centimeters
$\mathbf{p}_{\text{i,obs}}$	chord's extremity
t_{corr}	corrected time
$\mathbf{cm^3/g.s^2}$	cubic centimeters per gram times squared seconds
Dyn	dynes
E_{R}	Earth's radius
$\mathbf{D}_{\text{eq}}$	equivalent diameter
$\mathbf{R}_{\text{eq}}$	equivalent radius
as_{f}	final angular separation

t_{f}	final time
F_{sky}	flux measured by the $\mathrm{AP}_{\mathrm{outer}}$
F_{source}	flux measured by the $\mathrm{AP}_{\mathrm{source}}$
$\mathbf{F}_{\mathrm{s}}$	Fresnel scale
p_{R}	geometric albedo in R-band
p_{V}	geometric albedo in V-band
GiB	gibibyte
$\mathbf{g/cm}^3$	gram per cubic centimeter
G	gravitational constant
h	hours
t_{img}	image's time
$\mathbf{AP}_{\mathrm{inner}}$	inner aperture of the sky annulus that measures the local sky background flux
as_{i}	initial angular separation
t_{i}	initial time
t_0	instant of the closest approach
km	kilometers
km/s	kilometers per second
β	linear coefficient
mag	magnitude
ΔM	magnitude variation
m	meters
$\mu\mathbf{m}$	micrometers
mas	milliarcseconds
F_{net}	net flux
F_{norm}	normalized flux
$\mathbf{M}_{\mathrm{corr}}$	object's corrected magnitude
ρ	object's density
Δ_{obs}	object's distance relative to the observer
$\mathbf{F}_{\mathrm{obj}}$	object's flux
Δ	object's geocentric distance
r	object's heliocentric distance

$\mathbf{M}_{\text{obj}}$ object's magnitude

$\mathbf{M}$ object's mass

O_{R} object's radius

$\mathbf{M}_{\text{obj}}(1, 1, \alpha)$ object's reduced magnitude

$\mathbf{e}$ orbit eccentricity

$\mathbf{i}$ orbit inclination

$\mathbf{a}$ orbit semi-major axis

$\mathbf{AP}_{\text{outer}}$ outer aperture of the sky annulus that measures the local sky background flux

κ overall shape of the fitting function

α phase angle

$\sigma_{\text{i,phot}}$ photometric uncertainty

$\mathbf{q}$ perihelion distance

$\phi_{\text{i,obs}}$ point of the observed light curve

$\phi_{\text{i,model}}$ point of the synthetic light curve

$\mathbf{p}_{\text{i,calc}}$ point over the ellipse

c polar axis

$\mathbf{R}_{\text{diff}}$ radial difference

σ_{rad} radial uncertainty

$\mathbf{m}_{\text{rel}}$ relative magnitude

Φ_{rot} rotation angle of the PSF x-axis

Δm rotational light curve amplitude

$\mathbf{P}$ rotational period

S_{R} search radius

$\mathbf{s}$ seconds

a semi-major axis

b semi-minor axis

V_{s} shadow velocity

$\mathbf{c}$ speed of light

$\mathbf{A}_{\text{sky}}$ squared area measured by the sky annulus ($\text{AP}_{\text{outer}} - \text{AP}_{\text{inner}}$)

$\mathbf{A}_{\text{source}}$ squared area measured by the $\text{AP}_{\text{source}}$

$\mathbf{cm}^2$ squared centimeters

std	standard deviation
S_{diam}	star's apparent diameter
$D_\star$	stellar distance
$M_\star$	stellar magnitude
$R_\star$	stellar radius
S	strength of the material
long	sub-planetary longitude
TiB	tebibyte
$\mathbf{T}_{\mathrm{J}}$	Tisserand parameter with respect to Jupiter
h_{top}	topography height
λ	wavelength

Contents

Chapter 1

Introduction

Neptune's discovery in 1846 and observed perturbations in Uranus' orbit motivated 19th-century astronomers to search for other distant planets in our SS, leading to the discovery of (134340) Pluto in 1930. After that, the planetary inventory appeared to be complete, with Pluto marking the outer edge of our planetary system (FERNÁNDEZ, 2020). Therefore, at the time, the known SS was composed of nine planets with its satellites, the Trojan asteroids located at Jupiter's Lagrange points, the comets, and the asteroid belt between Mars and Jupiter.

Pluto's discovery triggered speculation about a population of planetesimals orbiting the Sun with distances greater than 30 au and sparked the debate about our planetary system's formation. Although the first TNO was only discovered in 1992, the pioneering work of EDGEWORTH (1943) and KUIPER (1951) resulted in cosmogonic models for SS formation and evolution. Both authors conjectured that the low density of material on the outer edge of the planetesimal disk prevented the solid fragments from collapsing into large bodies. Therefore, a reservoir of planets' embryos may exist at distances between ≈ 30 and 300 au (FERNÁNDEZ, 2020). In this context, TNOs are remnants of the processes that originated the current structure of our planetary system (BARUCCI *et al.*, 2008). Also, valuable sources of information to improve our knowledge about the SS and a constant test to the current cosmogonic models (MORBIDELLI *et al.*, 2008; NESVORNÝ and MORBIDELLI, 2012). For instance, the lack of small craters found in the Pluto-Charon system indicates less than expected small impactors during the formation and evolution of the outer SS (SINGER *et al.*, 2019). In this context, the size-frequency distribution of TNOs smaller than 100 km provides essential information about the SS formation and dynamical evolution.

Hundreds of Centaurs, objects whose orbits are contained between Jupiter and Neptune, and TNOs have been observed since the discovery of (2060) Chiron (KOWAL *et al.*, 1979) and (15760) Albion (JEWITT and LUU, 1993), respectively. However, mainly due to their faintness and small angular sizes as seen from Earth, the physical knowledge of these distant populations is still scarce and fragmented. For instance, up to date, color information is available for about 340 objects (ALVAREZ-CANDAL *et al.*, 2019), and spectra also have been acquired for dozens of objects (PEIXINHO *et al.*, 2020; PINILLA-ALONSO *et al.*, 2020). Only two objects were visited by a spacecraft (SPENCER *et al.*, 2020a,b), and 178 have a size and albedo derived from space-based thermal observations (MÜLLER *et al.*, 2020). But the above-mentioned observational approaches have a high operational cost and can only be used to study a few individuals.

Last decade's technological advances allowed for ground-based direct and indirect observations. Thus, professional telescopes performed direct observations to improve objects' astrometry (ASSAFIN *et al.*, 2010; CAMARGO *et al.*, 2014) or even to study their rotation (HROMAKINA *et al.*, 2018; WONG *et al.*, 2019). One of the most well-succeeded strategies to characterize Centaurs and TNOs from Earth-based observations is the stellar occultation method, which consists of observing a background star while a small body passes in front of it, blocking its flux for a few seconds. Stellar occultation has the advantage of not being dependent on the telescope's or object's size, only on the stellar magnitude and prediction accuracy.

Astronomers used stellar occultations decades ago, in March 1977 and July 1985, to discover the ring systems around Uranus and Neptune, respectively. However, the first detection of a TNO by stellar occultation was made only 12 years ago, when ELLIOT *et al.* (2010) observed 2003 TX_{300} from two well-separated observatories in Hawaii. Since then, an international collaboration between researchers from Brazil (BRA), Spain (ESP), and France (FRA), the so-called Lucky Star project[1], has been using occultations to characterize many distant objects (BRAGA-RIBAS *et al.*, 2019; ORTIZ *et al.*, 2020b).

The main objective of this thesis is to perform a joint analysis of results from stellar occultations and direct observations. Stellar occultation provides an accurate limb, and the rotational light curve allows us to constrain the absolute magnitude and albedo. Finally, we developed a methodology for topography identification in stellar occultation data and a model to characterize the relief detected on the projected limb.

At the beginning of this Ph.D. (August 2018), the sample of objects characterized by stellar occultation data was limited to $\approx$ 11 TNOs and two Centaurs. At that time, the second release of the *Gaia* catalog (GAIA COLLABORATION *et al.*, 2016b) was about to be published, leaving the object's ephemeris as the primary source of uncertainty in the prediction of stellar occultation events. Therefore, the collaboration was working with classical astrometry observations and the analysis of low-quality occultation data to improve small bodies' astrometry and, consequently, the stellar occultation predictions. In the project's first years, we completed and published the analysis of 37 stellar occultation events by 19 TNOs and four Centaurs. We established lower limits of diameter for some objects and derived accurate astrometry to improve objects' ephemeris. The list of studied targets and the derived coordinates were published in ROMMEL *et al.* (2020).

[1] https://lesia.obspm.fr/lucky-star/index.php

This work presents the prediction, campaign efforts, and data analysis of nine stellar occultation events by the dwarf planet candidate (307261) 2002 MS_4, hereafter MS4. The most successful observation involved 116 telescopes and happened on August 8, 2020, when 61 observers detected the occultation. The derived profile revealed remarkable features in the object's limb, which led to a search for topographic studies on other TNOs. Up to date, only the Pluto-Charon system (GRUNDY, 2020) and (486958) Arrokoth (SPENCER *et al.*, 2020a), the targets of NASA's New Horizons mission (WEAVER and STERN, 2008), have detailed information about superficial features. But a theoretical approach published by JOHNSON and MCGETCHIN (1973) helped us to constrain our results.

The occultation detections also motivated the submission of a proposal to observe this object from the Southern Astrophysical Research Telescope (SOAR) in the second semester of 2020 (Appendix D). Such an observational run aimed to derive the MS4 rotational light curve near the occultation date and obtain the rotational phase. Although the proposal was approved, the COVID-19 pandemic prevented the observations. So, we searched for public images and studied them to derive as much rotational information as possible. We tried three distinct approaches: i) relative photometry of sequential nights of data, ii) star background subtraction, and iii) absolute photometry of all available images. Details and limitations of each method are described in Sect. 3.2. Sect. 4.1.2.1, 4.1.2.2, and 4.1.2.3 present the results of each analysis. Finally, the discussion and conclusions from the joint analysis are presented in Sect. 5.

Chapter 2

The Trans-Neptunian Objects and Centaurs

In the middle of the 19th century, the architecture of our planetary system was composed of nine planets, its satellites, the asteroid belt between Mars and Jupiter, Jupiter's Trojans, and some comets, i.e., a largely empty place. Nevertheless, theoretical researchers such as LEONARD (1930), EDGEWORTH (1943), and KUIPER (1951) suggested that some material of the primordial solar nebula could remain in the ultra-Neptunian region. The existence of such discs of small objects implies that the idea of an early Sun surrounded by a Laplacian disk of material was reasonable. And that accretion processes dominated the inner part of the disc forming the large planetary objects, leaving the outer edge material to aggregate only by collisions (FERNÁNDEZ, 2020).

2.1 Discoveries

The theoretical predictions, the development of the Charge Coupled Device (CCD) (BOYLE and SMITH, 1970; SMITH, 1976), and the discovery of a mysterious slow-moving object on October 1977 - (2060) Chiron[1] (KOWAL *et al.*, 1979) motivated David C. Jewitt and Jane X. Luu to start their search for small bodies beyond Neptune in 1987. The program was carried out with the 2.2 m University of Hawaii telescope (Mauna Kea, Hawaii). Only five years later, the first TNO was discovered - 1992 QB_1, currently known as (15760) Albion (JEWITT and LUU, 1993). This provisional designation followed the current naming convention, starting with the discovery year and then the half-month. The second letter and the numerical suffix indicate the discovery order within that half-month. Therefore, the 1992 QB_1 was the 27th small body discovered in the second half of August 1992.

[1]Named after the wisest centaur in Greek Mythology. A detailed description of the Chiron's discovery impact can be found on HODGSON (1978).

Meanwhile, multiple observers' detected the Chiron's anomalous brightening in 1988/89, leading to the cometary activity hypothesis. The cometary coma first appeared in images taken at Lowell Observatory on April 1989, sparking a burst in the research of the "largest well-observed comet nucleus" (HARTMANN *et al.*, 1989, 1990). Therefore, at the time, strong evidence pointed to Chiron as a large and active distant comet, presenting both short and long-term outbursts (LUU, 1993).

Observational runs led by David Rabinowitz allowed for the discovery of a Chiron-like object from observations at Kitt Peak observatory in January 1992 as part of the Spacewatch project (SCOTTI *et al.*, 1992)[2]. 1992 AD showed no signs of cometary activity (HAINAUT *et al.*, 1992) and was redder than any other known asteroid or comet (BUIE and BUS, 1992; MUELLER *et al.*, 1992). Even though, as with Chiron terminology, it was named after a Greek mythological character - (5145) Pholus[3]. In the following four years, astronomers detected four additional planet-crossers objects: (7066) Nessus (1993 HA_2), 1994 TA, 1995 DW_2, and (8405) Asbolus (1995 GO). Based on the statistics of the discoveries, it became clear that those objects belong to a significant population of small bodies with short-lived orbits between the giant planets (HORNER *et al.*, 2004), currently known as the Centaurs (STERN and CAMPINS, 1996). The list of known Centaurs and TNOs increases every day and is publicly available on the MPC web page[4]. Figure 2.1 shows the number of objects discovered every year since 1977.

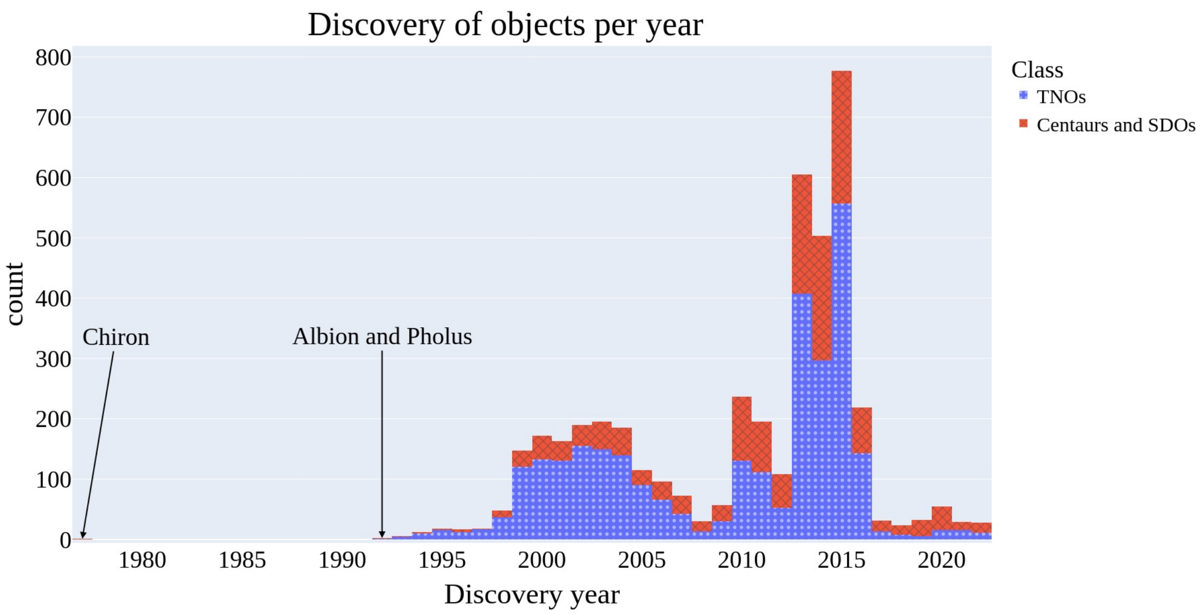

Figure 2.1: Number of distant SS objects discovered every year, according to MPC list, TNOs are presented in blue.

[2]More information about this project and discoveries can be found on https://web.archive.org/web/20081029054125/http://spacewatch.lpl.arizona.edu/outerss_text.html

[3]Details about the terminology are available on https://www.minorplanetcenter.net/db_search/show_object?object_id=5145

[4]Visited on November 9, 2022, the numbers here presented are from https://minorplanetcenter.net/iau/lists/Centaurs.html and https://minorplanetcenter.net/iau/lists/TNOs.html

The discovery rate clearly is not constant in time (Fig. 2.1) and increased significantly between 1999 and 2005, mainly due to observations at Mauna Kea (Hawaii), Kitt Peak (Arizona), and Cerro Tololo Inter-American Observatory (CTIO) (Vicuña). The successful observations increased the known population to around a thousand members by mid-2006. Among them, 130 have Pluto-like orbital parameters, and one object has a similar size to (136199) Eris (BROWN *et al.*, 2006; SICARDY *et al.*, 2011).

In this context, the International Astronomical Union (IAU) held a general meeting in August 2006 and debated the definition of a planet. As a result, the scientific community decided that Pluto was the first member of a new class of objects, the dwarf planets. The other confirmed dwarf planets in the trans-Neptunian region are (136108) Haumea, (136199) Eris, and (136472) Makemake (VERBISCER *et al.*, 2022b). Therefore, citing the IAU resolution B5[5], the current classification of SS bodies, except satellites, is:

1) A planet is a celestial body that
   a) is in orbit around the Sun,
   b) has sufficient mass for its self-gravity to overcome rigid body forces so that it assumes a hydrostatic equilibrium (nearly round) shape, and
   c) has cleared the neighborhood around its orbit.
2) A "dwarf planet" is a celestial body that
   a) is in orbit around the Sun,
   b) has sufficient mass for its self-gravity to overcome rigid body forces so that it assumes a hydrostatic equilibrium (nearly round) shape,
   c) has not cleared the neighborhood around its orbit, and
   d) is not a satellite.
3) All other objects, except satellites, orbiting the Sun shall be referred to collectively as "Small Solar System Bodies".

The number of discoveries began to increase again with the Panoramic Survey Telescope and Rapid Response System 1 (Pan-STARRS 1)[6], which operated at many telescopes between 2008 and 2014. Early in 2013, the operations of the Outer Solar System Origins Survey (OSSOS)[7] started (BANNISTER *et al.*, 2016). Later that year, the Dark Energy Survey (DES)[8] began an extensive study of the universe's expansion and discovered hundreds of small outer solar system bodies. In conclusion, the three surveys' discoveries (Pan-STARRS 1, OSSOS, and DES) comprise half of all known objects. Despite DES being operational, the discovery numbers have decreased since the end of OSSOS operations in 2018 (a detailed description of optical surveys is made by BANNISTER (2020)). However, it is expected that by the end of the Legacy Survey of Space and

[5] `https://www.iau.org/static/resolutions/Resolution_GA26-5-6.pdf`

[6] Details about the project can be obtained on `https://outerspace.stsci.edu/display/PANSTARRS/`.

[7] A detailed survey description is available on `http://www.ossos-survey.org/about.html`

[8] More information can be obtained at project's web page `https://www.darkenergysurvey.org/`.

Time (LSST), the astronomical community will know more than ≈ 40000 TNOs larger than 200 km (LSST SCIENCE COLLABORATION *et al.*, 2009). Therefore, it is just a matter of time before the discovery numbers rise again.

2.2 Dynamical classification

These distant bodies can be classified in different ways according to their size, color, composition, and so on. Nevertheless, due to the considerable distance from Earth and its small size, their physical characteristics are difficult to obtain. On the other hand, the orbital parameters are accessible and provide insights into the SS's evolutionary history. Therefore, the astronomical community uses dynamical properties to classify these objects into sub-populations.

The pioneering works in dynamical classification are those of ELLIOT *et al.* (2005) and GLADMAN *et al.* (2008). Therefore, according to these primary works, the small objects in the outer solar system, except satellites and Trojans, can be divided into:

a) Jupiter Family Comets (JFCs): objects with a Tisserand parameter (TISSERAND, 1896) with respect to Jupiter (T_J[9]) lower than 3.05 and a q lower than 7.35 au;
b) Centaurs: objects with an orbit between the giant planets;
c) Inner Oort cloud bodies: objects with semi-major axis greater than 2000 au;
d) Scattered Disc Objects (SDOs): objects that currently have extreme orbits, usually a perihelion distance between 20 and 40 au, a semi-major axis around 90 au, and e ≈ 0.6;
e) Detached TNOs: non-scattering objects with e > 0.24 that are not so far away that forces external to the solar system can affect their current dynamics ($a < 2000$ au). Also, they are dynamically decoupled from Neptune's influence;
f) Resonant TNOs: individuals trapped in place by the Mean Motion Resonance (MMR) with Neptune. The largest subgroup of objects is the plutinos: named after their most prominent member, Pluto. It comprises the objects that are in the 2:3 MMR region (39.4 au);
g) Classic TNOs: objects with e < 0.25. It can be divided into inner ($a < 39.4$ au), outer ($a > 47.8$ au), and main classical belt. Due to its orbital inclination, it can also be classified as a Hot (i > 5°) or Cold (i < 5°) classical object.

Figure 2.2a presents a not-in-scale scheme of orbital eccentricity as a function of the semi-major axis, showing the location of each class of objects, as defined above. It is important to mention that the curved line starting between Jupiter and Saturn is not a perihelion curve. Instead, it is the boundary between JFCs and other objects. Departing

[9] A dynamical quantity that is approximately conserved during an encounter of a small body with Jupiter. It can be calculated under the restricted three-body problem using the object's orbital elements: a, orbit eccentricity (e), and orbit inclination (i).

from Gladman's scheme, KHAIN *et al.* (2020) developed an automated method to identify MMR with Neptune and updated some classes (Fig. 2.2b). The main changes rely on the classification of Centaurs and SDOs, as follows:

1. Centaurs: objects that suffer strong orbit perturbations due to the proximity with the giant planets. It can be divided into two sub-populations: inner Centaurs with semi-major axis smaller than Neptune's, and outer Centaurs, which have perihelion distances shorter than Neptune's semi-major axis (q $<$ 30 au) and semi-major axes larger than Neptune's ($a > 30$ au);
2. SDOs: objects with orbits fully outside the region of the giant planets that suffer rapid and significant variations in their semi-major axis.

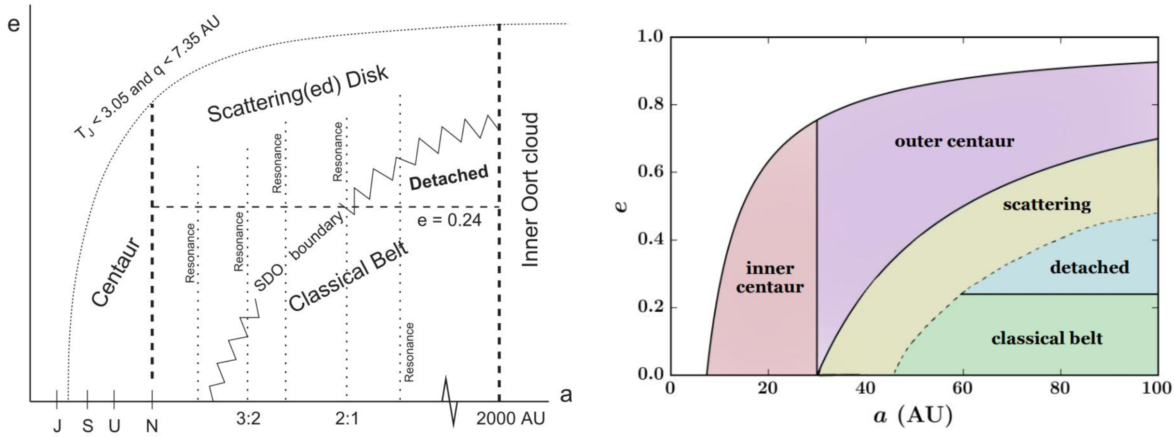

(a) (b)

Figure 2.2: The cartoon (not in scale) for the nomenclature scheme proposed by GLADMAN *et al.* (2008) and KHAIN *et al.* (2020), respectively. a) The giant planet's positions are indicated by its first letters: Jupiter (J), Saturn (S), Uranus (U), and Neptune (N), and the T_J is the Tisserand parameter with respect to Jupiter. b) The solid black curves indicate a constant perihelion distance with q = 7.35 au and q = 30 au (top to bottom).

TRUJILLO and SHEPPARD (2014) noticed that distant orbits within the scattered disk population presented an unexpected clustering in their argument of perihelia. The authors suggested that a super-Earth-mass at 250 au can maintain such alignment but cannot put objects in such orbits. BATYGIN and BROWN (2016, 2021) showed that objects' perihelion positions and orbital planes are tightly confined. The authors stated that an outer planet with about ten times the Earth's mass could maintain such alignment. Its perihelion must be 180° away from the observed bodies' perihelion direction. Such a planet's existence–the "Planet Nine", can inject Oort cloud objects into inner orbits and helps to explain other sub-populations, like the objects with extreme orbital inclinations. The discovery of long-period TNOs with $a > 1000$ au has supported the hypothesis and the search for the "Planet Nine".

Combining orbital and surface information allows the identification of clusters of objects with similar properties, i.e., a possible common origin. The so-called collisional families are remnants of a disruptive collision of the parent planetesimal. Many of those sub-populations are known in the main belt (ZAPPALÀ *et al.*, 1995; NESVORNÝ *et al.*, 2015), but up to date, only one was discovered in the trans-Neptunian region–the Haumea family (BROWN *et al.*, 2007). Except for Haumea and its satellites, the other ten confirmed members are (VILENIUS *et al.*, 2018):

Table 2.1: List of confirmed members of the Haumea collisional family.

Designation	**Reference**
(24835) 1995 SM_{55}	RAGOZZINE and BROWN (2007)
(19308) 1996 TO_{66}	RAGOZZINE and BROWN (2007)
(86047) 1999 OY_{3}	RAGOZZINE and BROWN (2007)
(55636) 2002 TX_{300}	RAGOZZINE and BROWN (2007)
(416400) 2003 UZ_{117}	SCHALLER and BROWN (2008)
(120178) 2003 OP_{32}	RAGOZZINE and BROWN (2007)
(612620) 2003 SQ_{317}	SNODGRASS *et al.* (2010)
(145453) 2005 RR_{43}	RAGOZZINE and BROWN (2007)
(308193) 2005 CB_{79}	SCHALLER and BROWN (2008)
(386723) 2009 YE_{7}	TRUJILLO *et al.* (2011)

2.3 Physical characteristics: current picture

This section intends to summarize the current knowledge about the physical properties of TNOs and Centaurs. As already stated, any direct measurement of these distant objects is complex and requires many hours of observations in large telescopes. Even with professional instruments, surface details, precise size, and shape measurements cannot be obtained with Earth-based observations of the reflected light. Despite the mentioned difficulties, some objects have been studied using different observational approaches, such as a) space-based observations taken by Herschel Space Observatory (HSO)[10], Spitzer Space Telescope (SST)[11], Hubble Space Telescope (HST)[12], and New Horizons spacecraft[13]; b) long exposure images from professional telescopes on Earth and; c) Earth/space-based stellar occultations. The following sections will outline essential concepts and results from all mentioned observational approaches.

[10] https://www.herschel.caltech.edu/
[11] https://www.spitzer.caltech.edu/science-themes/mission
[12] https://hubblesite.org/mission-and-telescope/the-telescope
[13] https://www.nasa.gov/mission_pages/newhorizons/overview/index.html

2.3.1 Equilibrium shapes

According to the IAU definition, to be classified as a dwarf planet, the small body must be in hydrostatic equilibrium, i.e., its gravity overcomes rigid body forces. It is not an easy-to-measure property, but it is related to the object's size and shape. Gravitational forces do not dominate smaller objects, and objects can depart from the equilibrium shapes. Depending on the object's composition and heliocentric distances, the critical diameter between both populations can vary. In the case of TNOs with densities around 1.3 gram per cubic centimeter (g/cm^3), the critical diameter is about 450 km (TANCREDI and FAVRE, 2008). It is thought that a significant fraction of TNOs present equilibrium shapes because they are larger than the mentioned critical diameter and are composed, as far we know, of materials with a fluid behavior (in geological timescales).

The pioneering work about the gravitational equilibrium of not differentiated rotating objects was made by CHANDRASEKHAR (1987). The author stated that an isolated body composed of an incompressible fluid would assume one of the following three-dimensional shapes, depending on the angular momentum:

a) **MacLaurin**: results from a low angular momentum. It consists of an oblate spheroid with axis $a = b > c$, where a is the semi-major axis, b the semi-minor axis, and c the polar axis (Fig. 2.3a);

b) **Jacobi**: is the equilibrium shape of an object with high angular momentum, which is an ellipsoid with three-axis $a > b > c$ (Fig. 2.3b);

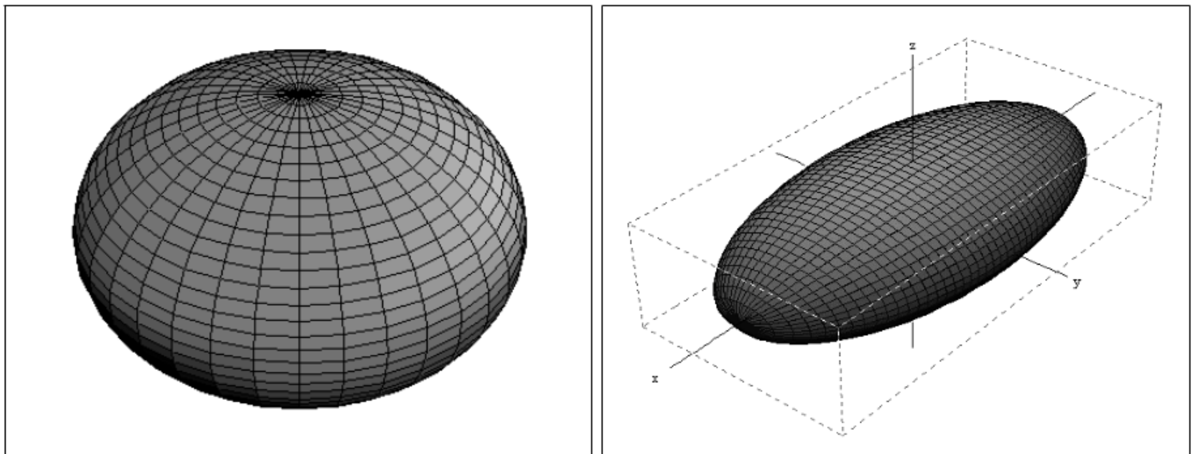

(a) Maclaurin (b) Jacobi

Figure 2.3: Example of a MacLaurin and a Jacobi form (see text). Image reproduced from BRAGA-RIBAS *et al.* (2013).

The author defined two non-dimensional parameters (Γ, Ω) that can be evaluated as a function of the object's axis to infer if the object has an equilibrium shape. MacLaurin forms have $\Gamma \leqslant 0.303$ and $\Omega \leqslant 0.374$, while Jacobi shapes have $0.303 \leqslant \Gamma \leqslant 0.39$ and $0.284 \leqslant \Omega \leqslant 0.374$. Finally, objects with Γ values above 0.39 do not have one of the hydrostatic equilibrium shapes defined above. For $\Omega > 0.374$ values, the angular velocity becomes more important, and the objects may fragment. The mentioned non-dimensional parameters are defined as

$$\Gamma = \frac{\mathrm{L}}{\sqrt{\mathrm{GM}^3 O_\mathrm{R}}}, \qquad \Omega = \frac{\omega^2}{\pi \mathrm{G}\rho},$$

L = angular momentum, O_R = object's radius,
G = gravitational constant, ω = angular velocity,
M = object's mass, ρ = object's density.

2.3.2 Rotation and shape

As stated above, a body with no internal cohesion adopts an equilibrium shape, which depends on its rotational rate. The centrifugal acceleration must be smaller or equal to the gravitational acceleration to maintain the material aggregated into a single body; otherwise, the object breaks into smaller pieces. The critical rotational period where the centrifugal forces overcome the gravitation can be calculated in many ways, depending on the information available and previous assumptions. DAVIDSSON (1999, 2001) took into account the internal cohesion of spherical and non-spherical solid objects. They used the material's tensile strength (expressed in Pascal), the object's radius, and density to calculate the period. In the case of prolate and oblate forms, the ratio of the axes is also considered. On the other hand, PRAVEC and HARRIS (2000) defined the critical period of a prolate spheroid considering only the amplitude of the magnitude variation and the object's density

$$P_\mathrm{crit} = 3.3\sqrt{\frac{1+\Delta m}{\rho}}, \tag{2.1}$$

where P_crit is expressed in h, rotational light curve amplitude (Δm) is given in mag and object's density (ρ) in g/cm^3.

An observer can measure the reflected light of a rotating body over an entire period to derive the Rotational Light Curve (RLC), i.e., the object's flux variation at a given wavelength as a function of time. The object's instrumental magnitude is determined as follows

$$\mathrm{M}_\mathrm{obj} = -2.5 \times \log(\mathrm{F}_\mathrm{obj}), \tag{2.2}$$

where F_obj is the measured flux of the TNO. However, the observed magnitude can vary according to the object's phase angle (α), i.e., the angle between the incident light and the observer direction, as seen from the object's surface (Fig. 3.8).

Continuous observations from Earth revealed that most airless bodies exhibit a brightness enhancement when phase angles are near zero–the opposition surge (GEHRELS, 1956). The intensity of such variations in brightness depends on the object's surface properties. Therefore, hints about the surface are obtained from the behavior of the so-called solar phase curves, i.e., the measured magnitudes as a function of the phase angle. With that, the object's absolute magnitude, i.e., the magnitude of the small body if observed at $\alpha = 0$ at a distance of one au from both the Sun and the Earth, can be calculated.

Even though Earth's orbit size restricts TNOs' solar phase curves up to $\alpha < 2°$, its analysis revealed strong correlations between the linear coefficient (β) and the observed wavelength, as well as with its dynamical class (RABINOWITZ *et al.*, 2007; SCHAEFER *et al.*, 2009). Therefore, a precise solar phase curve may provide invaluable information about the object's surface composition and dynamical classification (Fig. 2.5b).

An attempt to increase the α coverage of TNOs has been ongoing since 2007 by the New Horizons mission. The spacecraft has monitored the photometric behavior of ≈ 30 objects from different viewing geometries ($\alpha < 170°$). The aim is to study the reflectance variation with the object's rotation at different phase angles to determine the solar phase curves, rotational periods, and pole directions. The last two parameters are essential to constrain the object's three-dimensional shape using the RLC's inversion method (PORTER *et al.*, 2022; VERBISCER *et al.*, 2022a,b). The pole direction is essential to determine the aspect angle (ζ), i.e., the angle between the observer and the spin axis at a given epoch (Fig. 3.8).

To illustrate the importance of the ζ in the rotational studies, we will assume two rotating objects in hydrostatic equilibrium with a MacLaurin spheroidal shape and a Jacobi ellipsoidal form, respectively. If $\zeta = 90°$, the photometry reveals distinct RLCs for each object (Fig. 2.4). On the other hand, with $\zeta \approx 0°$, the observer will always see the same surface section, and the RLC will be flat in both cases.

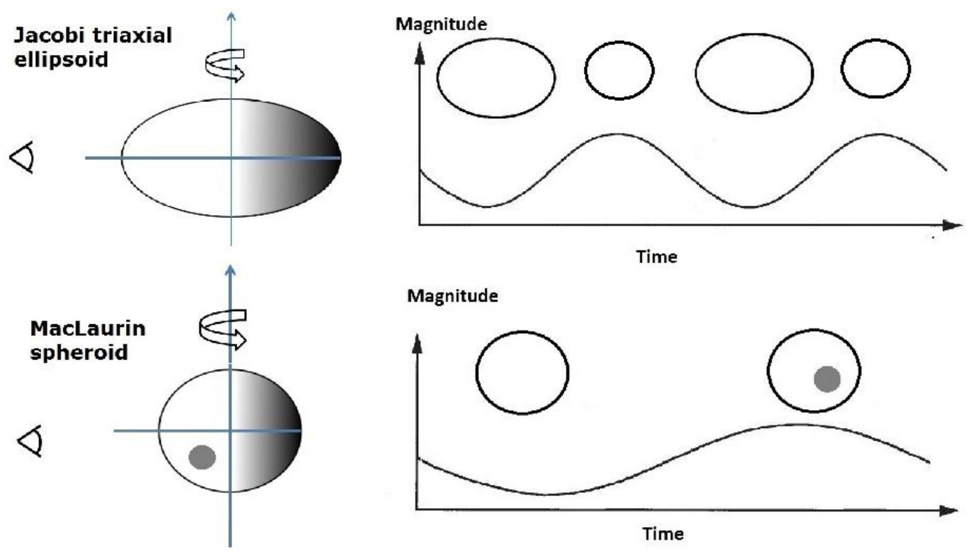

Figure 2.4: Representation of an object with a MacLaurin/Jacobi shape and the resulting RLCs when observed equator-on ($\zeta = 90°$). The lower rotational light curve is caused by the dark spot on the object's simulated surface. Image reproduced from THIROUIN *et al.* (2014).

Objects in hydrostatic equilibrium generally present sinusoidal RLCs, as shown in Fig. 2.4. Due to its elongation, the Jacobi forms present double-peaked curves with amplitudes greater than ≈ 0.15 mag (DUFFARD *et al.*, 2009). Meanwhile, the MacLaurin shapes with featureless surfaces have flat RLCs. If variegation on the superficial albedo exists, the RLCs may present a single peak and small amplitudes. In some cases, it is hard to distinguish between both possibilities. But once done, the Δm can provide a lower limit for the object's elongation by calculating the ratio between the object's axis assuming an equatorial view ($\zeta = 90°$) as follows (THIROUIN, 2013),

$$\Delta m = 2.5 \log\left(\frac{a}{b}\right). \tag{2.3}$$

Despite being a powerful method to derive information about the physical properties of small bodies, only 5% of the Centaurs have some rotational information, with a mean rotational period (P) of 8.1 h (PEIXINHO *et al.*, 2020). Some surveys have been done to acquire rotational information from TNOs and provided a mean P of 8.45 $\pm$ 0.58 h (THIROUIN and SHEPPARD, 2019). According to the authors, the cold classical population has slower rotators with a mean P of 9.48 $\pm$ 1.53 h, and confirmed members of the Haumea collisional family are thought to be faster with a mean P of 6.27 $\pm$ 1.19 h (THIROUIN *et al.*, 2016). No studies dedicated to the rotational properties of hot classical TNOs are available, so it is reasonable to assume a rotational period in the range of 8-9 h for this population. In terms of rotational light curve amplitude, about 65% of the TNOs have $\Delta m < 0.2$ mag. Trends to large Δm are present in small bodies observed by OSSOS (ALEXANDERSEN *et al.*, 2019) and large objects classified as Plutinos and classical cold objects observed from Lowell's observatory (THIROUIN and SHEPPARD, 2018, 2019).

It is common to find variations in solar phase curves (DOBSON *et al.*, 2021) and the RLC's shape or amplitude over many years. They may be caused by changes in ζ (as stated before), unknown satellites (FERNÁNDEZ-VALENZUELA *et al.*, 2019), recent impacts, cometary activity, shifts in the pole direction, multiple objects (RABINOWITZ *et al.*, 2020), or even due to the presence of rings (DUFFARD *et al.*, 2014). For instance, the RLC of the contact binary 2001 QG_{298} observed in 2003 and again in 2010 presented a considerable variation in the shape and amplitude due to observational circumstances (SHEPPARD and JEWITT, 2004; LACERDA, 2011). A complete review of the current knowledge about binaries in the trans-Neptunian region is presented by (NOLL *et al.*, 2020). In conclusion, the rotational analysis provides fundamental information about the object's three-dimensional shape, surface, binarity, and dynamical origin (HANUŠ *et al.*, 2018).

2.3.3 Surface and atmosphere

Object surface information can be obtained using different filters in Earth- and space-based photometric observations. To date, observations of $\approx$ 258 Centaurs and TNOs have been analyzed and classified into the BB, BR, IR, or RR taxonomic groups. This classification scheme is based on a multivariate analysis of the object's BVRJI colors, where BB stands for blue and RR for red colors. The other two are intermediary groups, between blue and red (BARUCCI *et al.*, 2001; BELSKAYA *et al.*, 2015). The TNOs are present in all groups. At the same time, most of the Centaurs belong to BR or RR classes (FULCHIGNONI *et al.*, 2008), a curious property since Centaurs are thought to be originated in the trans-Neptunian region. A trend for red surfaces was also found on the classical belt of TNOs, currently known as the cold classical population, thought to hold the most pristine surfaces (DORESSOUNDIRAM *et al.*, 2008). The plot in Fig. 2.5a presents a combination of the albedo measured by the HSO and spectral slopes from the literature. LACERDA *et al.* (2014a) identified two types of surfaces: dark neutral (blue points) and bright red objects (red points).

Photometric studies in the visible wavelength are an accessible and fast observational approach to studying large amounts of TNOs. Therefore, many studies about objects' visible colors are available in the literature. However, a controversy is being debated by the community regarding the bi-modality presented by some objects (PEIXINHO *et al.*, 2012). In this context, AYALA-LOERA *et al.* (2018) and ALVAREZ-CANDAL *et al.* (2019) analyzed the data under a new approach; they defined an absolute color (H_V-H_R) and a relative phase coefficient ($\Delta\beta = \beta_V - \beta_R$). The authors found a strong anti-correlation between both parameters indicating that redder objects have steeper phase curves (smaller $\Delta\beta$) when observations are performed in the R filter compared to observations in the V filter, and the opposite holds for bluer objects. These findings do not support the bi-modal thesis and present an intrinsic common property for objects in distinct orbits (Fig. 2.5b).

Surface physical and chemical properties can be studied by modeling the object's near-infrared spectrum. Acquiring spectral information for such faint objects is hard, but once it is obtained, the spectrum probes the upper surface layers and provides hints about the presence of minerals and ice (COOK *et al.*, 2023). The absorption features are used to identify chemicals and, combined with albedo information, constrain the surface models, making them converge for a pure or diluted state (BARUCCI *et al.*, 2008). Among the models available in the literature, the widest used to constrain physical-chemical surface properties was proposed by HAPKE (1981), which gives hints about grain sizes, abundances, and surface scattering properties (DEMEO, 2010). The approach is used to obtain composition maps of Pluto from New Horizons images, where latitudinal variations of methane and nitrogen ice are detected (PROTOPAPA *et al.*, 2017). Other interesting features were identified in the TNOs spectrum, like methanol and crystalline water ice

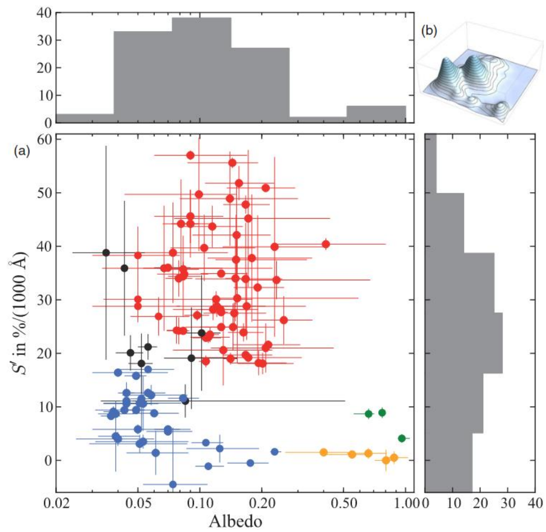

(a) Image from LACERDA *et al.* (2014a).

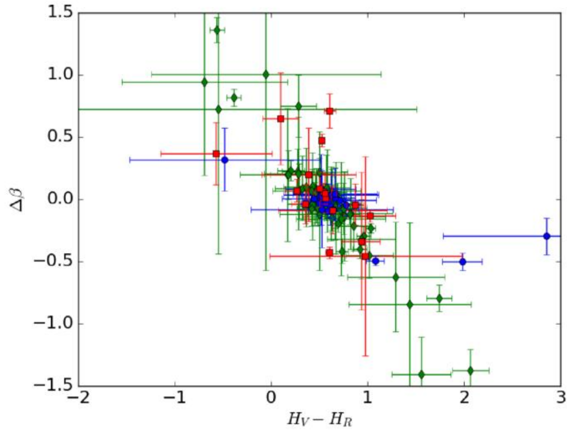

(b) Image from AYALA-LOERA *et al.* (2018).

Figure 2.5: (a) Albedo measured by HSO plotted against visible color quantified by the spectral slope, S', in units of %/(1000 Å). Blue indicates objects with dark neutral color, red dots mark the reddest bodies, Haumea-type surfaces are in orange, large TNOs in green, and black points have ambiguous surface color. (b) Relation between absolute color and relative phase coefficient for about 110 objects. Colors indicate the orbital semi-major axis, where: $a < 40$ au are in blue, green diamonds show objects in the range $40 < a <50$ au, and red squares present bodies with $a > 50$ au.

signatures detected in (136108) Haumea, (50000) Quaoar, (5145) Pholus, (83982) Crantor, (90482) Orcus, (120348) 2004 TY_{364}, and (145453) 2005 RR_{43} (GOURGEOT *et al.*, 2016; SOUZA-FELICIANO *et al.*, 2018).

The knowledge about topography on distant small solar system bodies is still scarce. The exceptions are the targets of the New Horizons mission: the Pluto-Charon system and (486958) Arrokoth. Detailed studies about the imaged fraction of their surfaces are available and reveal some topography (MOORE *et al.*, 2016; NIMMO *et al.*, 2017; SPENCER *et al.*, 2020a). Pluto's imaged hemisphere presented features between -3 km and 4 km, and crater diameters between 0.5 and 250 km. Charon, with a diameter of 1012 km, presents relief features with a variation in elevation of about 25 km, mainly near the Serenity and Mandjet chasms (Fig. 2.6a). The largest observed crater in Charon is the 6 km deep Dorothy Gale, whose diameter is 230 km. Arrokoth, despite being a much smaller object, also has a large crater in its smaller lobe (Fig. 2.6b). It has ≈ 7 km in diameter and 6 km in depth (SPENCER *et al.*, 2020a).

Using the model proposed by JOHNSON and MCGETCHIN (1973) to analyze when an object's self-gravity overcomes the material strength on planetary satellites, we can estimate the scale of supported topography by calculating the

$$h_{\rm top} \leqslant \frac{3\gamma {\rm S}}{4\pi\rho^2 O_{\rm R} {\rm G}}, \tag{2.4}$$

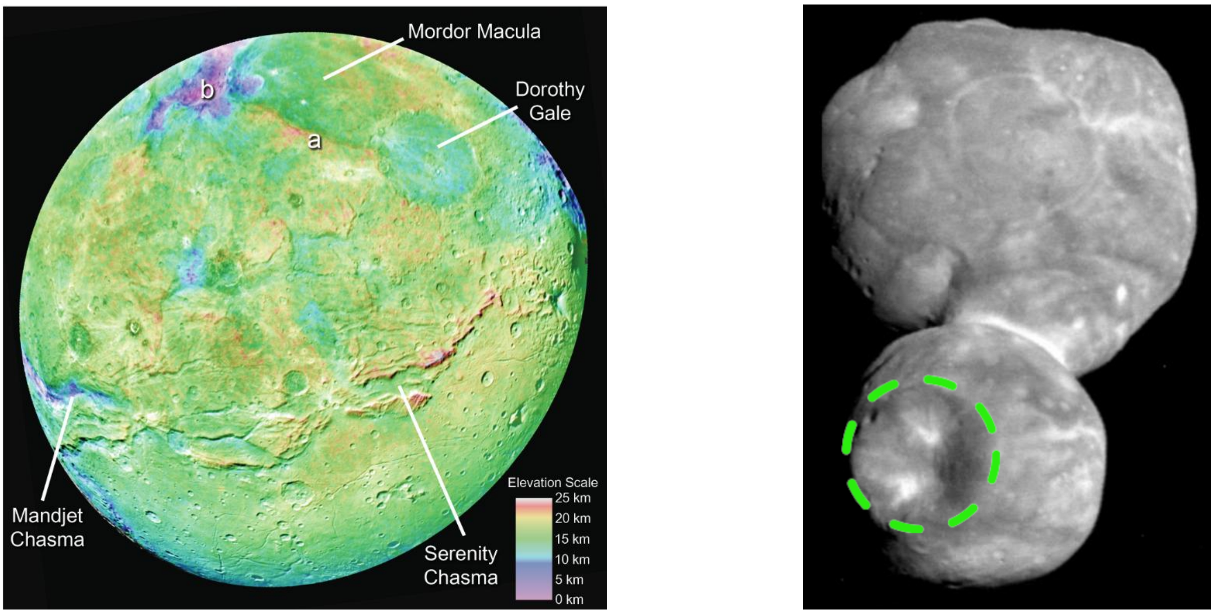

(a) (b)

Figure 2.6: (a) Digital Elevation Model map of Charon. Image reproduced from MOORE *et al.* (2016). (b) Arrokoth craters image taken by New Horizons, where the green circle indicates the region of the largest crater. Image adapted from (SPENCER *et al.*, 2020a).

where $G = 0.00000006674184$ cm^3/g.s^2 is the gravitational constant (G), S is the strength of the material, ρ is the object's density given in g/cm^3, $O_{\rm R}$ is the object's radius expressed in centimeters (cm), and γ is a non-dimensional value that represents the strength of the material with depth, i.e., $\gamma = 1$ at the surface and γ increases toward the nucleus. Using Pluto and Charon's published radius, density (NIMMO *et al.*, 2017), and strength for icy bodies strength of the material $(\mathrm{S})_{\rm ice} = 0.0303 \times 10^9$ Dyn/cm^2, the limits for supported topography in those objects are obtained with Eq. 2.4 and presented in Fig. 2.7. For example, the lower limit for supported topography on Pluto (blue) and Charon (green) surfaces is obtained using $\gamma = 1$ (crosses). However, if material strength increases toward the nucleus, we can use $\gamma = 2$ (dots) to derive topography height closer than the elevations observed by New Horizons.

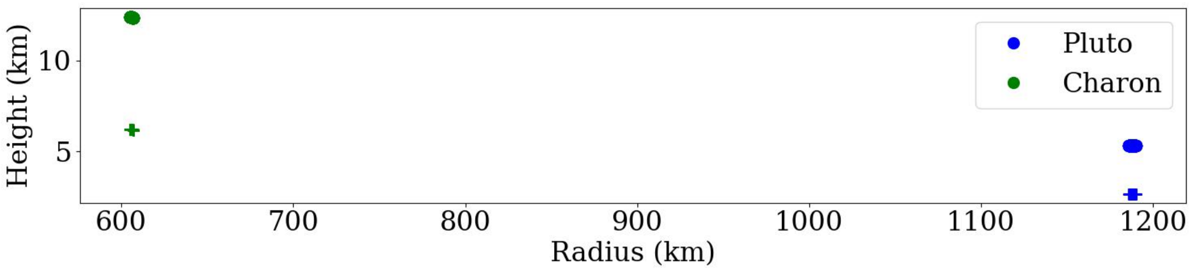

Figure 2.7: Height of supported topography on Pluto (blue) and Charon (green) surfaces, as obtained with Eq. 2.4 and published values for density and radius. Crosses indicate the result using $\gamma = 1$, and dots are for $\gamma = 2$.

A different approach that can be used to estimate topography scales in rocky asteroids and icy satellites was described by TANCREDI and FAVRE (2008). The authors used the relative roughness parameter (THOMAS, 1989) to characterize the departure of an object's limb from the fitted ellipse in a probe image. The parameter is computed by dividing the RMS of the fitted ellipse by the object's radius. As a result, the authors find that planetary satellites in hydrostatic equilibrium have a diameter between 400 - 500 km and a relative roughness smaller than 1%. However, irregular satellites have smaller diameters and greater relative roughness ($< 5\%$).

A stellar occultation also was responsible for detecting a superficial feature on the TNO 2003 AZ_{84}. The usual occultation light curves for airless objects present sharp drops in the star flux (see BRAGA-RIBAS *et al.*, 2013; BENEDETTI-ROSSI *et al.*, 2016; VARA-LUBIANO *et al.*, 2022). However, in February 2012, one of the observers registered the gradual star's disappearance followed by an abrupt reappearance. One explanation for such an effect on a light curve is the presence of topography in the object's limb. Fig. 2.8 presents both hypotheses formulated by the authors to explain the feature in the occultation light curve, a chasm, or a depression. The equivalent diameter of 2003 AZ_{84} is 784 km, and the chasm model presents a 23 km deep and 8 km large structure, much more profound than chasms observed on the Charon surface. The alternative explanation is a shallow depression with a length of $\approx$ 80 km and a depth of $\approx$ 13 km inside the craters range observed in Charon (DIAS-OLIVEIRA *et al.*, 2017).

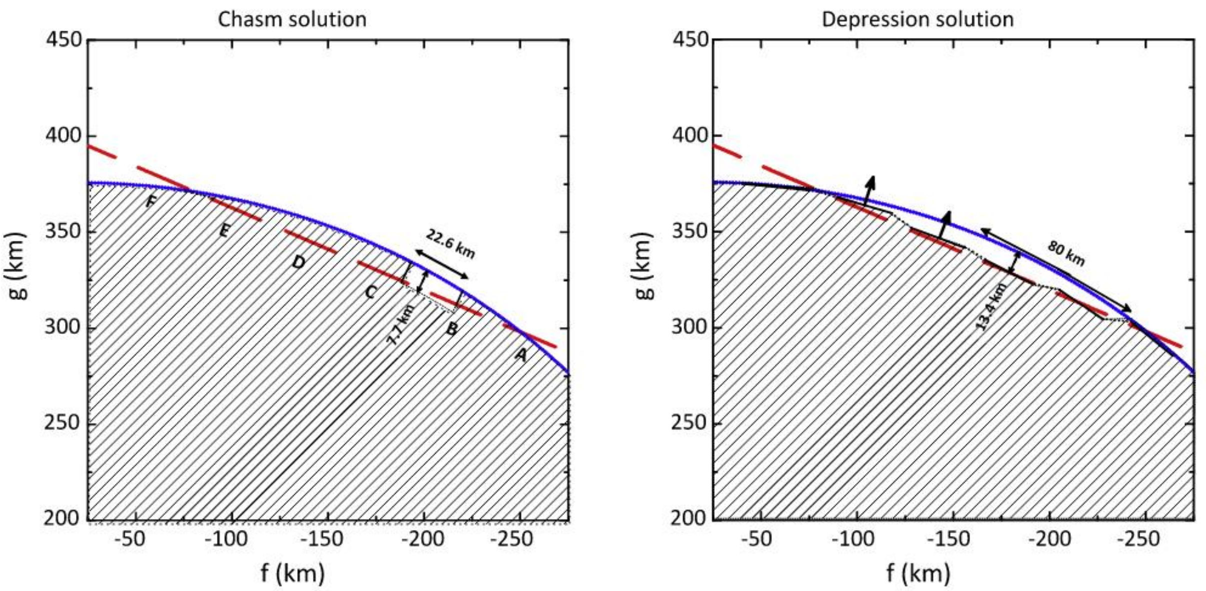

Figure 2.8: Both solutions regarding the topography detected on 2003 AZ_{84} during a stellar occultation observation. Star's apparent path is from right to left, and red segments present its motion during each exposure interval. Image reproduced from DIAS-OLIVEIRA *et al.* (2017).

Regarding atmospheric studies in TNOs, the only confirmed global atmosphere in TNOs is for Pluto. It was discovered in 1988 during a stellar occultation and has been extensively studied by stellar occultations (HUBBARD *et al.*, 1988; ELLIOT *et al.*, 1989; MEZA *et al.*, 2019; PORO *et al.*, 2021; SICARDY *et al.*, 2021), spectroscopy (OWEN *et al.*, 1993; LELLOUCH *et al.*, 2022), and New Horizons in situ observations (FORGET *et al.*, 2021; FAN *et al.*, 2022). The CH_4 and N_2 volatiles identified on Pluto was also inferred to be present in Eris and Makemake, making them good candidates to support at least a seasonal atmosphere (HOFGARTNER *et al.*, 2019; YOUNG *et al.*, 2020). However, the lack of atmosphere detection on stellar occultations by both dwarf planets combined with the similar-to-Pluto spectrum and Eris's high albedo favors the hypothesis of resurfacing mechanisms (SICARDY *et al.*, 2011; ORTIZ *et al.*, 2012). In conclusion, despite the great effort that has been made to search for global and local atmospheres in the largest known TNOs, only upper limits have been placed (SICARDY *et al.*, 2011; BRAGA-RIBAS *et al.*, 2013; ORTIZ *et al.*, 2017; MORGADO *et al.*, 2022; SANTOS-SANZ *et al.*, 2022).

2.3.4 Satellites, jets, and ring systems

Although HST images revealed a close binary object in the Centaur population in 2007 (GRUNDY *et al.*, 2007), no satellites around a Centaur object are known. The discovery of the first satellite of a TNO dates back to 1978 when Pluto's largest moon was detected–Charon (SMITH *et al.*, 1978). Since then, another four were observed: Nix, Hydra, Kerberos, and Styx (WEAVER *et al.*, 2005; SHOWALTER *et al.*, 2011, 2012). Besides Pluto, many other TNOs have small companions, such as Haumea, Eris (BROWN, 2005a,b), Makemake (PARKER *et al.*, 2016), Quaoar, Orcus, 2002 UX_{25}, 2003 AZ_{84} (BROWN and SUER, 2007), Salacia (NOLL *et al.*, 2006), and others[14].

A stellar occultation by Chiron on November 1993 revealed the first measurement of confined material orbiting a Centaur or TNO (BUS *et al.*, 1996; RUPRECHT *et al.*, 2015). Both events revealed light curves with sharp and narrow dips about 300 km from Chiron. As Chiron presented cometary activity in the past, this material probably came from superficial ejections and may be lost quickly. On the other hand, a stable and continuous ring system may still exist around Chiron (ORTIZ *et al.*, 2015; SICKAFOOSE *et al.*, 2020). The discussion about the structure surrounding Chiron is ongoing and needs more data to be solved.

An occultation by the Centaur (10199) Chariklo on June 2013 revealed the first ring system around a small solar system object (BRAGA-RIBAS *et al.*, 2014). It is composed of two confined rings (CR1 and CR2) surrounding Chariklo at 390 and 405 km, respectively (Fig. 2.9a). Both are separated by only $\approx$ 7 km and have an observed width between 4.8 and 9.1 km (MORGADO *et al.*, 2021). Following Chariklo, the first ring around a TNO was also detected in a stellar occultation. The occultation by Haumea on January 2017

[14]The complete list of small binary bodies can be found on `http://www.johnstonsarchive.net/astro/asteroidmoonslist3.html`

revealed an equatorial ring distant about 2,287 km from the main body (ORTIZ *et al.*, 2017), has a width of ≈ 70 km and is located near the 1:3 MMR with Haumea's spin period (Fig. 2.9b). The most curious property of these ring systems is that both are close to the 1:3 MMR with the main body spin and inside the classical Roche limit[15].

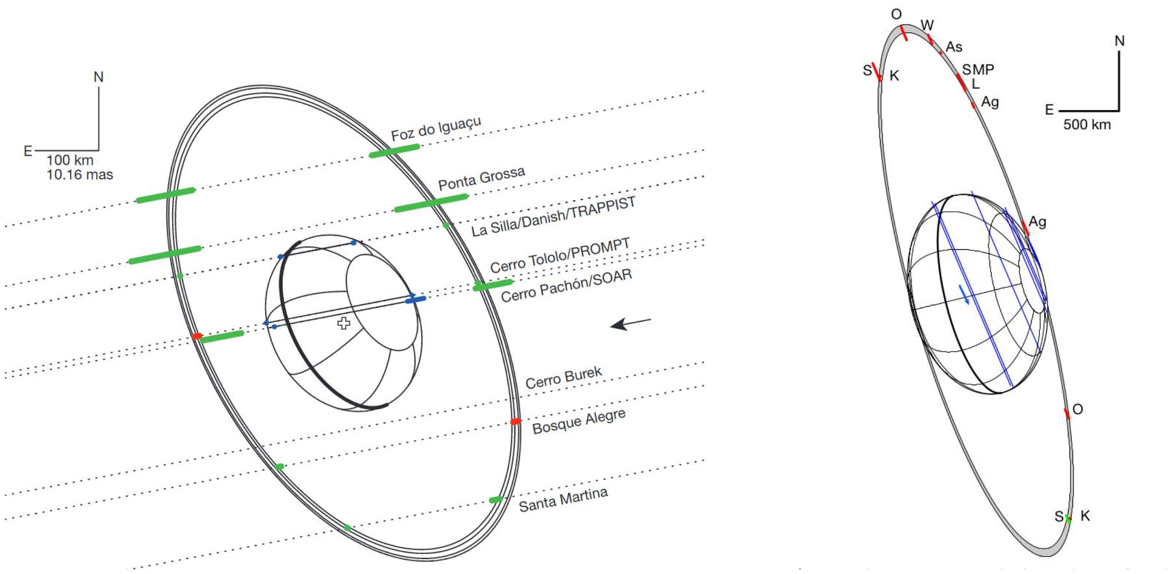

(a) (b)

Figure 2.9: Rings systems (not in scale) around (a) Chariklo and (b) Haumea. Blue segments market detections of the main object, and green lines the detection of rings. Images reproduced from BRAGA-RIBAS *et al.* (2014) and ORTIZ *et al.* (2017), respectively.

These discoveries opened a new field of study, the dynamics involving the origin and maintenance of such structures bound in orbit around objects with such low gravitational fields. For instance, SICARDY *et al.* (2019) performed a detailed study about the stability of the rings detected in Chariklo and Haumea. The authors have shown that topography or elongated shapes may explain the current location of the rings, i.e., when scaling to ring distances in giant planets, they are far from the main body. One of the conclusions is that co-rotation resonance 1:2 must be inside the Roche limit, and rings most likely may be observed in fast rotators. Therefore, although only two objects have confirmed rings, these structures may be more common than thought for small objects in the outer solar system, and the search for new rings is ongoing.

Another curious property of Chariklo's ring system is the small gap between the two confined rings. A general argument for such confinement is the existence of shepherd satellites, such as found on the ϵ ring of Uranus (MELITA and PAPALOIZOU, 2020). However, up to date, no satellites have been observed around Chariklo. Thus, the study of rings around small objects is currently an active research field (LEIVA *et al.*, 2020; GIULIATTI WINTER *et al.*, 2021; MADEIRA *et al.*, 2022). Finally, all the described

[15]"The 'Roche limit is the distance from a planet within which its tides can pull apart a strengthless compact object." (TISCARENO *et al.*, 2013, p.1).

structures observed in Centaurs and TNOs are the first steps of a new field of study: the environment of small objects and the dynamics involved in maintaining such structures.

2.4 Future perspectives

Our current view of Centaurs and TNOs depicts small icy bodies composed of a mixture of water ice, other volatiles, and minerals. The measured albedos are between 0.09 for Quaoar and 0.86 for Eris. The surface's colors vary from gray-blue (BB) to bright red (RR). Also, it is thought that a correlation exists between the visible red colors and the surface composition. For instance, DALLE ORE *et al.* (2015) found that ultra-red objects might contain methanol/hydrocarbon ices on their presumably pristine surfaces. Sunlight irradiation on the pristine volatile ice mixture can produce the observed organic materials. This chemical alteration process is still in progress, as evidenced by the Centaurs' slightly higher organic amounts.

The bulk density of TNOs and Centaurs is the key to better understanding their chemical composition and internal structure. For instance, a pure water ice body will present a density of 1 g/cm^3, while an object composed of an ice/rock mixture would present densities between 2 - 2.5 g/cm^3. However, to calculate the object's bulk density, we need to measure its size and mass. The sizes can be derived from thermal observations from space, and when a satellite exists, the mass can be obtained by dynamic calculations. However, only a few objects have known satellites or even a good main body size determination. Table 2.2 presents the objects with a density determination/estimation from the literature.

Table 2.2: Densities of Centaurs and TNOs as published in the literature.

N°	Name	Class	ρ (g/cm^3)	Reference
281371	2008 FC76	CEN	>0.28	HROMAKINA *et al.* (2018)
10199	Chariklo	CEN	$0.97^{+3.0}_{-1.8}$	LEIVA *et al.* (2017)
10199	Chariklo	CEN	$0.796^{+0.02}_{-0.04}$	LEIVA *et al.* (2017)
5145	Pholus	CEN	0.5	TEGLER *et al.* (2005)
24835	1995 SM55	TNO	>0.6	THIROUIN *et al.* (2016)
26308	1998 SM165	TNO	$0.59^{+0.16}_{-0.13}$	KOVALENKO *et al.* (2017)
469306	1999 CD158	TNO	>0.85	
86047	1999 OY3	TNO	>0.12	THIROUIN *et al.* (2016)
612148	2000 CG105	TNO	>0.61	
47932	2000 GN171	TNO	>0.62	DOTTO *et al.* (2008)
612239	2001 QC298	TNO	$1.14^{+0.34}_{-0.3}$	VILENIUS *et al.* (2014)
139775	2001 QG298	TNO	$0.59^{+0.143}_{-0.047}$	LACERDA and JEWITT (2007)
275809	2001 QY297	TNO	$0.92^{+1.3}_{-0.27}$	VILENIUS *et al.* (2014)

Continued on next page

Table 2.2: Densities of Centaurs and TNOs as published in the literature.

N°	Name	Class	ρ (g/cm^3)	Reference
524366	2001 XR254	TNO	$1.0^{+0.96}_{-0.56}$	VILENIUS *et al.* (2014)
126719	2002 CC249	TNO	>0.34	THIROUIN and SHEPPARD (2017)
612349	2002 GH32	TNO	>2.56	THIROUIN *et al.* (2016)
95626	2002 GZ32	TNO	>0.37	DOTTO *et al.* (2008)
55636	2002 TX300	TNO	>0.15	HROMAKINA *et al.* (2018)
55637	2002 UX25	TNO	0.8±0.13	BROWN and BUTLER (2017)
119979	2002 WC19	TNO	3.47 ± 1.7	KOVALENKO *et al.* (2017)
208996	2003 AZ84	TNO	0.87 ± 0.001	DIAS-OLIVEIRA *et al.* (2017)
——	2003 HA57	TNO	>0.87	THIROUIN *et al.* (2016)
——	2003 HX56	TNO	>0.41	
120178	2003 OP32	TNO	>0.41	HROMAKINA *et al.* (2018)
612620	2003 SQ317	TNO	0.86-2.67	LACERDA *et al.* (2014b)
416400	2003 UZ117	TNO	>0.31	THIROUIN *et al.* (2016)
455502	2003 UZ413	TNO	>0.72	PERNA *et al.* (2009)
			>1.161	SANTOS-SANZ *et al.* (2021)
84922	2003 VS2	TNO	$1.4^{+1}_{-0.3}$	BENEDETTI-ROSSI *et al.* (2019)
90568	2004 GV9	TNO	>0.37	DOTTO *et al.* (2008)
444030	2004 NT33	TNO	>0.16	HROMAKINA *et al.* (2018)
612891	2004 TT357	TNO	>0.78	THIROUIN *et al.* (2017)
144897	2004 UX10	TNO	>0.22	PERNA *et al.* (2009)
469708	2005 GE187	TNO	>0.89	THIROUIN *et al.* (2016)
145451	2005 RM43	TNO	>0.15	PERNA *et al.* (2009)
145452	2005 RN43	TNO	>0.2	HROMAKINA *et al.* (2018)
145453	2005 RR43	TNO	>0.47	PERNA *et al.* (2009)
202421	2005 UQ513	TNO	>0.2	HROMAKINA *et al.* (2018)
225088	2007 OR10	TNO	1.75 ± 0.07	KISS *et al.* (2019)
229762	2007 UK126	TNO	1.04 ± 0.17	GRUNDY *et al.* (2019)
315530	2008 AP129	TNO	>0.48	THIROUIN *et al.* (2016)
470599	2008 OG19	TNO	0.609 ± 0.004	FERNÁNDEZ-VALENZUELA *et al.* (2016)
386723	2009 YE7	TNO	>1.22	THIROUIN *et al.* (2016)
469705	|=Kagara	TNO	$1.1^{+0.66}_{-0.56}$	KOVALENKO *et al.* (2017)
148780	Altjira	TNO	$0.3^{+0.5}_{-0.14}$	VILENIUS *et al.* (2014)
486958	Arrokoth	TNO	0.155 - 0.6	KEANE *et al.* (2022)
66652	Borasisi	TNO	$2.1^{+2.6}_{-1.2}$	VILENIUS *et al.* (2014)
65489	Ceto	TNO	$0.64^{+0.16}_{-0.13}$	SANTOS-SANZ *et al.* (2012)
136199	Eris	TNO	2.52 ± 0.05	SICARDY *et al.* (2011)
136108	Haumea	TNO	1.885 ± 0.08	ORTIZ *et al.* (2017)
38628	Huya	TNO	0.83 ± 0.03	SANTOS-SANZ *et al.* (2022)

Continued on next page

Table 2.2: Densities of Centaurs and TNOs as published in the literature.

N°	Name	Class	ρ (g/cm^3)	Reference
47171	Lempo	TNO	$0.62^{+0.13}_{-0.12}$	MOMMERT *et al.* (2012)
136472	Makemake	TNO	1.7 ± 0.36	ORTIZ *et al.* (2012)
385446	Manwë	TNO	0.75	GRUNDY *et al.* (2014)
341520	Mors-Somnus	TNO	>0.46	THIROUIN *et al.* (2014)
90482	Orcus	TNO	1.4-2 ± 0.3	BROWN and BUTLER (2018)
134340	Pluto	TNO	1.857 ± 0.006	NIMMO *et al.* (2017)
50000	Quaoar	TNO	2.13 ± 0.29	BROWN and BUTLER (2017)
120347	Salacia	TNO	1.26 ± 0.16	
79360	Sila-Nunam	TNO	0.73 ± 0.28	VILENIUS *et al.* (2012)
			$0.73^{+0.23}_{-0.37}$	GRUNDY *et al.* (2012)
88611	Teharonhiawako	TNO	$0.6^{+0.36}_{-0.33}$	VILENIUS *et al.* (2014)
42355	Typhon	TNO	$0.36^{+0.08}_{-0.07}$	SANTOS-SANZ *et al.* (2012)
174567	Varda	TNO	1.78 ± 0.06	SOUAMI *et al.* (2020)
			1.23 ± 0.04	
20000	Varuna	TNO	$0.992^{+0.86}_{-0.15}$	LACERDA and JEWITT (2007)

Precisely on this point, the stellar occultation technique can make outstanding contributions. The method has demonstrated that precision at km-level on sizes and shapes can be derived from multichord detections, including the possibility of measuring the satellites, atmosphere, and rings. With the advance of accurate predictions, we can derive even features on an object's surface. Although amateur networks have contributed to our research worldwide, most observers have small telescopes and can only observe bright stars, which are rarely occulted by a Centaur or TNO. In the future, we expect that larger telescopes and faster CCD cameras will be available to these astronomers, allowing the observation of fainter targets. Also, future fully dedicated robotic networks, arranged in the Earth's north-south direction, are being planned (ORTIZ *et al.*, 2020b).

Recent projects like the Legacy Survey of Space and Time (LSST), James Webb Space Telescope (JWST), Extremely Large Telescope (ELT), and Thirty Meter Telescope (TMT) already have specific programs to observe stellar occultations or may be able to include such runs (SCHWAMB *et al.*, 2018; ORTIZ *et al.*, 2020b). Also, space telescopes already in operation allow some tests to verify equipment feasibility to observe such events (MORGADO *et al.*, 2022). Other possibilities are telescopes attached to stratospheric balloons and airplanes, e.g., the Stratospheric Observatory for Infrared Astronomy (SOFIA), or even observing occultations in the radio domain with Earth-based radiotelescopes (ORTIZ *et al.*, 2020b).

As stated above, our knowledge about the SS formation and evolution is tight to the knowledge about Centaurs and TNOs. Especially the size, density, and orbital distribution of these distant bodies constrain the current SS formation models. Recent results are mainly based on a combination of different observational methods (like those described in this work). However, with the new results, new questions arise about key processes, like the planetesimal accretion and transport of material. In this context, some open questions are:

1. Cryovolcanism was recently confirmed on Pluto's surface (SINGER *et al.*, 2022). However, is cryovolcanism present on other TNOs?
2. How many binaries exist? Are they remnants of Mega-collisions? Has the formation process favored the binaries formation in some orbital regions?
3. What is the fraction of the trans-Neptunian belt that is primordial? What fraction was implanted from inner regions?
4. What fraction of the Centaurs and TNOs have atmosphere or ring systems? Are these structures stable or transient?
5. What is the size-frequency distribution of craters in the outer solar system?
6. What is the upper limit of supported topography on mid-size TNOs?
7. Topography can create resonances in an object's surroundings and consequently create/maintain rings?

Chapter 3

Methods

3.1 Stellar occultation

A stellar occultation occurs when an object obscures a distant star from the perspective of the observer's referential. In a typical occultation, the star will abruptly disappear as the small airless body moves in front of it. The stellar flux, as a function of time–OLC, is obtained by recording a sequence of images. An accurate astrometric position and the body profile can be derived from single or multiple light curves of the same event (SICARDY *et al.*, 2011; BRAGA-RIBAS *et al.*, 2013; GOMES-JÚNIOR *et al.*, 2015; BENEDETTI-ROSSI *et al.*, 2016; LEIVA *et al.*, 2017; BENEDETTI-ROSSI *et al.*, 2019; DESMARS *et al.*, 2019; BUIE *et al.*, 2020a; GOMES-JÚNIOR *et al.*, 2020; ORTIZ *et al.*, 2020a; ROMMEL *et al.*, 2020; SOUAMI *et al.*, 2020; SANTOS-SANZ *et al.*, 2021; MORGADO *et al.*, 2022).

Another key aspect of the method is the possibility of studying surrounding structures and following them up over time. For example, the OLCs may detect secondary events caused by rings, dust, or satellites (BUS *et al.*, 1996; ORTIZ *et al.*, 2012; BRAGA-RIBAS *et al.*, 2014; ORTIZ *et al.*, 2015; RUPRECHT *et al.*, 2015; ORTIZ *et al.*, 2017; MEZA *et al.*, 2019; MORGADO *et al.*, 2021). Similarly, the star's gradual disappearance or reappearance may reveal an atmosphere or even local superficial topography (ELLIOT *et al.*, 1989; DIAS-OLIVEIRA *et al.*, 2017; SICARDY *et al.*, 2019, 2021; MARQUES OLIVEIRA *et al.*, 2022). In addition, the data may not only expose information about the occulting object but also allow the discovery of a companion star (BÉRARD *et al.*, 2017; SICKAFOOSE *et al.*, 2019; LEIVA *et al.*, 2020).

Currently, the stellar occultations field plays an important role in adequately characterizing and understanding small bodies from the outer SS. Ground-based detections provide the size and shape of distant small bodies with sub-kilometric accuracy, and such results only compete with in-situ observations made by a spacecraft. The particular case of (486958) Arrokoth is an excellent example to illustrate the power of stellar occultation data. The object was observed during a stellar occultation in July 2017 (BUIE *et al.*, 2020b) and visited by the New Horizons mission (WEAVER and STERN, 2008) in January 2019 (STERN *et al.*, 2019). A comparison between the results from both observations is presented in Fig. 3.1.

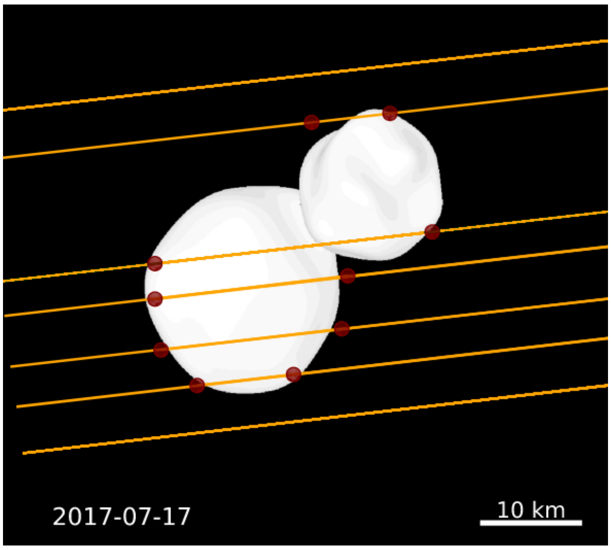

Figure 3.1: Comparison between the (486958) Arrokoth limb derived from stellar occultation and from New Horizons data. The lines represent stellar occultation data with dots marking the disappearance and reappearance instants, while in white is the limb derived from the spacecraft data. Image adapted from BUIE *et al.* (2020b).

The success of a stellar occultation depends on the following factors: accurate predictions, accurate recording of time, target star with high Signal-to-Noise Ratio (SNR), and a data reduction procedure that considers all the known effects in the light curve, e.g., Fresnel diffraction and Earth's precession. Therefore, the work with occultations involves three main stages: prediction, observations, and data analysis. The following sections will describe the particularities and details needed for each stage.

3.1.1 Prediction

The prediction of stellar occultation events is based on comparing stars' and objects' geocentric positions on the sky plane (as described by ASSAFIN *et al.* (2010) and GOMES-JÚNIOR *et al.* (2022)). The search radius ($S_{\rm R}$) around the object's ephemeris is defined by Eq. 3.1, considering the object's geocentric distance (Δ), the Earth's radius ($E_{\rm R}$), and the object's radius ($O_{\rm R}$). Every star that falls inside this searching region is a candidate for a stellar occultation event, i.e., we consider that a reliable prediction must have uncertainties of the same order as the body's apparent radius on the sky plane

$$S_{\rm R} = \tan^{-1}\left(\frac{E_{\rm R} + O_{\rm R}}{\Delta}\right). \tag{3.1}$$

For each candidate star on a plane tangent to the celestial sphere with the observer in the Earth's center, we can calculate the geometric quantities needed to detect the stellar occultation. Firstly, consider two consecutive body positions close to the star, and at respective initial time (t_{i}) and final time (t_{f}), with $t_{\mathrm{f}} > t_{\mathrm{i}}$. Then, the instant ($t_0$) and the separation between the object and star at the Closest Approach (C/A) configuration can be determined,

$$\mathrm{C/A} = \sqrt{{as_{\mathrm{i}}}^2 - \left(\frac{{as_{\mathrm{i}}}^2 - {as_{\mathrm{f}}}^2 + {\Delta O_{\mathrm{if}}}^2}{2\Delta O_{\mathrm{if}}}\right)^2}, \tag{3.2}$$

$$t_0 = t_{\mathrm{i}} + (t_{\mathrm{f}} - t_{\mathrm{i}})\sqrt{\frac{{as_{\mathrm{i}}}^2 - (\mathrm{C/A})^2}{{\Delta O_{\mathrm{if}}}^2}}, \tag{3.3}$$

where as_{i} and as_{f} are the initial and final angular separation between the star and the initial/final ephemeris position. The ΔO_{if} is the angular separation between object's initial and final positions. Then, the shadow velocity (V_{s}) is calculated using the object's geocentric distance (Δ),

$$V_{\mathrm{s}} = \frac{\Delta.\sin(\Delta O_{\mathrm{if}})}{t_{\mathrm{f}} - t_{\mathrm{i}}}. \tag{3.4}$$

Finally, with the propagated star's coordinates and the object's position at the instant of the closest approach (t_0), the shadow direction (P/A) can be calculated. By calculating the Local Solar Time (LST), one can check if the event's C/A will happen during day or night time

$$\mathrm{LST} = t_0 + long, \tag{3.5}$$

where *long* is the sub-planetary longitude obtained from the difference between the Right Ascension (RA) and the mean sidereal time in Greenwich. The calculated parameters allow the drawing of the so-called occultation map (Fig. 3.2) representing the predicted shadow path over the Earth's surface, the shadow direction, the shadow velocity, the Closest Approach, the instant of the closest approach, Right Ascension and Declination of the target star. Also, the stellar magnitudes are normalized to a reference shadow velocity of 20 km/s by

$$M_{\star}{}^{*} = M_{\star} + 2.5\log_{10}\left(\frac{V_{\mathrm{s}}}{20}\right). \tag{3.6}$$

The 20 kilometers per second (km/s) value is a typical velocity of stellar occultations occurring around Pluto's opposition. Therefore, $M_{\star}{}^{*}$ may highlight slower events even if they involve fainter stars (ASSAFIN *et al.*, 2010).

Although stellar occultation is a powerful and well-recognized technique, some problems arise when small and distant objects come into the picture. For instance, to ensure a stellar occultation by the largest TNO–Pluto, the required precision of the prediction must be better than 40 milliarcseconds (*mas*). In the past, a great effort was made to

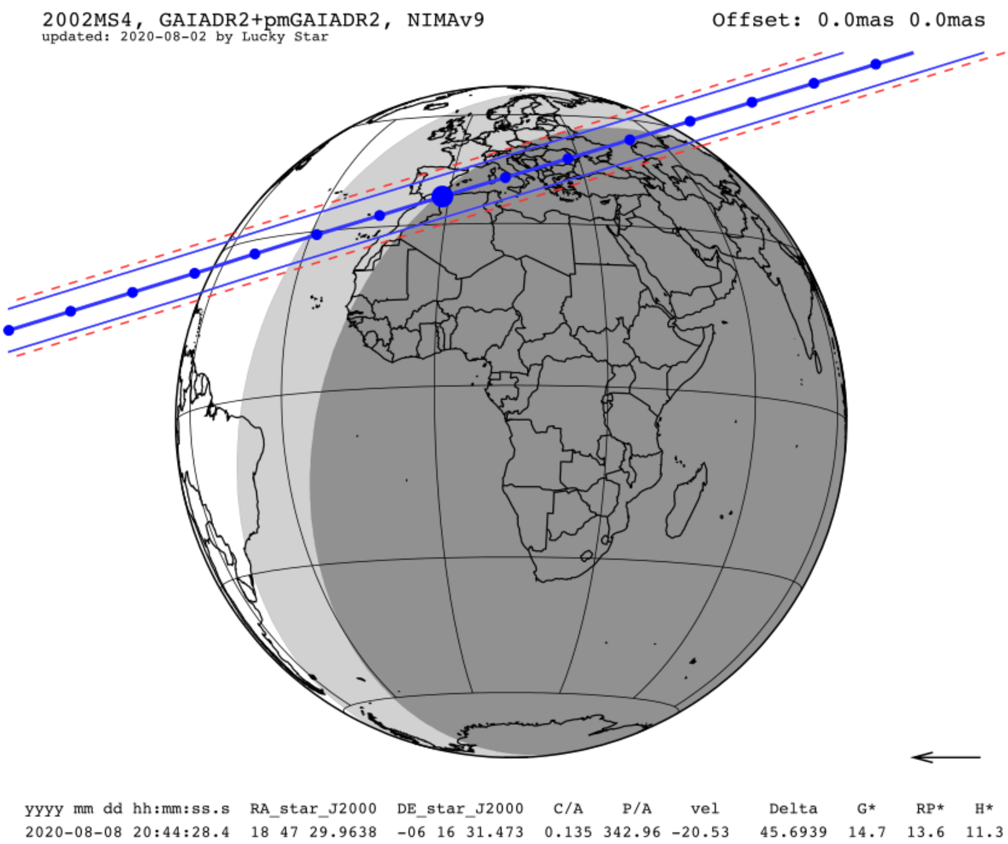

Figure 3.2: Example of an occultation map showing the predicted shadow path (blue lines) with uncertainties (dashed red lines). The blue dots present the shadow center every minute, with the largest one showing the instant of the C/A. The global grayscale presents the locations where it will be day or night. The arrow in the bottom right corner indicates the shadow direction. The information at the top and bottom is helpful for campaign preparation (see text).

build an accurate stellar catalog. The so-called Wield Field Imager (WFI) catalog allowed us to refine stellar positions and the ephemeris of many TNOs. Thus, improving the predictions of stellar occultations (ASSAFIN *et al.*, 2010, 2012; CAMARGO *et al.*, 2014).

Due to the sub-*mas* accuracy of the star catalogs provided by the *Gaia* mission (GAIA COLLABORATION *et al.*, 2016b), the accuracy of the stellar position is no longer a problem. The current occultation predictions depend mainly on the ephemerides' quality because *Gaia* DR3 only provided astrometry for eight Centaurs and 24 TNOs (TANGA *et al.*, 2022). Therefore, periodic astrometric runs have been performed on OPD and Sierra Nevada Observatory - Spain (OSN). In addition, astrometric positions derived from previous stellar occultations are collected, even if they are single-chord detections (ROMMEL *et al.*, 2020). Finally, ephemerides are refined through the NIMA method (DESMARS, 2015). It weighs the object's position based on the stellar catalog used on the astrometric analysis, the number of positions obtained per night, and the observational site. If needed, the object's position relative to the target star can be derived in the days preceding the stellar occultation, and the prediction is improved (ORTIZ *et al.*, 2020b). All prediction maps and complementary information from this stage are publicly available on the Lucky Star web page[1].

The most promising events are filtered across all predictions to conduct observational campaigns. The selection is based on the object's scientific interest, the target star's magnitude, the event's velocity, and the availability of observers inside the shadow path. For instance, the abundance of small telescopes on the Earth's surface is greater than that of large facilities. Therefore, the selection will favor events involving stars with G mag $\leqslant 18$. We are aware of only six occultation detections involving fainter stars. All the predictions and campaigns are available to registered users of the recently implemented Occultation Portal[2] (OP, KILIC *et al.*, 2022). Designed to manage all stellar occultation campaigns from a central server, Occultation Portal (OP) allows the organization of the images' upload, register of equipment, and observational sites.

3.1.2 Observational campaigns

The sky motion of a TNO seen from Earth during short periods of time is mainly due to the parallax motion as the Earth travels in its orbit, and typical speeds are between 15 and 20 km/s. Therefore, for object sizes between 200 and 2000 km, the stellar occultation can last 10 to 100 s. Such fast events require cameras capable of capturing a large number of images in a short period of time. Simultaneously, the detector must be sensitive enough to detect the star in short exposure times.

Some instruments frequently used to record stellar occultation events are the models built by Raptor[3], Watec[4], QHY174M-GPS[5], and Andor[6]. They are equipped with the well-known CCD detector or its cheaper successor, the Complementary Metal Oxide Semiconductor (CMOS) detector. Both are composed of a silicon chip containing an array of photosensitive units - the pixels. During each exposure, the received photons are converted into electrons and stored inside the pixels. The difference between them is in the readout method. In a CCD, the charge stored in each pixel is read individually, converted into a voltage, and becomes a digital signal. In the CMOS detector, the charge is converted into voltage within the pixel. Then, quickly entire lines are read out and converted into a digital signal (GREFFE *et al.*, 2021).

A reliable time source is another requisite to acquire trustful stellar occultation data. Usually, the camera is synchronized with the Universal Time (UT) using a Global Po-

[1] https://lesia.obspm.fr/lucky-star/predictions.php
[2] https://occultation.tug.tubitak.gov.tr/
[3] `https://www.raptorphotonics.com/`
[4] `https://www.wateccameras.com/`
[5] `https://www.qhyccd.com/`
[6] `https://andor.oxinst.com/products/scientific-cmos-emccd-and-ccd-research-cameras`

sitioning System (GPS) or a Network Time Protocol (NTP). The acquisition instant is recorded in the image header or, in the case of video recordings, written over the frames by an auxiliary system named Video Time Inserter (VTI). Even if the observer uses the GPS during the video acquisition, time shifts are required to achieve absolute time according to the camera model[7]. Finally, the recorded data and all information about the observation can be uploaded to the OP or sent directly to the researchers.

Despite having an accurate prediction and all the mentioned requisites, there is no guarantee of a successful observation. At the observational stage, many variables still play substantial roles. The most evident difficulties are the weather, the star's elevation above the horizon, the lunar phase, the organization logistics, and the training of local observers. Another critical aspect is covering the shadow path with enough observing stations, i.e., the broader the coverage in the perpendicular shadow direction, the higher the chances of success (ORTIZ *et al.*, 2020b).

In spite of all the mentioned requirements and difficulties, the evolution of the number of occultations slowly increased between 2009 and 2014 (Fig. 3.3) due to collaboration observational efforts (ASSAFIN *et al.*, 2010; CAMARGO *et al.*, 2014). In 2015, these predictions were unavailable, and the number of detections decreased. It accelerated again in 2016 with the first release of the *Gaia* catalog. Consequently, the success rate inside the international collaboration in 2020 was one detection for every 5.5 attempts. By success, we mean the detection of the stellar occultation from at least one site (ORTIZ *et al.*, 2020b). The successful detections of TNOs and Centaurs also motivated the prediction and observation of other SS objects, for instance, stellar occultations by satellites and Trojans. Therefore, despite a decrease in the detection of TNOs and Centaurs in Fig. 3.3, the total number of observed events continues to increase. These numbers and additional information on detected events are publicly available in our database (BRAGA-RIBAS *et al.*, 2019).

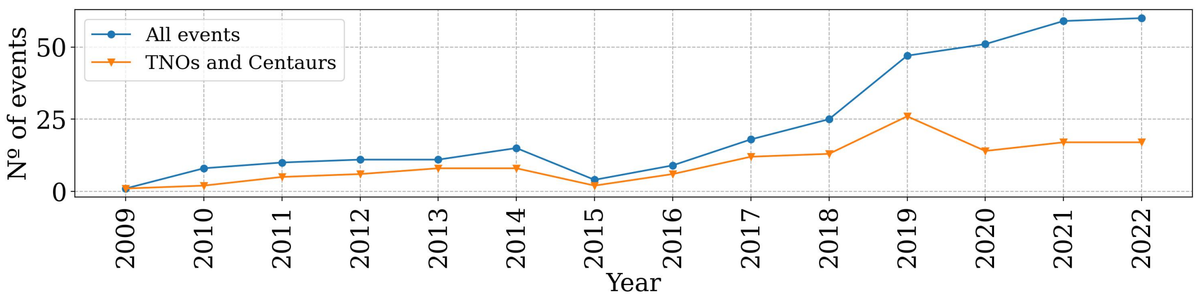

Figure 3.3: Since 2009, the plot presents all stellar occultation detections as a function of time (blue dots). The orange triangles show the events caused by TNOs or Centaurs, except Pluto.

[7]A detailed analysis for some camera models is available on `http://www.dangl.at/ausruest/vid_tim/vid_tim1.htm#wat_910hx`

3.1.3 Differential aperture photometry

The standard data archival format for astronomical data sets is the Flexible Image Transport System (FITS)[8]. However, depending on the available equipment, an observer can acquire data in video format: avi[9], adv[10], or ser[11]. In those cases, before any analysis, the video is submitted to TANGRA[12] (PAVLOV, 2020) or AUDELA[13] with each frame converted into a FITS file. In addition, depending on the acquisition software, the data set can be recorded in different image formats like cpa[14] or jpg[15], also needing to be converted to FITS format. When available, calibration images (bias, flats, and darks) are used to correct the science images using the standard Image Reduction and Analysis Facility (IRAF, BUTCHER and STEVENS, 1981; TODY, 1993) or PYTHON algorithms such as those available on ASTROPY package (ASTROPY COLLABORATION *et al.*, 2013). Once all FITS images are calibrated, the next step is to derive the flux as a function of time.

Aperture photometry is a method to calculate the flux of a source by picking concentric apertures around it (Fig. 3.4). The inner aperture radius must be optimized to obtain the highest SNR. Then, the source flux is measured by summing all Analogical Digital Units (ADUs) inside the inner circle. Next, the sky brightness per pixel is computed by picking an annulus around the inner aperture. It is desirable to leave a dead zone between the inner aperture and the sky annulus and not include faint background sources in the sky annulus. The ignored pixels are essential to avoid measuring nearby stars' flux or even the same pixel's flux twice.

In differential aperture photometry, the aim is to eliminate Earth's atmosphere influence. Therefore, the photometry is performed for the target star (red circle) and a set of well-isolated comparison stars (blue circles in Fig. 3.4) present on the FOV. The number of comparison stars depends on the FOV of the image, how many suitable stars are available, and how much the FOV moves, i.e., the same selected comparison stars must be present on all images. Then, the flux from the target star is divided by the average flux of all comparison sources. Also, the flux ratio outside the occultation is flattened and normalized to unity using a polynomial fit. The outcome of the differential aperture photometry is the OLC, i.e., the normalized flux ratio as a function of time (Fig. 3.5).

Several software and packages are available to perform differential aperture photometry

---

[8] A complete description is available on https://fits.gsfc.nasa.gov/fits_standard.html

[9] Audio Video Interleave.

[10] Astro Digital Video. More information can be found in http://www.astrodigitalvideoformat.org/

[11] A simple image sequence format. Documentation can be found in http://www.grischa-hahn.homepage.t-online.de/astro/ser/

[12] TANGRA documentation can be found on the developer web page http://www.hristopavlov.net/Tangra3/

[13] http://audela.org/dokuwiki/doku.php/en/start

[14] A compressed image file associated with PRISM (http://www.prism-astro.com/fr/index.html).

[15] Developed by the Joint Photographic Experts Group (JPEG) in 1992 to turn images smaller and easy to share.

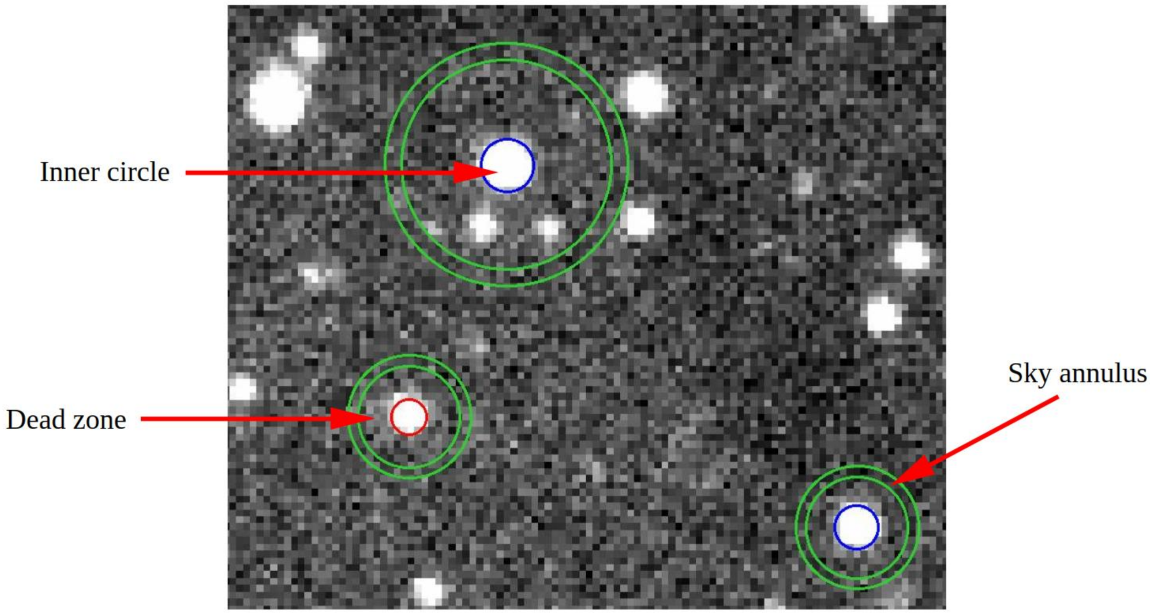

Figure 3.4: Example of a FITS image containing the target star, marked by the red circle, and comparison stars in blue. The regions between both green circles are the sky annulus for each source, where its radius can change according to the presence of nearby stars.

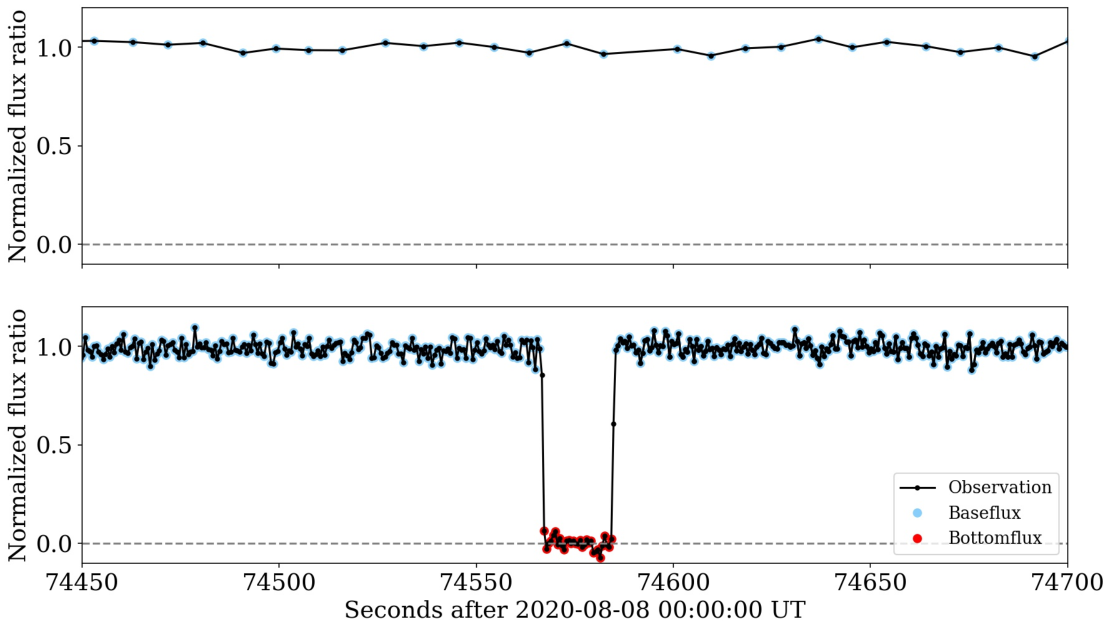

Figure 3.5: Black points represent the mid-time of each exposure (*observation*), red dots mark the images where the target star disappears (*bottomflux*), and the images outside the event are in blue (*baseflux*). The upper panel shows an example of a negative light curve, while the bottom panel presents a positive detection of a stellar occultation. The *baseflux* points were normalized to unity using a polynomial fit. The normalized points were plotted as a function of time, counting from midnight (UT) of August 8, 2020.

on the FITS images[16]. In this work, all OLC were derived using the Platform for Reduction of Astronomical Images Automatically (PRAIA, ASSAFIN *et al.*, 2011). The algorithm's main output is a file containing information about the chosen sources and the parameters used in the aperture photometry. To mention some examples, it includes columns with the Julian Date of the mid-exposure, the apertures radius, the sky background contributions, the individual flux of the target, and each of the comparison stars.

A light curve that detects the stellar occultation is named positive, while the data that does not reveal a drop in the target star flux is called negative. For example, Fig. 3.5 presents a negative and a positive light curve of the August 8, 2020, stellar occultation by 2002 MS_4. The observers acquired the data sets at distinct Earth surface locations, and black points represent the central instant of the exposure. The fluxes outside the event are normalized to unity and considering that this TNO is very faint, i.e., undetectable by the setup in such short exposures, the flux goes to zero during the occultation.

3.1.4 Modeling the positive light curves

We must consider some aspects when building a model for a positive light curve. Firstly, on the images, when the distance between the target star and occulting body is smaller than the image's Point Spread Function (PSF), it is impossible to separate both fluxes. Therefore, outside the event, the measured flux refers to target + object (*baseflux*). When the star disappears, only flux contributions (*bottomflux*) from the object and/or from sky brightness remains (Fig. 3.5). To investigate the origin of the *bottomflux*, one can estimate the magnitude variation (ΔM) in a given band using the object's ($\mathrm{M_{obj}}$) and stellar magnitude ($M_\star$) shown in Eq. 3.7. As the measured magnitude depends on the observational apparatus, the magnitude drop may differ for different observers[17]

$$\Delta M = \mathrm{M_{obj}} - M_\star + 2.5\log(1 + 10^{0.4(M_\star - \mathrm{M_{obj}})}). \tag{3.7}$$

Secondly, the diffraction pattern of a planar wave produced by an object with sharp edges (no atmosphere) should be calculated. The diffraction pattern depends on the object's shape (ROQUES *et al.*, 1987), but our targets' actual shape is usually unknown. In addition, each occultation measurement is a path through the object's projected limb. Therefore, only a unidimensional bar shape diffraction model is used for modeling the OLC. The effect of the so-called Fresnel diffraction on the light curves (Fig. 3.6b) is a smoother stellar disappearance (and reappearance). Eq. 3.8 determines the primary Fres-

[16]For instance, the Limovie (`http://astro-limovie.info/limovie/limovie_en.html`), PyMovie (`https://occultations.org/observing/software/pymovie/`), and Tangra (`http://www.hristopavlov.net/Tangra3/`).

[17]This procedure is also valid for cases where a known companion star is present. If the angular separation between both stars is smaller than the image's PSF, the second star will contaminate the measured flux. Therefore, one can calculate the magnitude drop using both stellar magnitudes and set a *bottomflux* discounting these flux contributions from the OLC.

nel scale (F_s) diffraction fringe considering the wavelength (λ) and the object's distance relative to the observer (Δ_{obs})

$$F_s = \sqrt{\frac{\lambda \Delta_{obs}}{2}}. \tag{3.8}$$

Another physical parameter that might affect the light curve is the apparent diameter of the star calculated at the object's geocentric distance (Δ). As the real star is not a punctual theoretic source, the larger the diameter, the slower its disappearance/reappearance behind the body. To better understand the stellar diameter influence on the light curve model, Fig. 3.6 presents two simulations of a stellar occultation by a typical 800 km TNO. On the left (a) is a schematic picture showing two stars with apparent diameters projected at the object's distance of 1 km and 30 km, respectively (yellow circles). The gray curved limb presents the object, and the red arrow shows the direction of its movement. The right side (b) presents the same observed light curve (black segments) and the synthetic model for each simulation (red line). The only difference between both models is the stellar diameter. However, the red curve from the bottom differs from that at the top, presenting a smoother immersion due to the larger diameter of the star.

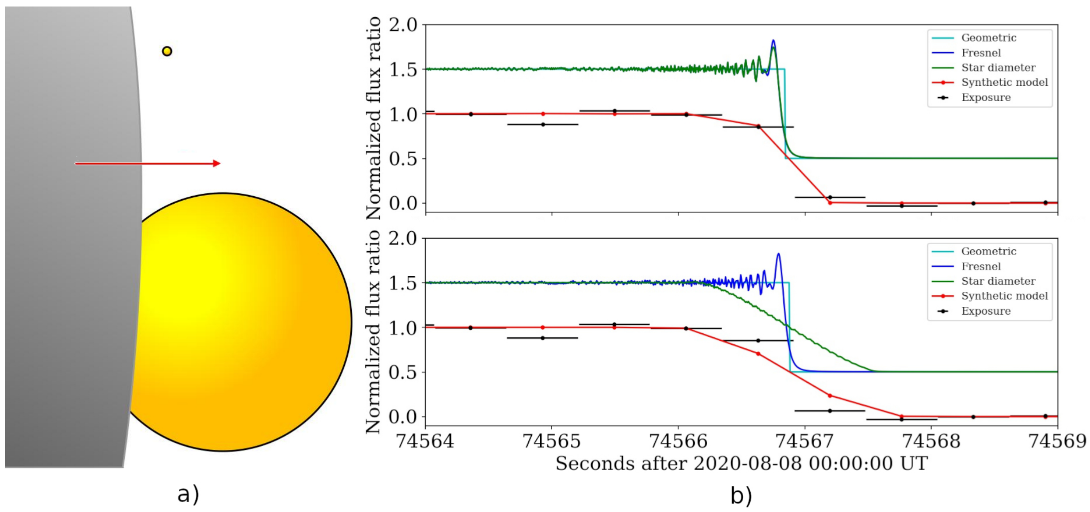

Figure 3.6: **a)** Here is a simulation of an 800 km TNO (gray arc) moving toward (red arrow) the stars (yellow circles). Both simulations used the same observational circumstances, except that the first star is 30 times smaller than the second one. **b)** Black segments represent each exposure, and red is the light curve synthetic model. The model was built starting from a simple geometric model (cyan), then adding the Fresnel (blue) and apparent stellar diameter projected at the object's distance (green) effects. The green, blue, and cyan curves were shifted in +0.5 mag for better visualization.

There are two approaches to determining the apparent stellar diameter: using a published stellar radius or estimating it with the B, V, and K mag. *Gaia* Data Release 2 (*Gaia* DR2) provides the stellar distance ($D_\star$) and estimation of the stellar radius ($R_\star$) for 77 million sources (ANDRAE *et al.*, 2018). Therefore, for those stars, the star's apparent diameter (S_{diam}) can be derived using trigonometry

$$S_{\text{diam}} = \frac{\Delta . R_\star}{D_\star}, \tag{3.9}$$

where Δ is the object's geocentric distance. Usually, when the radius information is unavailable, the alternative is to use the empirical models provided by VAN BELLE (1999) and KERVELLA *et al.* (2004). They use stellar B, V, and K mag to calculate their angular size at a given distance. The result may differ according to the star's type: the main sequence, giant, or super-giant. The Kervella model is also valid for dwarf and sub-giant stars.

A stellar occultation converts time resolution into spatial resolution using the shadow velocity (V_{s}). Usually, the exposure time is long enough to dominate over Fresnel diffraction and the S_{diam} effects, as shown in the first model in Fig. 3.6b. However, in some cases with short cycle times, the stellar diameter may become relevant when modeling an OLC, as simulated in the second model in Fig. 3.6b. As a result, one may use stellar occultation data to characterize the small body and also to study some physical aspects of the star (LEVINE *et al.*, 2021).

Finally, the quality of the synthetic model is tested by comparing it with the observed data. A χ^2 statistic is calculated for each synthetic model generated inside a loop. Eq. 3.10 compares each point of the observed light curve ($\phi_{\text{i,obs}}$) with the point of the synthetic light curve ($\phi_{\text{i,model}}$) and divides the result by the photometric uncertainty ($\sigma_{\text{i,phot}}$). The aim is to explore a time interval around the immersion/emersion instants and build a plot with all χ^2 values as a function of time. The lowest χ^2 determines the immersion/emersion instants. The uncertainties are taken from the time interval between χ^2_{min} and $\chi^2_{\text{min}} + 1$ / $\chi^2_{\text{min}} + 9$ limits, for 1σ and 3σ, respectively (GOMES-JÚNIOR *et al.*, 2022)

$$\chi^2 = \sum_{1}^{\text{N}} \left(\frac{(\phi_{\text{i,obs}} - \phi_{\text{i,model}})^2}{{\sigma_{\text{i,phot}}}^2} \right). \tag{3.10}$$

In summary, modeling a positive OLC involves i) a simple model for a spherical body without atmosphere occulting a point source of light, the so-called geometric model; ii) the wavelength of the observation; iii) the exposure time; iv) the stellar diameter at the object's geocentric distance, and v) the central fringe of Fresnel diffraction. Many tools are available to build such models and determine the instant of the star's disappearance/reappearance[18]. In this work, all instants were derived using the *sora.lightcurve* module provided by the open-source Stellar Occultation Reduction and Analysis (SORA)[19] package - version 0.2 (GOMES-JÚNIOR *et al.*, 2022).

[18] For instance Pyote (`https://occultations.org/observing/software/pymovie/`)
[19] https://sora.readthedocs.io/

3.1.5 Limb determination and further results

Each positive OLC of the same event measures a cross-track of the projected limb. Hence, for a specific positive light curve, immersion, and emersion represent the instants where the line of sight between the observer and the star matches the object's edges. The relative position between the body and the star during immersion/emersion gives the local limb distance from the object's center on a plane (f, g) perpendicular to the line of sight. At this stage, observers' geodetic coordinates, the small body ephemeris, the planetary ephemeris, and the stellar position are required to create the perpendicular plane and to project all occultation instants on it.

The observers must provide the observing geographic coordinates. The *sora.observer* module refers them to the geocenter. Next, the object's ephemeris, which is also geocentric, is provided by the user to the *sora.ephem* module. Finally, the stellar parameters are retrieved by the *sora.star* module directly from the *Gaia* catalog. Then, following the formalism provided by BUTKEVICH and LINDEGREN (2014), the stellar coordinates are propagated to the occultation epoch. Finally, they are corrected by the parallax for an observer in the geocenter. This work uses geocentric stellar coordinates due to the occultation geometry. However, the topocentric stellar position may be necessary for events involving closer stars or farther objects (see discussion in GOMES-JÚNIOR *et al.* (2022)).

As already stated, a plane (f, g) is created, tangent to the line connecting the Earth's center to the star, and all occultation instants are projected on it. Each positive detection provides two points on the new plane - a positive chord. Observations from the same site or at the same latitude of the shadow's path will be superposed and provide only one effective chord. Negative data can also be projected on the tangent plane using the initial and final instant of the observation.

It is expected that large objects have reached one of the hydrostatic equilibrium shapes described in Sect. 2.3.1, and the two-dimensional projection of these equilibrium figures at the sky plane can be described by an ellipse. Therefore, when three or more effective chords are available, M = 5 free parameters are fitted to N $\geqslant$ 6 points to obtain the object's profile. The fitted parameters are the:

- apparent semi-major axis (a');
- apparent oblateness (ϵ'=(a'-b')/a');
- apparent position angle of the semi-minor axis (PA$'$), counting positively from the local celestial north and increasing to the east;
- apparent object's center (f', g').

The elliptical fit is evaluated by calculating the $\mathrm{R_{diff}}$ between the chord's extremity ($\mathrm{p_{i,obs}}$) and the point over the ellipse ($\mathrm{p_{i,calc}}$) (Fig. 3.7), and using it to derive the χ^2 statistic

$$\chi^2 = \sum_{\mathrm{i=1}}^{\mathrm{N}} \frac{(\mathrm{p_{i,obs}} - \mathrm{p_{i,calc}})^2}{{\sigma_{\mathrm{rad}}}^2 + {\sigma_{\mathrm{calc}}}^2}, \tag{3.11}$$

where σ_{rad} is the uncertainty of each chord extremity projected in the radial direction, and σ_{calc} is an optional uncertainty parameter in Stellar Occultation Reduction and Analysis (SORA) that is attributed to the limb model (MORGADO *et al.*, 2021), the latter accounting for the difference between the observed and the mean limb. It can be considered the typical or expected topography size in the radial direction (as described in Sect. 4.1.1.4). Finally, the fit quality can be evaluated by calculating the χ^2 per degree of freedom, $\chi^2_{\text{pdf}} = \chi^2_{\text{min}}/(N - M)$.

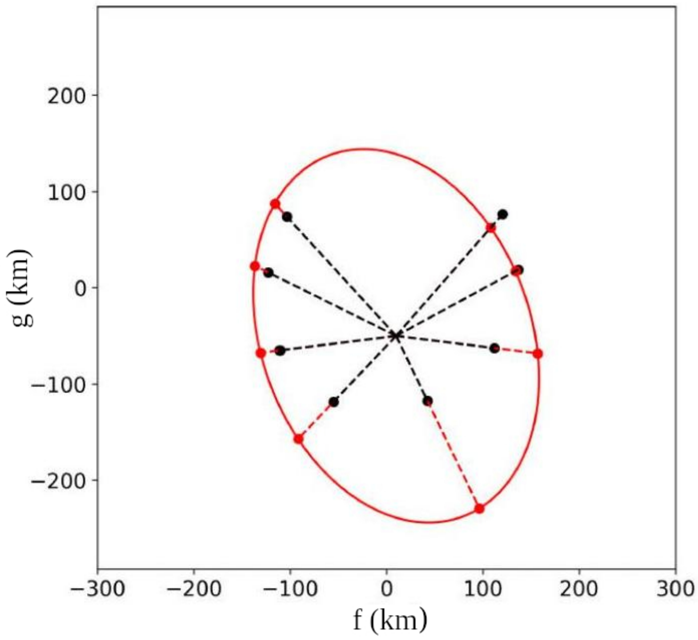

Figure 3.7: The chord's extremities are marked by black points. The fitted ellipse is presented by a solid red line. Distances of each observed point to the fitted ellipse center are in dashed black lines. Finally, the radial distance between the observed points and the ellipse is shown by red dashed lines. Image adapted from GOMES-JÚNIOR *et al.* (2022).

Therefore, the quality of the derived limb depends on the number of effective chords and the presence of close negatives. When less than three positive chords are obtained, a circular limb is fitted to single- and double-chord detections. The result is a minimum size for the body's semi-major axis and an astrometric position (ROMMEL *et al.*, 2020). Finally, using the Monte Carlo approach, SORA generates thousands of limb models, calculating the χ^2 for each one. The minimum χ^2 value represents the best limb fit, and a plot with χ^2 as a function of time is provided for each fitted parameter. The 1σ and 3σ uncertainties are determined from the difference between χ^2_{min} and $\chi^2_{\text{min}} + 1$ and $\chi^2_{\text{min}} + 9$, respectively. The final limb solution may be limited by a close negative chord using the *filter_negative_chord* functionality of SORA. The mentioned function allows a tolerance value in the radial direction, and when the best limb is found, the velocity perpendicular to the limb is calculated for each chord's extremity. It is then used to recalculate the immersion/emersion instants and recalculate the limb. Usually, there are no significant changes in the instant values, except if the positive chord is almost tangent to the limb.

In summary, stellar occultation data can provide astrometric positions and the two-dimensional shape of the object's limb. The equivalent radius (R_{eq}) is also a direct result and is defined as the circular limb with the same projected area as the fitted elliptical limb ($R_{eq} = a'\sqrt{1-\epsilon'}$). Also, structures present in the body's vicinity may be detected in the OLCs. Other objects' physical parameters can be improved by adding external information. For instance, the rotational information is essential to determine the object's three-dimensional shape and albedo (subjects of the following chapter).

3.2 Rotational light curves

The photometric light curve measures flux as a function of time. For instance, an astronomer can observe an asteroid for days, measure the reflected sunlight on each image, and obtain its magnitude variation throughout the observation period–a light curve (Eq. 2.2). The main mechanisms that produce variation in the observed flux are changes in the observational geometry and the object's rotation. The basic geometry of the observation of an asteroid from Earth's surface is presented in Fig. 3.8. The angle between the incident sunlight on the asteroid's surface and the reflected light in the observer's direction is called α. The ζ is the angular distance between the line of sight and the asteroid's spin axis. The Δ is the object's geocentric distance, the Δ_{obs} is the object's distance relative to the observer, and r is the object's heliocentric distance. Therefore, the observed brightness may vary according to variations in the mentioned angles.

Brightness variations also may be caused by the object's rotation if it is elongated or has superficial albedo features (see Fig. 2.4). Therefore, identifying periodic signals in the photometric light curves can provide hints about the object's shape and surface properties. However, before starting the search for periodic signals, the flux contributions due to the observational geometry must be corrected. First, the object's magnitude (M_{obj}) is corrected for the object's geocentric distance (Δ) and object's heliocentric distance (r) to obtain the reduced magnitude

$$M_{obj}(1, 1, \alpha) = M_{obj} - 5.\log_{10}(\Delta.r), \tag{3.12}$$

The object's reduced magnitude ($M_{obj}(1, 1, \alpha)$) is defined as the magnitude if the object was at 1 au from both Earth and Sun.

As the $M_{obj}(1, 1, \alpha)$ varies with the α, it is plotted as a function of the α to build the phase effect curve (Fig. 3.9). The brightness variation depends on the superficial properties but tends to increase abruptly with α near to 0°–the opposition effect. Due to the opposition effect, non-linear functions have been fitted to the asteroid's phase

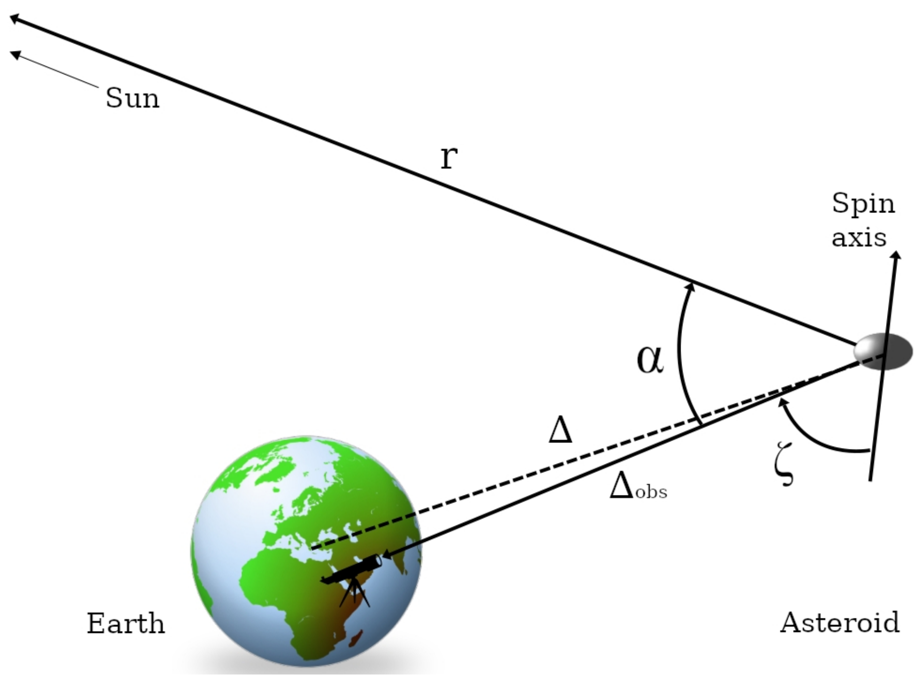

Figure 3.8: Illustration showing the observational geometry of an asteroid seen from Earth's surface (see text).

curves since 1956 (GEHRELS, 1956). Nowadays, many models are available to study phase curves, especially the models proposed by (BELSKAYA and SHEVCHENKO, 2000; MUINONEN *et al.*, 2010; PENTTILÄ *et al.*, 2016).

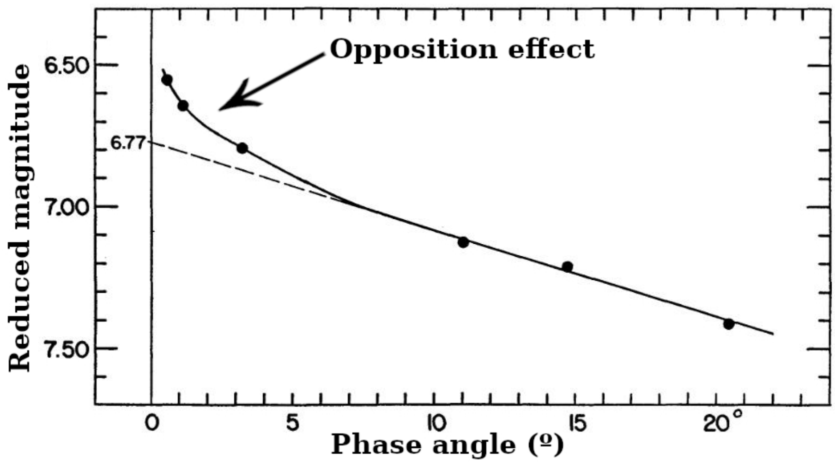

Figure 3.9: Phase curve of Massalia asteroid showing the observed points (black) and the fitted model (solid line). The dashed line shows the estimated absolute magnitude. The arrow points to the opposition effect at lower α. Image adapted from GEHRELS (1956).

In the case of the TNOs, Earth-based observations are limited to $\alpha < 2^\circ$, well within the opposition effect region (Fig. 3.10), which prevents the use of the same photometric models developed for the main belt asteroids. On the other hand, TNOs phase curves are well described by a linear function within this restricted phase angle region (ALVAREZ-CANDAL *et al.*, 2016). Therefore, the absolute magnitude in V-band and linear coefficient can be derived for a given wavelength (λ). The absolute magnitude in V-band ($\mathrm{H_V}$) is defined as the magnitude if the object was at $\alpha = 0°$ and distant by 1 au from both the Earth and the Sun. The β represents the phase effect curve inclination and is expressed in magnitude per degrees (mag/°). Finally, the $\mathrm{M_{obj}}(1, 1, \alpha)$ is corrected by the phase effect using the following equation,

$$\mathrm{M_{corr}} = \mathrm{M_{obj}}(1, 1, \alpha) - (\beta.\alpha + \mathrm{H_V}). \tag{3.13}$$

Also related to asteroid distance from Earth, a one-way light time must be calculated and subtracted from image time. The corrected instant is calculated as follows

$$t_{\mathrm{corr}} = t_{\mathrm{img}} - \frac{\Delta_{\mathrm{obs}}}{\mathrm{c}}, \tag{3.14}$$

where c is the speed of light and t_{img} the image's time. The object's corrected magnitude ($\mathrm{M_{corr}}$) and corrected time (t_{corr}) are then used for periodicity estimations. The commonly used approaches to determine rotational periods (P) of main belt asteroids are i) the Phase Dispersion Method (PDM), ii) the Pravec-Harris method, and iii) the Lomb-Scargle (LS) periodogram. Despite being developed for asteroids, they are perfectly applicable to determine the rotational period of Centaurs and TNOs.

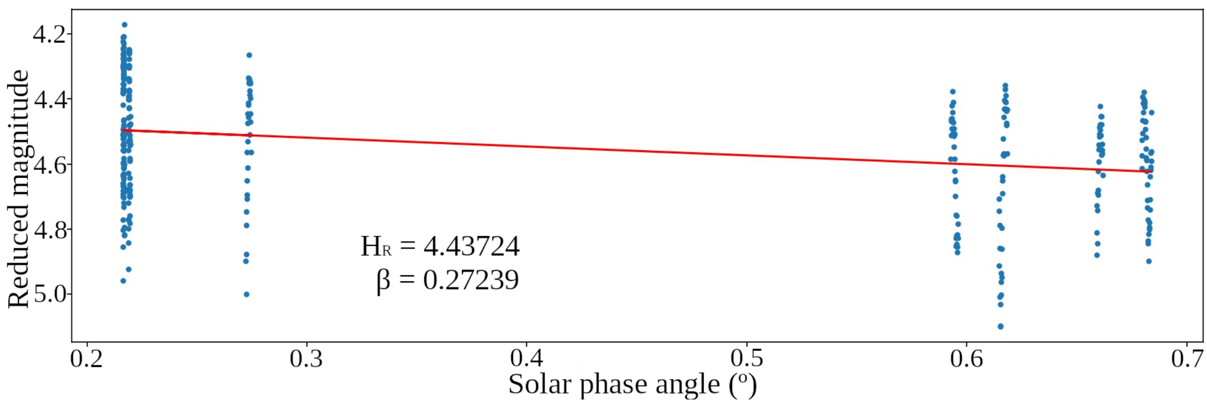

Figure 3.10: Example of a phase curve of a TNO–2008 $\mathrm{OG_{19}}$. Blue points are the reduced magnitudes obtained in this work and the red solid line is the linear fit. The $\mathrm{H_R}$ and β are similar to the results obtained by FERNÁNDEZ-VALENZUELA *et al.* (2016) when analyzing the same image sets.

The PDM method was developed by STELLINGWERF (1978) and is well suited for data with poor time coverage, time gaps, and that have non-sinusoidal magnitude variations. The most-likely rotational period (P) is the one that gives the minimum value for the ratio between phased and original data dispersion (Θ), as follows,

1. measure the magnitudes variance overall data

$$\sigma^2_{\mathrm{mag}} = \sum_{i=1}^{N} \frac{(x_i - \overline{x})^2}{(N-1)},$$

where N is the number of observed points, the x_i the measurements, and the $\overline{x}$ is the mean value over all x_i points;

2. fold the data for a given candidate period;
3. measure the phased data dispersion

$$\sigma_{\mathrm{M}}^2 = \frac{\sum_j^M (n_j - 1)s_j^2)}{\sum_j^M (n_j - M)},$$

where M is a given sample with n_j data points with similar phase. The s_j is the variance of each sample M and;

4. calculate the Θ value,

$$\Theta = \frac{\sigma_{\mathrm{M}}^2}{\sigma_{\mathrm{mag}}^2}.$$

The Pravec-Harris method was first developed by HARRIS *et al.* (1989) and later improved by PRAVEC *et al.* (1996). It consists of fitting Fourier series of any degrees to the $\mathrm{M_{corr}}$ points. Therefore, the object's reduced magnitude at an arbitrary instant t and α can be expressed as

$$M_{\mathrm{obj}}(1,1,\alpha,t) = \mathrm{M_{corr}} + \sum_{n=1}^{\mathrm{m}} \left[A_n . \sin\left(\frac{2\pi n}{\mathrm{P}}\right)(t - t_0) + B_n . \cos\left(\frac{2\pi n}{\mathrm{P}}\right)(t - t_0) \right], \quad (3.15)$$

where t_0 is the zero-point time chosen at (or near) the middle of the observational run, A_n and B_n are the Fourier coefficients at n order. The best fit is derived by using a least-squares fit on the data and finding the minimum variance.

The Lomb-Scargle (LS) approach was implemented by LOMB (1976), and studied by SCARGLE (1982). It is a modified version of the Fourier spectral analysis, deeply connected with the least-square analysis. The main difference is that LS accounts for unevenly spaced data. This is possible because LS does not use the interval of time, it gives weight to each data point. The most likely P is the one that maximizes the periodogram (a detailed discussion about periodograms is made by VANDERPLAS (2018)). Fig. 3.11 presents the periodogram obtained for the 2008 $\mathrm{OG_{19}}$ analysis with the LS method.

According to VANDERPLAS (2018) analysis of many time series, the LS is one of the best-known algorithms for finding periodicity in time series with unequal sampling and occupies a unique correspondence point among the above-mentioned techniques: motivated by the Fourier analysis, but also can be considered a least-square method. Therefore, knowing that our data are irregularly spaced in time and that Astropy v5.1 has *Lomb-Scargle*[20] class ready to use, this method was chosen to the analysis performed in this work. The chosen code was based on other well-known tools for periodicity search, the

[20]Documentation available on https://docs.astropy.org/en/stable/timeseries/lombscargle.html.

AstroML[21] and gatspy[22].

The uncertainty related to the highest peak in the periodogram being the true period is expressed by the peak height compared to the spurious background peaks. Also known as false-alarm probability, this property depends on the number of points and their SNR, i.e., fewer observations or observations with low SNR generates background peaks at the same scale of the true peak. Therefore, to evaluate the peak significance of our analysis, here we used the *false_alarm_probability* method provided by *LombScargle* class.

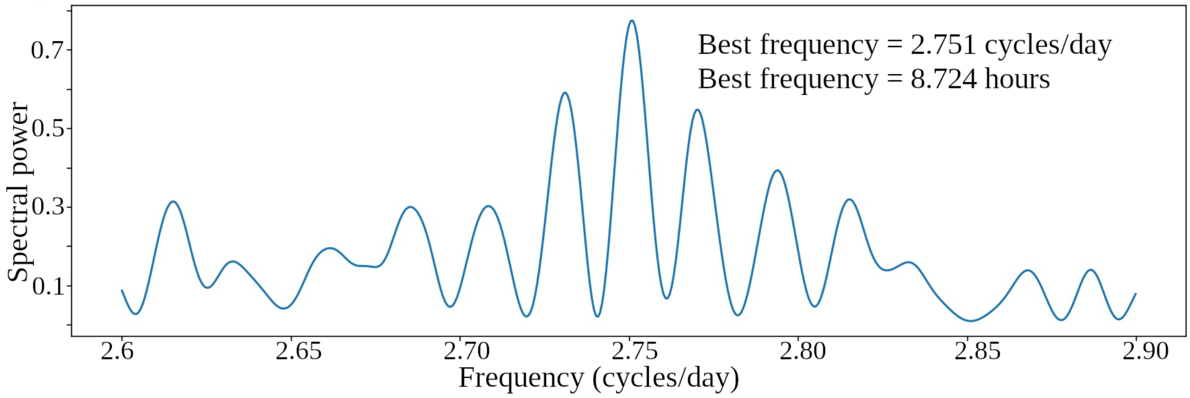

Figure 3.11: Example of a LS periodogram for the 2008 OG_{19} data. The best frequency is marked by the highest peak and is consistent with the published value.

The primary property derived from a periodic search is the rotational period. Once done, the magnitude variation can be measured (Δm). Generally, a $\Delta m = 0.15$ threshold is employed to differentiate RLCs produced by variation in the superficial albedo from those caused by shape variations (DUFFARD *et al.*, 2009; THIROUIN *et al.*, 2010; THIROUIN, 2013). Thus, measuring the reflected light as a function of time allows us to determine, or at least constrain, some physical aspects, such as the object's global shape and fluctuations in surface brightness.

Several observational efforts have been performed within the scientific collaboration to derive the RLC of small bodies from the outer SS. Usually, the strategy is to acquire good photometric images on consecutive nights (FERNÁNDEZ-VALENZUELA *et al.*, 2016, 2019; ORTIZ *et al.*, 2017, 2020a; SANTOS-SANZ *et al.*, 2021; VARA-LUBIANO *et al.*, 2022). The RLC is then obtained using relative photometry, i.e., using stars as a comparison to derive the object's flux (as described in Sect. 3.1.3). The method is accurate and works to derive the object's rotational information from images taken close in time. For instance, for an object with P = 8 hours, three sequential nights usually are enough to derive the RLC. Therefore, is the usual starting point to search for rotational periods (Sect. 3.2.1). Other two strategies to obtain the object's flux were also tested in this work: the Difference Image Analysis (DIA) and the absolute photometry.

[21] More details in https://www.astroml.org/
[22] Documentation available on https://www.astroml.org/gatspy/

3.2.1 Relative photometry

The procedure of deriving photometric light curves using relative photometry is similar to the differential aperture photometry described in Sect. 3.1.3, except that more comparison stars are selected, and the flux ratio is used to calculate the relative magnitude (m_{rel}). Here, the comparison stars are chosen according to i) their vicinity to the target; ii) the occurrence in all images; iii) a similar object's magnitude; iv) their distance from other sources; v) the lack of flags for duplicity or photometric fluctuations in the *Gaia* DR3 catalog. A combination of the flux of all comparison stars provides the calibration flux (F_{cal}), which is then used to calculate the m_{rel}

$$m_{rel} = -2.5 \ . \log_{10} \left(\frac{F_{obj}}{F_{cal}} \right) , \tag{3.16}$$

where F_{obj} is the sky-subtracted flux of the object of interest. Then the photometric light curve is built by plotting the m_{rel} as a function of time (Fig. 3.12), which is also corrected by light-time (Eq. 3.14). The best apertures are established for each observational night after an interactive process that tests different apertures and measures the dispersion of the final curve. Then, the apertures that provide the lowest dispersion are chosen. The observational geometry contributions can be neglected for data acquired on sequential nights or separated by a few days only. Therefore, the obtained light curves are submitted to a periodic search. As mentioned above, in this work, we only used the LS approach.

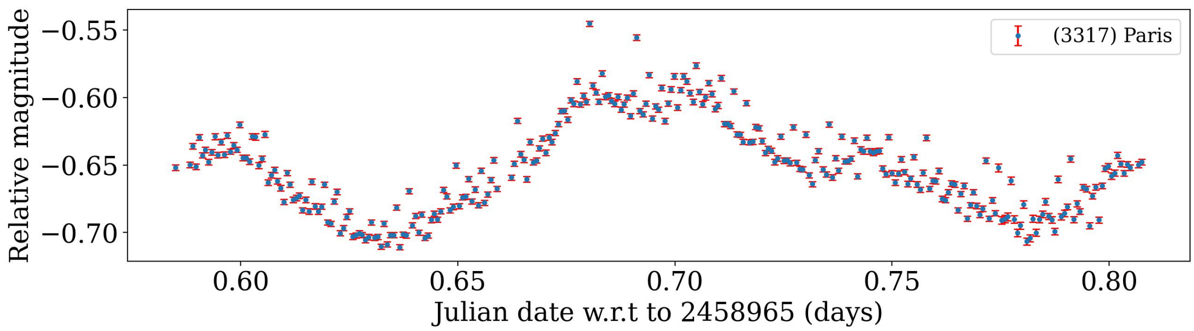

Figure 3.12: Example of a photometric light curve obtained with relative photometry of one observational night on OPD.

3.2.2 Difference Image Analysis - DIA

The Difference Image Analysis (DIA) and co-addition methods have been playing an indispensable role in time-domain astronomy since TOMANEY and CROTTS (1996). The authors used this approach to monitor microlensing activity in their images. The step-by-step procedure was to sample the PSF of the brightest stars common to all images, to solve the WCS, to determine the convolution kernel from the brightest stars by computing the ratio of the Fourier transform, and stacking the best images to build the template image. Finally, they subtracted the template from the entire data set and published the candidates for microlensing events. However, division operations in the Fourier space are not stable and this approach cannot guarantee optimal results (HU *et al.*, 2022).

ALARD and LUPTON (1998)'s pioneering work laid the foundation for image subtraction as we know it today. The so-called Optimal Image Subtraction (OIS) method decomposes the convolution kernel into a set of base functions in the image space. Therefore, the kernel can be derived using a straightforward least-squares analysis overall pixels of both images (Fig. 3.13). ALARD (2000) improved the algorithm by adding a space-varying kernel composed of Gaussian functions multiplied by a polynomial. As a result, it became the standard approach for DIA on astronomical images. The most popular tools that use the above-described methodology are the HOTPANTS (BECKER, 2015) and the DIAPL2[23] implementations (WOZNIAK, 2000).

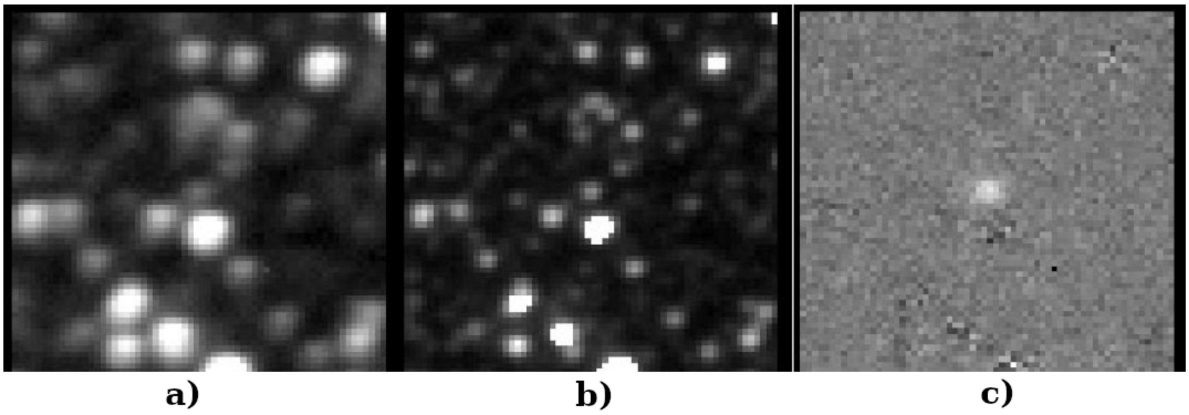

Figure 3.13: Example of a) a science image, b) a template image built from the stack of many science images, and c) the result of the DIA method, showing the flux of the transient source. Image adapted from ALARD and LUPTON (1998).

Following the image space approach, BRAMICH (2008), and MILLER *et al.* (2008) introduced the Delta Basis Functions (DBFs). The method minimizes user dependency and improves kernel flexibility. It considers the kernel as a discrete pixel array and solves it directly using linear least squares. In addition, DBFs can compensate for sub-pixel misalignments between images. The algorithm was tested to search for microlensing events by ALBROW *et al.* (2009). Also, tested in simulated images and some time-series observations by BRAMICH *et al.* (2016). The last work details the many advantages of using DBFs to build convolution kernels.

Another image subtraction algorithm version explores a numerical approach based on cross-convolution kernels. It can provide subtracted images with uncorrelated backgrounds and minimal remaining artifacts. The most prominent algorithms that use this

[23]The code and user manual are publicly available on the author's web page http://users.camk.edu.pl/pych/DIAPL/

strategy are the Python implementations named PROPERIMAGE[24] and ZOGI[25], both based on ZACKAY *et al.* (2016) and ZACKAY and OFEK (2017) papers. The last one has been used in the pipelines of the Zwicky Transient Facility (ZTF) (MASCI *et al.*, 2019) and the MeerLICHT project (PATERSON, 2019)[26].

Recently, a newer approach was proposed by HU *et al.* (2022). The authors introduced the Sacadic Fast Fourier Transformation (SFFT) algorithm [27]. The SFFT uses the DBFs to decompose the kernel, but the image subtraction is made in the Fourier space. This allows for improvements in computational performance without losing the advantage of accommodating spatial variations across the images.

This work tests the DIAPL2 and the PROPERIMAGE tools with images of 2002 MS_4 in a crowded FOV. DIAPL2 is entirely based on Alard's method and PROPERIMAGE uses Zackay's implementation. Therefore, we expect to identify which algorithm has a better performance in deriving photometry of moving objects in crowded FOVs. For the PROPERIMAGE trimmed images are used to improve the processing speed and the subtraction efficiency. The results from both approaches are presented in Sect. 4.1.2.2.

3.2.3 Massive absolute photometry

Generally, the tools designed to obtain information about moving SS objects are proprietary routines or hard-coded scripts[28]. Moreover, they usually require a collection of incompatible software packages implemented in different languages, leaving the user with the option of manually linking the pieces[29]. Also, many large telescopes have their own software implementations for standard calibration and astrometric solutions. Therefore, there is a lack of homogeneity among the available photometric tools and the scientific community usually makes use of scripts written in the commercial Interactive Data Language® (IDL)[30]. In particular, most publications about TNOs and Centaurs (FERNÁNDEZ-VALENZUELA *et al.*, 2016) use a collection of scripts written in IDL but based on DAOPHOT routines (STETSON, 1987). Usually, these scripts are used in a semi-automatic way to derive precise RLCs from a few nights of observation, but the entire procedure cannot be used with gibibytes (GiBs)[31] of data.

In this context of big data sets[32], we are seeing explosive growth in the collection of

[24]Documentation available on https://pypi.org/project/properimage/

[25]Script and documentation publicly available on https://github.com/pmvreeswijk/ZOGY

[26]Available on http://hdl.handle.net/11427/29987

[27]The algorithm is publicly available on https://github.com/thomasvrussell/sfft.

[28]For instance the PINPOINT astrometry tool (http://pinpoint.dc3.com/).

[29]For instance, Image Reduction and Analysis Facility (IRAF) to standard calibration, PRAIA for photometry, Pyedra for phase curve fitting (https://github.com/milicolazo/Pyedra), and so on.

[30]https://www.l3harrisgeospatial.com/Software-Technology/IDL

[31]The international electrotechnical commission created the binary system for measuring data capacity on computers in 1998, and according to this system one tebibyte corresponds to 2^{30} bytes–a unit of data that is eight binary digits long.

[32]For instance the *Gaia* mission (https://sci.esa.int/web/gaia), the LSST project (https://www.

information that is rapidly changing our scientific paradigms. As a result, astronomers and professionals worldwide are challenged to develop new ways to access and use this enormous amount of information. Therefore, there is a global community of developers maintaining the international standard scripts for massive data processing: Apache™ Hadoop®[33] and Spark™[34]. These open-source tools are being widely used and tested by thousands of individuals and companies worldwide.

The lack of homogeneity of the whole data processing and the increasing amount of data makes massive data processing an arduous task by using the usual tools. Those drawbacks motivated the Granada group to design and implement the local massive processing system mainly composed of the Observing Manager (OM) and Massive prOcessing Of aStronomical imagEs (Moose) - version 2 (M2) algorithms. A local system implies using a huge amount of storage for catalogs (tebibytes (TiBs)[35]), but it affords parallel access, reducing the computation time and eliminating the external data dependence/connection. As a result, all tools are compatible, use open-source codes, and are ready to manage massive astronomical image processing. In addition, the algorithms do not change when the problem grows in size. It is only needed an increase in the computational resources (CPU, disk, etc.).

Fig. 3.14 presents the system's architecture used in this work to perform image calibration and photometry. The OM and M2 algorithms are implemented using the SCALA programming language on top of the massive data processing tools (Hadoop®, Yarn, and Spark™). The algorithms are executed on a computation cluster (set of computers) configured to manage all the mentioned tools. The resources provided by every single computer are managed by one last tool called Apache™ Hadoop® Yarn[36]. The results derived from the algorithms described in this work were stored in a MongoDB database[37].

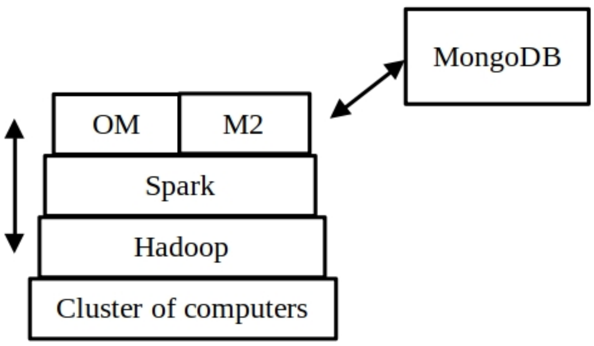

Figure 3.14: Illustration of the system used to process massively the astronomical images used in this work.

lsst.org/), and theSquare Kilometre Array (SKA) telescope (https://www.skatelescope.org/).

[33] https://hadoop.apache.org/

[34] https://spark.apache.org/

[35] One tebibyte corresponds to 2^{40} bytes or 1 024 GiB.

[36] https://hadoop.apache.org/docs/stable/hadoop-yarn/hadoop-yarn-site/YARN.html

[37] https://www.mongodb.com/

Furthermore, the whole system is scalable and can run in a commodity cluster computing[38]. The scalability means that when the problem size increase or decreases, it is only necessary to change the number of computation resources (Central Processing Unit (CPU), Random Access Memory (RAM), disk) while keeping the same algorithms. The main conclusion is that with this system, the same algorithm designed and implemented in cheap hardware can run on (and take advantage of) the resources of large and expensive computation clusters, avoiding script adaptations.

As already mentioned, the main algorithms are the OM and the M2, which run on top of a JAVA Virtual Machine, which communicates them with the other tools mentioned above. OM and M2 are publicly available through an open-source repository in GitLab[39], except for some specific parameter calculations like parallax angles, astrometry plate solving, and the JPL/SPICE parameters[40]. Details of each algorithm and the steps used to process the astronomical images are described below.

3.2.3.1 Observing Manager (OM)

OM was designed to work with files in FITS format[41] and is devoted to automatic image classification and calibration. A general view of OM's decision tree and a summary of the processing steps are presented in Fig. 3.15.

Stage 1: to speed up the process, the OM default configuration will manage only FITS images with a data type of 16 bits. However, it can be rebuilt using the proper FITS data type and process images with 8, 32, or 64 bits. OM can recursively process the images' directory, parse the header information, and create a unified table where each FITS record (header's keyword) is a column. Each table row will contain the header's record values of the individual images.

Then, OM can classify the images in bias, dark, flats, or science, and include this information on the image's header. This task is critical and complex because it uses the FITS record to identify (classify) the type of images. Typically, the original information on those records does not have a unified format, sometimes the information is (partially) missing, has spelling mistakes and uses different languages (i.e., English, French, Spanish, Italian, etc.).

The next step is to group the files by observational nights[42]. Then, inside each group, OM searches for the calibration images to build the master bias, master dark, and master

[38] Parallel computing that involves the use of large numbers of already-available computing components to get the greatest amount of useful computation at low cost.

[39] https://gitlab.com/users/rmorales_iaa/projects

[40] JPL/SPICE is a free and open source tool but is not available in the mentioned GitLab repository. Users must search in the respective official repositories.

[41] As defined by the documentation available https://fits.gsfc.nasa.gov/fits_standard.html

[42] The observational night starts 12 h before and ends 12 h after midnight UT, i.e., if the image was acquired on February 03, 2022, at 01:30:00 UTC, then it belongs to the observational night of February 02, 2022.

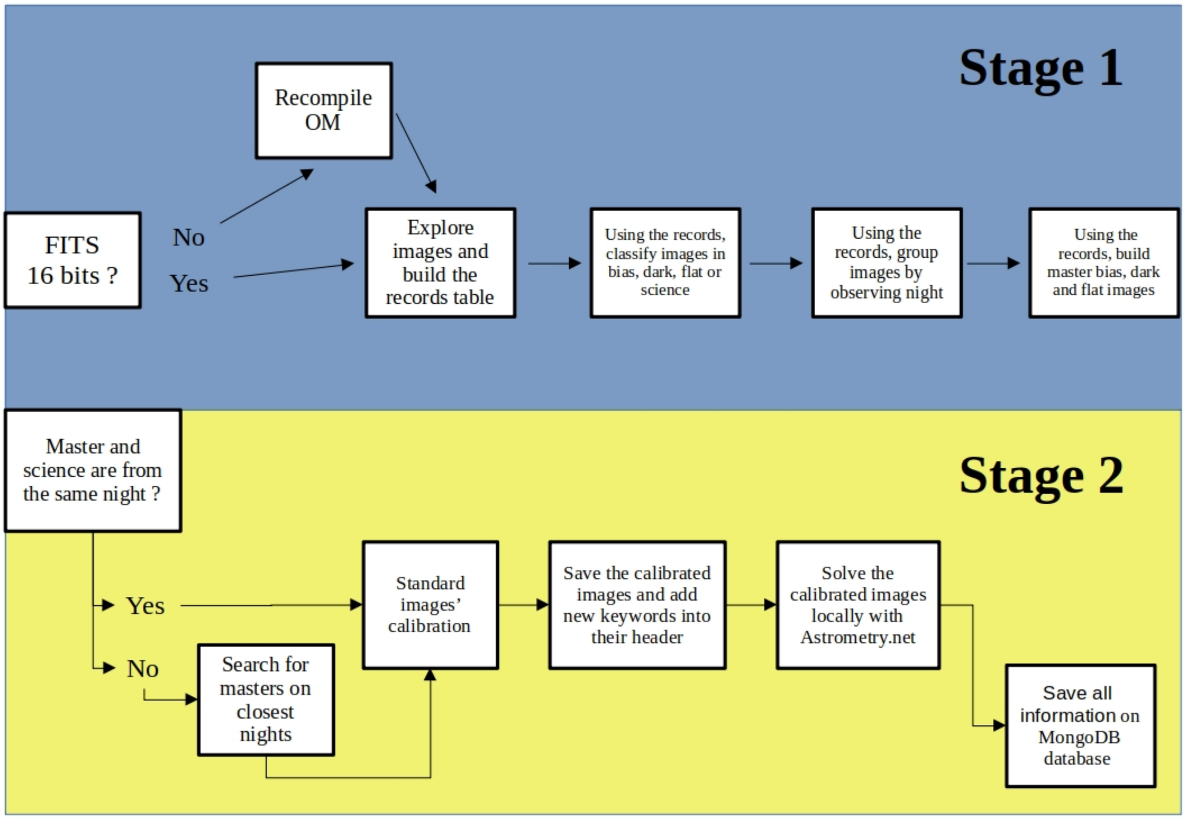

Figure 3.15: The flowchart shows each step of the massive image processing performed by the OM algorithm.

flat images. During this procedure, OM considers some crucial information about the image acquisition, such as the telescope and instrument used, the pixel scale, filters, image binning, the size of the FOV, and the exposure time. In the end, if the user decides that a debug session is required, the algorithm can show all the images used to calibrate some specific science image.

Stage 2 begins with the standard calibration of the science images by bias, dark, and flats. First, OM matches the science image characteristics with the master images inside the same group. However, if some master image is missing, OM will search for master images in the closest groups in time (up to a 15 days interval). The masters are then used to perform the standard calibration by bias, darks, and flats of the scientific images. Usually, the images acquired by big telescopes do not need dark calibration because the CCD temperature is low enough turning thermal effects to be negligible.

In the end, OM searches for the image's center and the pixel scale records. Then submit the calibrated images to a local installation of Astrometry.net[43] algorithm (LANG *et al.*, 2010) to derive their WCS's solutions. The pixel scale and image center information helps Astrometry.net to find the WCS solution faster. If the mentioned records are unavailable, only the FITS file is submitted to Astrometry.net, and a more time-consuming

[43]Documentation available on https://astrometrynet.readthedocs.io/en/latest/

blind astrometry starts. Despite being a blind search of the image's FOV, some default parameters may help to run this step faster. For instance, if a range of image sizes is provided, Astrometry.net will use only indexers of similar size to match the asterisms identified in the FITS files. At this stage, Astrometry.net uses the indexers from the Two Micron All Sky Survey (2MASS) catalog[44].

The final output generated by OM is a set of calibrated science images with the WCS solutions and the master bias, dark, and flats used during the calibration process. Furthermore, the resulting images have new FITS records that homogenize the image's and FOV's information. Finally, all the information and results produced by OM (including a hyperlink to the original calibrated images) are saved on the MongoDB database.

3.2.3.2 Massive prOcessing Of aStronomical imagEs (Moose) - v2

M2 is a set of algorithms and scripts developed to refine astronomical images' astrometry and perform aperture photometry (Fig. 3.4). The aim is to obtain the asteroid's flux variation and their astrometric positions as a function of time. Note that, to speed up the process, all M2 activities are made locally (no external access nor internet is needed), including the Jet Propulsion Laboratory (JPL) information management and the access to *Gaia* DR3 catalog. The general step-by-step for massively processing the images with M2 is described below and can be divided into three stages as presented in Fig. 3.16 and 3.17.

Stage 1: M2 receives the *main.conf* file, which contains the required directories path, object's name, and the default constants to process the images. Then, using a local installation of the SPICE toolkit[45], M2 propagates the asteroid's orbit, searches for images in the OM's astrometric database, and returns a list of FITS that may contain the target. Next, groups of files are built according to the FOV limits information. Each group defines a squared sky region, typically with 1° x 1°, without intersection with other groups. Finally, a query is made to the local *Gaia* DR3, and a sub-*Gaia* catalog involving only the observed sky region is created. The sub-*Gaia* catalog contains an *info* directory that stores the FOV limits for each group of images, and numbered directories that comprise information on individual images in the same group.

Next, M2 uses the internal source detection algorithm and FIT-WCS algorithm imported from Astrometry.net to solve the individual images and refine the WCS solutions. The source detection algorithm uses the *sextractor.background* estimator imported from SExtractor algorithm[46] (BERTIN and ARNOUTS, 1996) for sky background calculations and a built-in script for estimation of the image average PSF. At this stage, the WCS calculations use the pixel scale information provided by OM and the

[44]For more information about this matching procedure see LANG *et al.* (2010).
[45]https://naif.jpl.nasa.gov/naif/toolkit.html
[46]https://sextractor.readthedocs.io/en/latest/Introduction.html

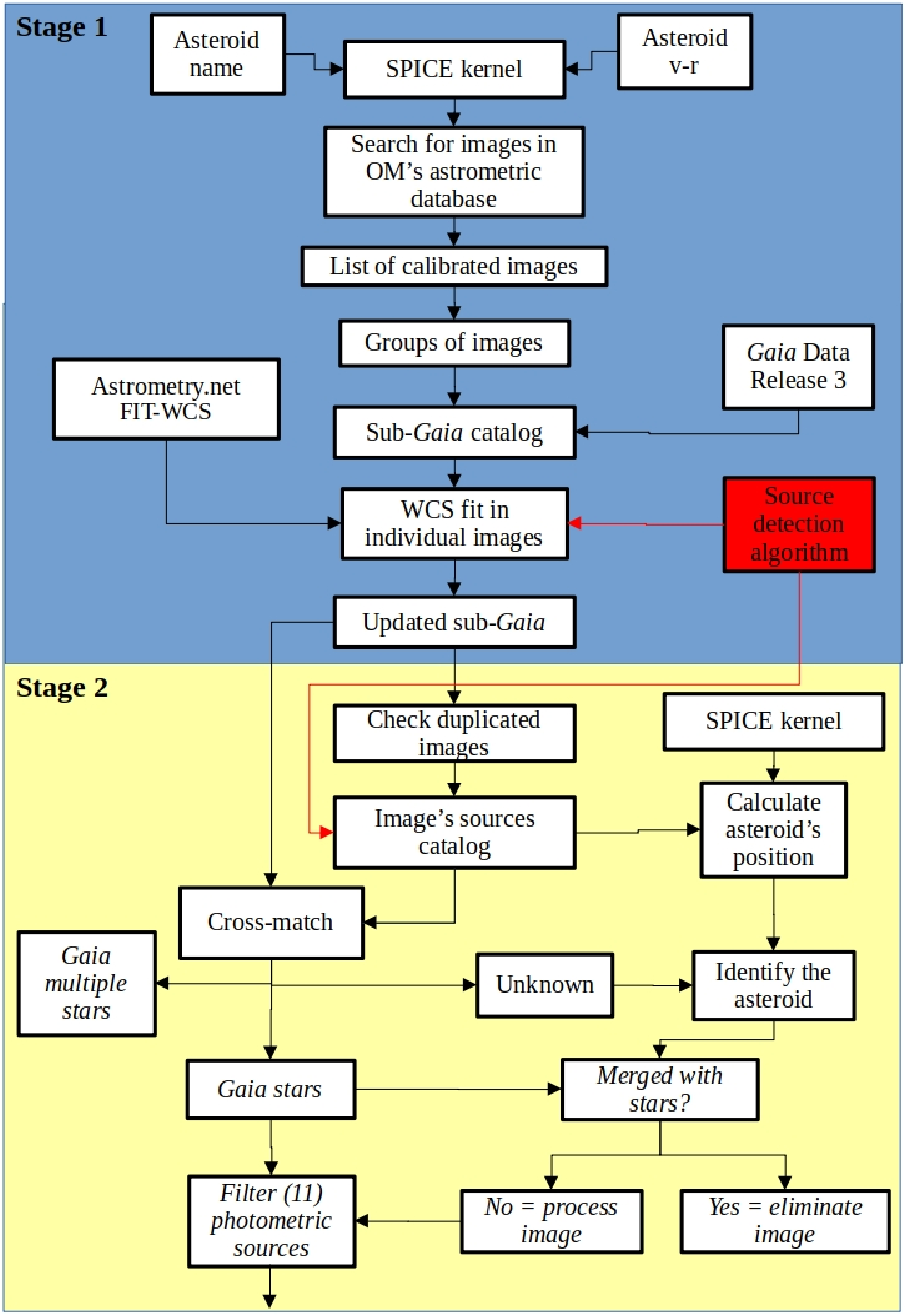

Figure 3.16: The flowchart presents each step of the massive image processing performed by M2.

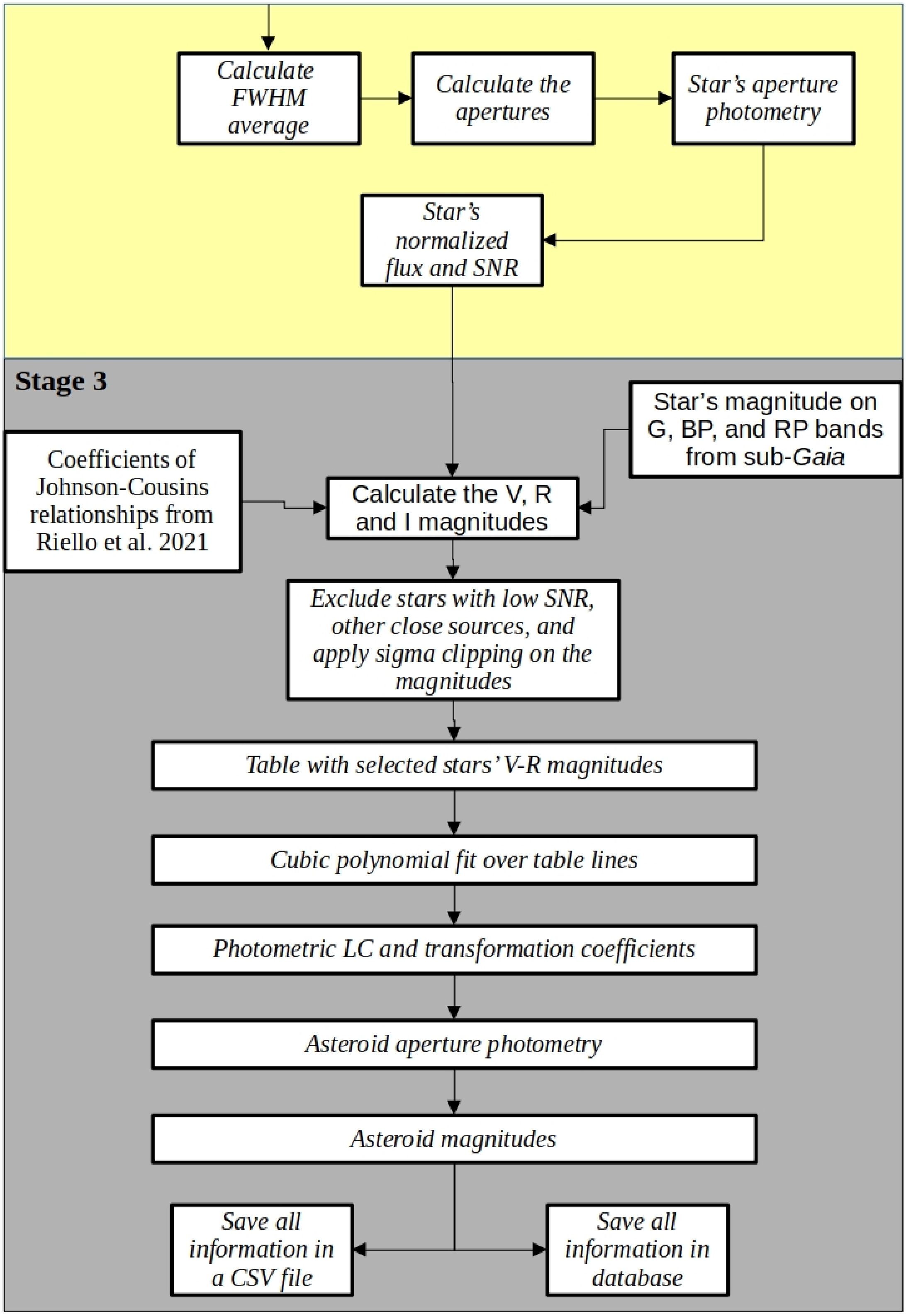

Figure 3.17: continued.

Gaia DR3 indexers, which were created previously using the *Gaia* source files available on http://cdn.gea.esac.esa.int/Gaia/gedr3/gaia_source/.

M2 provides other options for PSF fitting, but this work uses the Moffat elliptical rotated PSF model. It consists of fitting the following equation to the detected sources

$$\mathrm{PSF_{model}} = B + \frac{A}{[C(x-x_0)^2 + D(y-y_0)^2 + E(x-x_0)(y-y_0)]^{\kappa}} \quad , \tag{3.17}$$

where B is the sky background level, A is the maximum value of the fitted PSF, (x_0, y_0) coordinates represent the source's center in pixel units, κ controls the overall shape of the fitting function, C, D, and E are defined as follows

$$C = \left(\frac{\cos(\Phi_{\mathrm{rot}}).2\sqrt{2^{1/\kappa}-1}}{\mathrm{FWHM_{min}}}\right)^2 + \left(\frac{\sin(\Phi_{\mathrm{rot}}).2\sqrt{2^{1/\kappa}-1}}{\mathrm{FWHM_{max}}}\right)^2 ,$$

$$D = \left(\frac{\sin(\Phi_{\mathrm{rot}}).2\sqrt{2^{1/\kappa}-1}}{\mathrm{FWHM_{min}}}\right)^2 + \left(\frac{\cos(\Phi_{\mathrm{rot}}).2\sqrt{2^{1/\kappa}-1}}{\mathrm{FWHM_{max}}}\right)^2 ,$$

$$E = 2.\sin(\Phi_{\mathrm{rot}}).\cos(\Phi_{\mathrm{rot}}).\left(\frac{2\sqrt{2^{1/\kappa}-1}}{\mathrm{FWHM_{min}}} - \frac{2\sqrt{2^{1/\kappa}-1}}{\mathrm{FWHM_{max}}}\right) ,$$

where Φ_{rot} is the rotation angle of the PSF x-axis concerning the center coordinates, the $\mathrm{FWHM_{min}}$ is the smallest Full-Width at Half Maximum of the fitted PSF, and $\mathrm{FWHM_{max}}$ the maximum. The final result from stage 1 is a sub-*Gaia* catalog and WCS solutions with accuracy around tens of *mas*.

Stage 2 starts by checking if duplicated images are present in the data set. Then, M2 calls the source detection script to build a general catalog of sources present in the FITS file. To be identified as a source, the pixels must be above the *noise level*, which is calculated by multiplying the image's sky background Root Mean Square (RMS) by a constant (usually 2.5). The following step is to make a cross-match between the generated catalog and sub-*Gaia* information. If an isolated source is identified as a *Gaia* DR3 star, it will be part of the *Gaia* catalog. If more than one *Gaia* DR3 star is identified as a single source in the image, this source is recorded in the *Gaia* multiples catalog. Finally, if the source present in the image is not *Gaia*, it will be part of the *unknown* catalog.

Next, SPICE is used to perform a focused search and to calculate the asteroid's position (x, y)[47] at the image's epoch. The time calculations include a correction for one-way light time using the Newtonian formulation provided by SPICE[48] (Eq. 3.14). Then a comparison between the calculated position (pixels units) and the *unknown* sources is performed. If

[47]A search for all asteroids present in the image also is possible with the ASTCHECK tool, which is part of the FIND ORB package developed by Bill J. Gray. But it was not necessary for this work.

[48]This correction is essential to obtain reliable rotational light curves, and more information is available on https://naif.jpl.nasa.gov/pub/naif/toolkit_docs/IDL/icy/cspice_spkezr.html

the asteroid is not found, the image is discarded. When the asteroid is identified in the *unknown* catalog, the algorithm verifies if it is merged with some *Gaia* star[49], and in the affirmative case, the image is also discarded. Otherwise, *Gaia* sources are filtered to build the image's photometric stars catalog. A total of 11 filters (Table 3.1) are applied to select the best photometric calibrators, but the spectral type is not considered here.

Table 3.1: If the source attends one of the items in this list of filters, it is not considered a photometric star and is not used to calibrate asteroid flux. †BP/RP excess factor estimated from the comparison of the sum of integrated BP and RP fluxes with respect to the flux in the G band. ‡Ruwe is the re-normalized unit weight error (for astrometry) given in the Gaia archive.

Filters that use stellar information from *Gaia* DR3 catalog	
Magnitude zero	High BP/RP excess factor†
High errors in RA and DEC	High errors in the proper motion
Invalid ruwe‡	Invalid magnitude
Filters that use source information from the image	
Saturated pixels	Wrong FWHM
Not matches with *Gaia* DR3 sources	Multiple matching with *Gaia* DR3 source
Wrong size (too large or small)	

Then, the average FWHM value of the selected sources is used to calculate the photometric apertures (Eq. 3.18, 3.19, and 3.20). By repeating this procedure in every FITS file, the *seeing* variations are considered in the analysis. Therefore, the apertures are calculated as follows,

$$\mathrm{AP_{source}} = \mathrm{FWHM_{AV}} \times 0.8, \tag{3.18}$$

$$\mathrm{AP_{inner}} = \mathrm{AP_{source}} + 11, \tag{3.19}$$

$$\mathrm{AP_{outer}} = \mathrm{AP_{inner}} + 5, \tag{3.20}$$

where $\mathrm{FWHM_{AV}}$ is the average image's FWHM obtained from the selected stars, the $\mathrm{AP_{source}}$ is the aperture that measures the source's flux, the $\mathrm{AP_{inner}}$ is the inner and $\mathrm{AP_{outer}}$ is the outer aperture of the sky annulus that measures the local sky background flux (Fig. 3.4). The constants (0.8, 5, and 11) were chosen due to Instituto de Astrofísica de Andalucía - Consejo Superior de Investigaciones Científicas (IAA-CSIC) researchers' experience with aperture photometry, but they can be edited in the *main.config* file if needed.

The normalized flux and the SNR of each source are calculated as follows,

$$F_{\mathrm{net}} = F_{\mathrm{source}} - \left(\frac{F_{\mathrm{sky}}}{\mathrm{A_{sky}}} \times \mathrm{A_{source}} \right), \tag{3.21}$$

[49]To be considered merged, the object must be closer than 10 pixels from the star in any direction.

$$F_{\text{norm}} = \frac{F_{\text{net}}}{exposure}, \tag{3.22}$$

$$\text{SNR} = \frac{F_{\text{net}}}{\sqrt{F_{\text{net}} + (F_{\text{sky}}/\text{A}_{\text{sky}}) \times \text{A}_{\text{source}}}}, \tag{3.23}$$

where F_{source} and F_{sky} are the flux (ADU) measured by the source's aperture and sky annulus (AP_{outer}–AP_{inner}), respectively. The A_{source} and A_{sky} are the measured squared area (px^2) by the $\text{AP}_{\text{source}}$ and sky annulus, respectively. Finally, F_{net} is the measured flux before normalization, and *exposure* corresponds to the image's exposure time in seconds.

Stage 3 starts with a query to the sub-*Gaia* catalog to retrieve the G, BP, and RP mag for each *Gaia* DR3 comparison star. Next, M2 transforms these *Gaia* magnitudes to Johnson-Cousins system using the equations provided by RIELLO *et al.* (2021), as follows

$$\begin{aligned} V &= G + 0.02704 - (x \times 0.01424) + (x^2 \times 0.2156) - (x^3 \times 0.01426), \\ R &= G + 0.02275 - (x \times 0.3961) + (x^2 \times 0.1243) + (x^3 \times 0.01396) - (x^4 \times 0.003775), \\ I_c &= G - 0.01753 - (x \times 0.76) + (x^2 \times 0.0991), \end{aligned} \tag{3.24}$$

where x is the difference between $BP - RP$ mag from the *Gaia* DR3 catalog. Then, it calculates the Johnson R and V mags as follows

$$R_{\text{mag}} = R - 2.5 \times \log_{10}(F_{\text{norm}}{}^{*}), \tag{3.25}$$

$$V_{\text{mag}} = V - 2.5 \times \log_{10}(F_{\text{norm}}{}^{*}), \tag{3.26}$$

where R and V are the expected magnitudes from the transformation between systems (Eq. 3.24). The $F_{\text{norm}}{}^{*}$ is the normalized flux of the star as calculated in stage 2. Then the light curve derived for each photometric star must pass through three additional filters: low SNR, outliers in V and R filters. For the remaining photometric stars, M2 build a table with two columns: R_{mag} and V-R color. Each line corresponds to one star.

When M2 fills the table with all *Gaia* DR3 photometric stars, a cubic polynomial fit is done overall the table lines. Fig. 3.18 presents an example of the distribution of the root-mean-square deviations for the fit made in R_{mag}. Note that fits accuracy is at the level of a few magnitude decimals. Then, the derived polynomial coefficients B0, B1, B2, and B3 are used to derive the asteroid's magnitude

$$\text{M}_{\text{obj}} = -2.5 \times \log_{10}(F_{\text{norm}}{}^{\text{obj}}) + B0 + [B1 \times (v-r)] + [B2 \times (v-r)^2] + [B3 \times (v-r)^3], \tag{3.27}$$

where $F_{\text{norm}}{}^{\text{obj}}$ is the asteroid's normalized flux from stage 2. The $v - r$ index must be provided according to published or expected values.

Finally, the corrections due to the observational geometry are made, as described at the beginning of this chapter. The main product of the entire analysis using OM and M2 is

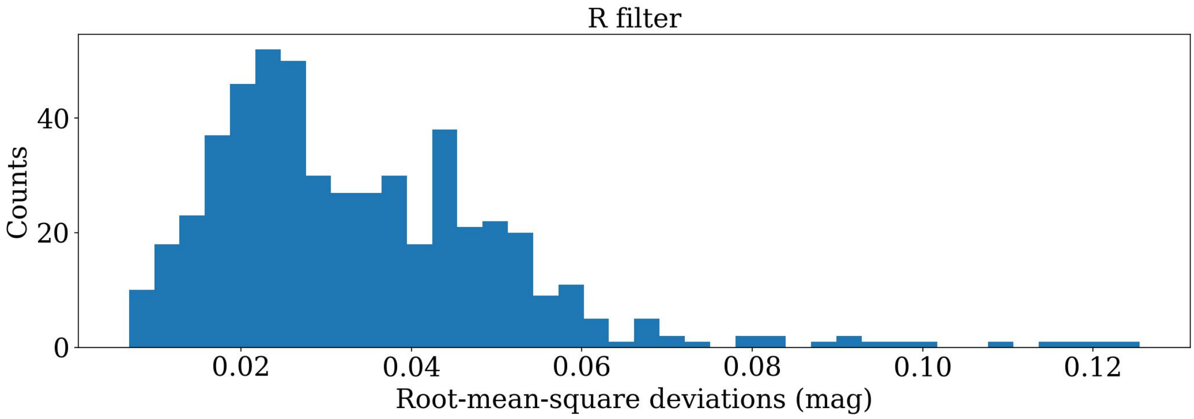

Figure 3.18: An example of the distribution of the root-mean-square residuals from the polynomial fit made to photometric star's magnitudes in Johnson R-band.

a table file, where each line corresponds to the information of one image that contains the asteroid. The columns contain information about the WCS fit, image time, normalized flux, the parameters used during the process, the asteroid's reduced magnitude, and others. Two additional files are also provided, showing the list of discarded and invalid images, i.e., images that failed in some of the above-mentioned steps. In addition, if used in the debug mode, the system provides PNG and FITS files with a small section of the image centered in the target asteroid, hereafter named *croppies*. Useful when a detailed investigation of the image is required in order to identify problems in the photometry.

The next steps, as described at the beginning of this section, include building the phase curve, removing outliers, fitting a linear function, and obtaining the absolute magnitude and β for a given band. The corrected-by-inclination M_{corr} is then submitted to the LS method and the frequency that maximizes the periodogram is the most likely to be the rotational period of the object. Fig. 3.10 and 3.11 present an example of a phase curve and periodogram for the 2008 OG_{19} object. It was obtained from a published image set processed in the above-described system, and the derived RLC is presented in Fig. 3.19. A comparison between the results obtained with OM/M2 system and the published information is shown in Table 3.2. The authors used relative photometry to obtain the result. Our results show that OM/M2 system, despite presenting noisier results, can effectively be used to derive RLCs of TNOs.

Table 3.2: Comparison between the nominal values of the published rotational parameters of 2008 OG_{19} and the ones obtained here. We used the same image set as FERNÁNDEZ-VALENZUELA *et al.* (2016) to obtain these results.

-	H_R (mag)	β_R (mag/°)	P (h)	Δm (mag)
Published	4.39	0.30	8.727	0.437
This example	4.43	0.27	8.724	0.465

Figure 3.19: 2008 OG_{19} rotational light curve as derived in this work using only the images published by FERNÁNDEZ-VALENZUELA *et al.* (2016).

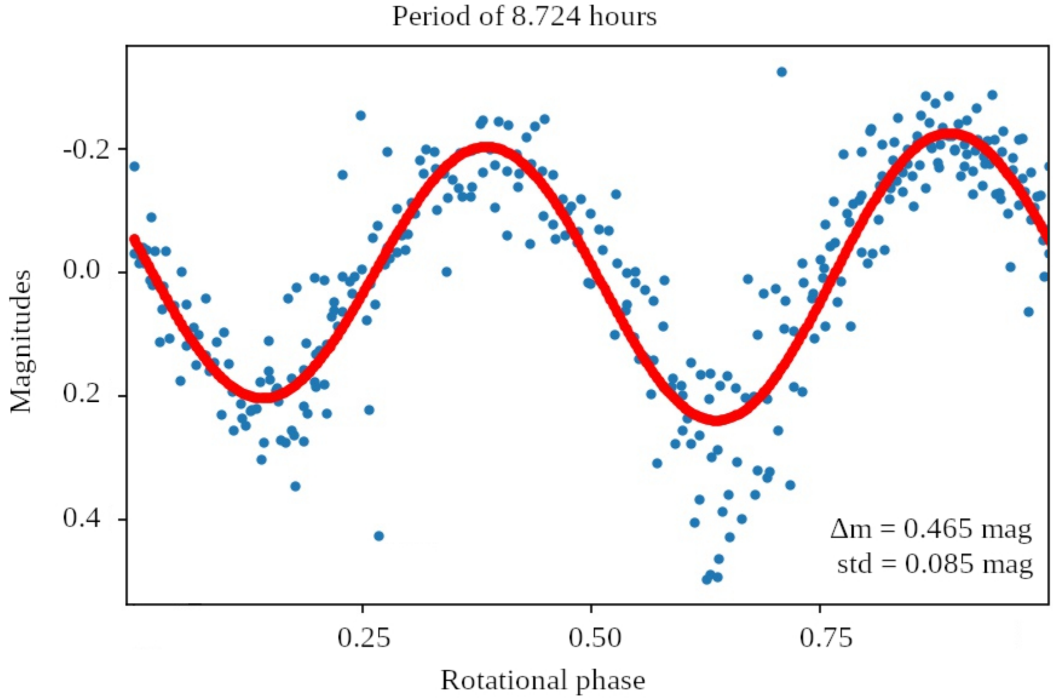

Chapter 4

Results

4.1 (307261) 2002 MS_4

The trans-Neptunian object (307261) 2002 MS_4, hereafter MS4, was discovered on June 2002[1], by Chad Trujillo and Michael Brown while using the Palomar mountain facilities as part of the Near-Earth Asteroid Tracking (NEAT) program (HELIN *et al.*, 1997)[2]. It is classified as a member of the main classical belt region (GLADMAN *et al.*, 2008). It is also categorized as a hot classical object due to its high orbital inclination[3] (details about classifying TNOs are available on MÜLLER *et al.* (2020)).

The first observations of MS4 were performed by the SST at wavelengths near 24 and 70 micrometers (μm). Also, on June 2005, TEGLER *et al.* performed 2.2 h of observations at the Vatican Advanced Technology Telescope (VATT) at the visible band to study the object's color. Finally, in September 2010, the HSO acquired images in the wavelength (λ) range of 60–210 μm. Using HSO data and re-analyzing the SST images, VILENIUS *et al.* derived the highest published equivalent diameter (D_{eq}) for MS4. The published measurements of its color, geometric albedo in V-band (p_V), absolute magnitude in V-band (H_V), and D_{eq} are presented in Table 4.1. Due to the expected size, MS4 is a dwarf planet candidate.

Despite being one of the largest known TNOs, due to its distance from Earth, MS4 is a faint source (with an apparent magnitude of $\approx$ 20.4, in V-band) currently moving in front of the galactic plane. Since its discovery, the field of view has been crowded with stars, and an object blended with background stars makes astrometric and photometric measurements hard to obtain. An exception happened in July 2011 when it passed in front of a dark cloud. Thus, it appeared well isolated from other stars in 100 images acquired

[1] The discovery and ephemeris information was announced on the Minor Planet Electronic Circulars (MPECs). The document is available online under the number id 2002-W27.

[2] More information and data sets available on https://sbn.psi.edu/pds/resource/neat.html

[3] The orbital parameters are: a = 41.8 au, e = 0.14, and i = 17.7° from Small-Body Database on December 2, 2022.

Table 4.1: Published information for 2002 MS_4. The abbreviations in the references column are defined as follows, ST08 = STANSBERRY *et al.* (2008), BR09 = BRUCKER *et al.* (2009), VI12 = VILENIUS *et al.* (2012), and TE16 = TEGLER *et al.* (2016).

p_V	D_{eq} (km)	H_V	B-V	V-R	B-R	Reference
$0.0841^{+0.0378}_{-0.0226}$	$726.2^{+122.9}_{-123.2}$					ST08
$0.073^{+0.058}_{-0.032}$	730^{+118}_{-120}					BR09
$0.051^{+0.036}_{-0.022}$	934 ± 47	4.0 ± 0.6				VI12
			0.69 ± 0.02	0.38 ± 0.02	1.07 ± 0.02	TE16

with the 3.6 m Telescopio Nazionale Galileo (TNG)[4] telescope. Relative photometry revealed a shallow Δm of 0.05 ± 0.01 mag and two possibilities for the rotational period: 7.33 h or 10.44 h (THIROUIN, 2013). Recently, the New Horizons' and ground-based observations permitted VERBISCER *et al.* to determine its phase curve. The authors found two values for the phase coefficient at the V-band (β_V) according to the phase angle (α) interval. The phase curve between $0.5^\circ < \alpha < 1.5^\circ$ has $\beta_V = 0.158$ mag/°, and for phase angle > 10 ° the β_V is 0.0284 mag/°.

4.1.1 Stellar occultation events

As already stated in Sect. 3.1.1, knowing the star's and object's position on the sky plane is essential to predict a stellar occultation event accurately. Therefore, since 2010, astrometric runs to refine MS4's orbit have been made in the following observatories: Pico dos Dias Observatory - Brazil (OPD), La Silla - Chile, German-Spanish Astronomical Center at Calar Alto - Spain (CAHA), and Pic du Midi observatory - France. The *Gaia* catalog's initial releases (GAIA COLLABORATION *et al.*, 2016a,b, 2018) provided accurate astrometry for the stars and improved the predictions of the stellar occultations by TNOs.

This work analyzes nine stellar occultations by MS4, predicted and observed within the European Research Council (ERC) *Lucky Star* project[5] (Table 4.2). The campaigns involved observatories from America, Africa, Europe, and Western Asia, and the default procedure for all campaigns was i) to update the ephemeris, ii) to update the predictions, iii) to select potential events, iv) to send alerts to potential observers within or close to the shadow path, and v) to collect and analyze the data. The observational circumstances of every station that participated in the campaigns are provided in Appendix A. A summary of the target stars' information is provided in Table 4.2.

[4] https://www.tng.iac.es/

[5] More information about the Lucky Star project is available on the project's web page: `https://lesia.obspm.fr/lucky-star/`

Table 4.2: The stars occulted by MS4 sorted by the date (day-month-year). Target star designation and geocentric stellar coordinates (ICRS) propagated to the instant of the closest approach (t_0) using the proper motion, parallaxes, and magnitudes from *Gaia* DR3 catalog. The star's apparent diameter (S_{diam}) in V-band at object's geocentric distance (Δ_{MS4}) is calculated following the KERVELLA *et al.* (2004) formalism and used the provided V and K magnitudes. It is important to mention that none of the stars have a duplicity flag in the *Gaia* DR3 catalog. The * symbol indicates that these errors are expressed in RA. cos(DEC).

Date	**Designation** *Gaia* **DR3**	**Propagated RA (hh mm ss.sssss)**	**Error*** (*mas*)	**Propagated Declination (DEC) (º ' '')**	**Error** (*mas*)	**V (mag)**	**K (mag)**	S_{diam} **(km)**	Δ_{MS4} **(au)**
09-07-2019	4253196402592965504	18 45 19.24565	0.15	-06 24 13.0031	0.12	15.00	14.15	0.19	45.62
26-07-2019	4253186506987951104	18 44 07.57274	0.54	-06 26 40.1240	0.46	17.78	16.27	0.08	45.67
	4253186477047835648	18 44 06.31756	0.13	-06 26 43.8948	0.11	15.45	11.66	0.98	45.68
19-08-2019	4253181804071259648	18 42 43.51905	0.24	-06 32 34.0868	0.19	16.51	16.59	0.05	45.88
26-07-2020	4253244201379441792	18 48 18.07372	0.12	-06 13 31.6134	0.12	14.76	12.61	0.47	45.60
08-08-2020	4253248324549054464	18 47 29.96384	0.12	-06 16 31.4727	0.10	14.62	11.13	1.19	45.70
24-02-2021	4253709191700784896	18 56 35.98731	0.25	-06 30 23.1569	0.23	16.51	12.96	0.53	47.05
14-10-2021	4252495635735083264	18 50 30.76176	0.31	-06 24 13.3375	0.27	15.83	13.44	0.34	46.52
10-06-2022	4253907305577009664	19 00 15.44628	0.23	-05 42 42.9960	0.21	15.10	13.00	0.39	45.48

4.1.1.1 Prediction and campaigns

This subsection is dedicated to describing the prediction and campaign efforts developed for each stellar occultation event.

July 9, 2019

This was the first stellar occultation campaign in that MS4 was detected. However, the prediction uncertainties were large, with ≈ 2,700 km perpendicular to the shadow direction (Fig. 4.1). Therefore, the probability of an observer inside the predicted shadow path actually detecting the event was only 16%. Other drawbacks were the high shadow velocity (V_s) and the faint target star. On the other hand, the shadow was passing through a region with large telescopes and over some collaborators with portable telescopes. Therefore, proposals for the large telescopes were prepared, and the observers with small telescopes were contacted by mail and motivated to observe.

A total of 10 telescopes tried to observe this stellar occultation event (Fig. 4.2), with three detecting the drop in the stellar flux (yellow markers). Other four sites acquired data, but it was negative (blue markers), including a close negative from Ponta Grossa station. The other three telescopes had bad weather or technical problems (white markers). In the end, the actual shadow path passed ≈ 700 km at the north of the prediction.

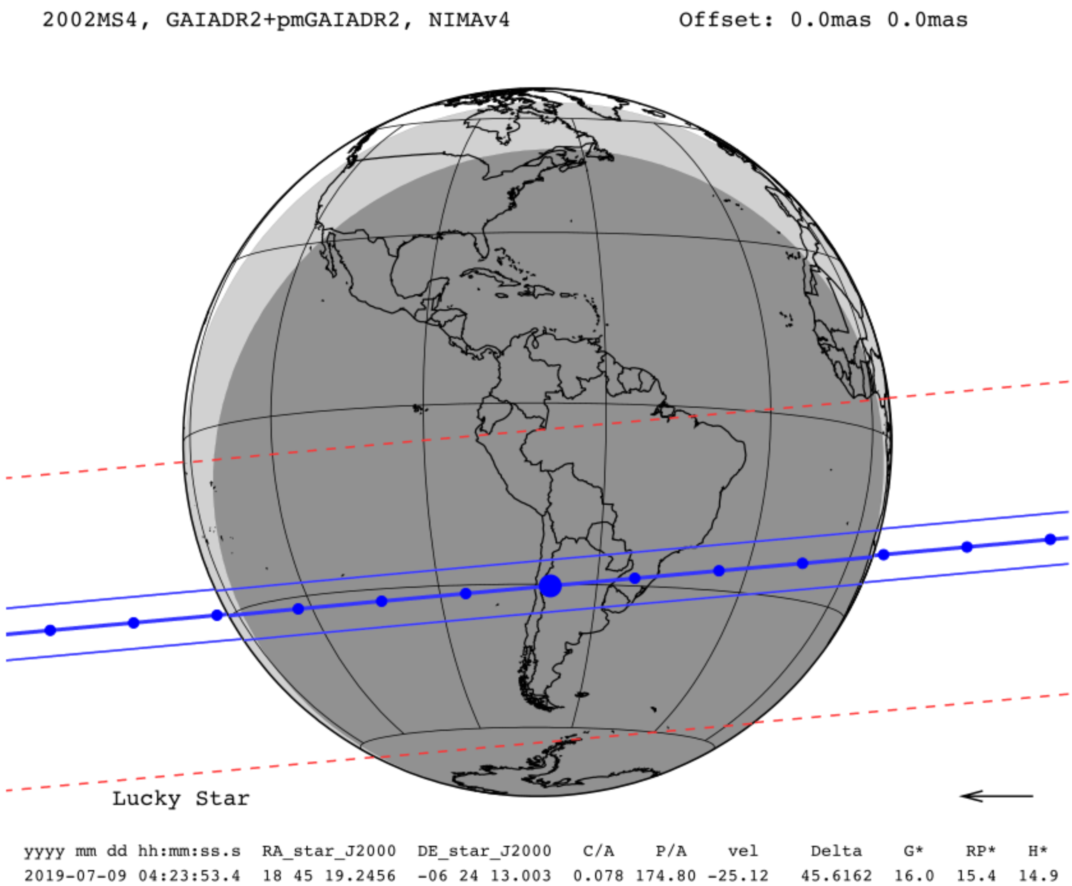

Figure 4.1: Prediction map containing all the information about the stellar occultation by MS4 on July 9, 2019.

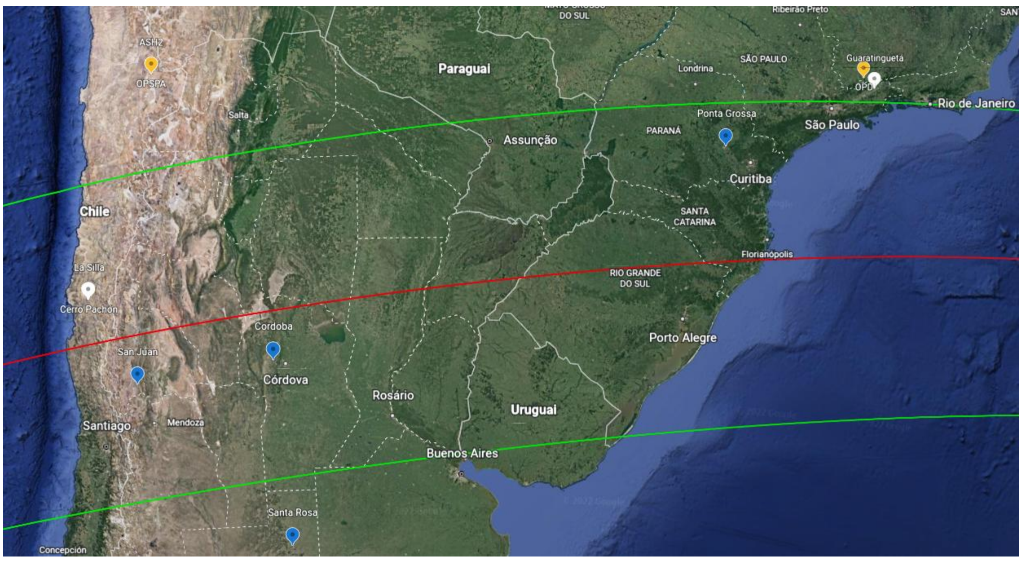

Figure 4.2: Predicted shadow path (green lines) and the location of telescopes that tried to observe the event (markers). Positive detections are indicated by yellow markers (two telescopes were in the same site), negatives are in blue, and bad weather or technical problems are indicated by white markers.

July 26, 2019

On July 26, 2019, two stars were occulted by MS4, and we detected both events (Fig. 4.3). First, MS4 occulted the star marked by the purple cross (left), with the shadow path crossed over South American observatories (Fig. 4.4). Then, about 7.5 h later, the second stellar occultation was observable from North America (Fig. 4.5).

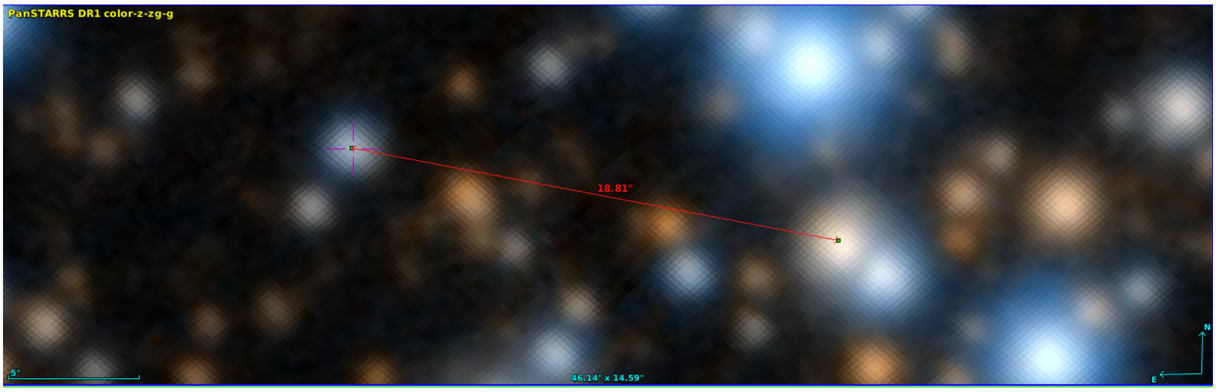

Figure 4.3: The FOV of MS4 on July 26, 2019, shows both target stars separated by the red arrow. The first stellar occultation involved the star marked by the purple cross.

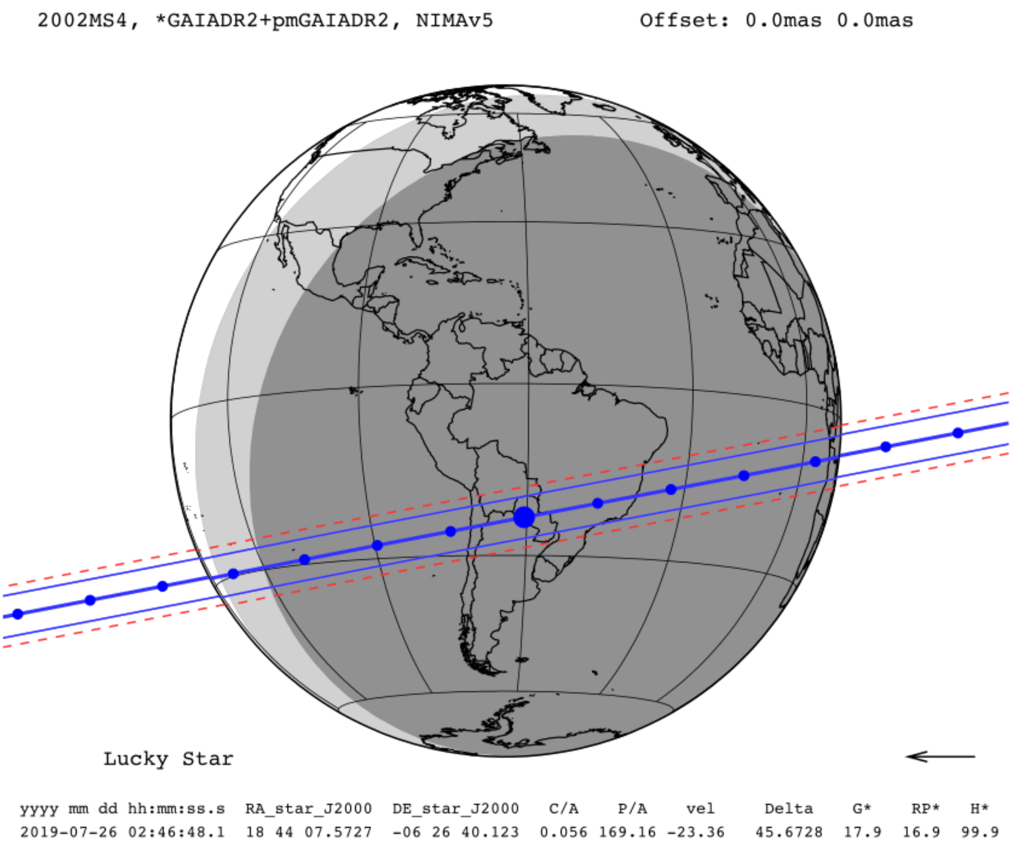

Figure 4.4: Prediction map that comprises all information about the first stellar occultation event by MS4 on July 26, 2019.

The detection of the stellar occultation on July 9 allowed for improvements in MS4's ephemeris. Therefore, these predictions had uncertainties of only ≈ 170 km, leading the probability of detection to ≈ 98%. In these campaigns, we contacted only observers near the predicted shadow path. It resulted in three positives from South America and one detection of the second stellar occultation from CAN.

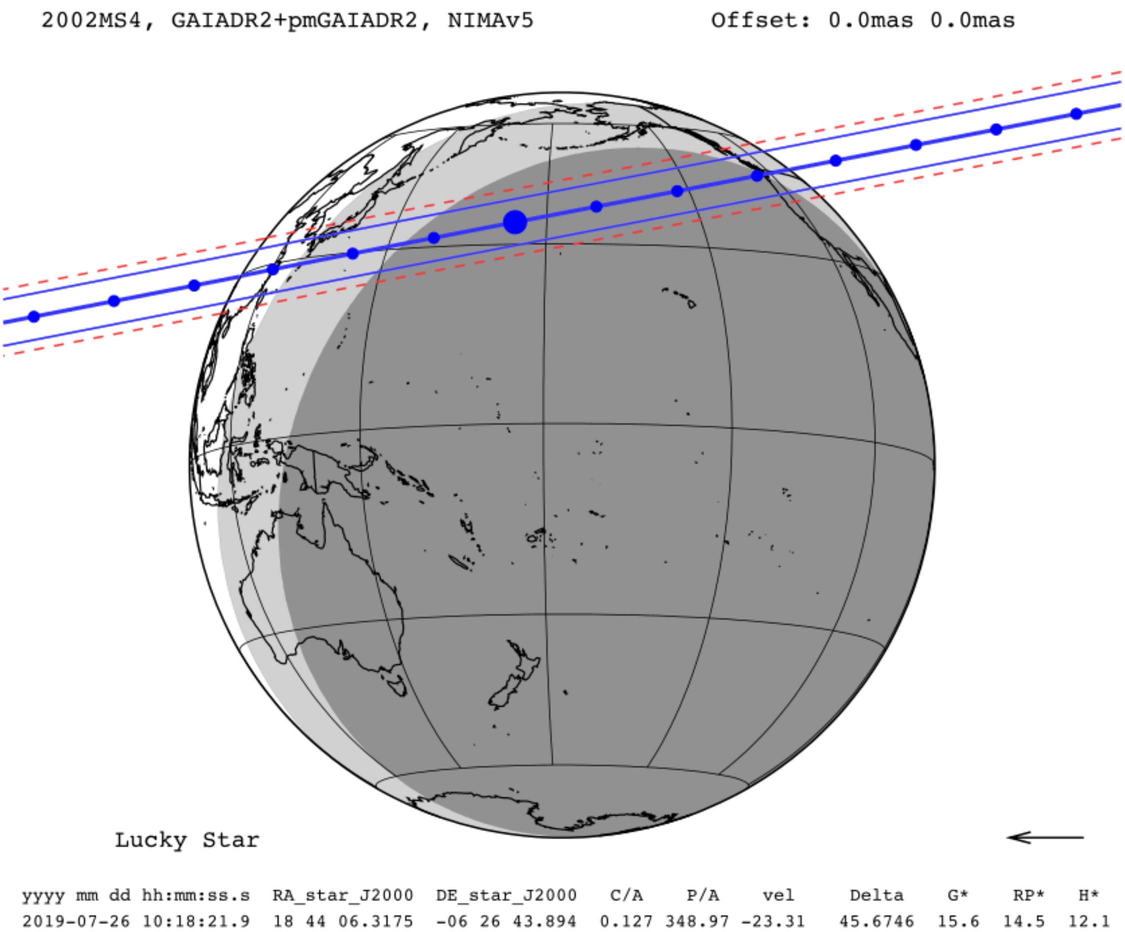

Figure 4.5: Prediction map that comprises all information about the second stellar occultation event by MS4 on July 26, 2019.

August 19, 2019

A stellar occultation by MS4 was crossing North America for the second time. Despite being low on the horizon for observers in CAN, this prediction was accurate and involved a relatively bright star (Fig. 4.6). Also, the V_s was smaller than the previous ones. Therefore, the same observer that detected the single chord on July 26 was contacted to observe this event. In the end, our collaborator and his colleague acquired two positive chords.

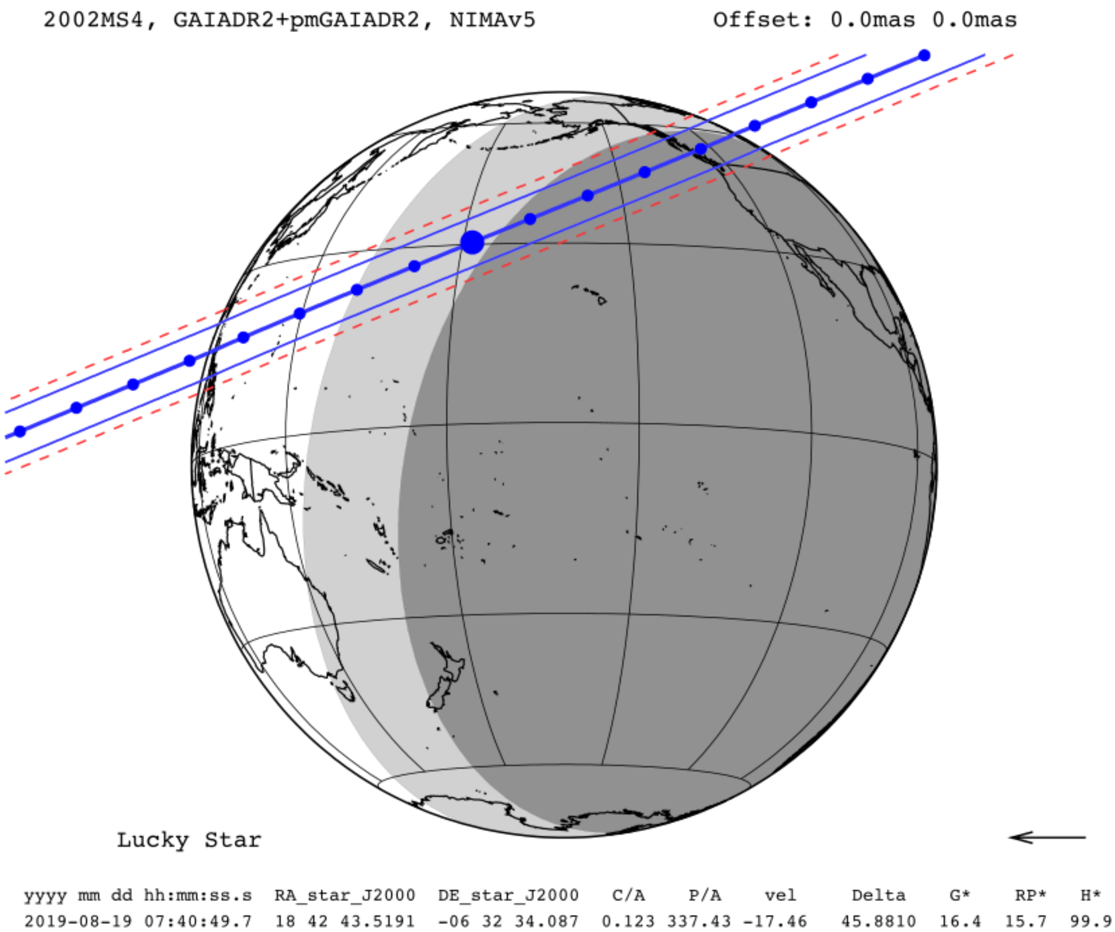

Figure 4.6: Prediction map of the stellar occultation by MS4 on August 19, 2019.

July 26, 2020

All the previous data maintained MS4 ephemeris accurate enough to predict this stellar occultation passing over South Africa (ZAF). At the time, we were preparing the campaign for the August 8 event. Therefore, this was an amazing opportunity to improve even more the ephemeris and double-check the prediction of the subsequent event. Four observers inside the predicted shadow in Africa were informed about this stellar occultation, and one observer near the shadow path in Argentina (ARG) also tried to observe. In the end, the South American and other two sites had bad weather, leading to a double detection from South Africa[6]. This data confirmed MS4 ephemeris and the shadow path for the next event.

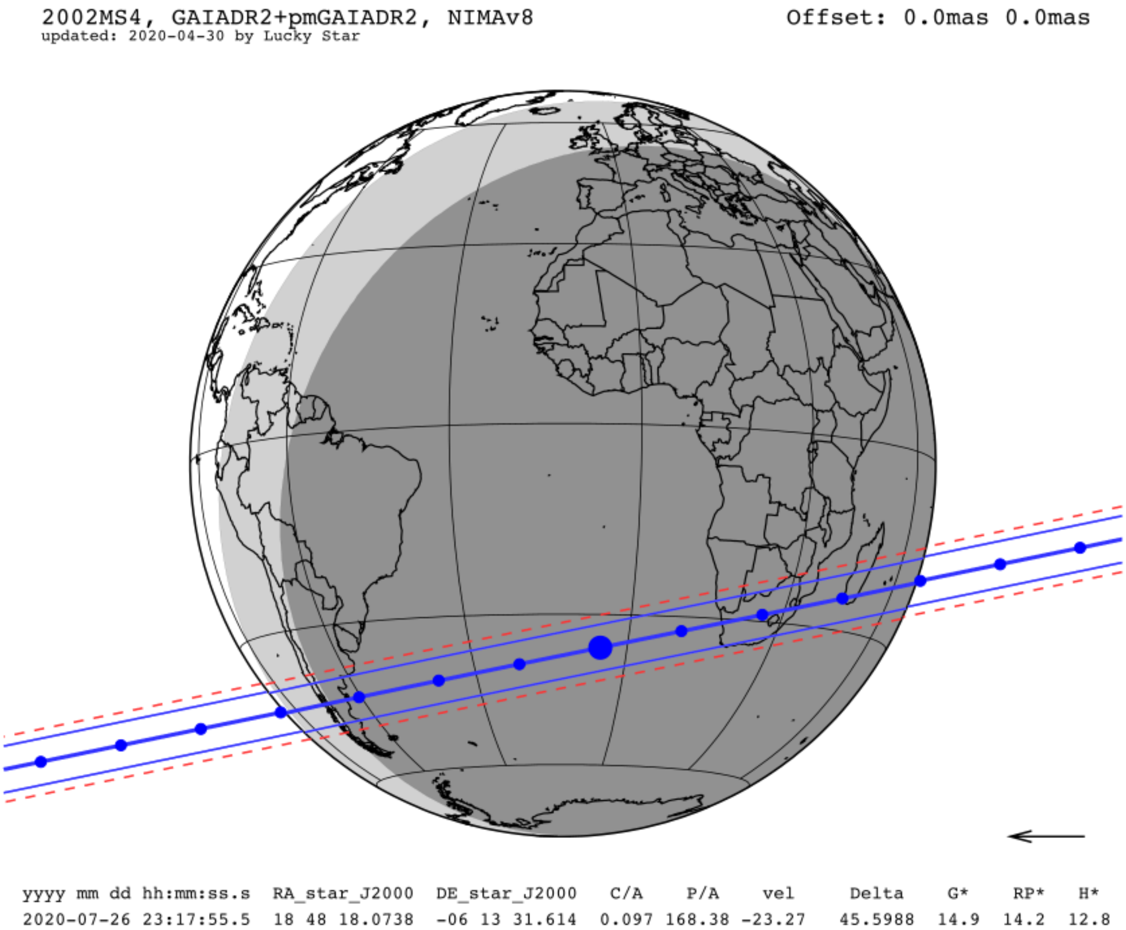

Figure 4.7: Prediction map of the stellar occultation by MS4 on July 26, 2020.

[6]Including a live transmission of the observation on Youtube.

August 8, 2020

This event involved a bright star (Gmag = 14.6 mag) and was visible from densely populated locations on Earth. The detection probability was 99.9%, with uncertainty in the prediction shadow path of only 119 km. Also, we built a dedicated campaign web page to inform observers about this event (Fig. 4.9). In the end, 116 telescopes tried to observe this event and reported its results to us (Fig. 4.10). The limb of the actual shadow path passed only 46 km at the south of the prediction, leading us to the most successful campaign ever obtained by our collaboration for a stellar occultation by a TNO.

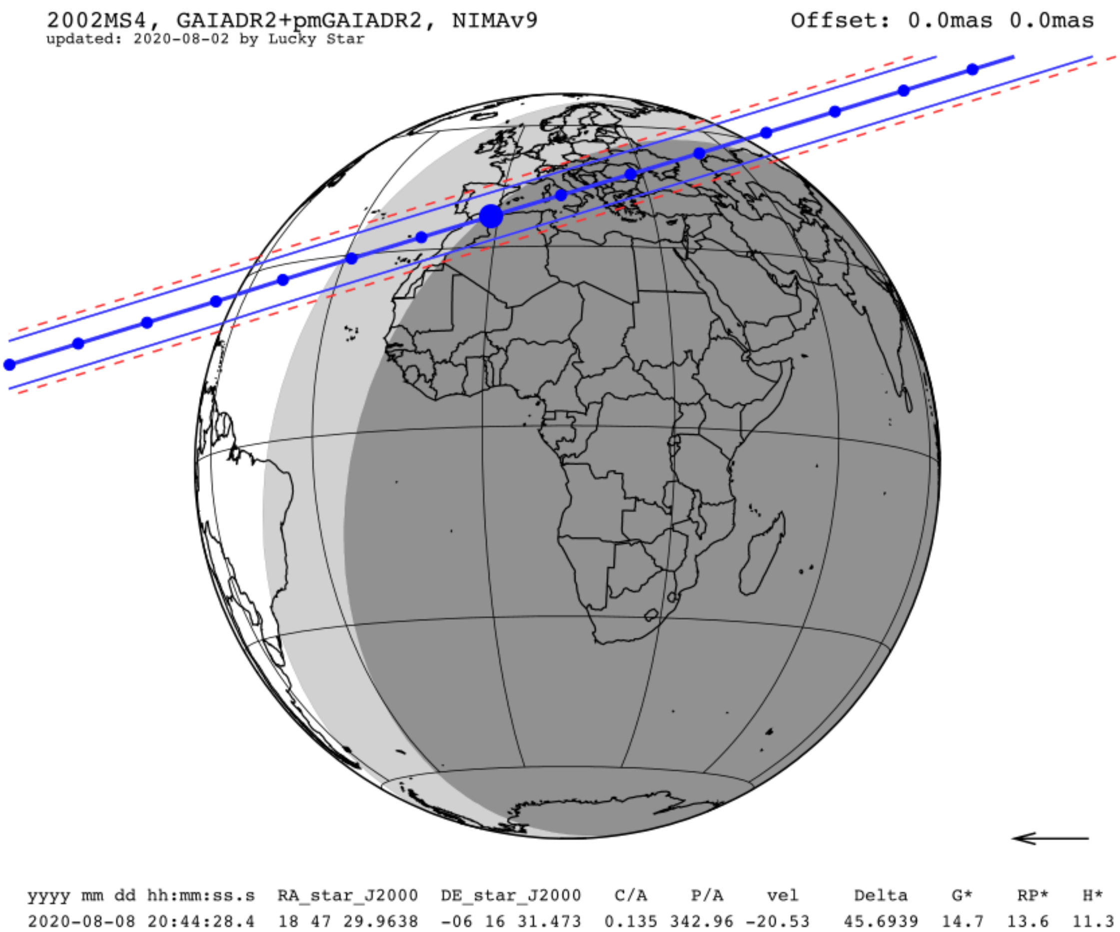

Figure 4.8: Prediction map of the stellar occultation by MS4 on August 8, 2020.

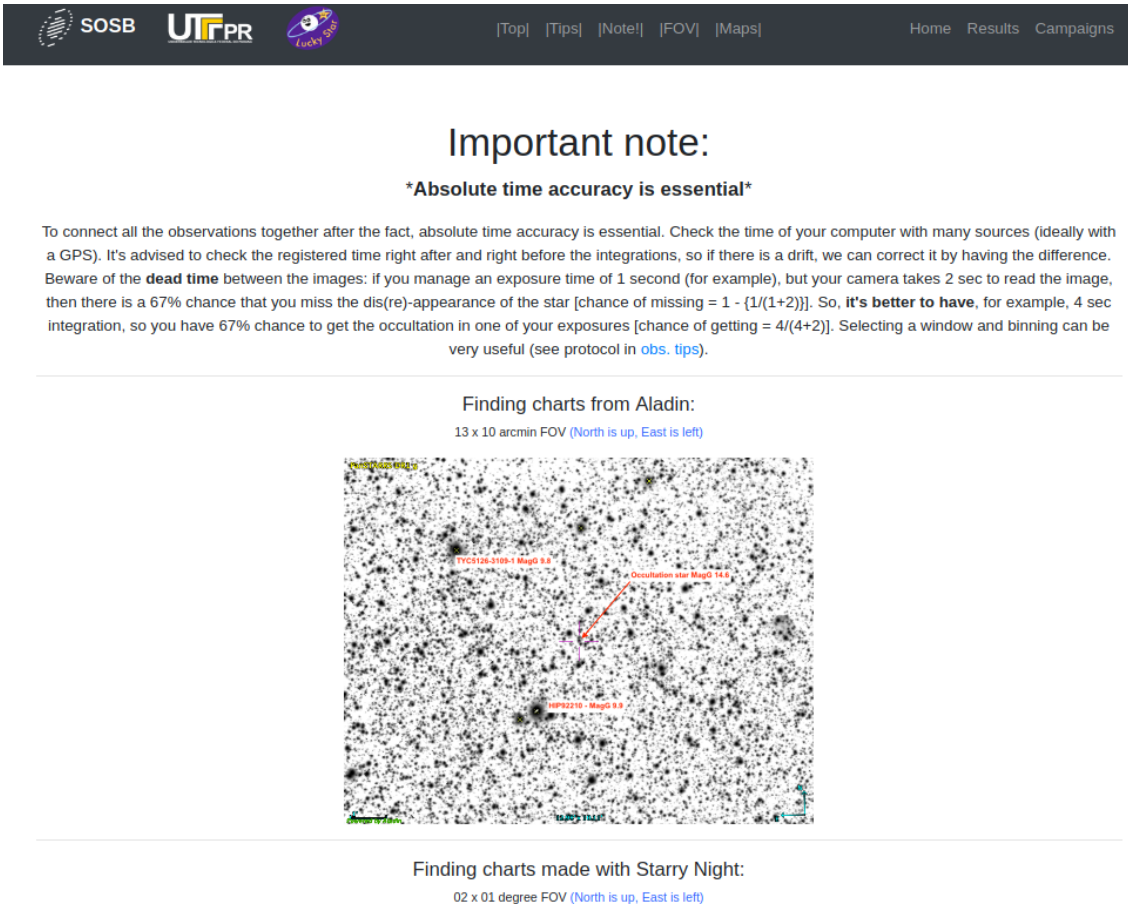

Figure 4.9: A small section of the campaign web page still available on https://lesia.obspm.fr/lucky-star/campaigns/2020-08-08_2002MS4.html

Figure 4.10: Green lines limit the predicted shadow path for the occultation by MS4 on August 8, 2020. The red line was the predicted centrality gray lines are the uncertainty of the predicted path. Yellow markers present the sites that acquired positive data. The negatives are in blue, and stations that reported bad weather or technical problems are represented by white markers.

February 24, 2021

We chose this prediction because it was visible from Chile (CHL). However, due to the faint star, the low elevation above the horizon for Chilean observers ($\approx 20^\circ$), and the proximity to the sunrise, not many observers were contacted for this campaign. Also, the probability of occultation on centrality was only 58.7%. In the end, only two telescopes at the same site in San Pedro de Atacama/CHL detected the stellar occultation - a single-chord detection. It was helpful to maintain MS4's ephemeris with small error bars.

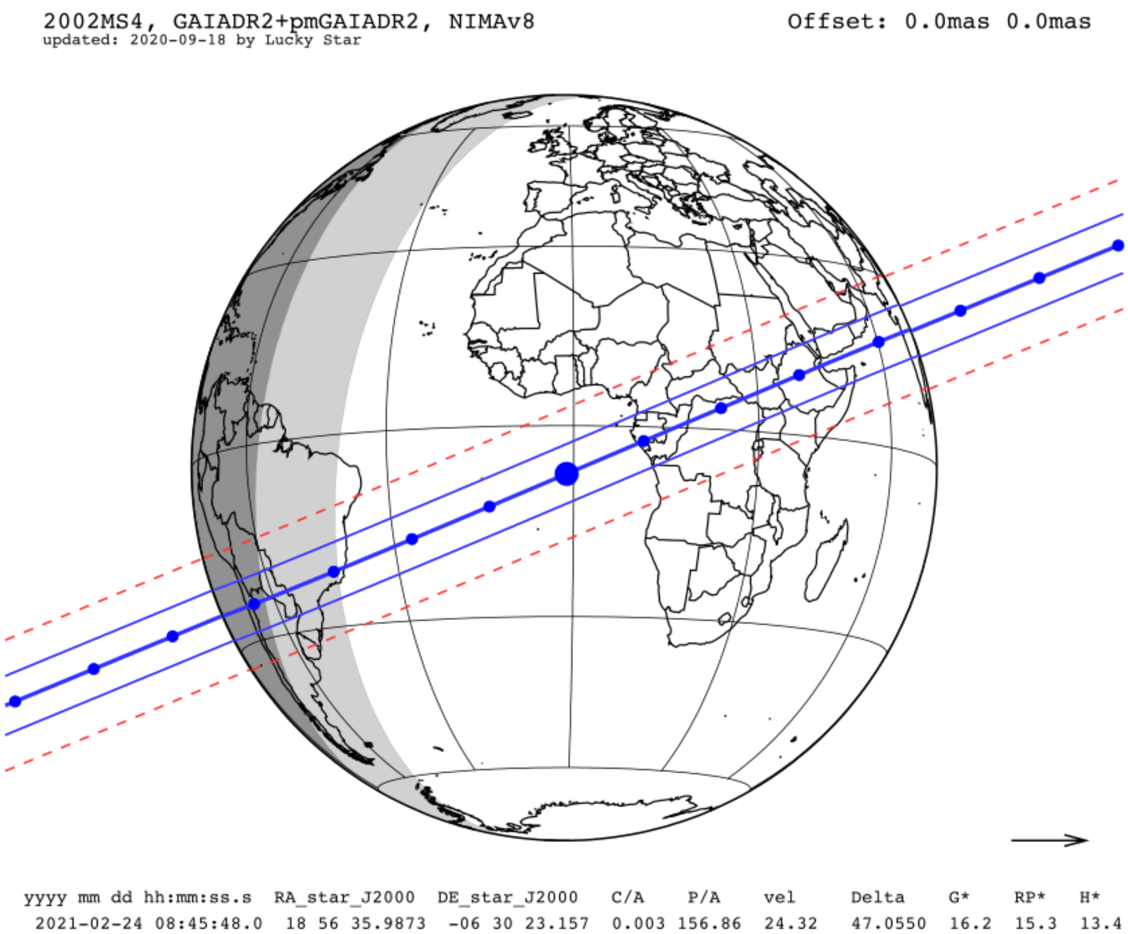

Figure 4.11: Prediction map of the stellar occultation by MS4 on February 24, 2021.

October 14, 2021

This prediction was similar in favoring conditions that the August 8, 2020 event. The target star was bright, and the V_s was lower enough to allow for observations from small portable telescopes. In addition, the shadow path was crossing a densely populated location on Earth, just after sunset, with a probability of centrality of 95.5%. The characteristics mentioned above usually help to motivate observers to participate in stellar occultation campaigns. Therefore, dozens of North American collaborators were contacted by mail to try this observation. However, this time the weather did not favor the observations. A total of 12 stations had bad weather or technical problems, and only two could acquire positive data—one from the United States of America (USA) and the other from CAN.

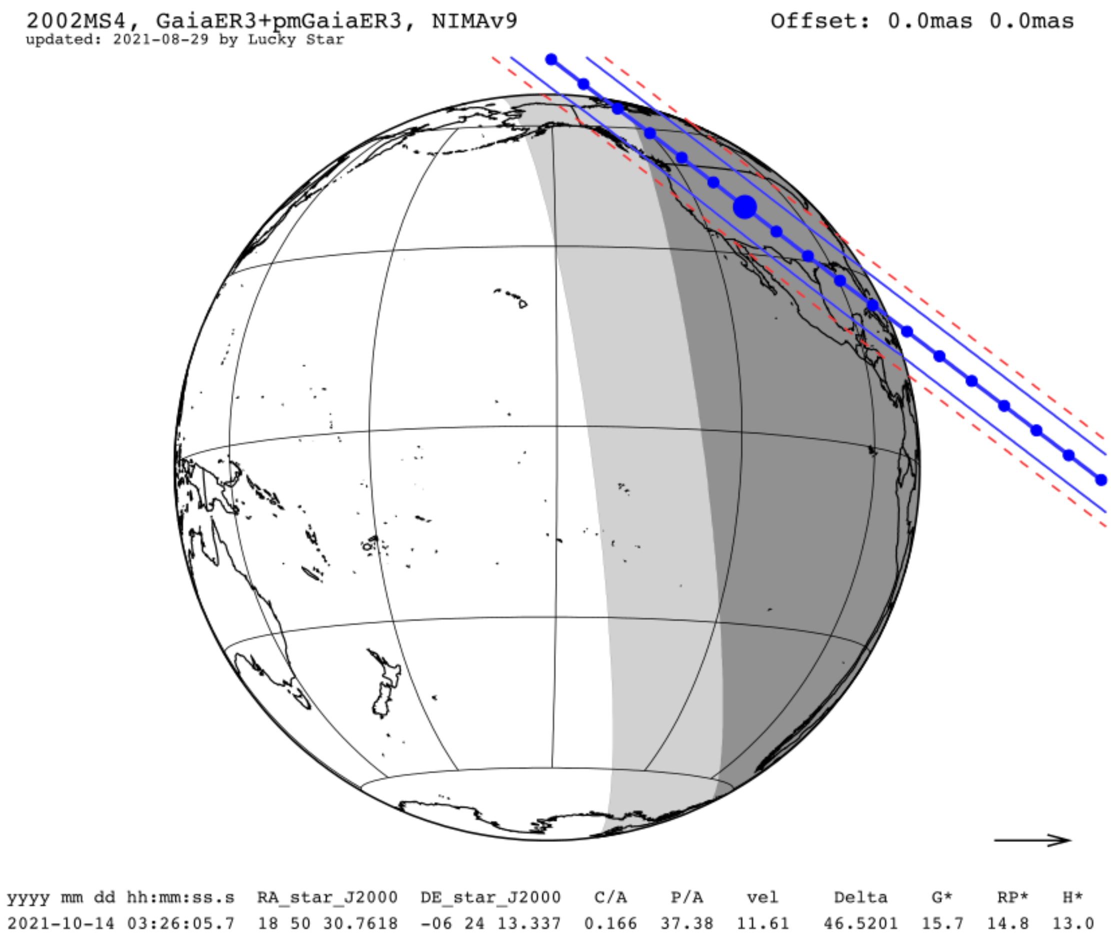

Figure 4.12: Prediction map of the stellar occultation by MS4 on October 14, 2021.

June 10, 2022

The idea behind the stellar occultation campaigns is to observe the event whenever possible and try to detect the object from as many stations as possible. Therefore, an event with a bright star and 90% of the probability of detection and crossing over large facilities in the Canary Islands/ESP seemed to be an excellent opportunity to acquire more data about MS4. The aim was to try to detect topography or surrounding structures. In the end, three equatorial chords were acquired. One from the USA and two from the Canary Islands.

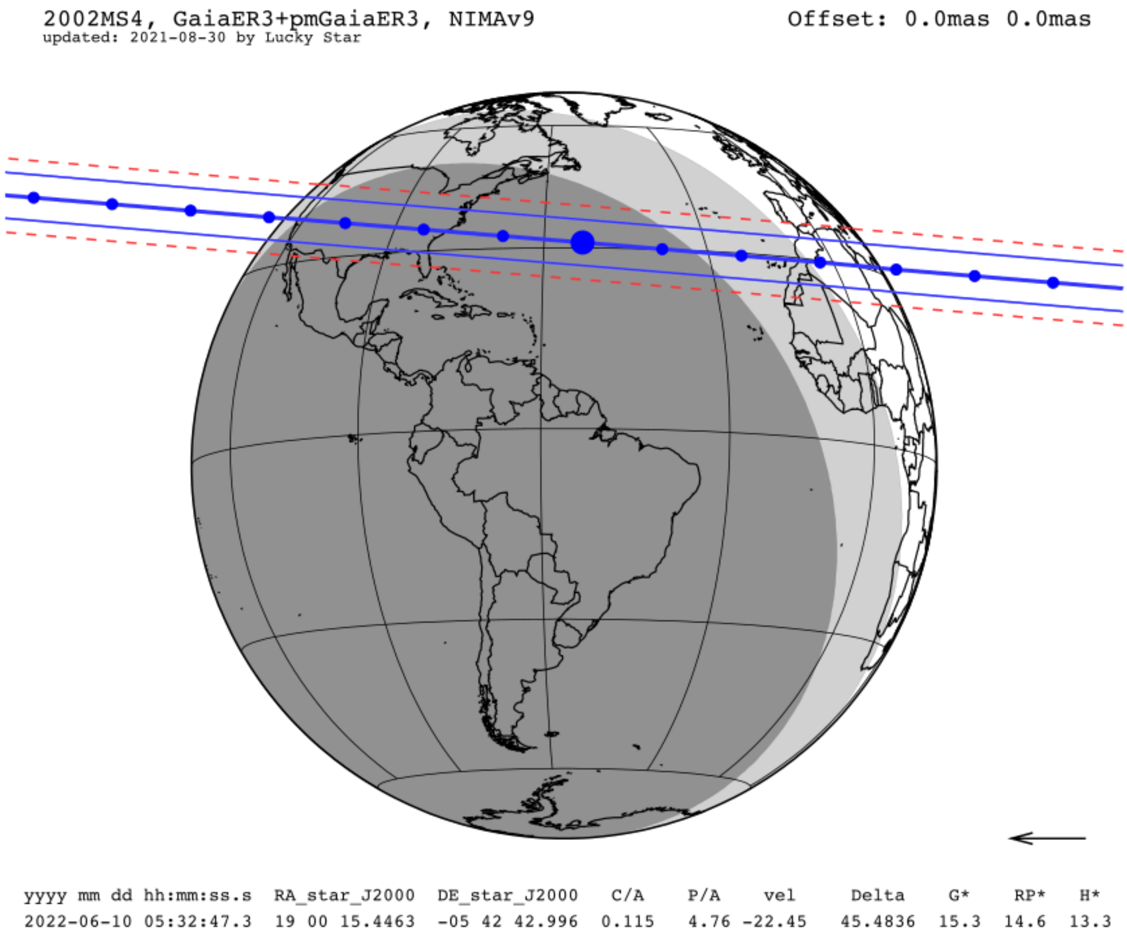

Figure 4.13: Prediction map of the stellar occultation by MS4 on June 10, 2022.

4.1.1.2 Photometry and instants determination

All the received image sets passed through the differential aperture photometry procedure described in Sect. 3.1.3 and, as already stated, some data needed to be converted into the FITS format. In addition, the observational campaigns involved a wide range of telescopes, from small portable ones (apertures between 0.13 m and 0.3 m) to large facilities like the Southern Astrophysical Research Telescope (SOAR, 4.1 m), the Liverpool telescope at Roque de Los Muchachos (2.0 m), Pico dos Dias Observatory - Brazil (OPD, 1.60 m), and Sierra Nevada Observatory - Spain (OSN, 1.5 m). Most observers did not use filters to maximize photon flux and get images with a better SNR. Even though some observers used GPS to acquire the time, the most common time source was the computer clock synchronization with a NTP, which resulted in time offsets in some positive chords.

PRAIA algorithm expects that the provided time is the start of the exposure time, and at the end of the photometry procedure, it adds half of the exposure time to get the middle instant of the image. However, the time written on the image or image's header may sometimes be the exposure's middle or end instant. Therefore, we searched for each instrument's specifications and (or) used the detailed analysis provided by Gerhard Dangl's web page[7] to apply time corrections on the light curves. In addition, when the observer reported time issues during data acquisition, we used close trustful chords as a reference to correct them[8]. All offsets applied to the positive chords and a detailed description of their observational circumstances are described in Appendix A.

The default light curve analysis described in Sect. 3.1.4 was applied to all data sets. A strong variation in the derived instants accuracy was identified along the 80 positive light curves here reported (between 0.006 s to $\approx$ 16 s). The main sources of such uncertainties are the exposure times (used to calculate the cycle time) and the Occultation Light Curve dispersion (OLC_σ). To illustrate these effects, Fig. 4.14 presents some examples of light curves here analyzed. In the *upper* panel, we present a noisier curve (a) with a cycle time of about 10% of the cycle time of the OLC with the lower dispersion presented in the right (b). The first light curve provided instant uncertainties of 0.26 s and 0.67 s, for immersion and emersion instants, respectively. Despite having lower dispersion, the OLC shown in (b) provide less accurate instants with uncertainties of $\approx$ 16 s. Therefore, the number of points per second has a large influence on the results obtained from occultations, i.e., with a higher cadence, we achieve more precise measurements of the object's limb.

In the *bottom* panel of Fig. 4.14 two OLCs with similar cycle times are presented to illustrate the influence of the data dispersion in instants determination. The light curve obtained from Victoria station (d) has about six times more dispersion than Massa's light curve (c). Which translates in error bars about six times greater for Victoria's light curve.

[7] http://www.dangl.at/ausruest/vid_tim/vid_tim1.htm#wat_910bd

[8] Usually, we trust more in data acquired with a GPS. However, some large facilities have an accurate NTP source of time and also have been considered trustful.

In conclusion, the light curve quality and the used exposure times are crucial to obtaining accurate results from stellar occultation data sets.

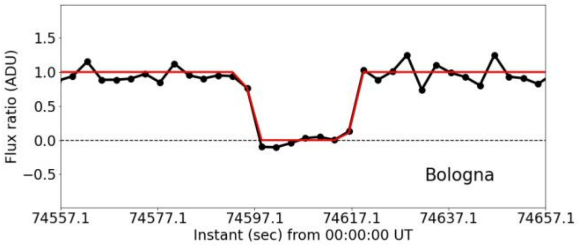

(a) cycle ≈ 3.0 s, $OLC_\sigma = 0.197$.

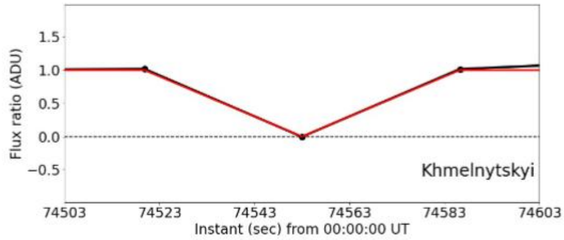

(b) cycle = 33.25 s, $OLC_\sigma = 0.078$.

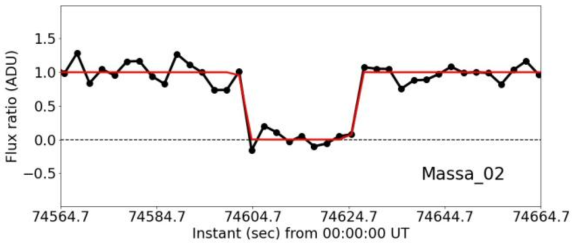

(c) cycle = 2.6 s, $OLC_\sigma = 0.119$.

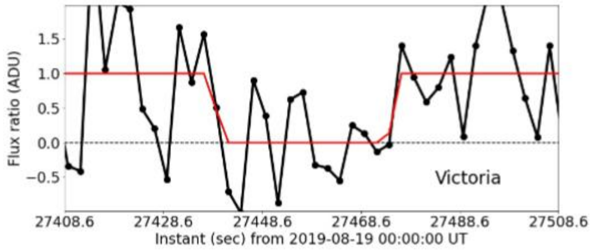

(d) cycle = 2.5 s, $OLC_\sigma = 0.695$.

Figure 4.14: Observed OLCs are in black, and the synthetic model is in red. Cycle time and light curve dispersion are indicated in the individual captions. The *upper* panel presents the light curve obtained from (a) Bologna/ITA and (b) Khmelnytskyi/UKR stations on the August 8, 2020 event. The *bottom* panel shows (c) the light curve obtained from Massa/ITA station on August 8, 2020, and (d) the light curve acquired from Victoria/CAN on August 19, 2019.

The other positive OLCs containing the normalized flux and the synthetic models are presented in Appendix B. The list of final immersion and emersion times (UT) with 1σ error bars and for all light curves are provided in Appendix C. Also, the S_{diam} used to determine such instants are provided by Table 4.2. Then, following the procedure described in Sect. 3.1.5, the instants are projected at the sky plane (f, g). Fig. 4.15 presents each occultation's positive (blue) and close negative chords (green). The plot origin is the object's center as predicted by the NIMA v9 ephemeris (DESMARS, 2015). Finally, a limb is fitted to the chords of each event to determine the object's profile at the instant of the closest approach (UT).

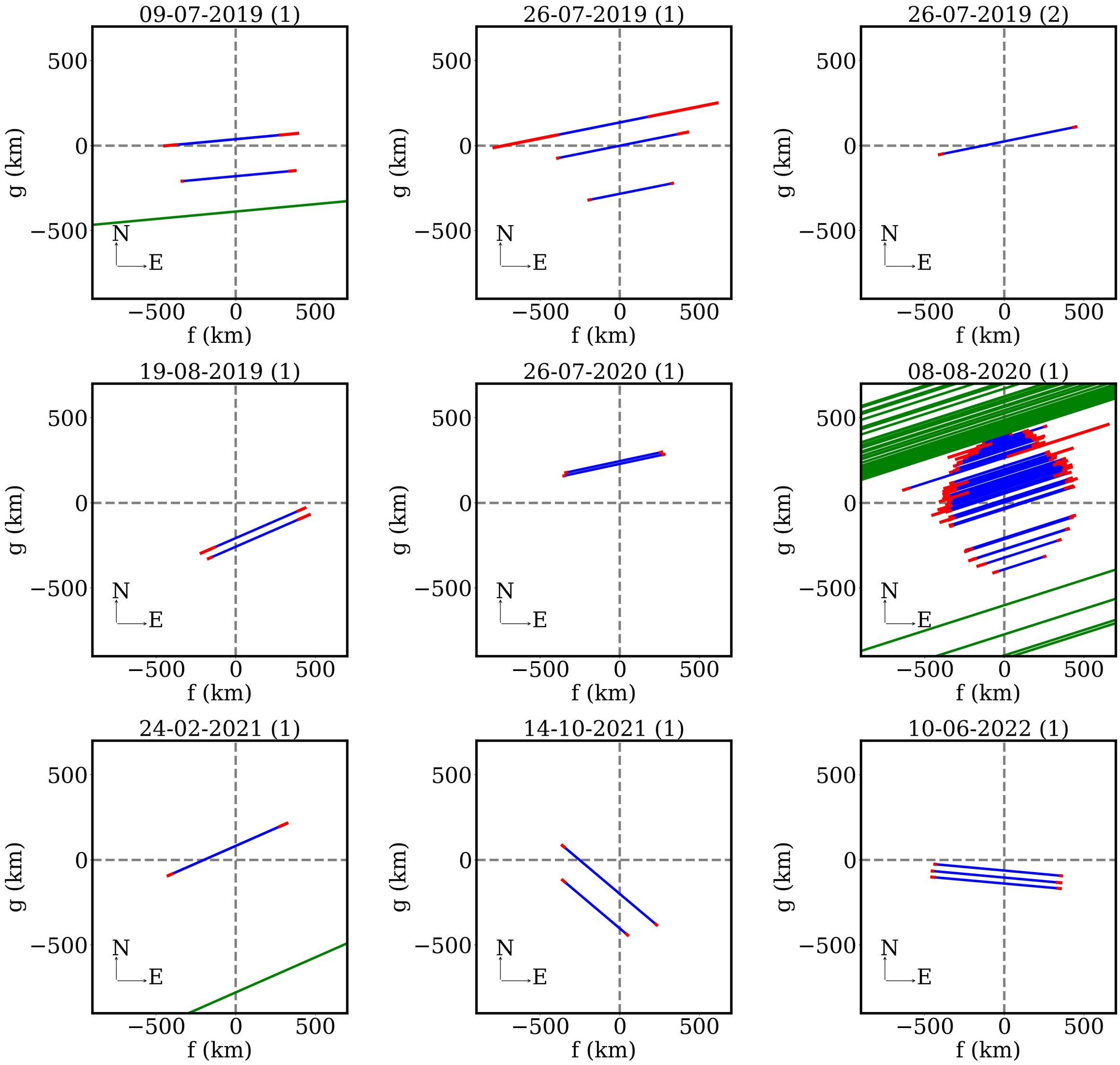

Figure 4.15: Projected at the sky plane are the negative (green) and positive (blue) chords (with 1σ error bars in red) of the nine stellar occultation events (sorted by date). Gray dashed lines indicate the predicted object's center position by NIMA v9 ephemeris. The number between parenthesis indicates the order of the event if on the same date.

4.1.1.3 Limb fitting

It is expected that large TNOs like 2002 MS_4 have reached one of the hydrostatic equilibrium shapes: Jacobi ellipsoid or MacLaurin spheroid. Therefore, an ellipse is the indicated shape to be fitted on the stellar occultation data (see Sect. 3.1.5). However, among the nine stellar occultation events, only three events provide more than 5 points to the limb-fitting procedure: 9 July 2019, 8 August 2020, and 10 June 2022 (Fig. 4.15). Therefore, we started the analysis by the multichord stellar occultation observed on August 8, 2020.

Due to its large diameter, it is also reasonable to suppose the presence of mountains and depressions on MS4's surface. Therefore, we calculated the theoretical lower limit for topography height ($h_{\rm top}$) supported by MS4's surface using the JOHNSON and

MCGETCHIN (1973) approach. Assuming that MS4 is mainly composed of ice with $S_{ice} = 0.0303\times10^9$ Dyn/cm^2 and has densities between ρ = 1.0 g/cm^3 and ρ = 2.0 g/cm^3. An exploration was performed using γ = 1 and radius values between 350 km and 450 km (Fig. 4.16) to derive the lower limit for topography supported on MS4's surface. As Charon has a global density of 1.7 g/cm^3, the ρ = 2.0 g/cm^3 seem a good value for lower topography limits determination of $\approx$ 7 km (dashed red line).

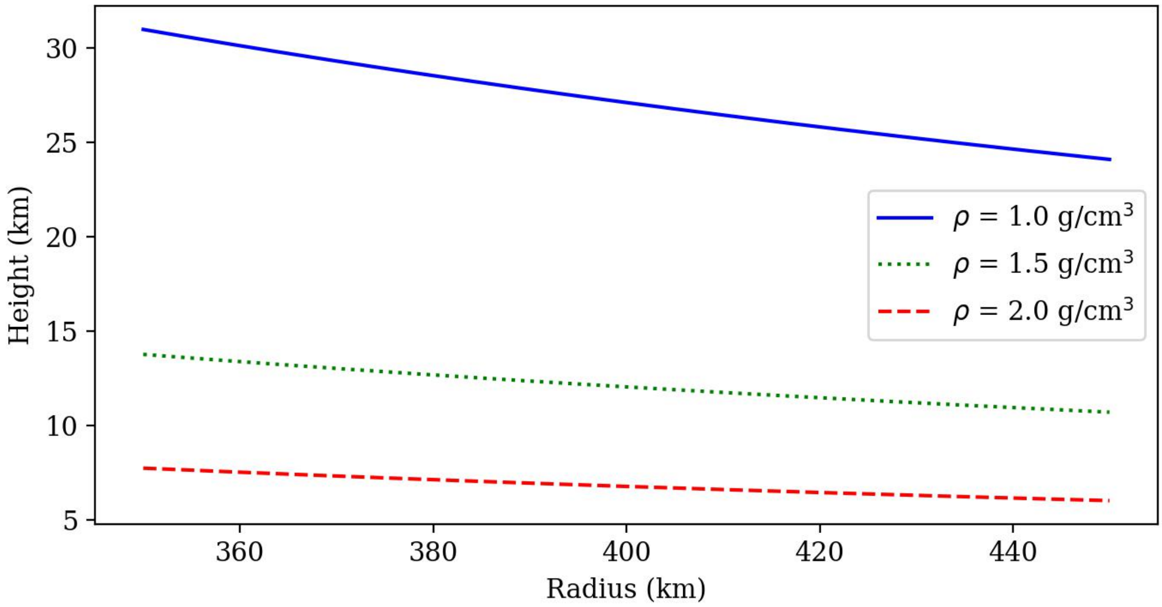

Figure 4.16: Height of the topography supported on MS4 surface according to the object's radius and object's density.

Due to some reported problems in time acquisition and because we suspect that large features are present in the northeast limb, 13 chords were selected among the 61 available: Grasse/FRA, Valbonne/FRA, Mátraszentistván/HUN, Catalonia/ESP, Massa/ITA, Roma/ITA, Hvar/HRV, Sassari/ITA, Odessa/UKR, Agerola/ITA, Algiers/DZA, La Palma/ESP and Çanakkale/TUR. The selection was based on a balance between time reliability, light curve SNR, and perpendicular separation from other positives. Therefore, the selected chords provide N = 26 independent points at the sky plane to fit the ellipse.

At this stage, we considered two different approaches to fit ellipses to the 26 selected points (Fig. 4.17): i) use only the 1σ event time uncertainties as derived from the occultation light curves (*upper* panel), and ii) add an uncertainty to the elliptical model (see Eq. 3.11) by using the *ellipse_error* function of SORA i.e., the fitted elliptical shape may differ from the actual limb projection with local irregularities up to this value (*bottom* panel, more information about the function is available on GOMES-JÚNIOR *et al.* (2022)). In total, six tests of limb fitting were performed. The first one did not use the *ellipse_error* function, and the other five involved values between 5 and 10 km.

The first approach provides an χ^2 per degree of freedom (χ^2_{pdf}) of 32, while the second gives a χ^2_{pdf} of 0.92 when using an *ellipse_error* of 7 km (Fig. 4.17 *bottom panel*). As

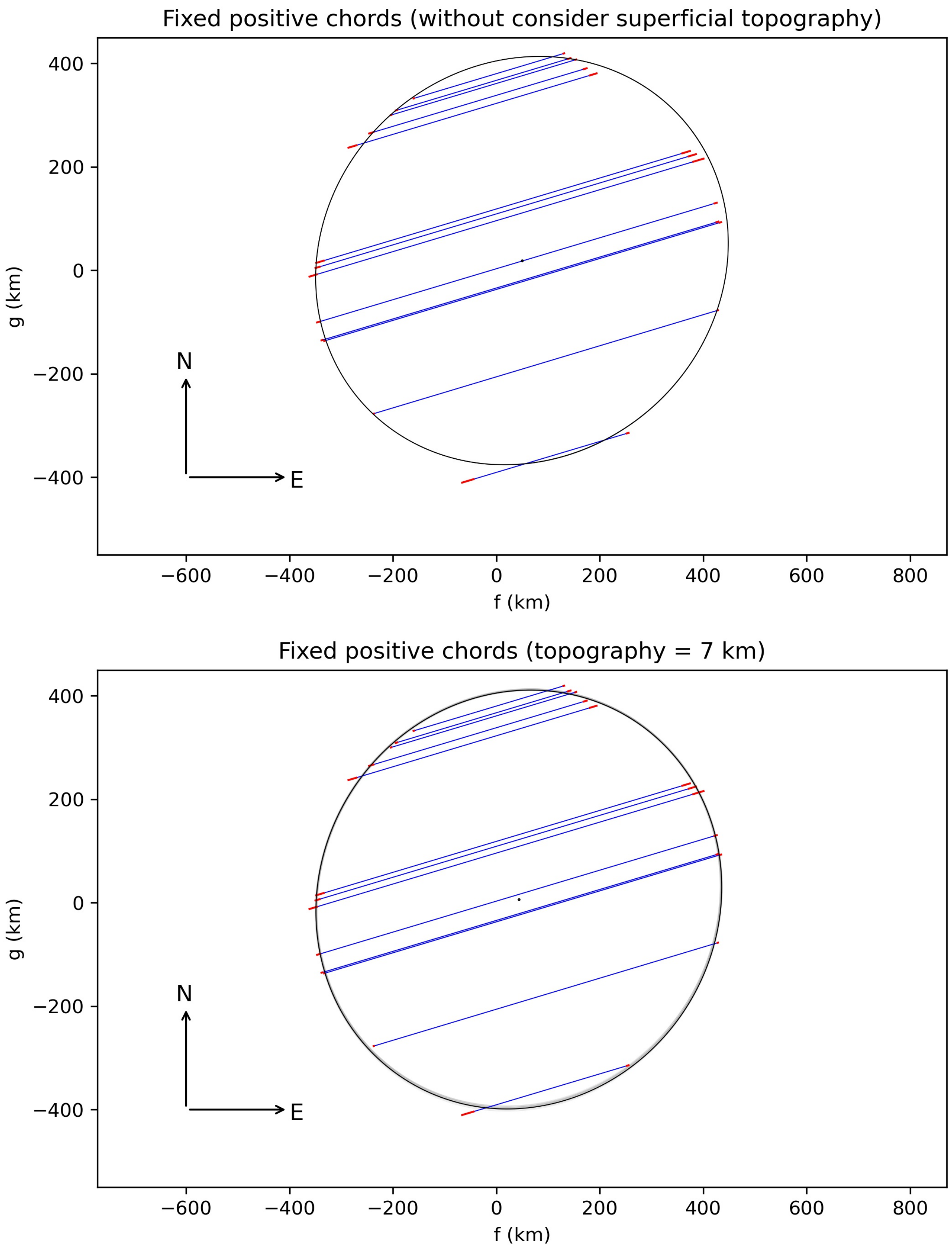

Figure 4.17: The 13 selected chords at the plane $(f,\, g)$ with the ellipse solutions within 1σ. Blue segments present the positive chords with uncertainties in red. *Upper* panel shows the limb solution for the first approach and the *lower* panel for the second (see text for details).

the latest solution presents a $\chi^2_{\rm pdf}$ closer than the expected theoretical value ($\chi^2_{\rm pdf} \approx 1$) and is in agreement with the lower theoretical limits determined before, we followed the analysis using the second approach. The elliptical solutions were filtered by the negative chord acquired at Montsec station, and the *filter_negative_chord* function also received a tolerance of 7 km. Therefore, although some elliptical solutions cross the negative segment (Fig. 4.18a), they are in agreement with the assumed topography of 7 km i.e., they are valid if a topography of up to 7 km is present in that region. The f', g' was calculated using the stellar position from *Gaia* DR3 (Table 4.2) and version 9 of NIMA ephemeris. The equivalent radius was calculated using the relation $R_{\rm eq} = a'\sqrt{1-\epsilon'}$. Using the equivalent radius ($R_{\rm eq}$), the Sun's H_V, and the published H_V for MS4, we obtained a p_V of 0.071 ± 0.12 (Eq. 4.1). Finally, the elliptical limb obtained for this stellar occultation data has the parameters presented in Table 4.3 and Fig. 4.18a.

$$p_V = \left(\frac{\rm au(km)}{R_{\rm eq}(\rm km)}\right)^2 \times 10^{0.4(H_{\rm sun}-H_{\rm obj})} \tag{4.1}$$

Table 4.3: Ellipse parameters (3σ) derived from the 13 selected chords admitting local topography up to 7 km.

f (km)	g (km)	PA′ (°)	a' (km)	ϵ'	$R_{\rm eq}$ (km)
43.4 ± 6.2	6.9 ± 9.3	121.3 ± 16.3	411.8 ± 9.9	0.066 ± 0.034	398 ± 12

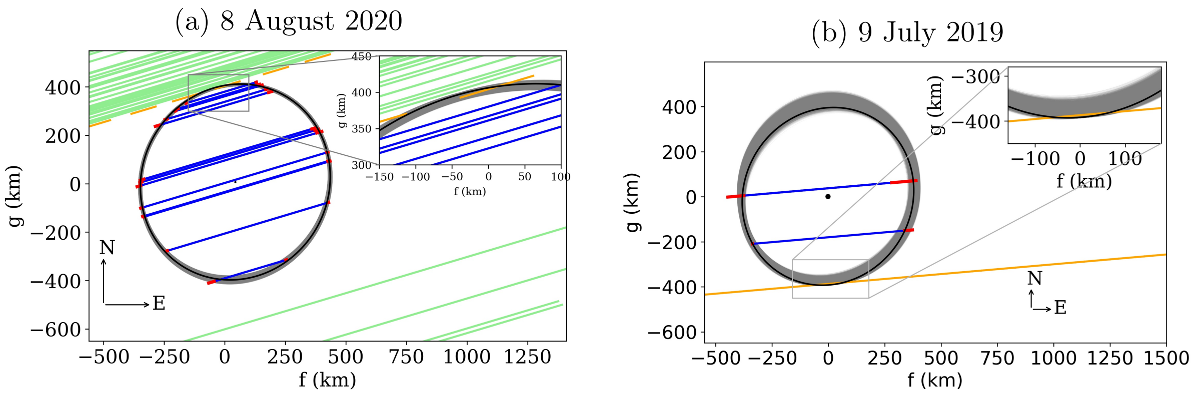

Figure 4.18: Limb fitting results for the multichord events we observed on a) 8 August 2020 and b) 9 July 2019. Positive detections are in blue, with 1σ uncertainties in red. In black is the best elliptical limb. The gray region presents all the limb solutions inside 3σ that survived the negative chord's filter. The upper right corner presents a zoom of the limb region delimited by the close negative.

Assuming that the MS4 has a Maclaurin shape the projected limb should have no significant variations among the stellar occultation events, i.e., the limb do not depend of the rotational phase. Therefore, we used the interval of parameters presented in Table

4.3 to fit MS4's limb over the chords acquired on other eight stellar occultation events. The f', g' was a free parameter, and the others were free only within the 3σ limits.

The July 9, 2019 event also has a close negative chord acquired from the Ponta Grossa observatory (Fig. 4.18b). Therefore, we filtered the elliptical solutions using this close negative with a tolerance of 7 km (as stated before). Two solutions for the center are equally possible in three events with single- and double-chord detections. On these events, the chosen limb solution is the closest one to the predicted by NIMA position. All ellipses fitted to the positive chords of the remaining seven occultations are presented in Fig. 4.19 and the final astrometric positions in Table 4.4.

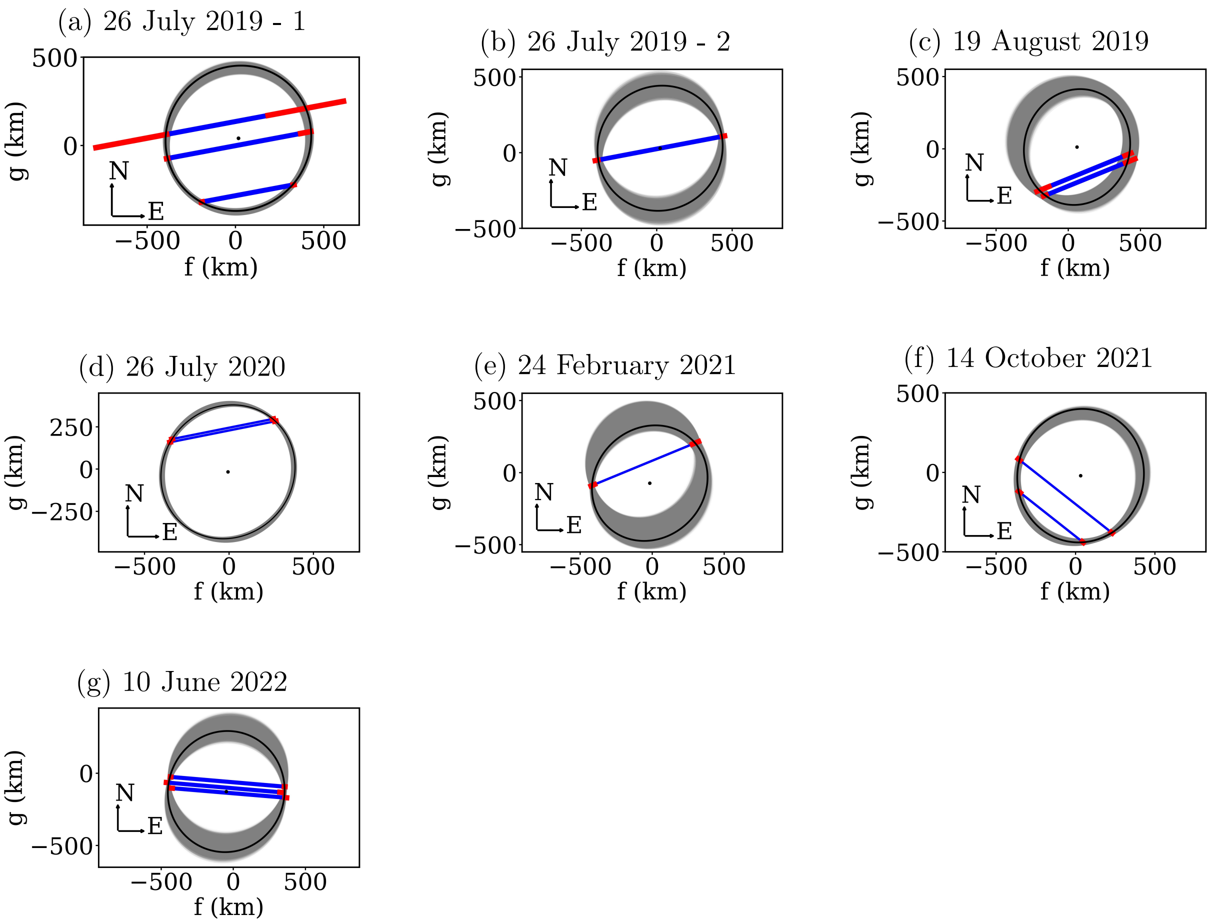

Figure 4.19: Limb-fitting to the remaining seven stellar occultation events. Blue segments are the positive chords with 1σ uncertainties in red. The best-fitted ellipse is in black, with the center presented by the black dot. The gray region presents all the limb solutions inside 3σ. For the c), d), and e) plots, the chosen center solution was the closest to the predicted-by-NIMA position.

Table 4.4: Astrometric information (ICRS) at closest approach instant (t_0) as obtained from the nine stellar occultation events observed between 2019 and 2022. The * symbol indicates that error bars are expressed in RA.cos(DEC).

Date	**Instant** (t_0)	**RA** (hh mm ss.ss)	**Uncertainties*** (*mas*)	**DEC** (° ' '')	**Uncertainties** (*mas*)
09-07-2019	04:23:49.08	18 45 19.245987	0.15	-06 24 13.05887	0.12
26-07-2019	02:47:08.52	18 44 07.573464	0.54	-06 26 40.17740	0.46
26-07-2019	10:18:43.02	18 44 06.315997	0.13	-06 26 43.76859	0.11
19-08-2019	07:41:52.28	18 42 43.51613	1.0	-06 32 33.9776	1.1
26-07-2020	23:17:56.04	18 48 18.075014	0.12	-06 13 31.70897	0.12
08-08-2020	20:44:27.26	18 47 29.961308	0.12	-06 16 31.34442	0.10
24-02-2021	08:45:52.82	18 56 35.987285	0.25	-06 30 23.15932	0.23
14-10-2021	03:26:05.50	18 50 30.768578	0.31	-06 24 13.20717	0.27
10-06-2022	05:32:47.30	19 00 15.446841	0.32	-05 42 42.8843	1.3

4.1.1.4 Topographic features

The knowledge about topography on TNOs is still limited to observations of the Pluto-Charon system, Arrokoth, and one detection of 2003 AZ_{84} during a stellar occultation (as stated in Sect. 2.3.3). Topography up to 11 km also was observed in Uranus' five major satellites, which have mean diameters between 472 and 1577 km (SCHENK and MOORE, 2020). Those few observations and the topography dependency with the object's size (TANCREDI and FAVRE, 2008) cannot provide a solid baseline for estimating topography in MS4. Then, in this work, we used the theoretical approach mentioned above to calculate the lower limit for supported topography on MS4, and we developed a method to search for more prominent features in the residuals of the stellar occultation data.

The first evidence of topography on MS4 came from the light curve acquired on Varages/FRA, the northernmost positive chord. Varages's light curve does not have dead time between two sequential exposures, and the exposure translates into a resolution of 1.97 km into the sky plane. The Fresnel diffraction and stellar diameter at MS4 geocentric distance are at the same level, 1.54 km and 1.19 km, respectively. The OLC (Fig. 4.20) presents a sharp ingress and a gradual egress above the noise level as shown in Fig. 4.20. The feature did not appear in any of the other high SNR light curves. Therefore, an occultation by a secondary star can be discarded. Thus, the most plausible explanation is a topographic feature where a portion of the star appeared during a few frames before egress, corresponding to a more than 20 km long feature in the chord's direction. The insert in Fig. 4.20 pictures the stellar position in each frame, represented by yellow circles, relative to a proposed limb in gray.

To investigate further the presence of topographic features in MS4, we evaluated the radial difference (R_{diff}) of each observed point relative to the best-fitted ellipse. Among all the R_{diff} points, we selected only the values larger than its 1σ uncertainty. The selected points are in black in Fig. 4.21, where the R_{diff} is presented as a function of the PA′ (°).

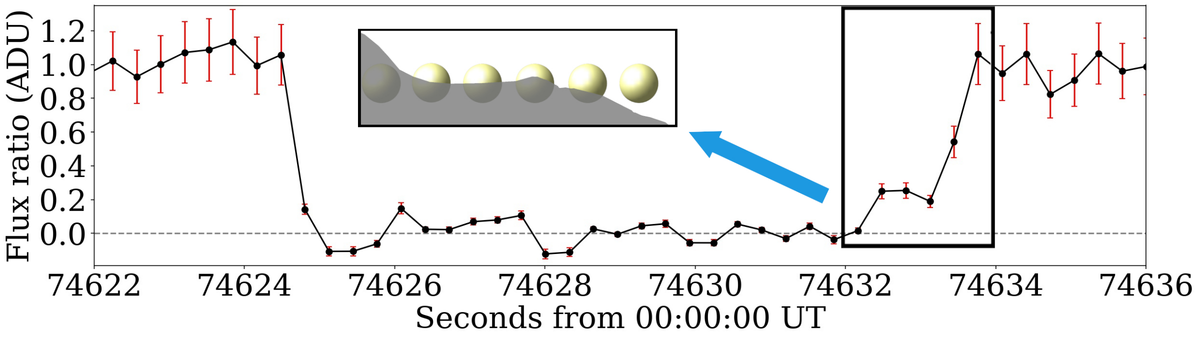

Figure 4.20: The normalized OLC acquired by Varages station on August 8, 2020 (black dots) with photometric uncertainties in red. The insert selects the egress region and illustrates a possible explanation for such a signal (see text).

The vertical red segments are Gaussian distributions with a standard deviation equal to the radial uncertainty ($\sigma_{\rm rad}$) and centered in the point. The frequency histogram on the right present the $\rm R_{diff}$ distribution, including the uncertainties.

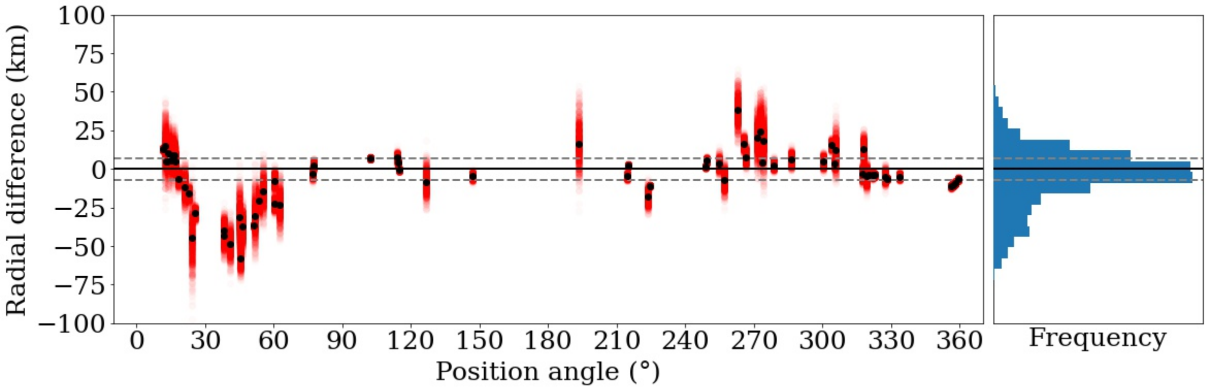

Figure 4.21: The $\rm R_{diff}$ points (black) with Gaussian uncertainties (red) are presented as a function of the PA′. The black line presents the best-fitted ellipse, and the gray dashed lines mark the 7 km topography. A histogram of data frequency considering the error bars is presented on the right side.

Given the assumed global topography variation of 7 km, the expectation for the $\rm R_{diff}$ points was a Gaussian distribution with a FWHM of 14 km and symmetric around zero, but the histogram is skewed negatively. Therefore, we can investigate the presence of subjacent topographic deviations when subtracting the expected Gaussian distribution from the general histogram (Fig. 4.22a). The Gaussian-subtracted histogram was divided into two groups, and new Gaussian functions were fitted on the residuals to derive the individual FWHM (Fig. 4.22b). Despite being merged, negative and positive curves are separated above the 1σ level, indicating some topography in both directions.

The histogram analysis revealed that at least one depression and one elevation might be present in our data set. In addition, from Fig. 4.21, it is clear that most of the deviations above the assumed 7 km of global topography are between PA′ = - 5° and PA′

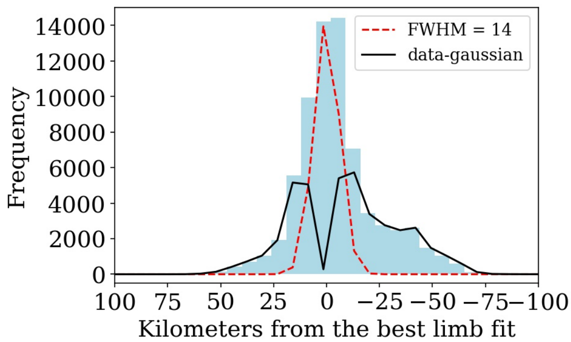

(a)

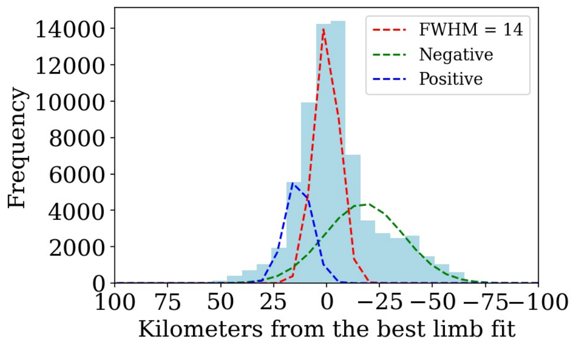

(b)

Figure 4.22: In blue is the same frequency histogram shown in Fig. 4.21, but rotated clockwise by 270°. The dashed red line shows the expected distribution with FWHM = 14. a) The solid black line presents the histogram after subtracting the Gaussian function in red. b) The negative and positive Gaussian curves fitted to the Gaussian-subtracted histogram are represented in green and blue, respectively.

= 125° (considering the PA′ as cyclical). This is the first time that many occultation chords sound a topography on a TNO.To fully characterize it, a method was developed using parabolic functions fitted to the R_{diff} points between the PA′ angles mentioned above.

Starting with a simple parabola $y(x) = w.x^2$, where the function minimum is zero, and it is symmetrical around the ordinates, we add coefficients associated with the quadratic term $y(x) = w.(x - z)^2$. Then, to model a depression or an elevation, we add a summation term to the function for accounting for the feature's depth (or height) and the distance from the ordinates around which it is symmetric. In addition, we defined all regions outside the parabola as being zero. In summary, we have the following models for a depression (Y_1) and an elevation (Y_2),

$$Y_1 = \begin{cases} 0 & y \geqslant 0 \\ w(x-z)^2 - k & y < 0 \end{cases} \qquad Y_2 = \begin{cases} 0 & y \leqslant 0 \\ w(x-z)^2 + k & y > 0, \end{cases}$$

where z is the center of the parabola and k accounts for the depth/height of the depression/elevation. Furthermore, the coefficient w is negative in the elevation and positive for the depression. As we identified three groups of topography, one large depression, followed by an elevation and another depression in the sequence, the overall model (Y_F) is defined by the summation of three parabolas

$$Y_F = Y_1 + Y_2 + Y_1. \tag{4.2}$$

The fitting procedure was done using a PYTHON library for non-linear optimization and curve-fitting problems named LMFIT[9]. It is built on and extends many numerical optimization methods available in the *scipy.optimize* library[10]. We started with the Differential Evolution (DE) minimization method (STORN and PRICE, 1997) and an initial set of parameters. This algorithm can explore large areas of the provided parameters space without getting trapped in a local minimum. Finally, the best-fitted model is presented in Fig. 4.23.

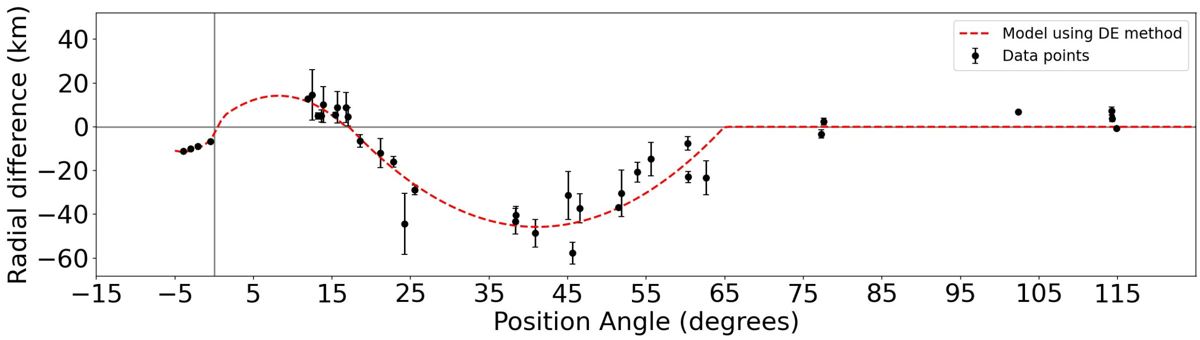

Figure 4.23: This plot presents the selected R_{diff} points as a function of the PA′ (black points). The gray horizontal line represents the best-fitted elliptical limb described above. The dashed red line shows the best solution for model fitting using DE.

Next, we explored the parameters' space to find the variance of the points relative to our topographic model. We used the Maximum likelihood via Monte-Carlo Markov Chain (MCMC) sampler - *emcee*[11](FOREMAN-MACKEY *et al.*, 2013) to estimate the posterior probability function, i.e., find the distribution of parameters consistent with the data set. Therefore, given an initial range of values for the w, z, and k parameters, the Maximum likelihood is calculated as follows

$$\ln P(y|x,w,z,k,f) = -\frac{1}{2}\sum_i \left\{ \frac{[y_i - Y_F]^2}{s_i^2} + \ln(2\pi s_i^2) \right\}, \tag{4.3}$$

where f is a fraction of uncertainty summed to the function to account for errors not considered in the provided uncertainty. Therefore, if we consider that points' error bars are underestimated, $s_i^2 = {\sigma_{\text{rad}}}^2 + f.Y_F^2$, otherwise $s_i^2 = {\sigma_{\text{rad}}}^2$. In this work, we investigated both approaches, and the results are present in Fig. 4.24.

The result of fitting Gaussians to the frequency histogram provides a first estimation of the features' sizes. There is evidence of a 44 km depth depression and an elevation of 15 km (Fig. 4.22b). Consistent results are derived by fitting a model composed of three parabolic functions to the points in the range of PA′ between - 5° and 125° (Fig. 4.24a and 4.24b). The agreement between both fitting approaches proposes the detection of an elevation followed by a large depression in the MS4's northeast limb.

[9]More about this library can be found in the https://lmfit.github.io/lmfit-py/
[10]https://docs.scipy.org/doc/scipy/reference/optimize.html
[11]Documentation available on https://emcee.readthedocs.io/en/stable/

We explored the space of parameters to better calculate the best-fitted model's uncertainty (Fig. 4.23). When using only points' errors, the result is a model with underrepresented uncertainties (Fig. 4.24a). On the other hand, the resulting error bars represent better the data set when we allow for unknown uncertainties (Fig. 4.24b). The last result shows that an additional error of ≈ 4.5 km must be considered to get a model that coherently describes the data. As the assumed 7 km of global topography was not considered here, the ≈ 4.5 km is not surprising.

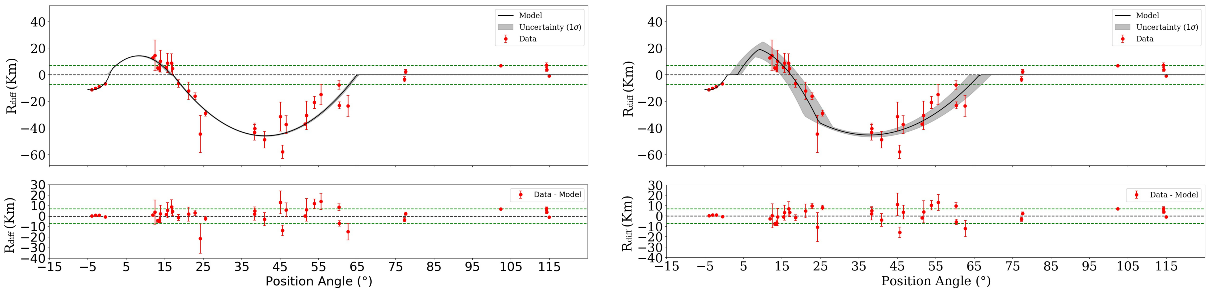

(a) (b)

Figure 4.24: *Upper* plots present the selected R_{diff} points as a function of the position angle (red points). The green dashed lines are the lower limit for the topography of 7 km. The black dashed line represents the best-fitted elliptical limb described above. The solid black line shows the best solution for model fitting using the DE method, and the shaded region is the 1σ uncertainty derived with the emcee sampler. Finally, lower graphs present the residuals after subtracting the models from the data. In (a) the derived model error bar only considers the points' uncertainties, and in (b) we allow for unknown uncertainties of about 4.5 km.

One can analyze the residuals after subtracting the models from the data to validate their quality. The lower plots in Fig. 4.24a and 4.24b show the residuals of each model, mainly inside the global topography limits (dashed green lines). Therefore, both are good descriptions of the detected local limb, but the second one gives slightly smaller residuals. In addition, the shaded 1σ error bars better represent the points distribution and it is our preferred solution.

This section showed that stellar occultation data detected a local limb with an 11 km depth depression followed by a 25^{+5}_{-12} km high elevation. The most prominent depression is 45.2 ± 3.2 km depth and has a diameter of 322 ± 39 km, and topography also was detected in one OLC acquired from Varages/FRA station (Fig. 4.20). The formation mechanisms of such large features on the 2002 MS_4 surface require more data and are out of the scope of this work.

4.1.2 Rotation

As stated above, MS4 is a faint object crossing the galactic plane, and it is challenging to observe it separated from background stars. However, despite the difficulty, telescopes worldwide acquired some images over the years. In this section, we describe the analysis of some data sets by using i) the usual relative photometry, ii) the Difference Image Analysis (DIA), and iii) the absolute photometry of images spread over many years.

4.1.2.1 Relative photometry

The relative photometry was applied to 71 images acquired from the TNG telescope following the procedure described in Sect. 3.2.1. Those images were selected among others because they were taken on sequential nights while MS4 was crossing in front of a dark cloud. The chosen apertures maximize the sources' SNR in the reference image. However, they are free to change according to *seeing* variations between sequential images. The first and last images are presented in Fig. 4.25. Green circles mark the calibration stars, the red circle measures the object's flux, and the pixels between the concentric blue circles are used to estimate the local background contributions. Despite some sky annulus being contaminated by nearby stars, PRAIA can overcome the problem and reject the contaminated pixels from background estimations.

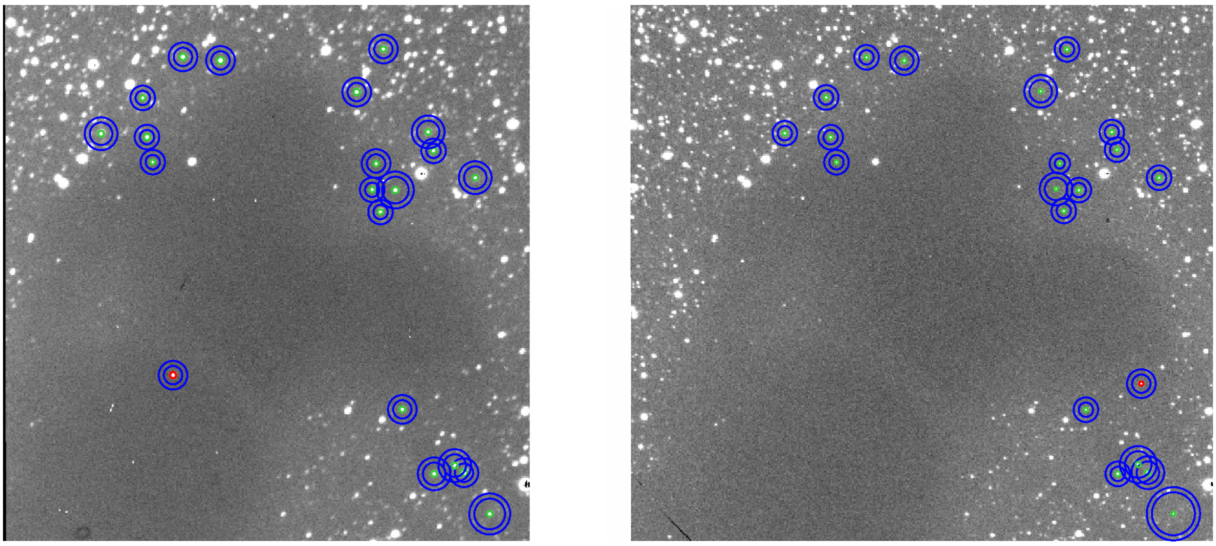

Figure 4.25: The first and last image of MS4 from the TNG telescope and submitted to the PRAIA algorithm. Green circles mark the calibration stars, the red circle the TNO, and the pixels between blue circles were used for local background estimations.

The measured median values of SNR and inner aperture for MS4 over the entire data set are 175 and 2.4 pixels, respectively. The m_{rel} as a function of time is presented in Fig. 4.26a, where the different symbols indicate the observational nights. Finally, the rotational light curve is derived from those points using the LS method (Fig. 4.26b and 4.26c). Despite being noisier, this result coincides with the published information (THIROUIN, 2013).

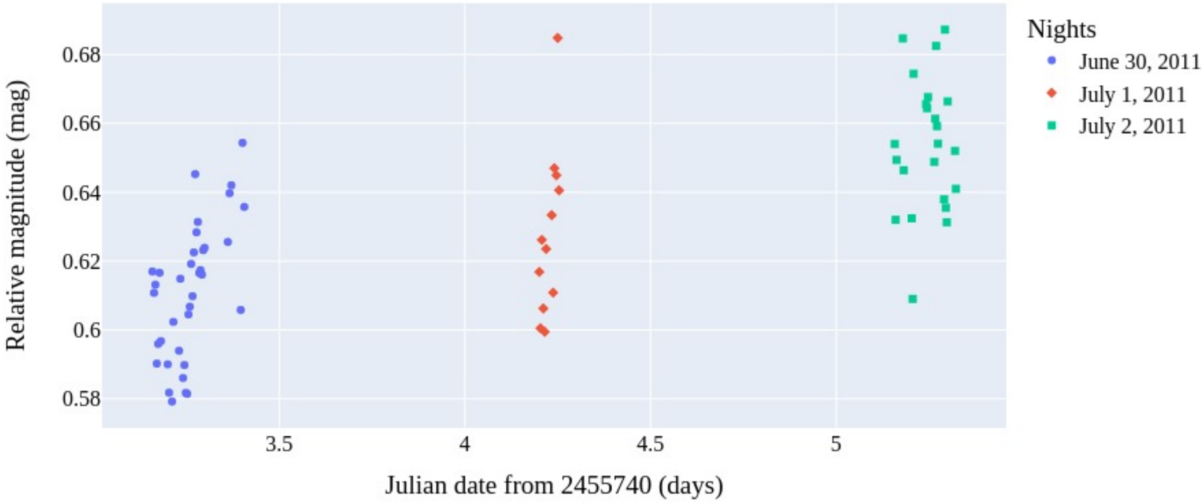

(a)

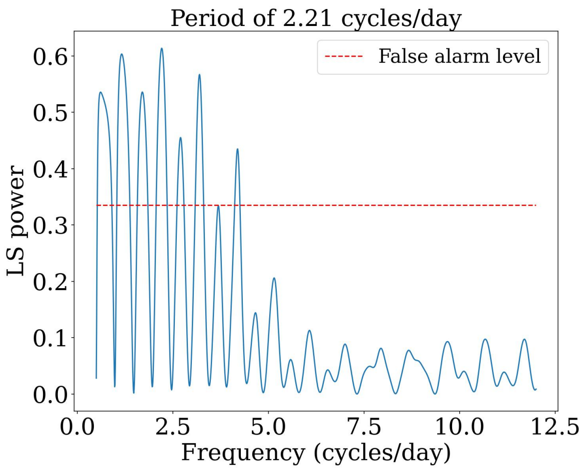

(b)

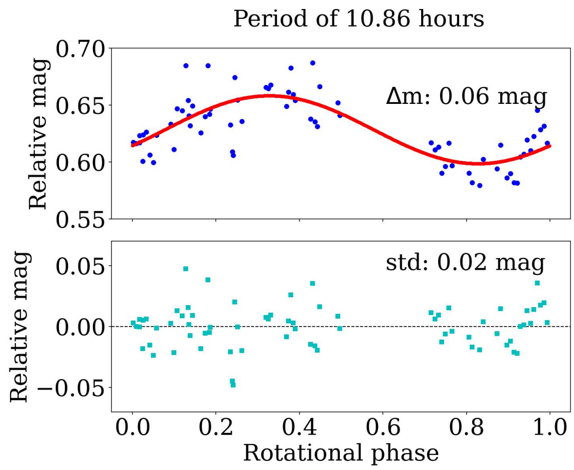

(c)

Figure 4.26: (a) The relative magnitude of 2002 MS_4 as a function of time. Each color represents one night of observation. (b) The Lomb-Scargle periodogram shows the strongest frequency (highest peak) at 2.1 cycles/day with 10.86 h. The dashed red line is a standard estimation of false alarms. (c) The rotational light curve with the best period found before. The lower plot shows the residuals after subtracting the model (red curve) from the relative magnitudes (blue dots).

4.1.2.2 Differential Image Analysis (DIA)

Since its discovery, MS4 has been observed in very dense stellar fields, except for the unique opportunity mentioned in Sect. 4.1.2.1. Therefore, we tested two image subtraction approaches to derive MS4's photometry free of contamination by background stars. The selected data set has 47 images acquired in the R filter at Pic du Midi observatory on July 17 and 18, 2020. No calibration files are available. The tested tools are the PROPERIMAGE and DIAPL2 implementations of Zackay's and Alard's methods, respectively.

PROPERIMAGE tool has a function to extract only the region of interest from the original images. Therefore, we extracted two square sections with 300 pixels from all original images. The chosen areas only contain MS4 on one of the nights, allowing us to use the same region to build the template image for the other night. Then, the two groups of images were aligned using the Astroalign python module[12]. The trimmed images on which MS4 is not present were co-added to build the template image for each night. The template image contains the median of the flux in each pixel of the aligned trimmed image. Finally, the template image (Fig. 4.27b) was subtracted from the original ones (Fig. 4.27a) to obtain the difference image (Fig. 4.27c).

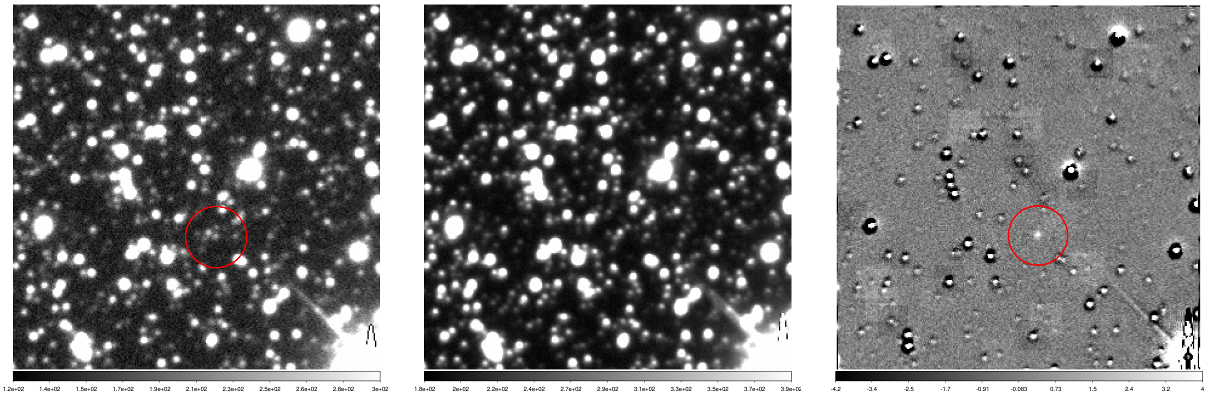

(a) (b) (c)

Figure 4.27: Example of trimmed and aligned images used in PROPERIMAGE. (a) The original image containing MS4 (red circle), (b) the template image, and (c) the difference between both images.

DIAPL2 follows the same steps described for PROPERIMAGE approach, except that it makes all automatically and uses the entire images. A comparison between the result obtained with each tool for the same original images is presented in Fig. 4.28. Despite both tools presenting a reasonable difference image, it is clear that PROPERIMAGE leaves more stellar flux behind. However, to check which method gives the best result overall the entire data set, we used PRAIA to perform the photometry of the subtracted images.

The flux measured by PRAIA in each difference image was divided by the median value of the night to obtain a normalized light curve. Then, the light curve was submitted to the LS method for periodic search, and the best period found was around 2 h (Fig. 4.29). Probably, this is a result of the poor coverage of the rotational phase. Therefore, we folded the data for both published period values (Fig. 4.30). As mentioned above, a larger standard deviation comes from PROPERIMAGE's results (0.10), while DIAPL2 presents only 0.05. A manual check of the four outliers near phase 0.2 revealed that they are caused by flux contamination of a nearby star that was not well subtracted by PROPERIMAGE. In the end, unfortunately, new rotational information of MS4 was not obtained using this approach.

[12]Documentation available on https://astroalign.quatrope.org/en/latest/.

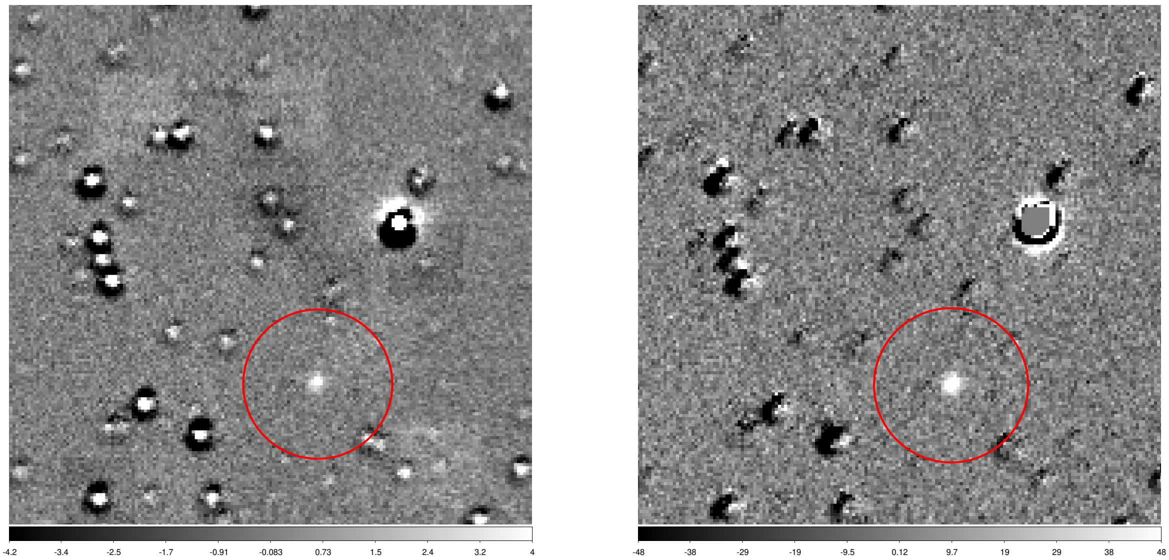

(a) (b)

Figure 4.28: Comparison between the result of subtracting the star background from the same image using the (a) PROPERIMAGE and (b) the DIAPL2 tools. Red circles show the position of MS4.

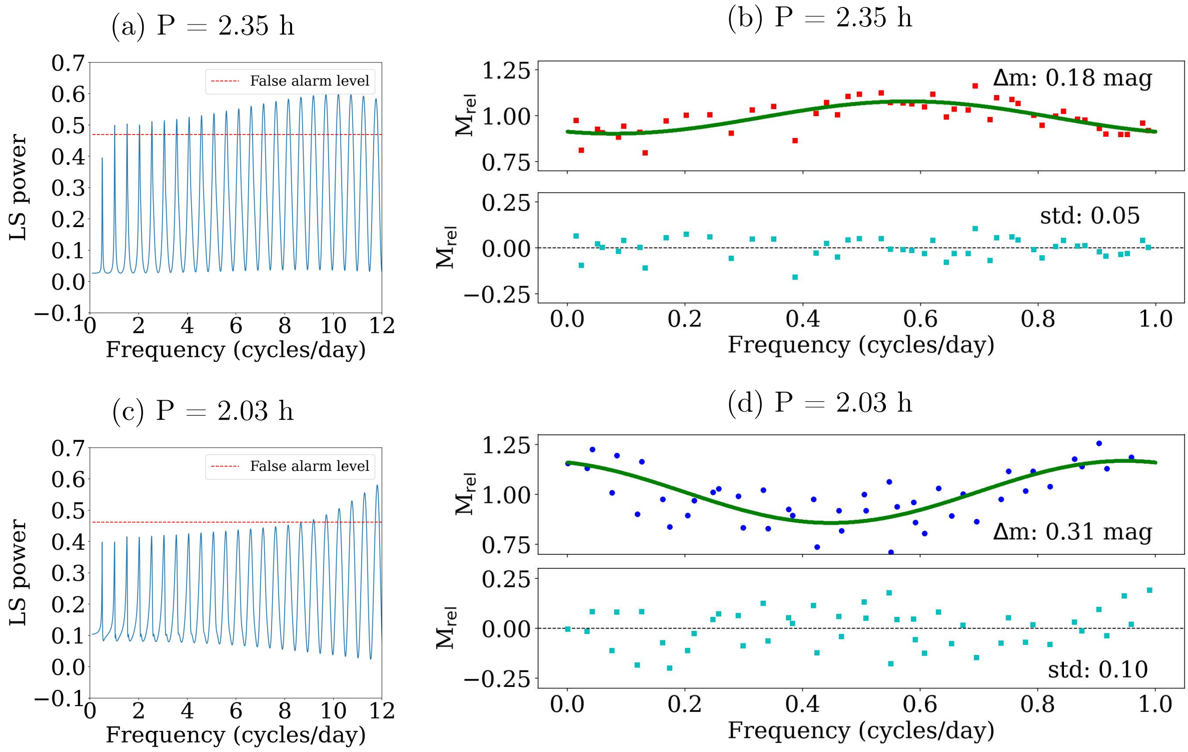

Figure 4.29: LS periodogram (a, c) and the RLC (b, d) obtained from the photometry of subtracted by background images. The upper panel shows the result for images manipulated with DIAPL2, and the lower panel images obtained with PROPERIMAGE tool. Note that a few peaks are just above the false-alarm probability (dashed red line), i.e., the probability of being the true signal is low (see Sect. 4.1.2).

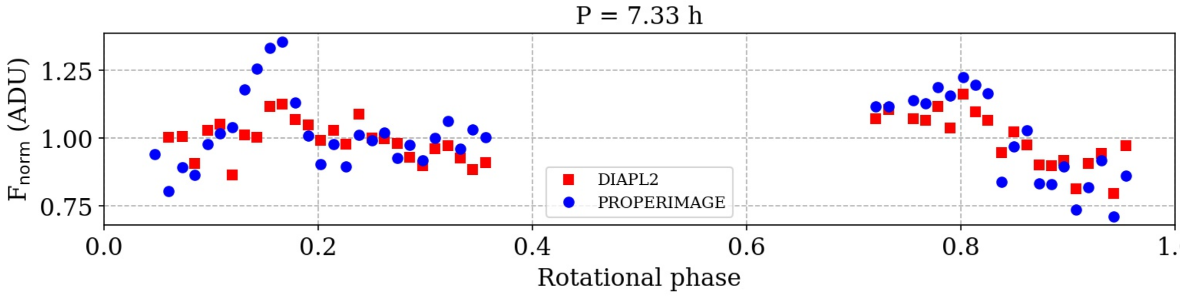

(a)

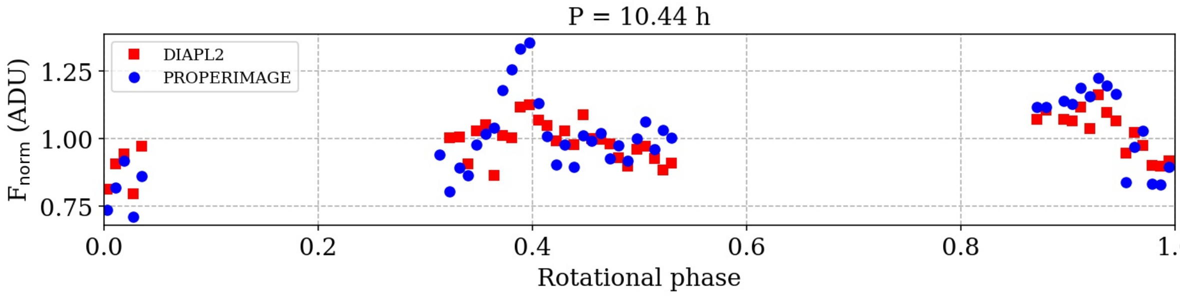

(b)

Figure 4.30: Normalized flux of 2002 MS_4 as measured by PRAIA on the difference images generated by DIAPL2 (red) and PROPERIMAGE (blue). (a) The 47 points folded by a rotational period of 7.33 h and (b) folded by 10.44 h.

4.1.2.3 Absolute photometry

The astronomical images used in this approach came from the private database of IAA-CSIC and the public repository of images called SSOIS. The IAA-CSIC has a team dedicated to studying the SS's minor bodies, and they periodically run observational campaigns on Spanish telescopes to derive the short-term variability of Centaurs and TNOs. All images acquired since 2001 by the IAA-CSIC team are stored in the mentioned database, and searching for MS4 images, 946 files were found (Table 4.5), mainly from the OSN and CAHA telescopes. Those images were already in the expected format, and no preparation was needed.

Table 4.5: List of images found in the IAA-CSIC private database with the predicted FOV of MS4.

Observatory Country	Telescope	Diameter (m)	Camera	pixel scale ("/px)	Images found
Calar Alto Spain	CAHA	1.23	SITe#2b_17	0.5	417
Sierra Nevada Spain	-	1.5	Roper	0.45	403
Roque-de-los-Muchachos Spain	TNG	3.58	LRS	0.5	100
Roque-de-los-Muchachos Spain	Liverpool	2.0	Optical Wide Field Camera IO:O	0.3	26

A search through the SSOIS[13] database (GWYN *et al.*, 2012) for public images with

[13] https://www.cadc-ccda.hia-iha.nrc-cnrc.gc.ca/en/ssois/

MS4 and associated calibration files was performed. A total of 1487 images from different instruments were identified in the SSOIS database in December 2021. In this study, we did not use image sets with less than eight images or exposure times smaller than 40 s. 582 images and the appropriate calibration files were obtained (Table 4.6). Despite having 70 images from the 1.3 m telescope in CTIO, the images are separated by several days, even months. Those small and isolated in-time data sets were not used in this analysis. A shell script was built using the ASTFITS function[14] provided by GNU Astro software[15] to convert the files into the standard FITS format and/or edit the image's header accordingly with the expected pattern. The script worked for 98.5% of the images, except for the Gemini data, which has a non-standard image/header format. Therefore, those images did not participate in the analysis.

Table 4.6: List of public images that may contain 2002 MS_4 according to the SSOIS portal. The list refers only to data sets with eight or more images and with exposure times larger than 40 s.

Telescope	**Images**	**Telescope**	**Images**
MPI/ESO	123	CTIO 0.9 m	41
Pan-STARRS 1	87	SOAR	26
CFHT	76	NTT	20
CTIO 1.3 m	70	VLT	16
CTIO 1.0 m	59	Gemini	8
CTIO 4.0 m	56		

Despite having the expected FITS format, the files acquired by the Pan-STARRS 1[16] and at the CTIO 1.0 m telescope present a white pattern all over the images (Fig. 4.31). They are too complex for our algorithms to comprehend. Therefore, the ASTCROP function by GNU Astronomy Utilities[17] was used to cut only for the image section that contains 2002 MS_4, except for the Pan-STARRS 1 data. Pan-STARRS 1 images were discarded due to the presence of the white patterns and also because of the low SNR.

The images isolated in time were also excluded from our data set. Usually, only three or four images separated by months from other data do not contribute much to the analysis. Therefore, the massive data processing system described in Sect. 3.2.3 received 309 public images, 47 images from the 1 m telescope located at Pic du Midi observatory - France[18], and 946 files from the IAA-CSIC database (Table 4.5). Finally, among the 1302 images submitted to the system described in Sect. 3.2.3, MS4 was found in only 518 images. Fig. 4.32 presents the number of processed images and the images' SNR as

[14] https://www.gnu.org/software/gnuastro/manual/html_node/Invoking-astfits.html

[15] I used the version 0.14, and more information is available on https://www.gnu.org/software/gnuastro/

[16] More information available on https://outerspace.stsci.edu/display/PANSTARRS/

[17] Documentation available on https://www.gnu.org/software/gnuastro/manual/html_node/Invoking-astcrop.html.

[18] The same data set used for Difference Image Analysis.

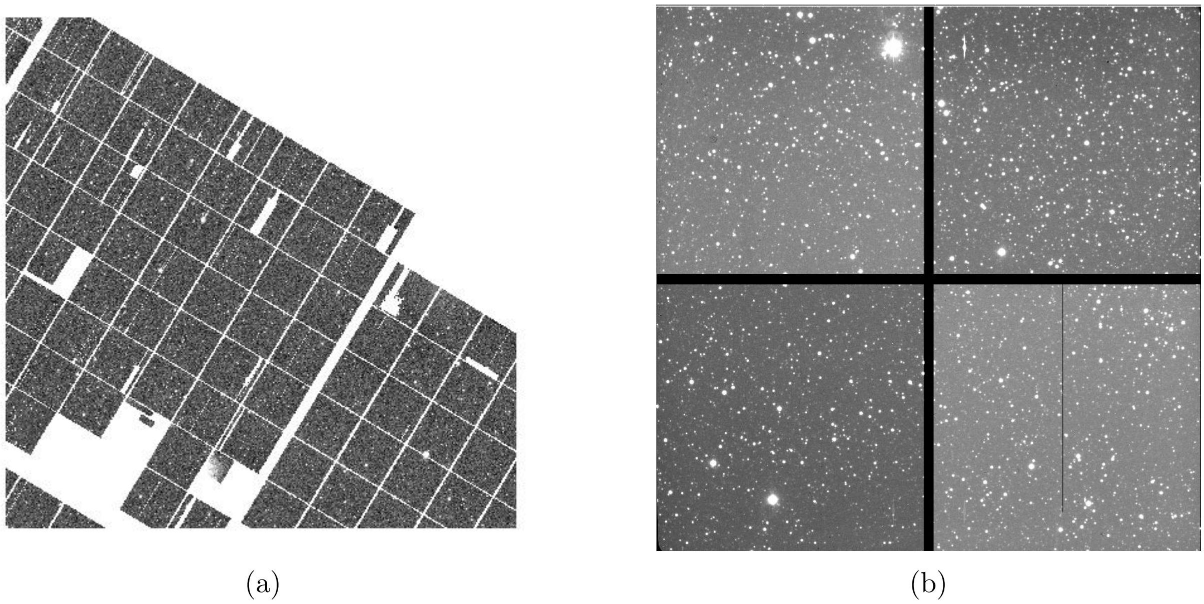

Figure 4.31: Image presenting the white patterns all over the FOV, acquired from a) Pan-STARRS 1 and b) CTIO 1 m telescopes.

a function of time. It is clear that the best data was acquired by TNG telescope in 2011 (as described in Sect. 4.1.2.1). Note that filters written in the image's header are not considered in the photometric analysis. Every image passes through the photometric star selection and calibration described in Sect. 3.2.3.

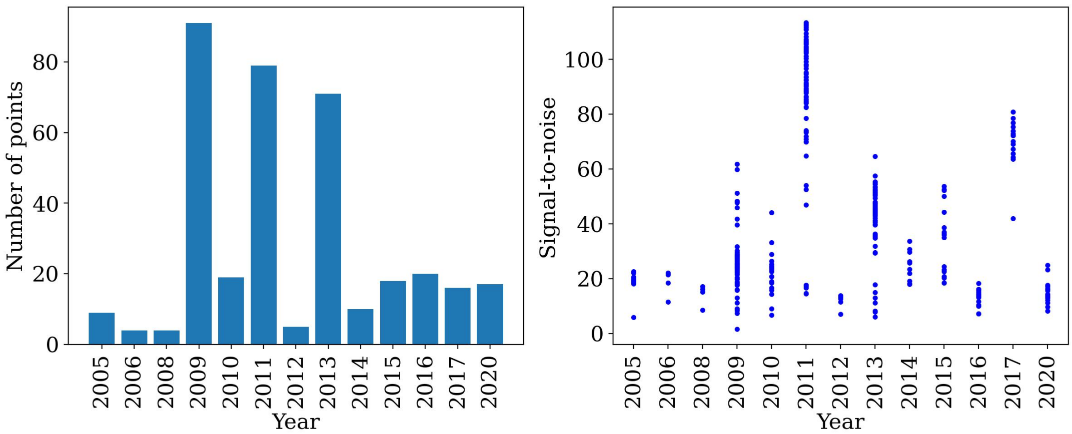

Figure 4.32: **Left:** Number of points distributed over time. **Right:** 2002 MS_4's signal-to-noise distribution over time.

Fig. 4.33a presents a general view of the object's reduced magnitude ($M_{obj}(1, 1, \alpha)$) as a function of the α, where colors refer to different telescopes. The linear fit shows a negative slope, which is probably due to the outliers. Therefore, the *croppy* files were verified manually to identify problems in the photometry. The most common problematic situations involved the detection of the TNO merged with a non-*Gaia* star (Fig. 4.34a and 4.34b), and, as a result, the measured magnitude was incorrect. In rare cases, the target

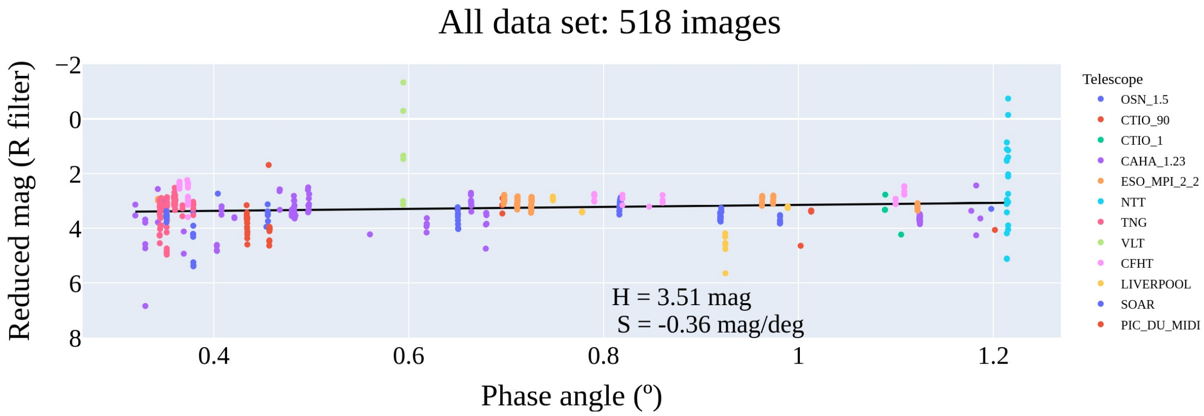

(a)

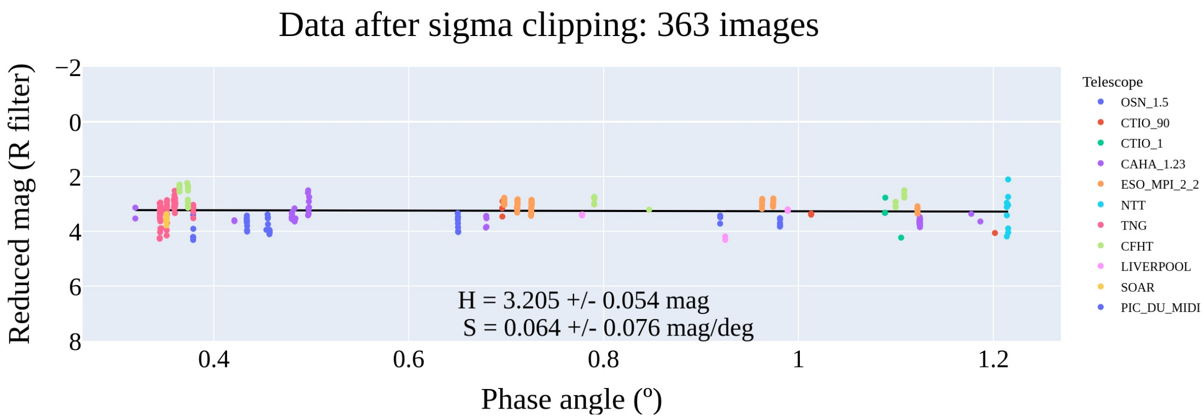

(b)

Figure 4.33: The plots present the reduced magnitude calculated by M2 as a function of the phase angle. The colors represent the different telescopes that acquired the images and are not identical for both plots. The solid black line presents the linear fit to all points. H_R and S are the coefficients resulting from the fit, corresponding to the absolute magnitude in R-band and slope, respectively. a) The entire data processed by M2 and b) the remaining points after the filtering process and sigma clipping (see text).

falls in a malfunctioning CCD area, and the defective pixels interfere with the measured flux (Fig. 4.34c and 4.34d). Finally, using stellar charts to compare the detected FOV with the expected one revealed that the image's WCS solution may be incorrect if fringing effects are present. In this case, the flux of a random star is measured instead of the TNO (Fig. 4.34e).

The detection problems mentioned above are expected when images with a crowded FOV from various instruments are submitted to the system. However, after excluding the problematic measurements, three groups still exhibit considerable deviations from the average, the images acquired by the Liverpool telescope, the Very Large Telescope (VLT), and the New Technology Telescope (NTT). Indeed, the visual inspection of VLT images revealed issues in filter identification, so they were excluded. The other two groups were maintained since there were no obvious concerns with the photometry, filter identification,

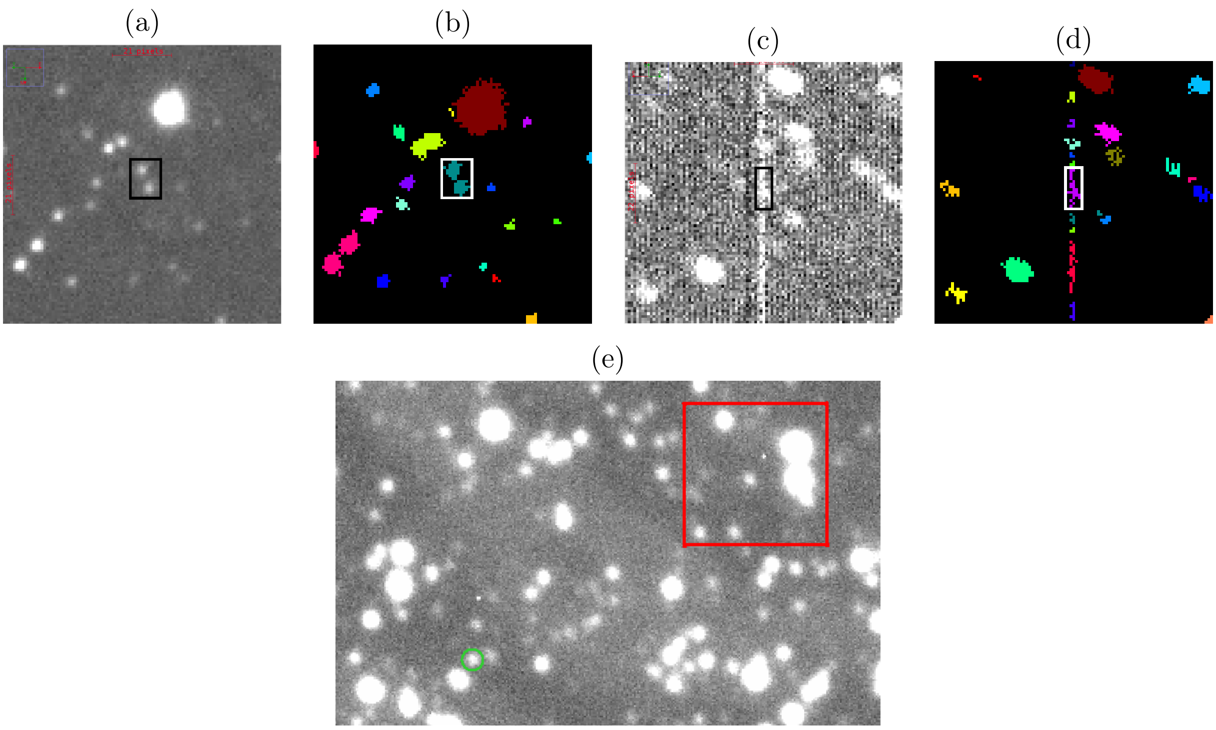

Figure 4.34: Original images that contain our TNO (*a*, *c*, and *e*) and the *croppies* made by M2 (*b* and *d*). Each color in the *croppies* represents a different source. *a*) Shows our target is close to but separated from a non-*Gaia* star. *b*) Shows that M2 interpreted both sources as being our TNO. *c*) and *d*) present the detection of bad pixels precisely in the position of 2002 MS_4. Finally, *e*) shows an example of a wrong WCS solution. This image has fringing, and the asteroid was identified as the source in the red square's center. In contrast, the correct source is marked by the green circle.

or contamination by nearby non-*Gaia* stars.

Then we applied a loop of sigma clipping to the remaining points using the NumPy library[19]. The sigma clipping ends when no more points are dropped, and the remaining points are presented in the plot of Fig. 4.33b. As a result, the H_R and the slope at the R filter are similar to the published values. However, these results should be used with caution since they do not consider other sources of uncertainty, i.e., the error bars only came from the linear fitting approach. In addition, as the MS4 color is not well constrained, we used the published value of $V - R = 0.38 \pm 0.02$ (TEGLER *et al.*, 2016) in Eq. 3.27, i.e., our results are also sensitive to the used color parameter.

As previously stated, the expected brightness fluctuations from MS4 rotation are Δm $= 0.05 \pm 0.01$ mag. However, after sigma clipping, the data standard deviation is 0.4 mag, eight times greater than the expected signal. Such a significant noise does not allow for periodic searches with the LS method. So this approach could not be used to determine MS4's rotational period and amplitude.

[19]Here, I used the numpy.polifyt class. Documentation available on https://numpy.org/doc/stable/reference/generated/numpy.polyfit.html.

4.2 2004 XR_{190}

This moderately red TNO (SHEPPARD, 2010) was discovered from observations made by the Canada–France Ecliptic Plane Survey (CFEPS) in Mauna Kea on December 11, 2004[20]. The analysis of the discovery images revealed an object with albedo between 0.04 and 0.16, which implies an equivalent diameter (D_{eq}) range of 425 - 850 km (ALLEN *et al.*, 2006). However, considering a slightly higher albedo (0.1 - 0.25), SCHALLER and BROWN (2007) obtained a diameter between 335 - 550 km.

2004 XR_{190}'s orbit has a semi-major axis of 57.48 au, an orbital eccentricity of 0.1°, and an unusual inclination of 46.6°. Due to its orbital parameters[21], it can be dynamically classified as a scattered or detached object. The only information available about its rotation is an upper limit for the RLC amplitude of 0.026 mag (KECSKEMÉTHY *et al.*, 2022). The authors calculated this value from the residuals of the measurements of the images acquired by the K2 mission[22] of the Kepler Space Telescope.

Lucky Star collaboration predicted a stellar occultation by this faint object (apparent magnitude of ≈ 22, in V-band) on January 22, 2021 (Fig. 4.35). The prediction uncertainties were about two times the Earth's diameter, leading to the probability of a centrality observation to only 1%. However, the star was bright, and some observers tried to acquire data. One station from USA and another from ESP detected the event (Table 4.7 and Fig. 4.36). Therefore, the actual shadow path passed slightly at the south of the nominal prediction.

Table 4.7: Observational circumstances and times as reported by the observers.

Observatory nearest city country	**Latitude (°) longitude (°) altitude (m)**	**Tel. aperture (m) instrument time source**	**Immersion emersion observers**
Westport Green Gao Westport USA	41.171083333 -73.327583333 285.0	0.356 QHY 174 GPS	23:44:16.44 ± 0.3 s 23:44:40.37 ± 0.3 s Kevin Green, Chang Gao
- Sant Esteve Sesrovires ESP	41.49375 1.872527778 180.0	0.4 Mintron 12V6HC-EX Garmin GPS 18 1PPS	23:39:23.20 ± 1.00 s 23:39:49.29 ± 1.67 s Carles Schnabel

Following the procedure described in Sect. 3.1.5 and using the immersion and emersion instants reported by the observers, a preliminary limb was fitted to the chords (Fig. 4.37). The ellipse search was limited to an apparent oblateness of 0.6 and an equatorial radius of 425 km (upper limit from published radius). The derived limb has an apparent semi-major axis of 358 ± 66 km (1σ) and an equivalent radius of 300 ± 85 km (Table 4.8). The astrometric position and the target star position used to obtain it are presented in Table 4.8. This result was used to refine 2004 XR_{190}'s ephemeris and predict new events.

[20] The discovery was announced in the MPECs under the number MPEC 2005-X72.
[21] According to Minor Planet Center web page, accessed on October 21, 2022.
[22] https://www.nasa.gov/mission_pages/kepler/main/index.html

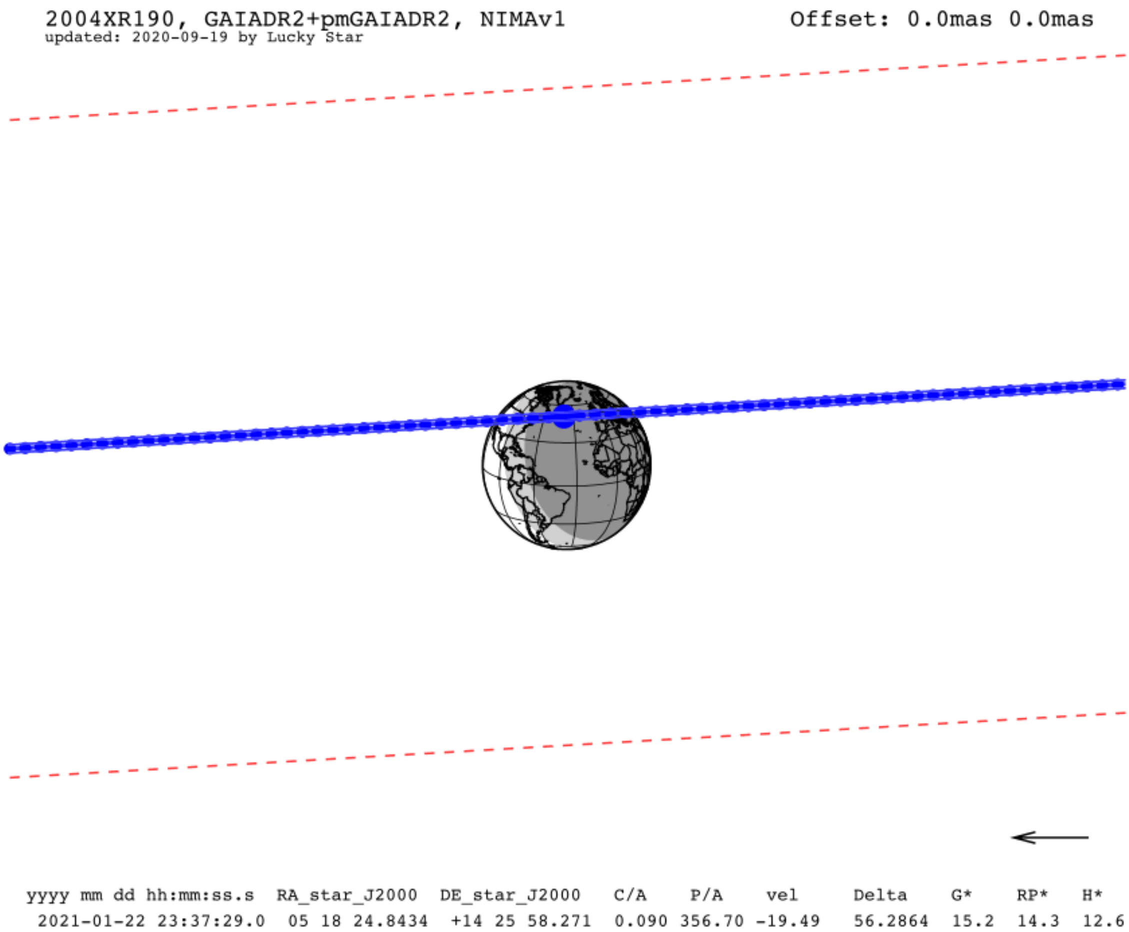

Figure 4.35: Prediction map containing all the information about the stellar occultation by 2004 XR_{190} on January 22, 2021.

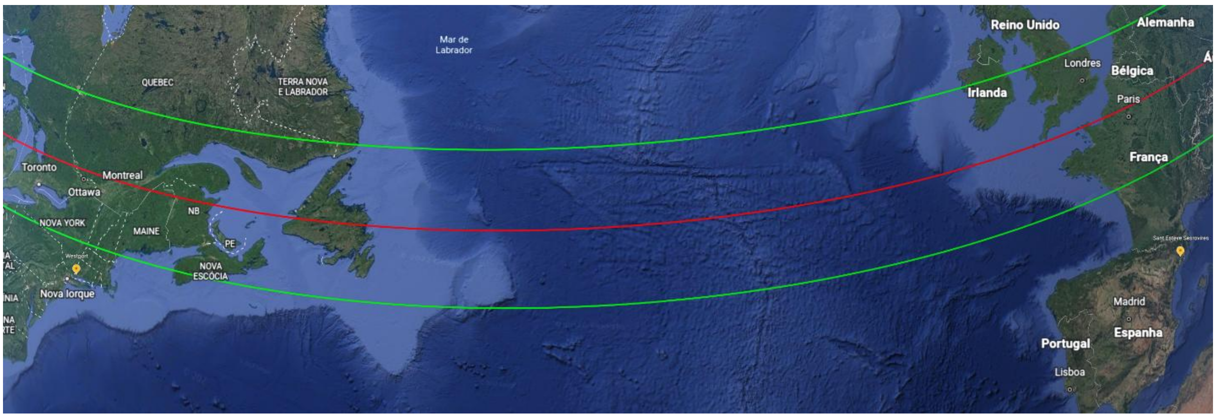

Figure 4.36: Predicted shadow path (green lines) and the location of both telescopes that detected the event (yellow markers).

Nowadays, the predictions have error bars of only 15% of Earth's diameter, a significant improvement that helps to prepare future observational campaigns.

The occultation detection also motivated photometric observations with the CAHA and SOAR telescopes. Despite only a few nights of data, the absolute photometry of those

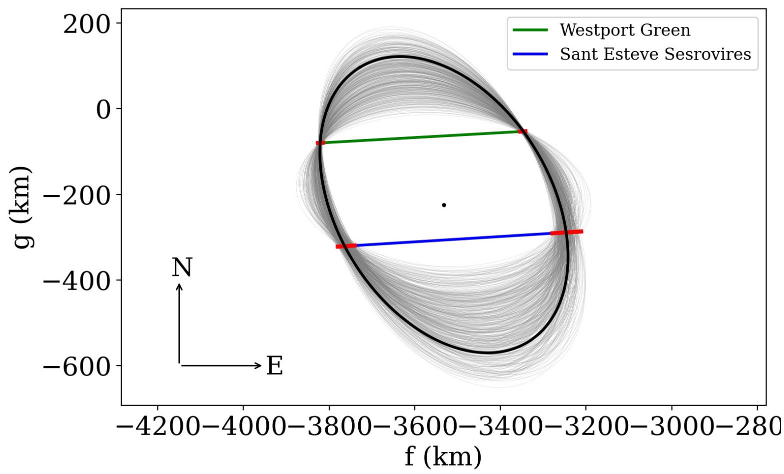

Figure 4.37: Double detection of the stellar occultation by 2004 XR_{190} on January 22, 2021. Red segments indicate instant uncertainties, and colors represent the data acquired in each site. The black ellipse is the best-fitted limb, and the gray region presents the solutions at the 1σ level.

images allowed us to derive some preliminary information about the object's rotation (following the procedure described in Sect. 3.2.3). The analysis revealed an H_R of 3.802 $\pm$ 0.022 mag (Fig. 4.38a) and many possibilities for the period (Fig. 4.38b). The best frequency provided by the LS periodogram gives a P = 19.47 h (Fig. 4.38c). However, the typical rotational frequency for TNOs is $\approx$ 8 h. Therefore, this result is probably some alias or noise present in the data. The preferred frequencies are shown in Fig. 4.38d and 4.38e referring to the second (10.57 h) or even the third peak (7.26 h).

Although more observations are needed to investigate 2004 XR_{190}'s rotational period, folding the data to the frequency intervals mentioned above, we obtained a Δm between 0.16 and 0.2 mags with a standard deviation (std) of $\approx$ 0.08 mag. This Δm is about ten times the published estimation (0.026 mag). So, despite not being conclusive, 2004 XR_{190}'s absolute magnitude and RLC amplitude were estimated using the absolute photometry approach. The stellar occultation detection and the derived rotational information enabled to derive of 2004 XR_{190}'s geometric albedo, information that is not available in the literature. Therefore, using the equivalent radius and absolute magnitude, the geometric albedo in R-band is p_R = 0.095 $\pm$ 0.23.

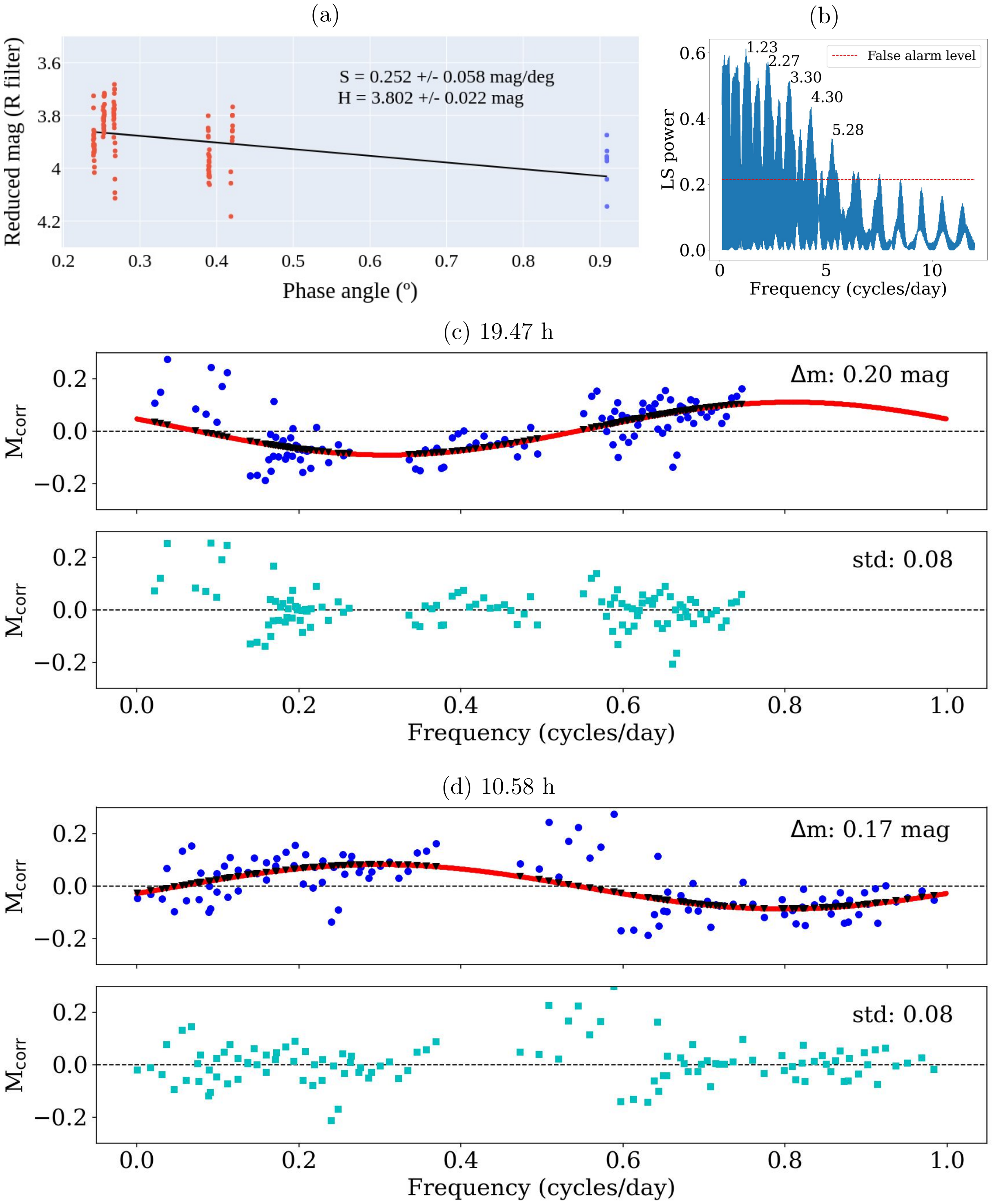

Figure 4.38: (a) The reduced magnitude of 2004 XR_{190} as a function of the phase angle. Blue points are 7 images acquired by the CAHA telescope on October 11, 2021, while in red are the data acquired by the SOAR telescope on December 1-3, 2021, and January 03, 2022. (b) LS periodogram showing the cycles that are above the false alarm probabilities. The plots in (c), (d), and (e) are the three derived RLCs, one for each possible rotational period (see text).

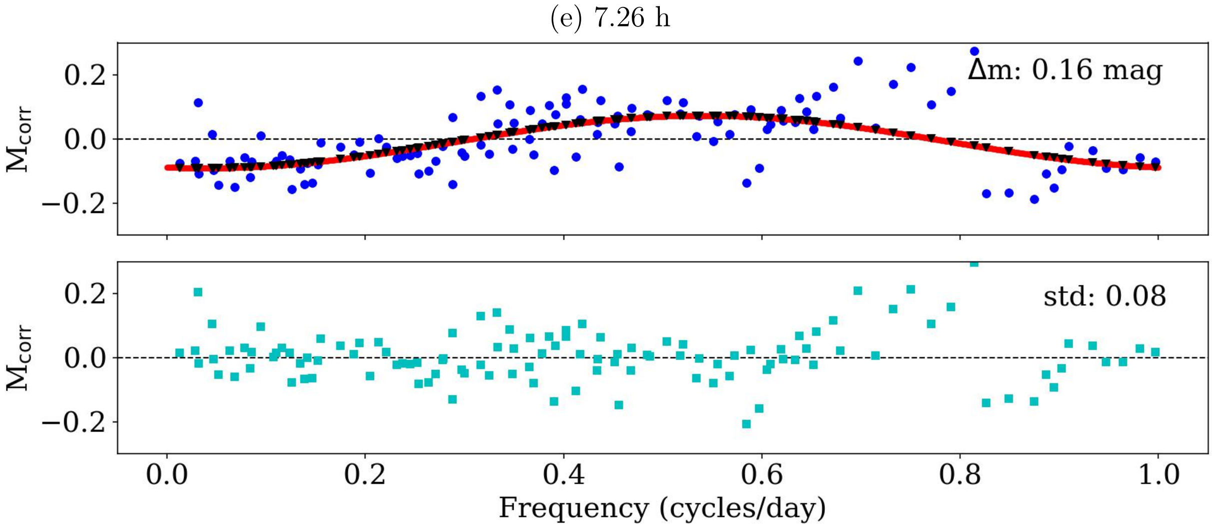

Figure 4.38: Continue.

Table 4.8: Ellipse and rotational parameters as derived by this work (see text). The ellipse is defined by a', ϵ', PA$'$, and f', g'. The H_R is the absolute magnitude in R-band, β_R is the β in the R band. 2004 XR_{190} geocentric coordinates were derived from the limb fitting and are given for the closest approach instant. The symbol * indicates that this error bar is given in RA. cos(DEC).

Elliptical limb parameters				
f' (km)	g' (km)	a' (km)	ϵ'	PA$'$ (°)
-3532 ± 22	-224 ± 38	358 ± 66	0.32 ± 0.14	35 ± 32
Photometric properties				
	Period (h)		H_R	β_R
19.47	10.57	7.26	3.802 ± 0.022	0.252 ± 0.058 mag/°

Astrometric position (ICRS)	**Instant (UT) hh:mm:ss.ss**	**Right Ascension (hh mm ss.ss ± *mas**)**	**Declination (° ’ ” ± *mas*)**
Star	23:45:21.5	05 18 24.84327 ± 0.20	+14 25 58.27080 ± 0.12
2004 XR_{190}		05 18 24.83701 ± 0.57	+14 25 58.34015 ± 0.94

4.3 Other objects

Besides the above-described study, about 2002 MS_4 and 2004 XR_{190}, collaborative work with stellar occultations by other objects also happened during the development of this thesis. Here a summary of contributions to published manuscripts and works in preparation is presented. Aperture photometry and instant determination are the most significant contributions to the stellar occultations by (84922) 2003 VS_2, (38628) Huya, (50000) Quaoar, (54598) Bienor, and Triton. Contributions regarding data analysis and software solutions happen to the stellar occultations by Europa and (10199) Chariklo.

Among all mentioned stellar occultation events, the contributions for Quaoar analysis are still in preparation to be published. I worked with two single-chord detections, one observed from OPD on March 2019 and the other from Tivoli/NAM on August 2019.

The last one detected both Quaoar and its satellite Weywot occulting the same star. The OLC put Weywot at $\approx$ 12,690 km from Quaoar, close to the published orbital radius (VACHIER *et al.*, 2012). However, the chord has a length of $\approx$ 175 km (Fig. 4.39), which is twice the diameter estimation published by FORNASIER *et al.* (2013).

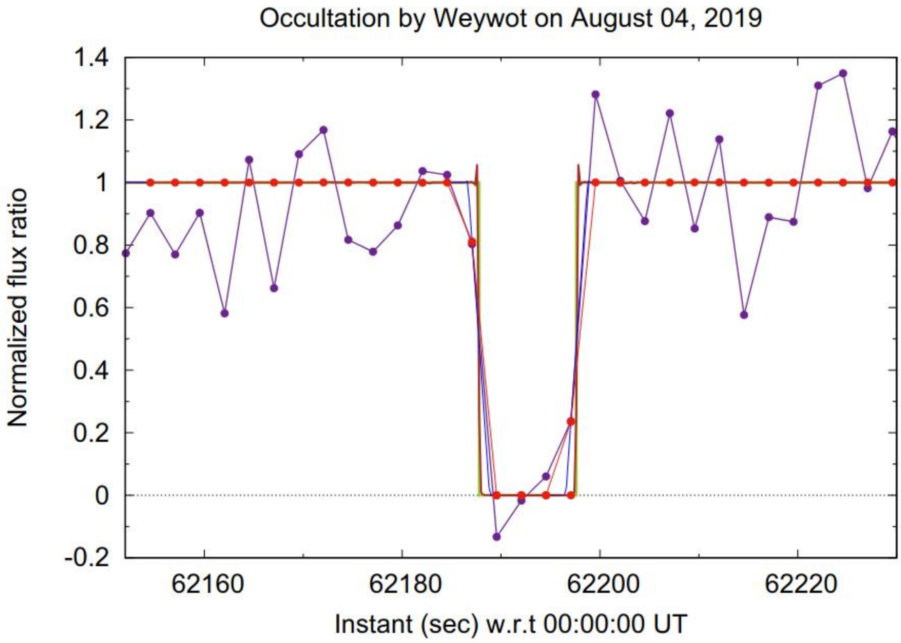

Figure 4.39: Occultation light curve acquired from Tivoli showing the drop in stellar flux due to Weywot (purple dots). Red dots present the synthetic light curve.

Among the published works, two Plutinos were characterized using stellar occultations: 2003 VS_2 and Huya. The 2003 VS_2 was observed in four stellar occultation events since 2013. However, the most successful campaign happened on November 2014 with 12 positive detections (BENEDETTI-ROSSI *et al.*, 2016; VARA-LUBIANO *et al.*, 2022). On the other hand, Huya's work is the most successful campaign for a TNO, with published results, up to date. It was detected from 21 stations in Europe in March 2019 (SANTOS-SANZ *et al.*, 2022).

Triton is the largest satellite of the planet Neptune and was observed during a stellar occultation on October 2017 from 90 telescopes located at USA, North Africa, and Europe. With such a large data set, human resources were requested to analyze all the light curves. As a result, the data provided amazing measurements of Triton's size and atmosphere (MARQUES OLIVEIRA *et al.*, 2022). Furthermore, one of the largest Centaurs, (54598) Bienor, was observed from five stations in January 2019, and the photometric analysis was also needed (FERNÁNDEZ-VALENZUELA *et al.*, 2022).

Besides the mentioned contributions, software improvements and discussions about stellar occultations by Europa and Chariklo were also made. Europa is one of the largest satellites of Jupiter and was detected from 5 stations during a stellar occultation in March

2017 (MORGADO *et al.*, 2019). Chariklo is the largest known Centaur, has rings, and has been largely studied by our collaboration in recent years. The published paper uses new detections of stellar occultation events to refine the system's physical parameters (MORGADO *et al.*, 2021). Finally, since the beginning of this project, I have made contributions to the development of the database on detected occultations, the Occultation Portal, and SORA (BRAGA-RIBAS *et al.*, 2019; GOMES-JÚNIOR *et al.*, 2022; KILIC *et al.*, 2022).

Chapter 5

Conclusions

This research begins with stellar occultations, one of the available techniques for studying Centaurs and TNOs. Indeed, the first results of this project proved that even with only a single detection and even if the source has a low SNR, we can use the data to constrain the object's size and derive a competitive astrometric position. Depending on the object, this position is critical for predicting the subsequent stellar occultation campaigns. For instance, 2004 XR_{190}'s double chords from a stellar occultation described in Sect. 4.2 reduced the prediction uncertainties from two Earth's diameters to only 15% in the current predictions. Therefore, 37 other events are analyzed, and accurate astrometry for 23 objects is obtained (ROMMEL *et al.*, 2020). In addition, the collaborative work with colleagues also resulted in six other publications involving data analysis during this Ph.D. course (Sect. 4.3).

Here we studied the hot classical TNO designated 2002 MS_4 from the view of nine stellar occultation events. The four events detected in 2019 paved the way for the extensive campaign scheduled for August 8, 2020. We know this object needs an accurate determination for the rotational period and that combining the rotational phase with stellar occultation helps constrain the physical properties. Therefore, we prepared an observational proposal to acquire images at the SOAR telescope, which was approved for the second semester of 2020 (Appendix D).

The stellar occultation on August 8, 2020 is the most successful campaign ever made for an occultation by a TNO, but the observations at SOAR were not performed due to the COVID-19 pandemic. A significant effort was made to obtain an accurate rotation period and amplitude for MS4. However, as it is in a dense stellar field, we could only measure its rotation period in one opportunity in 2011, when it crossed in front of a dark cloud. We analyzed images with a dense stellar field taken over many years and from different facilities using DIA and absolute photometry, but we could not obtain reliable results.

The multichord occultation detection allowed us to accurately derive MS4's projected size and shape. The derived limb has a small oblateness and can be taken as representative of the profile that we would have from the other eight stellar occultation events. Therefore, these data present a roughly round object with little fluctuations in the projected profile over time. There are two hypotheses for such "constancy" in the observed limb on all the occultation detections i) an aspect angle near 0° and ii) a MacLaurin spheroidal shape. Both hypotheses can also explain the small amplitude of the published RLC if albedo variations exist on the object's surface.

The equivalent area diameter derived from August 8, 2020, is about 130 km smaller than the results obtained with thermal observations. Despite agreeing at the 2σ level, this difference may indicate the presence of a large satellite (ORTIZ *et al.*, 2020a). In addition, we identified significant features in the object's profile by analyzing the R_{diff} between the best-fitted ellipse and observed points. Especially in the northeast area, where variations of dozens of km were observed. To derive the size of such features, we followed two steps,

1. plotting a R_{diff} frequency histogram and fitting Gaussian functions to it;
2. fitting a model compound of parabolic functions and using MCMC to estimate its uncertainties.

The first step estimated the scale of the observed topography by measuring the FWHM of the Gaussian fits. However, the second approach provided precise measurements of at least one elevation and one depression. This is the first multichord stellar occultation detection of topography in a TNO, and the length of the most extensive feature corresponds to $\approx$ 40% of MS4 equivalent diameter.

Main belt asteroids with diameters in the range of 1-500 km have shown craters with 45% of the object's mean diameter (BURCHELL and LELIWA-KOPYSTYNSKI, 2010). Saturn moons like Tethys and Mimas also have large craters corresponding to about 30% to 40% of objects' mean diameters (DOUGHERTY and SPILKER, 2018). Therefore, if the observed depression at the 2002 MS_4 profile is a crater, it has a similar diameter to the mentioned large impact craters. The difference is that MS4 is farther out, and this might be the largest crater ever observed in the trans-Neptunian region. As stated above, in this orbital region, only Pluto, Charon, and Arrokoth have detailed information about craters on their surface. Still, the largest ones represent only 11%, 22%, and 16% of their mean diameters (semi-major axis for Arrokoth), respectively.

In addition, the observed feature on the MS4 limb is only a lower limit for the suspected crater. There is an example of a crater with larger proportions in the Vesta south pole. Vesta is the second largest main belt object, with a mean diameter of 523 km. Despite a large body, it does not have a hydrostatic equilibrium shape (KARIMI *et al.*, 2017). The main reason might be two overlapping giant impact features at the south pole, as revealed by the Dawn mission (SCHENK *et al.*, 2012). The youngest one is named Rheasilvia and has a diameter of $\approx$ 460 km (Fig. 5.1). Such crater diameter represents about 80% of the mean diameter of Vesta, double the average ratio for craters in smaller main belt asteroids. Therefore, Vesta is considered an irregular body and, differently from MS4, its RLC has a reasonable amplitude of 0.19 mag (FORNASIER *et al.*, 2011). Therefore, we investigated the variability on the object's rotational light curve that the observed depression might cause. We found that the missing area due to the crater candidate roughly corresponds to 2.5% of the total ellipse area, as obtained from stellar occultation multichord data. Therefore, unless the feature is larger than observed in our data, it seems insufficient to explain a variation of 5% in the published rotational light curve.

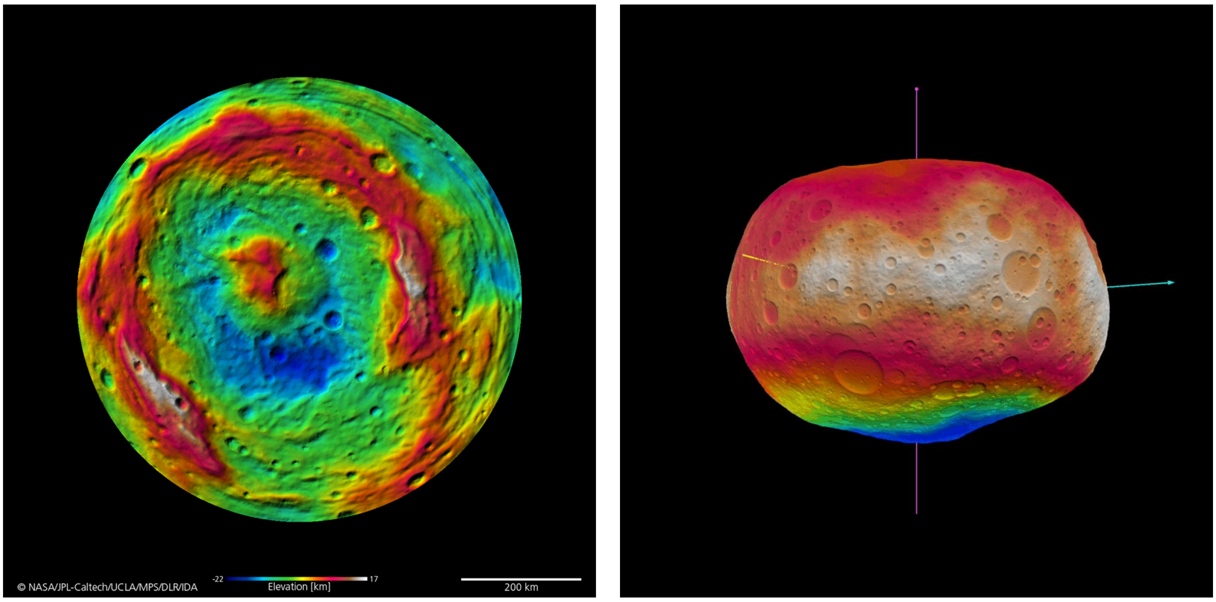

(a) (b)

Figure 5.1: Vesta images provided by NASA solar system exploration web page.

Regarding deepness, JOHNSON and MCGETCHIN (1973) already stated a theoretical way to study supported topography on the surface of large objects. The authors stated that larger and denser bodies may support lower topography and that objects with diameters below 1000 km may support topography higher than 10% of its mean radius. This proportion was not observed in the Charon surface but proved true for MS4. The deepness of the observed depression is about 11% of the mean radius. Therefore, is this topography large enough to turn the MS4 shape into an irregular form? Do the observed superficial features cause the brightness variations observed in the rotational light curve?

The direct image collection found for 2002 MS_4 and analyzed by the OM/M2 system spans phase angles ranging from 0.3° to 1.2°, providing enough coverage of the phase curve interval observable from Earth. Therefore, an absolute magnitude and slope for the R-band are derived. Our result, corrected by the published V-R color, coincides with the published absolute magnitude in the V-band (considering the error bars). Furthermore, even though the phase interval slightly differs from the interval reported by VERBISCER *et al.* (2022b), the R-band slope determined in this work is close to the published value for V-band. The difference between both slope values is only 0.018 mag/°. Therefore, the major conclusions regarding the physical characteristics of 2002 MS_4:

- The area equivalent diameter derived from stellar occultation data differs by about 138 km from the most recently published value. It may indicate the presence of an unknown satellite as suggested for 2002 TC_{302} in similar circumstances (ORTIZ *et al.*, 2020a), but the error bars from the thermal diameter are large and can accommodate the difference within 2σ;
- According to our measurements, the MS4's surface has at least one depression with a depth of 45.1 ± 1.5 km and a length of 322 ± 39 km. Also, a mountain with 25^{+4}_{-5} km high is present near this large depression. The observed depression diameter corresponds to about 40% of the equivalent diameter, an unusual size relation among all observed topography in the outer solar system's small bodies. Therefore, more data is needed to constrain its size and formation mechanisms;
- If a collision caused this significant topography, could MS4 be the parent body of a second collisional family still to be discovered in the trans-Neptunian region?
- Using the corrected by color H_R obtained from absolute photometry, the derived geometric albedo is $p_V = 0.104 \pm 0.026$.
- Despite not being conclusive, considering only the limb derived from stellar occultation data and the shallow RLC, a MacLaurin equilibrium shape seems appropriate for this object.

Recently, we also studied the physical properties of the unusual high-inclined TNO named 2004 XR_{190}. Despite the poor ephemeris and the FOV with few stars, we detected one stellar occultation in January 2021. This detection allowed constraining the object's equivalent diameter well inside the published range. In addition, the occultation results prompted photometric observations at CAHA and SOAR, and early data processing using the OM/M2 system yielded H_R and Δm values compatible with objects in hydrostatic equilibrium.

During this work, significant advances were made regarding tools for image photometry and background subtraction. We found that DIAPL2 had a better performance in not calibrated images with a crowded FOV. We also demonstrated that PRAIA has optimal results when used to derive rotational light curves by differential aperture photometry. Finally, OM/M2 system capabilities are presented by deriving a well-populated phase curve. Also, as described in this work, the absolute photometry allowed for absolute magnitude and phase coefficient determination in the R-band for both 2002 MS_4 and 2004 XR_{190}. Results show the potential of massively processing photometric images, including public images acquired for other scientific purposes.

At the end of this project, the sample of objects with published physical properties based on stellar occultation data increased to roughly 36 TNOs, five Centaurs, and three planetary satellites. These numbers do not consider the publications about Pluto's atmosphere evolution and the dynamics of Chariklo's/Haumea's rings. Furthermore, many events are still being analyzed and will be published in the following years, which includes the 2002 MS_4 results described in this work (Appendix E). Therefore, the stellar occultation field is quickly growing and will probably increase even more in the following years. This motivated my participation in the development of the OP and SORA. The OP has been used to store and organize occultation data sets, and with SORA, we analyzed all the occultation light curves presented in this work.

Although the *Gaia* DR2 catalog provides some astrometric information for small objects in the outer solar system, the orbit uncertainties quickly increase with time due to the small orbital coverage. Therefore, the collaboration continues to perform classic astrometry to maintain objects' ephemerides accurately. These dedicated missions usually happen in Brazilian or Spanish telescopes and require human resources. I have participated in dozens of these observational runs, acquiring experience with large facilities like the 1.6 m telescope in OPD. As a result, our international program to obtain accurate physical properties of TNOs and Centaurs has predicted hundreds of stellar occultations per year. The successful observations, i.e., with at least one detection, have increased, reaching the mark of about sixty events detected in 2021. A new era for stellar occultation observations is coming with the discovery of thousands of objects by the LSST, and we must be prepared.

Bibliography

ALARD, C., 2000, "Image subtraction using a space-varying kernel", Astron. Astrophys. Suppl., v. 144 (jun.), pp. 363–370. doi: 10.1051/aas:2000214.

ALARD, C., LUPTON, R. H., 1998, "A Method for Optimal Image Subtraction", Astrophys. J., v. 503, n. 1 (ago.), pp. 325–331. doi: 10.1086/305984.

ALBROW, M. D., HORNE, K., BRAMICH, D. M., et al., 2009, "Difference imaging photometry of blended gravitational microlensing events with a numerical kernel", Mon. Not, Roy. Astron. Soc., v. 397, n. 4 (ago.), pp. 2099–2105. doi: 10.1111/j.1365-2966.2009.15098.x.

ALEXANDERSEN, M., BENECCHI, S. D., CHEN, Y.-T., et al., 2019, "OSSOS. XII. Variability Studies of 65 Trans-Neptunian Objects Using the Hyper Suprime-Cam", Astrophys. J. Suppl., 244(1):19. doi: 10.3847/1538-4365/ab2fe4.

ALLEN, R. L., GLADMAN, B., KAVELAARS, J. J., et al., 2006, "Discovery of a Low-Eccentricity, High-Inclination Kuiper Belt Object at 58 AU", Astrophys. J. Lett., v. 640, n. 1 (mar.), pp. L83–L86. doi: 10.1086/503098.

ALVAREZ-CANDAL, A., PINILLA-ALONSO, N., ORTIZ, J. L., et al., 2016, "Absolute magnitudes and phase coefficients of trans-Neptunian objects", Astron. Astrophys., 586:A155. doi: 10.1051/0004-6361/201527161.

ALVAREZ-CANDAL, A., AYALA-LOERA, C., GIL-HUTTON, R., et al., 2019, "Absolute colours and phase coefficients of trans-Neptunian objects: correlations and populations", Mon. Not, Roy. Astron. Soc., v. 488, n. 3 (set.), pp. 3035–3044. doi: 10.1093/mnras/stz1880.

ANDRAE, R., FOUESNEAU, M., CREEVEY, O., et al., 2018, "Gaia Data Release 2. First stellar parameters from Apsis", Astron. Astrophys., 616:A8. doi: 10.1051/0004-6361/201732516.

ASSAFIN, M., CAMARGO, J. I. B., VIEIRA MARTINS, R., et al., 2010, "Precise predictions of stellar occultations by Pluto, Charon, Nix, and Hydra for 2008-2015", Astron. Astrophys., 515:A32. doi: 10.1051/0004-6361/200913690.

ASSAFIN, M., VIEIRA MARTINS, R., CAMARGO, J. I. B., et al., 2011, "PRAIA - Platform for Reduction of Astronomical Images Automatically". In: *Gaia follow-up network for the solar system objects : Gaia FUN-SSO workshop proceedings*, pp. 85–88, jun.

ASSAFIN, M., CAMARGO, J. I. B., VIEIRA MARTINS, R., et al., 2012, "Candidate stellar occultations by large trans-Neptunian objects up to 2015", Astron. Astrophys., 541:A142. doi: 10.1051/0004-6361/201118349.

ASTROPY COLLABORATION, ROBITAILLE, T. P., TOLLERUD, E. J., et al., 2013, "Astropy: A community Python package for astronomy", Astron. Astrophys., 558:A33. doi: 10.1051/0004-6361/201322068.

AYALA-LOERA, C., ALVAREZ-CANDAL, A., ORTIZ, J. L., et al., 2018, "Absolute colours and phase coefficients of trans-Neptunian objects: H_V - H_R and relative phase coefficients", Mon. Not, Roy. Astron. Soc., v. 481, n. 2 (dez.), pp. 1848–1857. doi: 10.1093/mnras/sty2363.

BANNISTER, M. T., 2020, "A darkness full of worlds: prospects for TNO discovery surveys". In: Prialnik, D., Barucci, M. A., Young, L. (Eds.), *The Trans-Neptunian Solar System*, pp. 439–453. doi: 10.1016/B978-0-12-816490-7.00020-5.

BANNISTER, M. T., KAVELAARS, J. J., PETIT, J.-M., et al., 2016, "The Outer Solar System Origins Survey. I. Design and First-quarter Discoveries", Astron. J., 152 (3):70. doi: 10.3847/0004-6256/152/3/70.

BARUCCI, M. A., FULCHIGNONI, M., BIRLAN, M., et al., 2001, "Analysis of Trans-Neptunian and Centaur colours: continuous trend or grouping?" Astron. Astrophys., v. 371 (jun.), pp. 1150–1154. doi: 10.1051/0004-6361:20010501.

BARUCCI, M. A., BOEHNHARDT, H., CRUIKSHANK, D. P., et al., 2008, "The Solar System Beyond Neptune: Overview and Perspectives". In: Barucci, M. A., Boehnhardt, H., Cruikshank, D. P., et al. (Eds.), *The Solar System Beyond Neptune*, p. 3.

BATYGIN, K., BROWN, M. E., 2016, "Evidence for a Distant Giant Planet in the Solar System", Astron. J., 151(2):22. doi: 10.3847/0004-6256/151/2/22.

BATYGIN, K., BROWN, M. E., 2021, "Injection of Inner Oort Cloud Objects into the Distant Kuiper Belt by Planet Nine", Astrophys. J. Lett., 910(2):L20. doi: 10.3847/2041-8213/abee1f.

BECKER, A., 2015. "HOTPANTS: High Order Transform of PSF ANd Template Subtraction". Astrophysics Source Code Library, record ascl:1504.004, abr.

BELSKAYA, I. N., SHEVCHENKO, V. G., 2000, "Opposition Effect of Asteroids", Icarus, v. 147, n. 1 (set.), pp. 94–105. doi: 10.1006/icar.2000.6410.

BELSKAYA, I. N., BARUCCI, M. A., FULCHIGNONI, M., et al., 2015, "Updated taxonomy of trans-neptunian objects and centaurs: Influence of albedo", Icarus, v. 250 (abr.), pp. 482–491. doi: 10.1016/j.icarus.2014.12.004.

BENEDETTI-ROSSI, G., SICARDY, B., BUIE, M. W., et al., 2016, "Results from the 2014 November 15th Multi-chord Stellar Occultation by the TNO (229762) 2007 UK_{126}", Astron. J., 152(6):156. doi: 10.3847/0004-6256/152/6/156.

BENEDETTI-ROSSI, G., SANTOS-SANZ, P., ORTIZ, J. L., et al., 2019, "The Trans-Neptunian Object (84922) 2003 VS_2 through Stellar Occultations", Astron. J., 158(4):159. doi: 10.3847/1538-3881/ab3b05.

BÉRARD, D., SICARDY, B., CAMARGO, J. I. B., et al., 2017, "The Structure of Chariklo's Rings from Stellar Occultations", Astron. J., 154(4):144. doi: 10.3847/1538-3881/aa830d.

BERTIN, E., ARNOUTS, S., 1996, "SExtractor: Software for source extraction." Astron. Astrophys. Suppl., v. 117 (jun.), pp. 393–404. doi: 10.1051/aas:1996164.

BOYLE, W. S., SMITH, G. E., 1970, "Charge coupled semiconductor devices", *The Bell System Technical Journal*, v. 49, n. 4, pp. 587–593. doi: 10.1002/j.1538-7305.1970.tb01790.x.

BRAGA-RIBAS, F., SICARDY, B., ORTIZ, J. L., et al., 2013, "The Size, Shape, Albedo, Density, and Atmospheric Limit of Transneptunian Object (50000) Quaoar from Multi-chord Stellar Occultations", Astrophys. J., 773(1):26. doi: 10.1088/0004-637X/773/1/26.

BRAGA-RIBAS, F., SICARDY, B., ORTIZ, J. L., et al., 2014, "A ring system detected around the Centaur (10199) Chariklo", Nature, v. 508, n. 7494 (abr.), pp. 72–75. doi: 10.1038/nature13155.

BRAGA-RIBAS, F., CRISPIM, A., VIEIRA-MARTINS, R., et al., 2019, "Database on detected stellar occultations by small outer Solar System objects". In: *Journal of Physics Conference Series*, v. 1365, *Journal of Physics Conference Series*, p. 012024, out. doi: 10.1088/1742-6596/1365/1/012024.

BRAMICH, D. M., 2008, "A new algorithm for difference image analysis", Mon. Not, Roy. Astron. Soc., v. 386, n. 1 (maio), pp. L77–L81. doi: 10.1111/j.1745-3933.2008.00464.x.

BRAMICH, D. M., HORNE, K., ALSUBAI, K. A., et al., 2016, “Difference image analysis: automatic kernel design using information criteria”, Mon. Not, Roy. Astron. Soc., v. 457, n. 1 (mar.), pp. 542–574. doi: 10.1093/mnras/stv2910.

BROWN, M. E., 2005a, “S/2005 (2003 UB_313) 1”, IAU Circ., v. 8610 (out.), pp. 1.

BROWN, M. E., 2005b, “S/2005 (2003 EL_61) 2”, IAU Circ., v. 8636 (dez.), pp. 1.

BROWN, M. E., SUER, T. A., 2007, “Satellites of 2003 AZ_84, (50000), (55637), and (90482)”, IAU Circ., v. 8812 (fev.), pp. 1.

BROWN, M. E., SCHALLER, E. L., ROE, H. G., et al., 2006, “Direct Measurement of the Size of 2003 UB313 from the Hubble Space Telescope”, Astrophys. J. Lett., v. 643, n. 1 (maio), pp. L61–L63. doi: 10.1086/504843.

BROWN, M. E., BUTLER, B. J., 2017, “The Density of Mid-sized Kuiper Belt Objects from ALMA Thermal Observations”, Astron. J., 154(1):19. doi: 10.3847/1538-3881/aa6346.

BROWN, M. E., BUTLER, B. J., 2018, “Medium-sized Satellites of Large Kuiper Belt Objects”, Astron. J., 156(4):164. doi: 10.3847/1538-3881/aad9f2.

BROWN, M. E., BARKUME, K. M., RAGOZZINE, D., et al., 2007, “A collisional family of icy objects in the Kuiper belt”, Nature, v. 446, n. 7133 (mar.), pp. 294–296. doi: 10.1038/nature05619.

BRUCKER, M. J., GRUNDY, W. M., STANSBERRY, J. A., et al., 2009, “High albedos of low inclination Classical Kuiper belt objects”, Icarus, v. 201, n. 1 (maio), pp. 284–294. doi: 10.1016/j.icarus.2008.12.040.

BUIE, M. W., BUS, S. J., 1992, “Physical observations of (5145) Pholus”, Icarus, v. 100, n. 2 (dez.), pp. 288–294. doi: 10.1016/0019-1035(92)90101-C.

BUIE, M. W., LEIVA, R., KELLER, J. M., et al., 2020a, “A Single-chord Stellar Occultation by the Extreme Trans-Neptunian Object (541132) Leleākūhonua”, Astron. J., 159(5):230. doi: 10.3847/1538-3881/ab8630.

BUIE, M. W., PORTER, S. B., TAMBLYN, P., et al., 2020b, “Size and Shape Constraints of (486958) Arrokoth from Stellar Occultations”, Astron. J., 159(4): 130. doi: 10.3847/1538-3881/ab6ced.

BURCHELL, M. J., LELIWA-KOPYSTYNSKI, J., 2010, “The large crater on the small Asteroid (2867) Steins”, Icarus, v. 210, n. 2 (dez.), pp. 707–712. doi: 10.1016/j.icarus.2010.07.026.

BUS, S. J., BUIE, M. W., SCHLEICHER, D. G., et al., 1996, "Stellar Occultation by 2060 Chiron", Icarus, v. 123, n. 2 (out.), pp. 478–490. doi: 10.1006/icar.1996.0173.

BUTCHER, H., STEVENS, R., 1981, "Image Reduction and Analysis Facility Development", *Kitt Peak National Observatory Newsletter*, v. 16 (jan.), pp. 6.

BUTKEVICH, A. G., LINDEGREN, L., 2014, "Rigorous treatment of barycentric stellar motion. Perspective and light-time effects in astrometric and radial velocity data", Astron. Astrophys., 570:A62. doi: 10.1051/0004-6361/201424483.

CAMARGO, J. I. B., VIEIRA-MARTINS, R., ASSAFIN, M., et al., 2014, "Candidate stellar occultations by Centaurs and trans-Neptunian objects up to 2014", Astron. Astrophys., 561:A37. doi: 10.1051/0004-6361/201322579.

CHANDRASEKHAR, S., 1987, *Ellipsoidal figures of equilibrium*. New York, Dover pubs.

COOK, J. C., PROTOPAPA, S., DALLE ORE, C. M., et al., 2023, "Analysis of Charon's spectrum at 2.21- μm from New Horizons/LEISA and Earth-based observations", Icarus, 389:115242. doi: 10.1016/j.icarus.2022.115242.

DALLE ORE, C. M., BARUCCI, M. A., EMERY, J. P., et al., 2015, "The composition of "ultra-red" TNOs and centaurs", Icarus, v. 252 (maio), pp. 311–326. doi: 10.1016/j.icarus.2015.01.014.

DAVIDSSON, B. J. R., 1999, "Tidal Splitting and Rotational Breakup of Solid Spheres", Icarus, v. 142, n. 2 (dez.), pp. 525–535. doi: 10.1006/icar.1999.6214.

DAVIDSSON, B. J. R., 2001, "Tidal Splitting and Rotational Breakup of Solid Biaxial Ellipsoids", Icarus, v. 149, n. 2 (fev.), pp. 375–383. doi: 10.1006/icar.2000.6540.

DEMEO, F. E., 2010, *The compositional variation of small bodies accross the solar system*. Doctoral Thesis, Observatoire de Paris, France, jan.

DESMARS, J., 2015, "Detection of Yarkovsky acceleration in the context of precovery observations and the future Gaia catalogue", Astron. Astrophys., 575:A53. doi: 10.1051/0004-6361/201423685.

DESMARS, J., MEZA, E., SICARDY, B., et al., 2019, "Pluto's ephemeris from ground-based stellar occultations (1988-2016)", Astron. Astrophys., 625:A43. doi: 10.1051/0004-6361/201834958.

DIAS-OLIVEIRA, A., SICARDY, B., ORTIZ, J. L., et al., 2017, "Study of the Plutino Object (208996) 2003 AZ_{84} from Stellar Occultations: Size, Shape, and Topographic Features", Astron. J., 154(1):22. doi: 10.3847/1538-3881/aa74e9.

DOBSON, M. M., SCHWAMB, M. E., FITZSIMMONS, A., et al., 2021, "New or Increased Cometary Activity in (2060) 95P/Chiron", *Research Notes of the American Astronomical Society*, 5(9):211. doi: 10.3847/2515-5172/ac26c9.

DORESSOUNDIRAM, A., BOEHNHARDT, H., TEGLER, S. C., et al., 2008, "Color Properties and Trends of the Transneptunian Objects". In: Barucci, M. A., Boehnhardt, H., Cruikshank, D. P., et al. (Eds.), *The Solar System Beyond Neptune*, p. 91.

DOTTO, E., PERNA, D., BARUCCI, M. A., et al., 2008, "Rotational properties of Centaurs and Trans-Neptunian Objects. Lightcurves and densities", Astron. Astrophys., v. 490, n. 2 (nov.), pp. 829–833. doi: 10.1051/0004-6361:200809615.

DOUGHERTY, M. K., SPILKER, L. J., 2018, "Review of Saturn's icy moons following the Cassini mission", *Reports on Progress in Physics*, 81(6):065901. doi: 10.1088/1361-6633/aabdfb.

DUFFARD, R., ORTIZ, J. L., THIROUIN, A., et al., 2009, "Transneptunian objects and Centaurs from light curves", Astron. Astrophys., v. 505, n. 3 (out.), pp. 1283–1295. doi: 10.1051/0004-6361/200912601.

DUFFARD, R., PINILLA-ALONSO, N., ORTIZ, J. L., et al., 2014, "Photometric and spectroscopic evidence for a dense ring system around Centaur Chariklo", Astron. Astrophys., 568:A79. doi: 10.1051/0004-6361/201424208.

EDGEWORTH, K. E., 1943, "The evolution of our planetary system", *Journal of the British Astronomical Association*, v. 53 (jul.), pp. 181–188.

ELLIOT, J. L., DUNHAM, E. W., BOSH, A. S., et al., 1989, "Pluto's atmosphere", Icarus, v. 77, n. 1 (jan.), pp. 148–170. doi: 10.1016/0019-1035(89)90014-6.

ELLIOT, J. L., KERN, S. D., CLANCY, K. B., et al., 2005, "The Deep Ecliptic Survey: A Search for Kuiper Belt Objects and Centaurs. II. Dynamical Classification, the Kuiper Belt Plane, and the Core Population", Astron. J., v. 129, n. 2 (fev.), pp. 1117–1162. doi: 10.1086/427395.

ELLIOT, J. L., PERSON, M. J., ZULUAGA, C. A., et al., 2010, "Size and albedo of Kuiper belt object 55636 from a stellar occultation", Nature, v. 465, n. 7300 (jun.), pp. 897–900. doi: 10.1038/nature09109.

FAN, S., GAO, P., ZHANG, X., et al., 2022, "A bimodal distribution of haze in Pluto's atmosphere", *Nature Communications*, 13:240. doi: 10.1038/s41467-021-27811-6.

FERNÁNDEZ, J., 2020, "Introduction: The Trans-Neptunian zone: past, present and future". In: Prialnik, D., Barucci, M. A., Young, L. (Eds.), *The Trans-Neptunian Solar System*, pp. 1–22. doi: 10.1016/B978-0-12-816490-7.00001-1.

FERNÁNDEZ-VALENZUELA, E., ORTIZ, J. L., DUFFARD, R., et al., 2016, "2008 OG_{19}: a highly elongated Trans-Neptunian object", Mon. Not, Roy. Astron. Soc., v. 456, n. 3 (mar.), pp. 2354–2360. doi: 10.1093/mnras/stv2739.

FERNÁNDEZ-VALENZUELA, E., MORALES, N., VARA-LUBIANO, M., et al., 2022, "The multichord stellar occultation by the centaur Bienor on January 11, 2019", *arXiv e-prints*, art. arXiv:2211.06931.

FERNÁNDEZ-VALENZUELA, E., ORTIZ, J. L., MORALES, N., et al., 2019, "The Changing Rotational Light-curve Amplitude of Varuna and Evidence for a Close-in Satellite", Astrophys. J. Lett., 883(1):L21. doi: 10.3847/2041-8213/ab40c2.

FOREMAN-MACKEY, D., HOGG, D. W., LANG, D., et al., 2013, "emcee: The MCMC Hammer", Publ. Astron. Soc. Pacific, v. 125, n. 925 (mar.), pp. 306. doi: 10.1086/670067.

FORGET, F., BERTRAND, T., HINSON, D., et al., 2021, "Dynamics of Pluto's Atmosphere". In: Stern, S. A., Moore, J. M., Grundy, W. M., et al. (Eds.), *The Pluto System After New Horizons*, pp. 297–319. doi: 10.2458/azu_uapress_9780816540945-ch013.

FORNASIER, S., MOTTOLA, S., BARUCCI, M. A., et al., 2011, "Photometric observations of asteroid 4 Vesta by the OSIRIS cameras onboard the Rosetta spacecraft", Astron. Astrophys., 533:L9. doi: 10.1051/0004-6361/201117600.

FORNASIER, S., LELLOUCH, E., MÜLLER, T., et al., 2013, "TNOs are Cool: A survey of the trans-Neptunian region. VIII. Combined Herschel PACS and SPIRE observations of nine bright targets at 70-500 μm", Astron. Astrophys., 555:A15. doi: 10.1051/0004-6361/201321329.

FULCHIGNONI, M., BELSKAYA, I., BARUCCI, M. A., et al., 2008, "Transneptunian Object Taxonomy". In: Barucci, M. A., Boehnhardt, H., Cruikshank, D. P., et al. (Eds.), *The Solar System Beyond Neptune*, p. 181.

GAIA COLLABORATION, BROWN, A. G. A., VALLENARI, A., et al., 2016a, "Gaia Data Release 1. Summary of the astrometric, photometric, and survey properties", Astron. Astrophys., 595:A2. doi: 10.1051/0004-6361/201629512.

GAIA COLLABORATION, PRUSTI, T., DE BRUIJNE, J. H. J., et al., 2016b, "The Gaia mission", Astron. Astrophys., 595:A1. doi: 10.1051/0004-6361/201629272.

GAIA COLLABORATION, BROWN, A. G. A., VALLENARI, A., et al., 2018, "Gaia Data Release 2. Summary of the contents and survey properties", Astron. Astrophys., 616:A1. doi: 10.1051/0004-6361/201833051.

GEHRELS, T., 1956, "Photometric Studies of Asteroids. V. The Light-Curve and Phase Function of 20 Massalia." Astrophys. J., v. 123 (mar.), pp. 331. doi: 10.1086/146166.

GIULIATTI WINTER, S., WINTER, O., RIBEIRO, T., et al., 2021, "Stable region around Chariklo and its main ring". In: *AAS/Division for Planetary Sciences Meeting Abstracts*, v. 53, *AAS/Division for Planetary Sciences Meeting Abstracts*, p. 407.10, out.

GLADMAN, B., MARSDEN, B. G., VANLAERHOVEN, C., 2008, "Nomenclature in the Outer Solar System". In: Barucci, M. A., Boehnhardt, H., Cruikshank, D. P., et al. (Eds.), *The Solar System Beyond Neptune*, University of Arizona Press, p. 43.

GOMES-JÚNIOR, A. R., GIACCHINI, B. L., BRAGA-RIBAS, F., et al., 2015, "Results of two multichord stellar occultations by dwarf planet (1) Ceres", Mon. Not, Roy. Astron. Soc., v. 451, n. 3 (ago.), pp. 2295–2302. doi: 10.1093/mnras/stv1081.

GOMES-JÚNIOR, A. R., ASSAFIN, M., BRAGA-RIBAS, F., et al., 2020, "The first observed stellar occultations by the irregular satellite Phoebe (Saturn IX) and improved rotational period", Mon. Not, Roy. Astron. Soc., v. 492, n. 1 (fev.), pp. 770–781. doi: 10.1093/mnras/stz3463.

GOMES-JÚNIOR, A. R., MORGADO, B. E., BENEDETTI-ROSSI, G., et al., 2022, "SORA: Stellar occultation reduction and analysis", Mon. Not, Roy. Astron. Soc., v. 511, n. 1 (mar.), pp. 1167–1181. doi: 10.1093/mnras/stac032.

GOURGEOT, F., CARRY, B., DUMAS, C., et al., 2016, "Near-infrared spatially resolved spectroscopy of (136108) Haumea's multiple system", Astron. Astrophys., 593:A19. doi: 10.1051/0004-6361/201526423.

GREFFE, T., SMITH, R., SHERMAN, M., et al., 2021, "Characterization of Low Light Performance of a CMOS sensor for Ultraviolet Astronomical Applications", *arXiv e-prints*, art. arXiv:2112.01691.

GRUNDY, W. M., STANSBERRY, J. A., NOLL, K. S., et al., 2007, "The orbit, mass, size, albedo, and density of (65489) Ceto/Phorcys: A tidally-evolved binary Centaur", Icarus, v. 191, n. 1 (nov.), pp. 286–297. doi: 10.1016/j.icarus.2007.04.004.

GRUNDY, W. M., BENECCHI, S. D., RABINOWITZ, D. L., et al., 2012, "Mutual events in the Cold Classical transneptunian binary system Sila and Nunam", Icarus, v. 220, n. 1 (jul.), pp. 74–83. doi: 10.1016/j.icarus.2012.04.014.

GRUNDY, W. M., BENECCHI, S. D., PORTER, S. B., et al., 2014, "The orbit of transneptunian binary Manwë and Thorondor and their upcoming mutual events", Icarus, v. 237 (jul.), pp. 1–8. doi: 10.1016/j.icarus.2014.04.021.

GRUNDY, W. M., NOLL, K. S., BUIE, M. W., et al., 2019, "The mutual orbit, mass, and density of transneptunian binary G!kú||'hòmdímà (229762 2007 UK_{126})", Icarus, v. 334 (dez.), pp. 30–38. doi: 10.1016/j.icarus.2018.12.037.

GRUNDY, W., 2020, "Pluto and Charon as templates for other large Trans-Neptunian objects". In: Prialnik, D., Barucci, M. A., Young, L. (Eds.), *The Trans-Neptunian Solar System*, pp. 291–305. doi: 10.1016/B978-0-12-816490-7.00013-8.

GWYN, S. D. J., HILL, N., KAVELAARS, J. J., 2012, "SSOS: A Moving-Object Image Search Tool for Asteroid Precovery", Publ. Astron. Soc. Pacific, v. 124, n. 916 (jun.), pp. 579. doi: 10.1086/666462.

HAINAUT, O., SMETTE, A., ZEILINGER, W., 1992, "1992 AD", IAU Circ., v. 5450 (fev.), pp. 2.

HANUŠ, J., DELBO', M., ALÍ-LAGOA, V., et al., 2018, "Spin states of asteroids in the Eos collisional family", Icarus, v. 299 (jan.), pp. 84–96. doi: 10.1016/j.icarus.2017.07.007.

HAPKE, B., 1981, "Bidirectional reflectance spectroscopy. I - Theory", J. Geophys. Res., v. 86 (abr.), pp. 3039–3054. doi: 10.1029/JB086iB04p03039.

HARRIS, A. W., YOUNG, J. W., BOWELL, E., et al., 1989, "Photoelectric observations of asteroids 3, 24, 60, 261, and 863", Icarus, v. 77, n. 1 (jan.), pp. 171–186. doi: 10.1016/0019-1035(89)90015-8.

HARTMANN, W. K., THOLEN, D. J., MEECH, K. J., et al., 1989, ""Asteroid" 2060 Chiron: Blurring the distinction between asteroids and comets", *Meteoritics*, v. 24 (dez.), pp. 274.

HARTMANN, W. K., THOLEN, D. J., MEECH, K. J., et al., 1990, "2060 Chiron: Colorimetry and cometary behavior", *Icarus*, v. 83, n. 1, pp. 1–15. ISSN: 0019-1035. doi: https://doi.org/10.1016/0019-1035(90)90002-Q. Disponível em: <https://www.sciencedirect.com/science/article/pii/001910359090002Q>.

HELIN, E. F., PRAVDO, S. H., RABINOWITZ, D. L., et al., 1997, "Near-Earth Asteroid Tracking (NEAT) Program", *Annals of the New York Academy of Sciences*, v. 822 (maio), pp. 6. doi: 10.1111/j.1749-6632.1997.tb48329.x.

HODGSON, R. G., 1978, "The Discovery of Chiron: Some Reflections", *Minor Planet Bulletin*, v. 5 (mar.), pp. 21–22.

HOFGARTNER, J. D., BURATTI, B. J., HAYNE, P. O., et al., 2019, "Ongoing resurfacing of KBO Eris by volatile transport in local, collisional, sublimation atmosphere regime", Icarus, v. 334 (dez.), pp. 52–61. doi: 10.1016/j.icarus.2018.10.028.

HORNER, J., EVANS, N. W., BAILEY, M. E., 2004, "Simulations of the population of Centaurs - I. The bulk statistics", Mon. Not, Roy. Astron. Soc., v. 354, n. 3 (nov.), pp. 798–810. doi: 10.1111/j.1365-2966.2004.08240.x.

HROMAKINA, T., PERNA, D., BELSKAYA, I., et al., 2018, "Photometric observations of nine Transneptunian objects and Centaurs", Mon. Not, Roy. Astron. Soc., v. 474, n. 2 (fev.), pp. 2536–2543. doi: 10.1093/mnras/stx2904.

HU, L., WANG, L., CHEN, X., et al., 2022, "Image Subtraction in Fourier Space", Astrophys. J., 936(2):157. doi: 10.3847/1538-4357/ac7394.

HUBBARD, W. B., HUNTEN, D. M., DIETERS, S. W., et al., 1988, "Occultation evidence for an atmosphere on Pluto", Nature, v. 336, n. 6198 (dez.), pp. 452–454. doi: 10.1038/336452a0.

JEWITT, D., LUU, J., 1993, "Discovery of the candidate Kuiper belt object 1992 QB_1", Nature, v. 362, n. 6422 (abr.), pp. 730–732. doi: 10.1038/362730a0.

JOHNSON, T. V., MCGETCHIN, T. R., 1973, "Topography on satellite surfaces and the shape of asteroids", Icarus, v. 18, n. 4 (abr.), pp. 612–620. doi: 10.1016/0019-1035(73)90064-X.

KARIMI, R., AZMOUDEH ARDALAN, A., VASHEGHANI FARAHANI, S., 2017, "The size, shape and orientation of the asteroid Vesta based on data from the Dawn mission", *Earth and Planetary Science Letters*, v. 475 (out.), pp. 71–82. doi: 10.1016/j.epsl.2017.07.033.

KEANE, J. T., PORTER, S. B., BEYER, R. A., et al., 2022, “The Geophysical Environment of (486958) Arrokoth—A Small Kuiper Belt Object Explored by New Horizons”, *Journal of Geophysical Research (Planets)*, 127(6):e07068. doi: 10.1029/2021JE007068.

KECSKEMÉTHY, V., KISS, C., SZAKÁTS, R., et al., 2022, “Light curves of transneptunian objects from the K2 mission of the Kepler Space Telescope”, *arXiv e-prints*, art. arXiv:2210.06571.

KERVELLA, P., THÉVENIN, F., DI FOLCO, E., et al., 2004, “The angular sizes of dwarf stars and subgiants. Surface brightness relations calibrated by interferometry”, Astron. Astrophys., v. 426 (out.), pp. 297–307. doi: 10.1051/0004-6361:20035930.

KHAIN, T., BECKER, J. C., LIN, H. W., et al., 2020, “Dynamical Classification of Trans-Neptunian Objects Detected by the Dark Energy Survey”, Astron. J., 159(4):133. doi: 10.3847/1538-3881/ab7002.

KILIC, Y., BRAGA-RIBAS, F., KAPLAN, M., et al., 2022, “Occultation portal: A web-based platform for data collection and analysis of stellar occultations”, Mon. Not, Roy. Astron. Soc., v. 515, n. 1 (set.), pp. 1346–1357. doi: 10.1093/mnras/stac1595.

KISS, C., MARTON, G., PARKER, A. H., et al., 2019, “The mass and density of the dwarf planet (225088) 2007 OR_{10}”, Icarus, v. 334 (dez.), pp. 3–10. doi: 10.1016/j.icarus.2019.03.013.

KOVALENKO, I. D., DORESSOUNDIRAM, A., LELLOUCH, E., et al., 2017, ““TNOs are Cool”: A survey of the trans-Neptunian region. XIII. Statistical analysis of multiple trans-Neptunian objects observed with Herschel Space Observatory”, Astron. Astrophys., 608:A19. doi: 10.1051/0004-6361/201730588.

KOWAL, C. T., LILLER, W., MARSDEN, B. G., 1979, “The Discovery and Orbit of (2060) Chiron”. In: Duncombe, R. L. (Ed.), *Dynamics of the Solar System*, v. 81, p. 245, jan.

KUIPER, G. P., 1951, “On the Origin of the Solar System”, *Proceedings of the National Academy of Science*, v. 37, n. 1 (jan.), pp. 1–14. doi: 10.1073/pnas.37.1.1.

LACERDA, P., 2011, “A Change in the Light Curve of Kuiper Belt Contact Binary (139775) 2001 QG_{298}”, Astron. J., 142(3):90. doi: 10.1088/0004-6256/142/3/90.

LACERDA, P., JEWITT, D. C., 2007, "Densities of Solar System Objects from Their Rotational Light Curves", Astron. J., v. 133, n. 4 (abr.), pp. 1393. doi: 10.1086/511772.

LACERDA, P., FORNASIER, S., LELLOUCH, E., et al., 2014a, "The Albedo-Color Diversity of Transneptunian Objects", Astrophys. J. Lett., 793(1):L2. doi: 10.1088/2041-8205/793/1/L2.

LACERDA, P., MCNEILL, A., PEIXINHO, N., 2014b, "The unusual Kuiper belt object 2003 SQ_{317}", Mon. Not, Roy. Astron. Soc., v. 437, n. 4 (fev.), pp. 3824–3831. doi: 10.1093/mnras/stt2180.

LANG, D., HOGG, D. W., MIERLE, K., et al., 2010, "Astrometry.net: Blind Astrometric Calibration of Arbitrary Astronomical Images", Astron. J., v. 139, n. 5 (maio), pp. 1782–1800. doi: 10.1088/0004-6256/139/5/1782.

LEIVA, R., SICARDY, B., CAMARGO, J. I. B., et al., 2017, "Size and Shape of Chariklo from Multi-epoch Stellar Occultations", Astron. J., 154(4):159. doi: 10.3847/1538-3881/aa8956.

LEIVA, R., BUIE, M. W., KELLER, J. M., et al., 2020, "Stellar Occultation by the Resonant Trans-Neptunian Object (523764) 2014 WC510 Reveals a Close Binary TNO", *The Planetary Science Journal*, 1(2):48. doi: 10.3847/PSJ/abb23d.

LELLOUCH, E., BUTLER, B., MORENO, R., et al., 2022, "Pluto's atmosphere observations with ALMA: Spatially-resolved maps of CO and HCN emission and first detection of HNC", Icarus, 372:114722. doi: 10.1016/j.icarus.2021.114722.

LEONARD, F. C., 1930, "The New Planet Pluto", *Leaflet of the Astronomical Society of the Pacific*, v. 1, n. 30 (jan.), pp. 121.

LEVINE, S. E., ZULUAGA, C. A., PERSON, M. J., et al., 2021, "Occultation of a Large Star by the Large Plutino (28978) Ixion on 2020 October 13 UTC", Astron. J., 161(5):210. doi: 10.3847/1538-3881/abe76d.

LOMB, N. R., 1976, "Least-Squares Frequency Analysis of Unequally Spaced Data", Astrophys. Space Sci., v. 39, n. 2 (fev.), pp. 447–462. doi: 10.1007/BF00648343.

LSST SCIENCE COLLABORATION, ABELL, P. A., ALLISON, J., et al., 2009. "LSST Science Book, Version 2.0". Disponível em: <https://arxiv.org/abs/0912.0201>.

LUU, J. X., 1993, "Cometary Activity in Distant Comets: Chiron", Publ. Astron. Soc. Pacific, v. 105 (set.), pp. 946. doi: 10.1086/133260.

MADEIRA, G., GIULIATTI WINTER, S. M., RIBEIRO, T., et al., 2022, "Dynamics around non-spherical symmetric bodies - I. The case of a spherical body with mass anomaly", Mon. Not, Roy. Astron. Soc., v. 510, n. 1 (fev.), pp. 1450–1469. doi: 10.1093/mnras/stab3552.

MARQUES OLIVEIRA, J., SICARDY, B., GOMES-JÚNIOR, A. R., et al., 2022, "Constraints on the structure and seasonal variations of Triton's atmosphere from the 5 October 2017 stellar occultation and previous observations", Astron. Astrophys., 659:A136. doi: 10.1051/0004-6361/202141443.

MASCI, F. J., LAHER, R. R., RUSHOLME, B., et al., 2019, "The Zwicky Transient Facility: Data Processing, Products, and Archive", Publ. Astron. Soc. Pacific, v. 131, n. 995 (jan.), pp. 018003. doi: 10.1088/1538-3873/aae8ac.

MELITA, M. D., PAPALOIZOU, J. C. B., 2020, "Apse-alignment in narrow-eccentric ringlets and its implications for the ϵ-ring of Uranus and the ring system of (10199) Chariklo", Icarus, 335:113366. doi: 10.1016/j.icarus.2019.06.027.

MEZA, E., SICARDY, B., ASSAFIN, M., et al., 2019, "Lower atmosphere and pressure evolution on Pluto from ground-based stellar occultations, 1988-2016", Astron. Astrophys., 625:A42. doi: 10.1051/0004-6361/201834281.

MILLER, J. P., PENNYPACKER, C. R., WHITE, G. L., 2008, "Optimal Image Subtraction Method: Summary Derivations, Applications, and Publicly Shared Application Using IDL", Publ. Astron. Soc. Pacific, v. 120, n. 866 (abr.), pp. 449. doi: 10.1086/588258.

MOMMERT, M., HARRIS, A. W., KISS, C., et al., 2012, "TNOs are cool: A survey of the trans-Neptunian region. V. Physical characterization of 18 Plutinos using Herschel-PACS observations", Astron. Astrophys., 541:A93. doi: 10.1051/0004-6361/201118562.

MOORE, J. M., MCKINNON, W. B., SPENCER, J. R., et al., 2016, "The geology of Pluto and Charon through the eyes of New Horizons", *Science*, v. 351, n. 6279 (mar.), pp. 1284–1293. doi: 10.1126/science.aad7055.

MORBIDELLI, A., LEVISON, H. F., GOMES, R., 2008, "The Dynamical Structure of the Kuiper Belt and Its Primordial Origin". In: Barucci, M. A., Boehnhardt, H., Cruikshank, D. P., et al. (Eds.), *The Solar System Beyond Neptune*, p. 275.

MORGADO, B., BENEDETTI-ROSSI, G., GOMES-JÚNIOR, A. R., et al., 2019, "First stellar occultation by the Galilean moon Europa and upcoming events between 2019 and 2021", Astron. Astrophys., 626:L4. doi: 10.1051/0004-6361/201935500.

MORGADO, B. E., SICARDY, B., BRAGA-RIBAS, F., et al., 2021, "Refined physical parameters for Chariklo's body and rings from stellar occultations observed between 2013 and 2020", Astron. Astrophys., 652:A141. doi: 10.1051/0004-6361/202141543.

MORGADO, B. E., GOMES-JÚNIOR, A. R., BRAGA-RIBAS, F., et al., 2022, "Milliarcsecond Astrometry for the Galilean Moons Using Stellar Occultations", Astron. J., 163(5):240. doi: 10.3847/1538-3881/ac6108.

MUELLER, B. E. A., THOLEN, D. J., HARTMANN, W. K., et al., 1992, "Extraordinary colors of asteroidal object (5145) 1992 AD", Icarus, v. 97, n. 1 (maio), pp. 150–154. doi: 10.1016/0019-1035(92)90065-F.

MUINONEN, K., BELSKAYA, I. N., CELLINO, A., et al., 2010, "A three-parameter magnitude phase function for asteroids", Icarus, v. 209, n. 2 (out.), pp. 542–555. doi: 10.1016/j.icarus.2010.04.003.

MÜLLER, T., LELLOUCH, E., FORNASIER, S., 2020, "Trans-Neptunian objects and Centaurs at thermal wavelengths". In: Prialnik, D., Barucci, M. A., Young, L. (Eds.), *The Trans-Neptunian Solar System*, pp. 153–181. doi: 10.1016/B978-0-12-816490-7.00007-2.

NESVORNÝ, D., BROŽ, M., CARRUBA, V., 2015, "Identification and Dynamical Properties of Asteroid Families". In: *Asteroids IV*, pp. 297–321. doi: 10.2458/azu_uapress_9780816532131-ch016.

NESVORNÝ, D., MORBIDELLI, A., 2012, "Statistical Study of the Early Solar System's Instability with Four, Five, and Six Giant Planets", Astron. J., 144(4):117. doi: 10.1088/0004-6256/144/4/117.

NIMMO, F., UMURHAN, O., LISSE, C. M., et al., 2017, "Mean radius and shape of Pluto and Charon from New Horizons images", Icarus, v. 287 (maio), pp. 12–29. doi: 10.1016/j.icarus.2016.06.027.

NOLL, K. S., LEVISON, H. F., STEPHENS, D. C., et al., 2006, "(120347) 2004 SB_60", IAU Circ., v. 8751 (set.), pp. 1.

NOLL, K., GRUNDY, W. M., NESVORNÝ, D., et al., 2020, "Trans-Neptunian binaries (2018)". In: Prialnik, D., Barucci, M. A., Young, L. (Eds.), *The Trans-Neptunian Solar System*, pp. 201–224. doi: 10.1016/B978-0-12-816490-7.00009-6.

ORTIZ, J. L., SICARDY, B., BRAGA-RIBAS, F., et al., 2012, "Albedo and atmospheric constraints of dwarf planet Makemake from a stellar occultation", Nature, v. 491, n. 7425 (nov.), pp. 566–569. doi: 10.1038/nature11597.

ORTIZ, J. L., DUFFARD, R., PINILLA-ALONSO, N., et al., 2015, "Possible ring material around centaur (2060) Chiron", Astron. Astrophys., 576:A18. doi: 10.1051/0004-6361/201424461.

ORTIZ, J. L., SANTOS-SANZ, P., SICARDY, B., et al., 2017, "The size, shape, density and ring of the dwarf planet Haumea from a stellar occultation", Nature, v. 550, n. 7675 (out.), pp. 219–223. doi: 10.1038/nature24051.

ORTIZ, J. L., SANTOS-SANZ, P., SICARDY, B., et al., 2020a, "The large trans-Neptunian object 2002 TC_{302} from combined stellar occultation, photometry, and astrometry data", Astron. Astrophys., 639:A134. doi: 10.1051/0004-6361/202038046.

ORTIZ, J. L., SICARDY, B., CAMARGO, J. I. B., et al., 2020b, "Stellar occultation by TNOs: from predictions to observations". In: Prialnik, D., Barucci, M. A., Young, L. (Eds.), *The Trans-Neptunian Solar System*, Elsevier, pp. 413–437, b. doi: 10.1016/B978-0-12-816490-7.00019-9.

OWEN, T. C., ROUSH, T. L., CRUIKSHANK, D. P., et al., 1993, "Surface Ices and the Atmospheric Composition of Pluto", *Science*, v. 261, n. 5122 (ago.), pp. 745–748. doi: 10.1126/science.261.5122.745.

PARKER, A. H., BUIE, M. W., GRUNDY, W. M., et al., 2016, "Discovery of a Makemakean Moon", Astrophys. J. Lett., 825(1):L9. doi: 10.3847/2041-8205/825/1/L9.

PATERSON, K., 2019, *Detecting optical transients and variables with MeerLICHT*. Doctoral Thesis, University of Cape Town, South Africa, mar.

PAVLOV, H., 2020. "Tangra: Software for video photometry and astrometry". Astrophysics Source Code Library, record ascl:2004.002, abr.

PEIXINHO, N., DELSANTI, A., GUILBERT-LEPOUTRE, A., et al., 2012, "The bimodal colors of Centaurs and small Kuiper belt objects", Astron. Astrophys., 546:A86. doi: 10.1051/0004-6361/201219057.

PEIXINHO, N., THIROUIN, A., TEGLER, S. C., et al., 2020, "From Centaurs to Comets - 40 years". In: Prialnik, D., Barucci, M. A., Young, L. (Eds.), *The Trans-Neptunian Solar System*, pp. 307–329. doi: 10.1016/B978-0-12-816490-7.00014-X.

PENTTILÄ, A., SHEVCHENKO, V. G., WILKMAN, O., et al., 2016, "H, G_1, G_2 photometric phase function extended to low-accuracy data", Planet. Space Sci., v. 123 (abr.), pp. 117–125. doi: 10.1016/j.pss.2015.08.010.

PERNA, D., DOTTO, E., BARUCCI, M. A., et al., 2009, "Rotations and densities of trans-Neptunian objects", Astron. Astrophys., v. 508, n. 1 (dez.), pp. 451–455. doi: 10.1051/0004-6361/200911970.

PINILLA-ALONSO, N., STANSBERRY, J. A., HOLLER, B. J., 2020, "Surface properties of large TNOs: Expanding the study to longer wavelengths with the James Webb Space Telescope". In: Prialnik, D., Barucci, M. A., Young, L. (Eds.), *The Trans-Neptunian Solar System*, pp. 395–412. doi: 10.1016/B978-0-12-816490-7.00018-7.

PORO, A., AHANGARANI FARAHANI, F., BAHRAMINASR, M., et al., 2021, "Study of Pluto's atmosphere based on 2020 stellar occultation light curve results", Astron. Astrophys., 653:L7. doi: 10.1051/0004-6361/202141718.

PORTER, S., BENECCHI, S., VERBISCER, A., et al., 2022, "The Poles and Shapes of Seven Kuiper Belt Objects as Measured from New Horizons". In: *44th COSPAR Scientific Assembly. Held 16-24 July*, v. 44, p. 239, jul.

PRAVEC, P., HARRIS, A. W., 2000, "Fast and Slow Rotation of Asteroids", Icarus, v. 148, n. 1 (nov.), pp. 12–20. doi: 10.1006/icar.2000.6482.

PRAVEC, P., ŠAROUNOVÁ, L., WOLF, M., 1996, "Lightcurves of 7 Near-Earth Asteroids", Icarus, v. 124, n. 2 (dez.), pp. 471–482. doi: 10.1006/icar.1996.0223.

PROTOPAPA, S., GRUNDY, W. M., REUTER, D. C., et al., 2017, "Pluto's global surface composition through pixel-by-pixel Hapke modeling of New Horizons Ralph/LEISA data", Icarus, v. 287 (maio), pp. 218–228. doi: 10.1016/j.icarus.2016.11.028.

RABINOWITZ, D. L., SCHAEFER, B. E., TOURTELLOTTE, S. W., 2007, "The Diverse Solar Phase Curves of Distant Icy Bodies. I. Photometric Observations of 18 Trans-Neptunian Objects, 7 Centaurs, and Nereid", Astron. J., v. 133, n. 1 (jan.), pp. 26–43. doi: 10.1086/508931.

RABINOWITZ, D. L., BENECCHI, S. D., GRUNDY, W. M., et al., 2020, "The Complex Rotational Light Curve of (385446) Manwë-Thorondor, a Multicomponent Eclipsing System in the Kuiper Belt", Astron. J., 159(1):27. doi: 10.3847/1538-3881/ab59d4.

RAGOZZINE, D., BROWN, M. E., 2007, "Candidate Members and Age Estimate of the Family of Kuiper Belt Object 2003 EL61", Astron. J., v. 134, n. 6 (dez.), pp. 2160–2167. doi: 10.1086/522334.

RIELLO, M., DE ANGELI, F., EVANS, D. W., et al., 2021, "Gaia Early Data Release 3. Photometric content and validation", Astron. Astrophys., 649:A3. doi: 10.1051/0004-6361/202039587.

ROMMEL, F. L., BRAGA-RIBAS, F., DESMARS, J., et al., 2020, "Stellar occultations enable milliarcsecond astrometry for Trans-Neptunian objects and Centaurs", Astron. Astrophys., 644:A40. doi: 10.1051/0004-6361/202039054.

ROQUES, F., MONCUQUET, M., SICARDY, B., 1987, "Stellar occultations by small bodies - Diffraction effects", Astron. J., v. 93 (jun.), pp. 1549–1558. doi: 10.1086/114438.

RUPRECHT, J. D., BOSH, A. S., PERSON, M. J., et al., 2015, "29 November 2011 stellar occultation by 2060 Chiron: Symmetric jet-like features", Icarus, v. 252 (maio), pp. 271–276. doi: 10.1016/j.icarus.2015.01.015.

SANTOS-SANZ, P., LELLOUCH, E., FORNASIER, S., et al., 2012, ""TNOs are Cool": A survey of the trans-Neptunian region. IV. Size/albedo characterization of 15 scattered disk and detached objects observed with Herschel-PACS", Astron. Astrophys., 541:A92. doi: 10.1051/0004-6361/201118541.

SANTOS-SANZ, P., ORTIZ, J. L., SICARDY, B., et al., 2021, "The 2017 May 20 stellar occultation by the elongated centaur (95626) 2002 GZ_{32}", Mon. Not, Roy. Astron. Soc., v. 501, n. 4 (mar.), pp. 6062–6075. doi: 10.1093/mnras/staa3881.

SANTOS-SANZ, P., ORTIZ, J. L., SICARDY, B., et al., 2022, "Physical properties of the trans-Neptunian object (38628) Huya from a multi-chord stellar occultation", Astron. Astrophys., 664:A130. doi: 10.1051/0004-6361/202141546.

SCARGLE, J. D., 1982, "Studies in astronomical time series analysis. II. Statistical aspects of spectral analysis of unevenly spaced data." Astrophys. J., v. 263 (dez.), pp. 835–853. doi: 10.1086/160554.

SCHAEFER, B. E., RABINOWITZ, D. L., TOURTELLOTTE, S. W., 2009, "The Diverse Solar Phase Curves of Distant Icy Bodies II. The Cause of the Opposition Surges and Their Correlations", Astron. J., v. 137, n. 1 (jan.), pp. 129–144. doi: 10.1088/0004-6256/137/1/129.

SCHALLER, E. L., BROWN, M. E., 2007, "Volatile Loss and Retention on Kuiper Belt Objects", Astrophys. J. Lett., v. 659, n. 1 (abr.), pp. L61–L64. doi: 10.1086/516709.

SCHALLER, E. L., BROWN, M. E., 2008, "Detection of Additional Members of the 2003 EL61 Collisional Family via Near-Infrared Spectroscopy", Astrophys. J. Lett., v. 684, n. 2 (set.), pp. L107. doi: 10.1086/592232.

SCHENK, P., O'BRIEN, D. P., MARCHI, S., et al., 2012, "The Geologically Recent Giant Impact Basins at Vesta's South Pole", *Science*, v. 336, n. 6082 (maio), pp. 694. doi: 10.1126/science.1223272.

SCHENK, P. M., MOORE, J. M., 2020, "Topography and geology of Uranian mid-sized icy satellites in comparison with Saturnian and Plutonian satellites", *Philosophical Transactions of the Royal Society of London Series A*, 378(2187):20200102. doi: 10.1098/rsta.2020.0102.

SCHWAMB, M. E., JONES, R. L., CHESLEY, S. R., et al., 2018, "Large Synoptic Survey Telescope Solar System Science Roadmap", *arXiv e-prints*, art. arXiv:1802.01783.

SCOTTI, J. V., RABINOWITZ, D. L., SHOEMAKER, C. S., et al., 1992, "1992 AD", IAU Circ., v. 5434 (jan.), pp. 1.

SHEPPARD, S. S., 2010, "The Colors of Extreme Outer Solar System Objects", Astron. J., v. 139, n. 4 (abr.), pp. 1394–1405. doi: 10.1088/0004-6256/139/4/1394.

SHEPPARD, S. S., JEWITT, D., 2004, "Extreme Kuiper Belt Object 2001 QG_{298} and the Fraction of Contact Binaries", Astron. J., v. 127, n. 5 (maio), pp. 3023–3033. doi: 10.1086/383558.

SHOWALTER, M. R., HAMILTON, D. P., STERN, S. A., et al., 2011, "New Satellite of (134340) Pluto: S/2011 (134340) 1", *Central Bureau Electronic Telegrams*, v. 2769 (jul.), pp. 1.

SHOWALTER, M. R., WEAVER, H. A., STERN, S. A., et al., 2012, "New Satellite of (134340) Pluto: S/2012 (134340) 1", IAU Circ., v. 9253 (jul.), pp. 1.

SICARDY, B., ORTIZ, J. L., ASSAFIN, M., et al., 2011, "A Pluto-like radius and a high albedo for the dwarf planet Eris from an occultation", Nature, v. 478, n. 7370 (out.), pp. 493–496. doi: 10.1038/nature10550.

SICARDY, B., LEIVA, R., RENNER, S., et al., 2019, "Ring dynamics around non-axisymmetric bodies with application to Chariklo and Haumea", *Nature Astronomy*, v. 3 (abr.), pp. 146–153. doi: 10.1038/s41550-018-0616-8.

SICARDY, B., ASHOK, N. M., TEJ, A., et al., 2021, “Pluto’s Atmosphere in Plateau Phase Since 2015 from a Stellar Occultation at Devasthal”, Astrophys. J. Lett., 923(2):L31. doi: 10.3847/2041-8213/ac4249.

SICKAFOOSE, A. A., BOSH, A. S., LEVINE, S. E., et al., 2019, “A stellar occultation by Vanth, a satellite of (90482) Orcus”, Icarus, v. 319 (fev.), pp. 657–668. doi: 10.1016/j.icarus.2018.10.016.

SICKAFOOSE, A. A., BOSH, A. S., EMERY, J. P., et al., 2020, “Characterization of material around the centaur (2060) Chiron from a visible and near-infrared stellar occultation in 2011”, Mon. Not, Roy. Astron. Soc., v. 491, n. 3 (jan.), pp. 3643–3654. doi: 10.1093/mnras/stz3079.

SINGER, K. N., MCKINNON, W. B., GLADMAN, B., et al., 2019, “Impact craters on Pluto and Charon indicate a deficit of small Kuiper belt objects”, *Science*, v. 363, n. 6430 (mar.), pp. 955–959. doi: 10.1126/science.aap8628.

SINGER, K. N., WHITE, O. L., SCHMITT, B., et al., 2022, “Large-scale cryovolcanic resurfacing on Pluto”, *Nature Communications*, 13:1542. doi: 10.1038/s41467-022-29056-3.

SMITH, B. A., 1976, “Astronomical imaging applications for CCDs”. In: *Charge-Coupled Device Technology and Applications*, pp. 135–138, jan.

SMITH, J. C., CHRISTY, J. W., GRAHAM, J. A., 1978, “1978 P 1”, IAU Circ., v. 3241 (jul.), pp. 1.

SNODGRASS, C., CARRY, B., DUMAS, C., et al., 2010, “Characterisation of candidate members of (136108) Haumea’s family”, Astron. Astrophys., 511:A72. doi: 10.1051/0004-6361/200913031.

SOUAMI, D., BRAGA-RIBAS, F., SICARDY, B., et al., 2020, “A multi-chord stellar occultation by the large trans-Neptunian object (174567) Varda”, Astron. Astrophys., 643:A125. doi: 10.1051/0004-6361/202038526.

SOUZA-FELICIANO, A. C., ALVAREZ-CANDAL, A., JIMÉNEZ-TEJA, Y., 2018, “Wavelet theory applied to the study of spectra of trans-Neptunian objects”, Astron. Astrophys., 614:A92. doi: 10.1051/0004-6361/201731464.

SPENCER, J. R., STERN, S. A., MOORE, J. M., et al., 2020a, “The geology and geophysics of Kuiper Belt object (486958) Arrokoth”, *Science*, 367(6481):aay3999. doi: 10.1126/science.aay3999.

SPENCER, J., GRUNDY, W. M., NIMMO, F., et al., 2020b, “The Pluto system after New Horizons”. In: Prialnik, D., Barucci, M. A., Young, L. (Eds.), *The Trans-Neptunian Solar System*, pp. 271–288, b. doi: 10.1016/B978-0-12-816490-7.00012-6.

STANSBERRY, J., GRUNDY, W., BROWN, M., et al., 2008, “Physical Properties of Kuiper Belt and Centaur Objects: Constraints from the Spitzer Space Telescope”. In: Barucci, M. A., Boehnhardt, H., Cruikshank, D. P., et al. (Eds.), *The Solar System Beyond Neptune*, University of Arizona Press, p. 161.

STELLINGWERF, R. F., 1978, “Period determination using phase dispersion minimization.” Astrophys. J., v. 224 (set.), pp. 953–960. doi: 10.1086/156444.

STERN, A., CAMPINS, H., 1996, “Chiron and the Centaurs: escapees from the Kuiper belt”, Nature, v. 382, n. 6591 (ago.), pp. 507–510. doi: 10.1038/382507a0.

STERN, S. A., WEAVER, H. A., SPENCER, J. R., et al., 2019, “Initial results from the New Horizons exploration of 2014 MU_{69}, a small Kuiper Belt object”, *Science*, 364(6441):aaw9771. doi: 10.1126/science.aaw9771.

STETSON, P. B., 1987, “DAOPHOT: A Computer Program for Crowded-Field Stellar Photometry”, Publ. Astron. Soc. Pacific, v. 99 (mar.), pp. 191. doi: 10.1086/131977.

STORN, R., PRICE, K., 1997, “Differential Evolution – A Simple and Efficient Heuristic for global Optimization over Continuous Spaces.” *Journal of Global Optimization*, v. 11, n. 4 (dez.), pp. 341–359. doi: 10.1023/A:1008202821328.

TANCREDI, G., FAVRE, S., 2008, “Which are the dwarfs in the Solar System?” Icarus, v. 195, n. 2 (jun.), pp. 851–862. doi: 10.1016/j.icarus.2007.12.020.

TANGA, P., PAUWELS, T., MIGNARD, F., et al., 2022, “Data Release 3: the Solar System survey”, *arXiv e-prints*, art. arXiv:2206.05561.

TEGLER, S. C., ROMANISHIN, W., CONSOLMAGNO, G. J., et al., 2005, “The period of rotation, shape, density, and homogeneous surface color of the Centaur 5145 Pholus”, Icarus, v. 175, n. 2 (jun.), pp. 390–396. doi: 10.1016/j.icarus.2004.12.011.

TEGLER, S. C., ROMANISHIN, W., CONSOLMAGNO, G. J., et al., 2016, “Two Color Populations of Kuiper Belt and Centaur Objects and the Smaller Orbital Inclinations of Red Centaur Objects”, Astron. J., 152(6):210. doi: 10.3847/0004-6256/152/6/210.

THIROUIN, A., ORTIZ, J. L., DUFFARD, R., et al., 2010, “Short-term variability of a sample of 29 trans-Neptunian objects and Centaurs”, Astron. Astrophys., 522: A93. doi: 10.1051/0004-6361/200912340.

THIROUIN, A., NOLL, K. S., ORTIZ, J. L., et al., 2014, “Rotational properties of the binary and non-binary populations in the trans-Neptunian belt”, Astron. Astrophys., 569:A3. doi: 10.1051/0004-6361/201423567.

THIROUIN, A., 2013, *Study of trans-neptunian objects using photometric techniques and numerical simulations*. Doctoral Thesis, University of Granada, Spain, jan.

THIROUIN, A., SHEPPARD, S. S., 2017, “A Possible Dynamically Cold Classical Contact Binary: (126719) 2002 CC_{249}”, Astron. J., 154(6):241. doi: 10.3847/1538-3881/aa96fb.

THIROUIN, A., SHEPPARD, S. S., 2018, “The Plutino Population: An Abundance of Contact Binaries”, Astron. J., 155(6):248. doi: 10.3847/1538-3881/aac0ff.

THIROUIN, A., SHEPPARD, S. S., 2019, “Light Curves and Rotational Properties of the Pristine Cold Classical Kuiper Belt Objects”, Astron. J., 157(6):228. doi: 10.3847/1538-3881/ab18a9.

THIROUIN, A., SHEPPARD, S. S., NOLL, K. S., et al., 2016, “Rotational Properties of the Haumea Family Members and Candidates: Short-term Variability.” Astron. J., 151(6):148. doi: 10.3847/0004-6256/151/6/148.

THIROUIN, A., SHEPPARD, S. S., NOLL, K. S., 2017, “2004 TT_{357}: A Potential Contact Binary in the Trans-Neptunian Belt”, Astrophys. J., 844(2):135. doi: 10.3847/1538-4357/aa7ed3.

THOMAS, P. C., 1989, “The shapes of small satellites”, Icarus, v. 77, n. 2 (fev.), pp. 248–274. doi: 10.1016/0019-1035(89)90089-4.

TISCARENO, M. S., HEDMAN, M. M., BURNS, J. A., et al., 2013, “Compositions and Origins of Outer Planet Systems: Insights from the Roche Critical Density”, Astrophys. J. Lett., 765(2):L28. doi: 10.1088/2041-8205/765/2/L28.

TISSERAND, F. F., 1896, *Traité de méchanique céleste*. Paris, Gauthier-Villars et fils.

TODY, D., 1993, “IRAF in the Nineties”. In: Hanisch, R. J., Brissenden, R. J. V., Barnes, J. (Eds.), *Astronomical Data Analysis Software and Systems II*, v. 52, *Astronomical Society of the Pacific Conference Series*, p. 173, jan.

TOMANEY, A. B., CROTTS, A. P. S., 1996, “Expanding the Realm of Microlensing Surveys with Difference Image Photometry”, Astron. J., v. 112 (dez.), pp. 2872. doi: 10.1086/118228.

TRUJILLO, C. A., SHEPPARD, S. S., 2014, “A Sedna-like body with a perihelion of 80 astronomical units”, Nature, v. 507, n. 7493 (mar.), pp. 471–474. doi: 10.1038/nature13156.

TRUJILLO, C. A., SHEPPARD, S. S., SCHALLER, E. L., 2011, “A Photometric System for Detection of Water and Methane Ices on Kuiper Belt Objects”, Astrophys. J., 730(2):105. doi: 10.1088/0004-637X/730/2/105.

VACHIER, F., BERTHIER, J., MARCHIS, F., 2012, “Determination of binary asteroid orbits with a genetic-based algorithm”, Astron. Astrophys., 543:A68. doi: 10.1051/0004-6361/201118408.

VAN BELLE, G. T., 1999, “Predicting Stellar Angular Sizes”, Publ. Astron. Soc. Pacific, v. 111, n. 766 (dez.), pp. 1515–1523. doi: 10.1086/316462.

VANDERPLAS, J. T., 2018, “Understanding the Lomb-Scargle Periodogram”, Astrophys. J. Suppl., 236(1):16. doi: 10.3847/1538-4365/aab766.

VARA-LUBIANO, M., BENEDETTI-ROSSI, G., SANTOS-SANZ, P., et al., 2022, “The multichord stellar occultation on 2019 October 22 by the trans-Neptunian object (84922) 2003 VS_2”, Astron. Astrophys., 663:A121. doi: 10.1051/0004-6361/202141842.

VERBISCER, A., PORTER, S., KAVELAARS, J. J., et al., 2022a, “Putting (486958) Arrokoth in Context: New Horizons Observations of Other Small Cold Classical Kuiper Belt Objects”. In: *44th COSPAR Scientific Assembly. Held 16-24 July*, v. 44, p. 201, jul.a.

VERBISCER, A. J., HELFENSTEIN, P., PORTER, S. B., et al., 2022b, “The Diverse Shapes of Dwarf Planet and Large KBO Phase Curves Observed from New Horizons”, *The Planetary Science Journal*, 3(4):95. doi: 10.3847/PSJ/ac63a6.

VILENIUS, E., KISS, C., MOMMERT, M., et al., 2012, "“TNOs are Cool”: A survey of the trans-Neptunian region. VI. Herschel/PACS observations and thermal modeling of 19 classical Kuiper belt objects”, Astron. Astrophys., 541:A94. doi: 10.1051/0004-6361/201118743.

VILENIUS, E., KISS, C., MÜLLER, T., et al., 2014, "“TNOs are Cool”: A survey of the trans-Neptunian region. X. Analysis of classical Kuiper belt objects from

Herschel and Spitzer observations", Astron. Astrophys., 564:A35. doi: 10.1051/0004-6361/201322416.

VILENIUS, E., STANSBERRY, J., MÜLLER, T., et al., 2018, ""TNOs are Cool": A survey of the trans-Neptunian region. XIV. Size/albedo characterization of the Haumea family observed with Herschel and Spitzer", Astron. Astrophys., 618: A136. doi: 10.1051/0004-6361/201732564.

WEAVER, H. A., STERN, S. A., 2008, "New Horizons: NASA's Pluto-Kuiper Belt Mission". In: Barucci, M. A., Boehnhardt, H., Cruikshank, D. P., et al. (Eds.), *The Solar System Beyond Neptune*, University of Arizona Press, p. 557.

WEAVER, H. A., STERN, S. A., MUTCHLER, M. J., et al., 2005, "S/2005 P 1 and S/2005 P 2", IAU Circ., v. 8625 (out.), pp. 1.

WONG, I., MISHRA, A., BROWN, M. E., 2019, "Photometry of Active Centaurs: Colors of Dormant Active Centaur Nuclei", Astron. J., 157(6):225. doi: 10.3847/1538-3881/ab1b22.

WOZNIAK, P. R., 2000, "Difference Image Analysis of the OGLE-II Bulge Data. I. The Method", Acta Astron., v. 50 (dez.), pp. 421–450.

YOUNG, L. A., BRAGA-RIBAS, F., JOHNSON, R. E., 2020, "Volatile evolution and atmospheres of Trans-Neptunian objects". In: Prialnik, D., Barucci, M. A., Young, L. (Eds.), *The Trans-Neptunian Solar System*, pp. 127–151. doi: 10.1016/B978-0-12-816490-7.00006-0.

ZACKAY, B., OFEK, E. O., 2017, "How to COAAD Images. I. Optimal Source Detection and Photometry of Point Sources Using Ensembles of Images", Astrophys. J., 836(2):187. doi: 10.3847/1538-4357/836/2/187.

ZACKAY, B., OFEK, E. O., GAL-YAM, A., 2016, "Proper Image Subtraction—Optimal Transient Detection, Photometry, and Hypothesis Testing", Astrophys. J., 830 (1):27. doi: 10.3847/0004-637X/830/1/27.

ZAPPALÀ, V., BENDJOYA, P., CELLINO, A., et al., 1995, "Asteroid families: Search of a 12,487-asteroid sample using two different clustering techniques." Icarus, v. 116, n. 2 (ago.), pp. 291–314. doi: 10.1006/icar.1995.1127.

Appendix A

Stellar occultation observational circumstances

The following tables summaries the observational circumstances of each station for the eight stellar occultations presented by this work. For better visualization, the tables were divided into two groups i) the 8 August 2020 event and ii) the other eight stellar occultations. The positive, negatives and overcast locations involved in the 8 August 2020 campaign are listed by the tables A.1, A.2 and A.3, respectively. Positive and negatives of the other eight events are present by the tables A.4 and A.5, respectively.

Table A.1: observational circumstances for all observatories that detected the stellar occultation by the main body on 8 August 2020. The * symbol indicates that this data was taken in drift scan mode.

Observatory, nearest city, country	**Latitude (°), longitude (°), altitude (m)**	**Telescope, aperture (m), filter**	**Time source, instrument**	**Exposure (s), cycle (s), correction (s)**	**Observers**
Domaine de La Blaque, Varages, France	+43.61239 +05.96363 468.0	Ritchey-Chrétien 0.5 Clear	GPS WATEC 910HX	0.32 0.32 -	Jean Lecacheux, Jean-Luc Plouvier
TAROT Calern, Caussols, France	+43.752001 +06.923613 1268.0	TAROT North 0.25 Clear	GPS Andor DZ936N-BEX2-DD	90.0* 90.0* -	Eric Frappa, Alain Klotz
Méo Station, Grasse, France	+43.7546 +06.9216 1323.1	Ritchey-Chrétien 1.54 Clear	NTP ZWO ASI1600MM	1.0 1.0 -	Dominique Albanese, Hervé Mariey
Caussols, Cannes, France	+43.753055556 +6.921666667 1268.0	- 0.40 Clear	NTP ZWO 294 MC -	3.0 4.0 +0.4	Raymond Behem, Jean Pierre Prost
Sta Maria de Montmagastrell, Lleida, Spain	+41.720166 +01.105361 318.0	- 0.406 Clear	NTP SBIG STL-11000	7.0 18.0 -4.0	Josep M. Bosch Ignés
Saint-Paul-en-Forêt, Cannes, France	+43.560124 +06.692868 45.0	- 0.2 Clear	NTP ZWO ASI290MM	2.0 2.22 -	Romain Fafet
Nice, Nice, France	+43.725902 +07.299875 364.0	- 0.4 Clear	GPS Raptor Photonics	0.3 0.3 -3.7	Stéfan Renner, Matthieu Conjat
Valbonne, Valbonne, France	+43.619604 +07.039157 174.0	François Giraud (TFG) 0.4 Clear	GPS WATEC 910HX	1.0688 1.5163 -0.5339	Florian Signoret
Crni Vrh, Crni Vrh, Slovenia	+45.94586111 +14.07122222 726.0	Cichocki Sky Survey 0.6 W (clear)	NTP Apogee Alta U16M	1.5984 3.1095 -	Herman Mikuz
Piszkéstető Mountain Station, Mátraszentistván, Hungary	+47.917833 +19.8955833 960.0	Ritchey-Chrétien-Coudé 1.0 Clear	NTP Andor iXon - 888	0.56115 0.56791 -	Róbert Szakáts
University of Ljubljana, Ljubljana, Slovenia	+46.043806 +14.5274444 400.0	- 0.25 Clear	NTP QHY 5III-178M	2.0 2.0 -	Bojan Dintinjana
Konkoly, Budapest, Hungary	+47.4999553 +18.9620488 470.0	- 0.3 Clear	NTP ASI178MM	1.0 1.0385 -	Andras Pal, Balazs Csak
Trieste, Trieste, Italy	+45.642721 +13.875383 400.0	Schmidt-Cassegrain 0.355 Luminance	NTP Apogee U Alta KAF-8300	4.0 5.0 +2.0	Paolo Di Marcantonio, Igor Coretti, Giulia Iafrate, Veronica Baldini
Sant Esteve Sesrovires, Catalonia, Italy	+41.494867 +01.8738 180.0	Newtonian 0.4 Clear	GPS Mintron 12V6HC-EX	1.28 1.28 - 1.28	Carles Schnabel, Martí Schnabel
ALMO Observatory, Bologna (Padulle), Italy	+44.627 +11.2805 19.0	Schmidt-Cassegrain 0.235 Clear	NTP ZWO ASI120mm	3.0 3.0 +1.0	Adriano Valvasori, Ernesto Guido
- Massa, Italy	+44.026083333 +10.138611111 41.0	Schmidt-Cassegrain 0.2 Clear	GPS WATEC 910BD	2.56 2.60 -2.56	Michele Bigi
G. Pascoli, Castelvecchio Pascoli, Italy	+44.0603 +10.4625 257.0	Newtonian 0.41 Clear	NTP Sony QHY22	1.5 4.0 +2.2	Roberto Bacci
Mount Agliale, Borgo a Mozzano, Italy	+43.99530 +10.51494 750.0	Newtonian 0.50 Clear	NTP FLI - Proline 4710	4.0 5.35 -	Fabrizio Ciabattari
Pistoiese Mountain, San Marcello Pistoiese, Italy	+44.063055 +10.804166 990.0	Newtonian 0.6 Clear	NTP (GPS-PPS) Apogee U6 Alta	1.0 3.13 -	Paolo Bacci, Martina Maestripieri, Marta Di Grazia

Table A.1 continued

Tavolaia, Sta. Maria a Monte, Italy	+43.736833 +10.673445 34.0	Newtonian 0.4 Clear	NTP ASI 174 MM	2.0 2.0 -2.0	Mauro Bachini, Giacomo Succi
Spica, Signa, Italy	+43.789336 +11.089922 50.0	- 0.3 Clear	NTP SBIG ST-402 XME	3.0 4.0 -	Mauro Bertini
Margherita Hack, Lastra a Signa, Italy	+43.742280556 +11.1030305556 216.0	- 0.356 Clear	NTP SBIG ST10XME	2.0 4.45 -	Nico Montigiani, Massimiliano Mannucci
Zalistci, Khmelnytskyi, Ukraine	+48.84778 +26.72139 100.0	- 0.5 V	GPS FLI 16070	2.0 33.2 -	T.O. Dementiev, O. M. Kozhukhov
- Sevilla, Spain	+37.346111 -5.980556 28.0	- 0.28 Clear	GPS QHY 174M	0.6 0.6 -	Jose Maria Madiedo
El Arenosillo, Huelva, Spain	+37.103889 -06.7338889 54.0	BOOTES-1B 0.3 Clear	NTP Andor Ixon	2.0 4.0 -0.7	Emilio Jesus Fernández García, Alberto J. Castro Tirado
ROASTERR-1, Cluj-Napoca, Romania	+46.820954 +23.596400 390.0	- 0.3 Clear	NTP atik 383L+	4.0 5.0 -	Lucian Hudin
Fuensanta de Martos, Fuensanta de Martos, Spain	+37.646389 -03.917468 710.0	Newtonian 0.36 Luminance	atom time SBIG ST-10xme	2.0 8.0 -	Jose Carrillo Gomez
- Fiastra, Italy	+43.057093 +13.173074 700.0	- 0.254 Clear	NTP SBIG ST8-XME	3.0 6.1 -	Alessio Ciarnella
- Dragsina, Romania	+45.703344 +21.436879 97.0	- 0.4 Clear	NTP ZWO ASI 1600MM-Pro	0.9 1.47 -	Liviu Stoian, Andrei Juravle
Cala D'Hort, Ibiza, Spain	+38.89111111 -1.24083333 130.0	- 0.5 Luminance	NTP Sbig STL11000	3.0 6.0 -	Ignacio de la Cueva Torregrosa, Marco Moreno Yuste
Alhendín, Granada, Spain	+37.1110313 -03.6394227 740.0	Newtonian 0.2 Clear	NTP ZWO ASI 178MM	5.0 5.125 -	Miguel Sánchez González
Sierra Nevada, Granada, Spain	+37.0641667 -03.384722 2896.0	T150 1.5 Clear	NTP Andor Ikon-L	1.0 2.0 -	Alfredo Sota, Pablo Santos Sanz, José Luis Ortiz, Nicolás Morales
Sierra Nevada, Granada, Spain	+37.0641667 -03.384722 2896.0	T90 0.9 Clear	NTP Roper VersArray	1.0 3.0 -	
Cancelada, Estepona, Spain	+36.461111111 -05.05444444 25.0	- 0.254 Luminance	Mount Sync MaxIm DL 6 ATIK - 460 ex	10.0 18.0 -	Juan Francisco Calvo Fernández
Cosmos, Marbella, Spain	+36.516229 -04.857376 70.0	- 0.355 Luminance	NTP ATIK 460ex	10.0 21.0 -	Fran Cuevas
Colle S. Agata, Roma, Italy	+41.94955555 +12.42855555 124.0	Schmidt-Cassegrain 0.28 Clear	GPS QHY174M	2.0 2.0 -	Claudio Costa
Hvar, Hvar, Croatia	+43.178944 +16.447748 190.0	- 1.06 Clear	NTP ASI294MC Pro	3.0 3.2 -	Stefan Cikota, Domagoj Ruždjak, Aleksandar Cikota
- Bacau, Romania	+46.50779 +26.80007 555.0	Newtonian 0.254 IR Cut	NTP ZWO ASI 178 MM	3.0 3.18 -	Radu Anghel
Agrustos, Sassari, Italy	+40.7278448 +09.6948317 20.0	SC 0.13 Clear	GPS QHY174 M	4.0 4.0 -	Salvatore Lamina
Campo Catino, Sgurgola, Italy	+41.821115 +13.3292867 1485.0	- 0.8 Clear	GPS QHY 174C	1.0 1.0 -3.0	Ugo Tagliaferri, Mario Di Sora, Giovanni Isopi

Table A.1 continued

Kharkov University, Kharkiv, Ukraine	+49.64083 +36.93389 156.0	Reflector AZT - 8 0.7 Luminance	NTP FLI ML4710	2.0 3.0 -	Y. Krugly, I. Slyusarev, V. Chiorny
Kharkov University, Kharkiv, Ukraine	+49.64083 +36.93389 156.0	Baker-Schmidt 0.36 R	NTP FLI PL1001E	4.0 5.0 -	Y. Krugly, A.Zheleznyak
Ceccano, Ceccano, Italy	+41.567717 +13.333301 178.0	- 0.432 Clear	NTP SBIG STL-6303E	3.5 4.0 -	Gianluca Masi
Stardust, Brasov, Romania	+45.641611 +25.621889 597.0	CPC800 0.2 Clear	NTP Atik 383L+	10.0 13.0 -	Lucian Curelaru
- Bârlad, Romania	+46.2313888 +27.6694444 70.0	EQMOD ASCOM 0.2 Luminance	NTP ASI 1600	8.0 8.8 -	Dumitru Ciprian Vîntdevară
Stardreams, Valenii de Munte, Romania	+45.203642 +26.045526 380.0	- 0.203 Clear	NTP ATIK 460ex	4.0 5.0 -	Radu Mihai Gherase
St. George, Ploiesti, Romania	+45.007213 +25.978711 243.0	- 0.19 Luminance	NTP ATIK 460EX mono	7.0 8.0 -18.0	Cristian Adrian Danescu
Odessa-Mayaki, Odessa, Ukraine	+46.39696195 +30.27127709 19.0	- 0.80 Clear	GPS QHY174M	1.0 1.0 -	V. Kashuba, N. Koshkin, V. Zhukov
Nastro Verde, Naples, Italy	+40.618714 +14.357628 275.0	SC Meade LX200 0.3556 Clear	NTP ASI 120 MM-S	2.5264 2.96 -3.2	Nello Ruocco
- Agerola, Italy	+40.6260833 +14.571555 708.0	SC C14 EDGE HD 0.355 Clear	NTP ASI 178 mono	0.6 0.6 -	Luigi Morrone
Algiers-Bouzareah, Algiers, Algeria	+36.79787333 +03.032248333 348.3	Ritchey-Chrétien 0.81 Clear	GPS WATEC 910 HX/RC	0.08 0.08 -0.04	D. Baba Aissa, Z. Gringahcene
Roque de Los Muchachos, La Palma, Spain	+28.7624 -17.8792 2363.0	Liverpool 2.0 V+R	NTP Andor DW485 (RISE)	0.6 0.6324 -	Pablo Santos-Sanz Nicolás Morales, José Luis Ortiz
EPTOs, Tijarafe, Spain	+28.741667 -17.92972223 1079.0	Marcon RC 0.40 Clear	NTP FLI PL4240	4.0 5.0 +1.0	Daniele Carosati
Astronomic Society of Tunisia, Ariana, Tunisia	+36.8842 +10.1949 5.0	- 0.203 Clear	GPS ZWO ASI 120 MM	2.0 2.0 -1.894	Sofien Kamoun
Teide, Spain	+28.3000 -16.5097 2390.0	Artemis 1.0 Clear	GPS Andor IKONL BEX2 DD	1.5 2.0 -	Artem Burdanov, Emmanuel Jehin
Teide, Spain	+28.3000 -16.5097 2390.0	TAR1 0.46 Clear	NTP FLI KL 400	1.0 1.0 -0.5	Miquel Serra-Ricart, Miguel R. Alarcón, Javier Licandro
- Catania, Italy	+37.69291 +14.97355 1727.0	- 0.91 Clear	NTP Developed at observatory	6.0 10.0 +2.0	A. Frasca, G. Catanzaro, R. Zanchez, Giuseppe Leto
Kuban State University, Kuban, Russia	+45.01667 +39.0333 76.0	Paramount ME 0.508 Luminance	GPS FLI PL1001E	3.0 5.0 -	A.L. Ivanov, V.A. Ivanov, N.B. Ivanova
Istanbul University, Çanakkale, Turkey	+40.09899 +26.47449 410.0	Ritchey-Chrétien 0.6 Clear	GPS Andor iXon Ultra 888	2.0 3.0 -	Süleyman Fişek, Oğuzhan Çakır, Simge Özer

Table A.2: Observational circumstances of all stations that acquired data of the 8 August 2020 event but did not detect the occultation. * This information is from http://www.ieec.cat/en/content/210/telescope-and-dome.

Observatory, nearest city, country	**Latitude (°), longitude (°), altitude (m)**	**Telescope, aperture (m), filter**	**Time source, instrument**	**Exposure (s), cycle (s), correction (s)**	**Observers**
Sternwarte Comthurey, Neustrelitz, Germany	+53.26608 +13.1901666 74.0	- 0.18 Clear	GPS QHY174	2.964 2.964	Konrad Guhl
Breitenweg, Herkenrath, Germany	+50.993310 +07.183794 200.0	RC 0.304 Clear	GPS Watec 120N+	2.56 2.56	Bernd Klemt
Biesenthal, Biesenthal, Germany	+52.759278 +13.663 263.0	Newtonian 0.3 Clear	GPS QHY174	? ?	Nikolai Wuensche
- Berlin, Germany	+52.516111 +13.427778 40.0	Newtonian 0.254 Clear	GPS DVTI	3.0 3.0	Christian Weber
Eppstein-Bremthal, Wiesbaden, Germany	+50.13816667 +08.364 256.0	Schmidt-Cassegrain 0.254 Clear	GPS QHY-174M	3.0 3.0	Oliver Kloes
Vierzon, Vierzon, France	+47.223258 +02.052731 100.0	- 0.25 Clear	Time Box ZWO 1600 M	1.5 ?	Lionel Rousselot
Borowiec, Poznan, Poland	+52.276896 +17.075216 123.0	- 0.4 Clear	NTP SBIG ST7	3.0 (S) 5.0	Anna Marciniak
Teplice, Teplice, Czech Republic	+50.63833 +13.84675 275.0	Planewave CDK17 0.43 Clear	TimeBox Apogee Aspen CG9000	0.5 0.58	Zdenek Moravec
Plzen, Plzen, Czech Republic	+49.69475 +13.321 339.0	- 0.303 Clear	GPS QHY 174	1.0 ?	Jiri Polak
Plzen, Plzen, Czech Republic	+49.7073333 +13.3321667 326.0	- 0.303 Clear	GPS QHY 174	1.0 ?	Michal Rottenborn
Ksiezyno, Bialystok, Poland	+53.075944 +23.102194 145.0	Newtonian 0.3 Clear	GPS QHY174	2.0 ?	Wojciech Burzynski, Maciej Borkowski
Ondrejov, Ondrejov, Czech Republic	+49.91056 +14.78364 528.0	- 0.65 Clear	NTP Moravian G2-3200	6.0 ?	Kamil Hornoch
Allariz, Orense, Spain	+42.2 -07.77 490.0	- 0.254 Clear	NTP QHY6	8.0 ∼10.0	Luis Perez
Buelach, Buelach, Switzerland	+47.51956 +08.57064 550.0	- 0.50 Clear	GPS DVTI	? ?	Stefan Meister
Max Planck Institut, Garching, Germany	+48.261388889 +11.671111111 480.0	- 0.61 Clear	GPS SBIG STX-16803	3.0 12.9	Vadim Burwitz, Piotr Sybilski, Wienczyslaw Bykowski, Thomas Müller
Giesing, Munich, Germany	+48.12194 +11.6072 500.0	Cassegrain 0.80 Orange	Computer Atik 3141	1.355 1.355	Bernd Gährken
Český Rudolec - Matějovec, Strmilov, Czechia	+49.08277778 +15.22841667 707.0	- 0.203 Clear	GPS QHY 174M	2.5 ?	Jiří Kubánek
Wendelstein, Brannenburg, Germany	+47.703638889 +12.012055556 1836.0	- 2.1 SDSS r + SDSS i	GPS 3kk	1.0 13.0	Michael Schmidt
Nonndorf, Waidhofen an der Thaya, Austria	+48.78695667 +15.23565667 549.0	- 0.254 Clear	GPS WAT-610BD	1.28 ?	Gerhard Dangl
Cannet, Riscle, France	+43.62093 -0.044685 180.0	- 0.40 Clear	GPS Watec 120N+	1.28 ?	Jean Jaques Castellani
Saint-Caprais, Rabastens, France	+43.874044 +01.718749 193.0	- 0.94 Clear	GPS WATEC 910HX	0.64 ?	Eric Frappa, Alain Klotz, Maylis Lavayssiere
PDlink, Cadca, Slovakia	+49.4042222 +18.7026306 680.2	- 0.4 Clear	NTP or GPS? QHY 5 III 290M	0.9945 0.9945 -	Peter Delincak
- Muzzano-Lugano, Switzerland	+45.9862778 +08.91958333 350.0	Schmidt-Cassegrain 0.23 Clear	GPS Watec 910/HX-RC	1.28 ?	Alberto Ossola

Table A.2 continued

Schiaparelli, Varese, Italy	+45.86778 +08.77083 1230.0	Reflector 0.84 Clear	NTP SBIG STX-16803	4.0 7.0	Luca Buzzi
- Kysucké Nové Mesto, Slovakia	+49.307305556 +18.765388889 469.0	- 0.252 Clear	GPS QHY174	380 380	Marian Urbaník
Belesta, Toulouse, France	+43.438391949 +01.83152549 234.0	- 0.20 Clear	GPS WATEC 910HX	0.64 ?	Andre Pascal
Latrape, Toulouse, France	+43.243969 +01.290111 350.0	- 0.305 UV-IR block	GPS Watec 910 HX/RC	5.12 ?	Michel Boutet, Jacques Sanchez
Suhora, Poreba Wielka, Poland	+49.5691728579 +20.06728579 1000.0	- 0.6 Clear	GPS Apogee Aspen-47	2.0 3.0 -	Waldemar Ogloza
Filzi School, Bolzano, Italy	+46.42278 +11.33833 280.0	RC Refractor 0.355 Clear	NTP ASI 294 pro	1.0 1.0 -	G. B. Casalnuovo
GiaGa, Pogliano Milanese, Italy	+45.54145833 +08.9954750 172.0	Schmidt-Cassegrain 0.356 Clear	NTP Moravian G2-3200 Mark II	4.0 12.33 -	Galli Gianni
Skalnaté Pleso, Tatranská Lomnica, Slovakia	+49.189355 +20.233816 1786.0	- 0.61 Clear	NTP SBIG ST-10XME	4.0 6.8 -	Marek Husárik
Skalnaté Pleso, Poprad, Slovakia	+49.1894 +20.2341 1786.0	- 1.3 Clear	NTP ZWO ASI 1600MM pro	1.0 1.0	Richard Komzik, Theodor Pribulla, Dusan Tomko
Chante-Perdrix, Dauban, France	+43.99972222 +05.6475 630.0	SC 0.275 Clear	NTP SBIG ST8-XME	2.0 4.1	Marc Serrau, X. Delmotte
Centro de Ciência Viva, Constância, Portugal	+39.49489 -08.32367 147.0	RC 0.508 Clear	GPS WATEC 910HX-RC	0.64 (E) ?	Rui Gonçalves, João Ferreira, Maximo Ferreira, Miguel Bento
Cima Ekar, Asiago, Italy	+45.8494453 +11.5688257 1369.9	- 0.67 Clear	NTP Moravian G4-16000	4.0 ?	Domenico Nardiello
Montsec, Catalonia, Spain	+42.051666 +0.7297222 1570	Joan Oró 0.8 V	NTP+GPS* MEIA3	5.0 ~8.85	Toni Santana
TURKSAT, Ankara, Turkey	+39.636632 +32.804157 950.0	TURKSAT 0.5 Clear	GPS FLI PL4240	3.0 5.0	Mehmed Naim Bagiran
TUBITAK National, Antalya, Turkey	+36.825271 +30.3333 2538.725	ACE T100 1.0 Clear	GPS SI 1100 Cryo	3.0 6.45	Yucel Kilic, Orhan Erece, Sila Eryilmaz
Çukurova University, Adana, Turkey	+37.059684 +35.3554 130.0	Pro RC 500 LK7 0.50 Clear	NTP Apogee Aspen CG6	5.0 5.0	Mahmut Tekeş
Adiyaman University, Adiyaman, Turkey	+37.751667 +38.225278 675.0	ADYU60 0.61 Clear	GPS Andor iKon-M 934	3.0 3.0	Eda Sonbas, Huseyin ER

Table A.3: observational circumstances of all sites that tried to observe the 8 August 2020 event but had bad weather or technical issues and do not acquired data. The symbol * indicates that the information is from Google Earth.

Observatory, Nnearest city, country	**Latitude (°), longitude (°), altitude (m)**	**Telescope aperture (m) filter**	**Time source, instrument**	**Observers**
Pinsoro, Pinsoro, Spain	+42.19916666 -01.3388888 365.0	- 0.28 Clear	GPS Mintron MTV-12V6HC-EX	Oscar Canales Moreno
Montseny, Sant Celoni, Spain	+41.7214 +02.5206 300.0	- 0.254 Clear	NTP ST8	Josep M. Trigo-Rodríguez
Sabadell, Sabadell, Spain	+41.55002777 +2.08333333 224.0	- 0.5 Clear	GPS Watec 910HX-RC	Carlos Perelló
Calar Alto, Almería, Spain	+37.22083245 -2.540997836 2168.0	- 1.23 Clear	NTP PlanetCam	Ricardo Hueso
Urseanu, Bucharest, Romania	+44.448611 +26.093056 100.0	- 0.405 Clear	NTP ZWO ASI 224 MC color	Dascalu Mihai
Traian - Ialomița, Slobozia, Romania	+44.761488 +27.341830 30.0	- 0.2 UV/IR Cut	NTP QHY 163 M	Daniel Nicolae Bertesteanu
TRAPPIST-North, Oukaimeden, Morroco	+31.2061 -7.8664 2751	- 0.6 Clear	NTP Andor IKONL BEX2 DD	Emmanuel Jehin
AGM, Marrakech, Morroco	+31.173411 -8.077456 400.0	- 0.355 Clear	NTP DMK 31AU03.AS	Mohammed Sabil
Specca, Ioannina, Greece	+39.60175 +20.87014 480.0	- 0.2 Clear	GPS Canon Eos 1200D	Georgios Lekkas
Empesos, Agrinion, Greece	+39.02570544 +21.31730396 334.0	- 0.25 Clear	Occult Flash Tag ZWO ASI 224 MC	Vagelis Tsamis, Kyriaki Tigani
- Amfiloxia, Greece	+38.805170 +21.173370 218.0	- 0.25 Clear	NTP ATIK 460exm	Nick Sioulas
Istanbul Univ., Istanbul, Turkey	+41.011749 +28.965718 60.0	İST40 0.4 Clear	NTP Moravian G2 8300	Süleyman Fişek, Oğuzhan Çakır
Athens University, Zografos, Greece	+37.968561 +23.783368 250.0	- 0.4 Clear	NTP ZWO ASI 290MM	Kosmas Gazeas
Eskisehir Univ., Eskisehir, Turkey	+39.8155* +30.5294* 785.0*	- 0.4 Clear	GPS FLI	Metin Altan
Ondokuz Mayıs Univ. Samsun, Turkey	+41.367727 +36.201576 150.0	- 0.37 Clear	GPS SBIG STL-4020M	Selami Kalkan

Table A.4: observational circumstances for all stations that detected 2002 MS_4 in a stellar occultation for the other eight events. The geographic coordinates for OPSPA and ASH2 are from horizons website.

Date	**Site/country (detection)**	**Latitude (° ' ") Longitude (° ' ") Altitude (m)**	**Telescope aperture (m) instrument**	**Exposure (s) cycle (s) time source**	**Observers**
09 July 2019	San Pedro de Atacama/CHL	22 57 11.4 S 68 10 47.6 W 2,396.9	OPSPA 0.4 Proline PL16803	2.0 ≈ 3.67 ?	Alain Maury, Joaquín Fábrega Polleri
		22 57 12.1 S 68 10 46.8 W 2,398.5	ASH2 0.407 SBIG STL11000	8.0 ≈ 10.5 NTP	Nicolás Morales
	Pico dos Dias/BRA	22 32 07.8 S 45 34 57.5 W 1,810.7	Perkin-Elmer 1.60 Andor Ixon 4269	0.3 ~1.65 GPS	Flavia L. Rommel, Rodrigo Boufleur
26 July 2019	San Pedro de Atacama/CHL	22 57 11.4 S 68 10 47.6 W 2,396.9	OPSPA 0.4 Proline PL16803	30.0 ≈ 31.9 ?	Alain Maury, Joaquín Fábrega Polleri
		22 57 12.1 S 68 10 46.8 W 2,398.5	ASH2 0.407 SBIG STL11000	25.0 ≈ 27.6 NTP	Nícolás Morales
	Paranal/CHL	24 36 57.9 S 70 23 26.0 W 2,479.2	SPECULOOS 1.0 Andor Tech	2.0 ≈ 4.0 ?	Emmanuel Jehin
	Pico dos Dias/BRA	22 32 07.78 S 45 34 57.5 W 1,810.7	Perkin-Elmer 1.60 Andor Ixon 4269	0.8 ≈ 0.813 GPS	Gustavo Benedetti Rossi
26 July 2019	Osoyoos/CAN	49 00 31.8 N 119 21 46.7 W 1,088.0	? ? QHY174M	2.0 2.0 GPS	Peter Ceravolo
19 August 2019	Victoria/CAN	49 32 02.0 N 119 33 27.0 W 0.0	Meade SCT 0.4 QHY174M	2.5 2.5 GPS	Bruce Gowe
	Osoyoos/CAN	49 00 31.8 N 119 21 46.7 W 1,088.0	? ? QHY174M	4.0 4.0 GPS	Peter Ceravolo
26 July 2020	Pretoria/ZAF	25 53 00.0 S 28 09 00.0 E 1,489.0	Celestron SCT 0.356 ZWOASI290MM	1.0 1.015 NTP	Clyde Foster
	Johannesburg/ZAF	26 06 20.0 S 27 57 03.0 E 1,547.0	- 0.305 ZWOASI290MM	2.0 2.015 NTP	Cory Schmitz
24 February 2021	San Pedro de Atacama/CHL	22 57 11.4 S 68 10 47.6 W 2,396.9	OPSPA 0.4 ZWO ASI6200MM Pro	10.0 ≈11.7 ?	Alain Maury, Joaquín Fábrega Polleri
		22 57 12.1 S 68 10 46.8 W 2,398.5	ASH2 0.407 SBIG STL11000	10.0 ≈12.8 NTP	Nicolás Morales
14 October 2021	Osoyoos/CAN	49 00 32.1906 N 119 21 46.268 W 0.0	? ? QHY174M	3.0 3.0 GPS	Peter Ceravolo
	Flagstaff/USA	35 12 10.4508 N 111 40 01.416 W 2216.0	Ritchey–Chrétien 0.318 CMOS	2.498 2.4996 GPS	Michael Collins
10 June 2022	Three Gate Farm/USA	33 20 51.5376 N 88 43 58.3114 W 93.05	Schmidt–Cassegrain 0.2 Atik 414ex via Ekos	5.0 5.4518 NTP	Jean-Francois Gout
	La Palma/ESP	28 45 45.0576 N 17 52 45.12 W 2387.63	Liverpool 2.0 Andor DW485 (RISE)	1.183 1.2226 NTP	René Duffard, Jose Luis Ortiz, Nicolás Morales
	Teide/ESP	28 18 00.00 N 16 30 34.92 W 2390.0	Artemis 1.0 Andor IKONL BEX2 DD	1.0 1.81 GPS	Emmanuel Jehin

Table A.5: observational circumstances for all stations that did not detect 2002 MS4 or had bad weather during the other seven stellar occultations. The geographic coordinates for SOAR are from the horizons website.

Date	Site/country (detection)	Latitude (° ' ") Longitude (° ' ") Altitude (m)	Telescope aperture (m) instrument	Exposure (s) cycle (s) time source	Observers
09 July 2019	Guaratinguetá/BRA (technical problems)	22 48 10.02 S 45 11 30.5 W 573.0	Meade LX200 0.4 SBIG ST7XME	- - -	Rafael Sfair, Thamiris Santana
	Ponta Grossa/BRA (negative)	25 05 22.2 S 50 05 56.4 W 909.0	Meade RC400 0.406 Merlin Raptor	1.5 1.5 GPS	Chrystian L. Pereira
	La Silla/CHL (bad weather)	29 15 32.1 S 70 44 01.5 W 2,375.0	NTT 3.58 SOFI	- - -	Emmanuel Jehin
	Cerro Pachón/CHL (bad weather)	29 15 39.5 S 70 44 21.1 W 2,693.9	SOAR 4.0 Merlin Raptor	- - -	Julio I. B. Camargo
	San Juan/ARG (negative)	31 47 54.7 S 69 17 44.1 W 2,552.0	CASLEO 2.15 PI-2040B	? ? ?	Luis A. Mammana, Eduardo F. Lajus
	Córdoba/ARG (negative)	31 21 24.58 S 64 35 34.41 W 864.0	? ? ?	? ? ?	Carlos A. Colazo
	Santa Rosa/ARG (negative)	36 38 16.0 S 64 19 28.0 W 182.0	- 0.3 ?	5.0 ? ?	Julio Spagnotto
26 July 2020	Sutherland/ZAF (bad weather)	32 22 32.0 S 20 48 38.9 E 1,750.6	? ? ?	? ? ?	Amanda Sickafoose
	La Reunion Island/FRA (bad weather)	? ? ?	? ? ?	? ? ?	Jean Paul, Piere Thierry
	Santa Rosa/ARG (bad weather)	36 38 16.0 S 64 19 28.0 W 182.0	? ? ?	? ? ?	Julio Spagnotto
		? ? ?	? ? ?	? ? ?	Aldo Javier Wilberger
24 February 2021	Cerro Pachón/CHL (negative)	29 15 39.5 S 70 44 21.1 W 2,693.9	SOAR 4.0 Merlin Raptor	1.0 1.0 GPS	Altair Gomes Júnior, Flavia L. Rommel, Julio I. B. Camargo
14 October 2021	North Carolina/USA (Negative ????????)	? ? ?	? ? ?	? ? ?	David Wake
	North Carolina/USA (Technical Problem)	? ? ?	? ? ?	? ? ?	R. Flynn
	Alberta/USA (Cloudy)	? ? ?	? ? ?	? ? ?	Phil Langill
	North Dakota/USA (Cloudy)	? ? ?	? ? ?	? ? ?	Sherry Fieber-Beyer
	Indiana/USA (Cloudy)	? ? ?	? ? ?	? ? ?	Adam W. Rengstor
	Illinois/USA (Cloudy)	? ? ?	? ? ?	? ? ?	Aart Olsen
	Idaho/USA (Cloudy)	? ? ?	? ? ?	? ? ?	Jason W. Barnes
	Kansas/USA (Cloudy)	? ? ?	? ? ?	? ? ?	Greg Rudnick
	New Mexico/USA (Cloudy)	? ? ?	? ? ?	? ? ?	Larry Molnar
	Ohio/USA (Cloudy)	? ? ?	? ? ?	? ? ?	Rush Swaney
	Oregon/USA (Cloudy)	? ? ?	? ? ?	? ? ?	Scott Fisher
	Montana/USA (Cloudy)	? ? ?	? ? ?	? ? ?	Bill Hanne

Appendix B

Stellar occultation light curves

This section provides the plots of all normalized light curves as a function of time (UTC). There are 80 light curves acquired during the nine stellar occultations observed between 2019 and 2021. Figures B.1, B.2, B.3, B.4 and B.5 presents the plots from the 8 August 2020 stellar occultation, plotted from the northernmost to the southernmost stations. Figures B.6 and B.7 show the 19 light curves from the other eight events. The black dots present the observational data and in red is the fitted model.

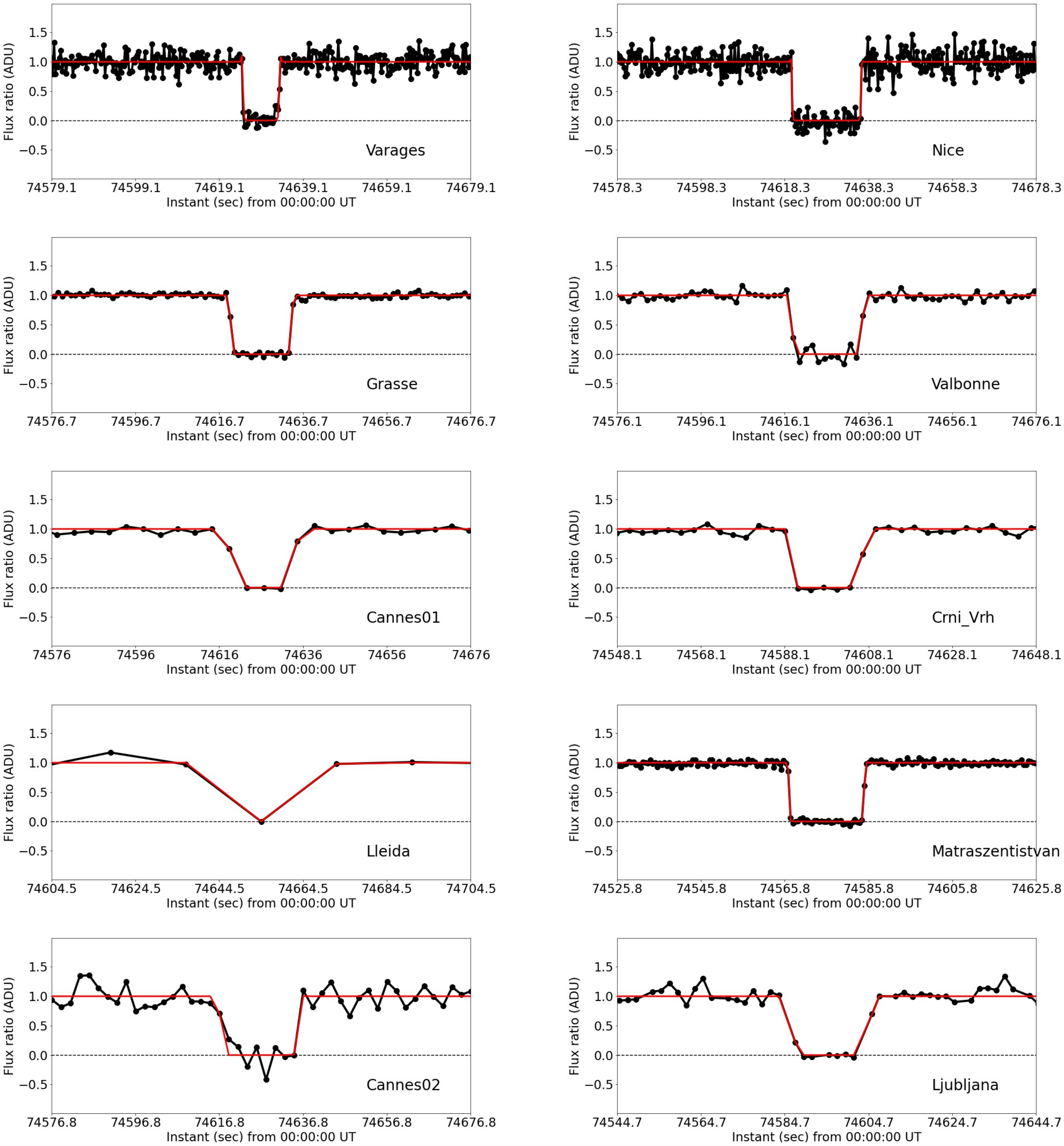

Figure B.1: the 61 normalized light curves, centered in the occultation instant, obtained on the 8 August 2020 campaign. The station that acquired the light curve is mentioned in each plot. Black points with uncertainties in red are the acquired data and blue line is the fitted model.

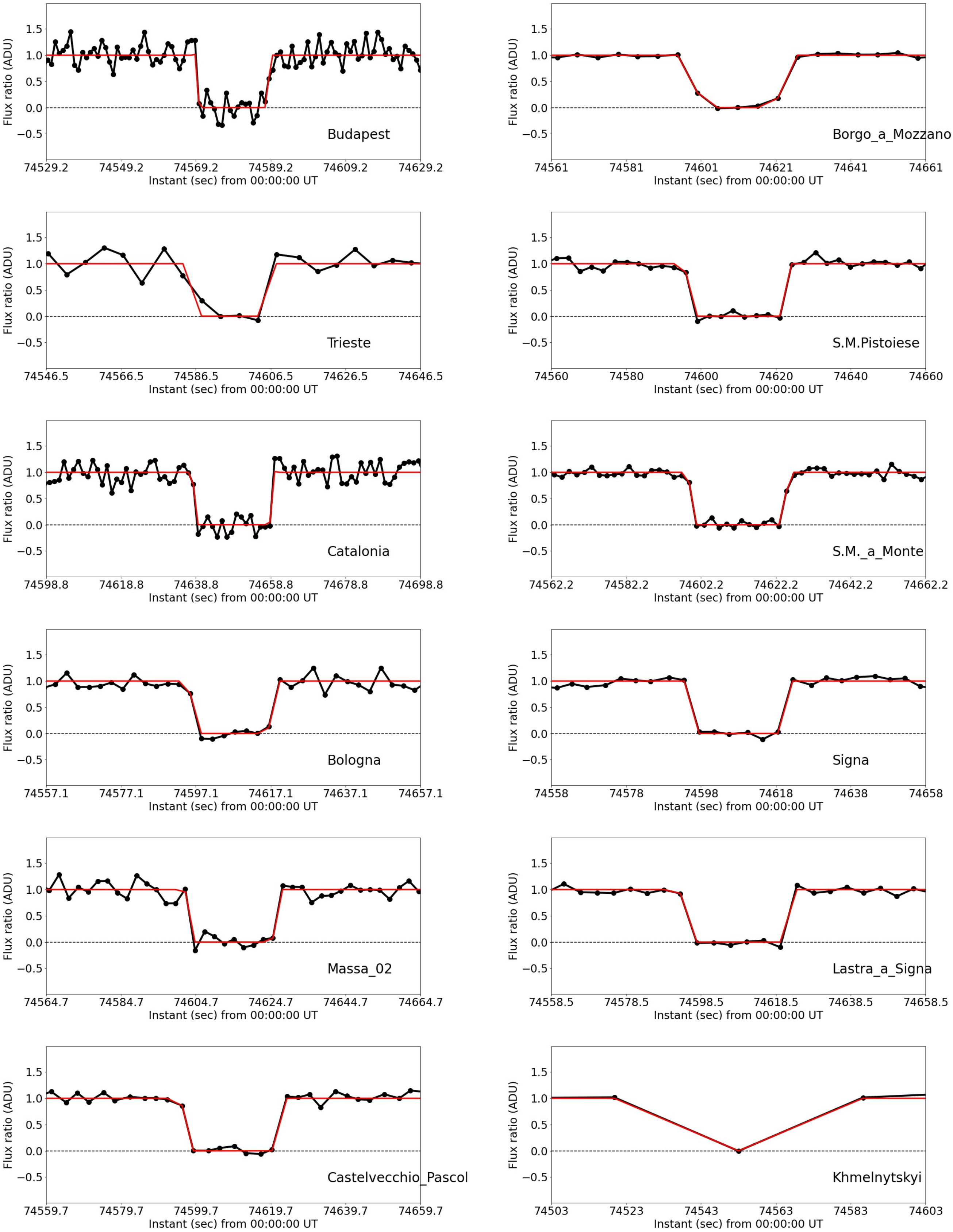

Figure B.2: Continue.

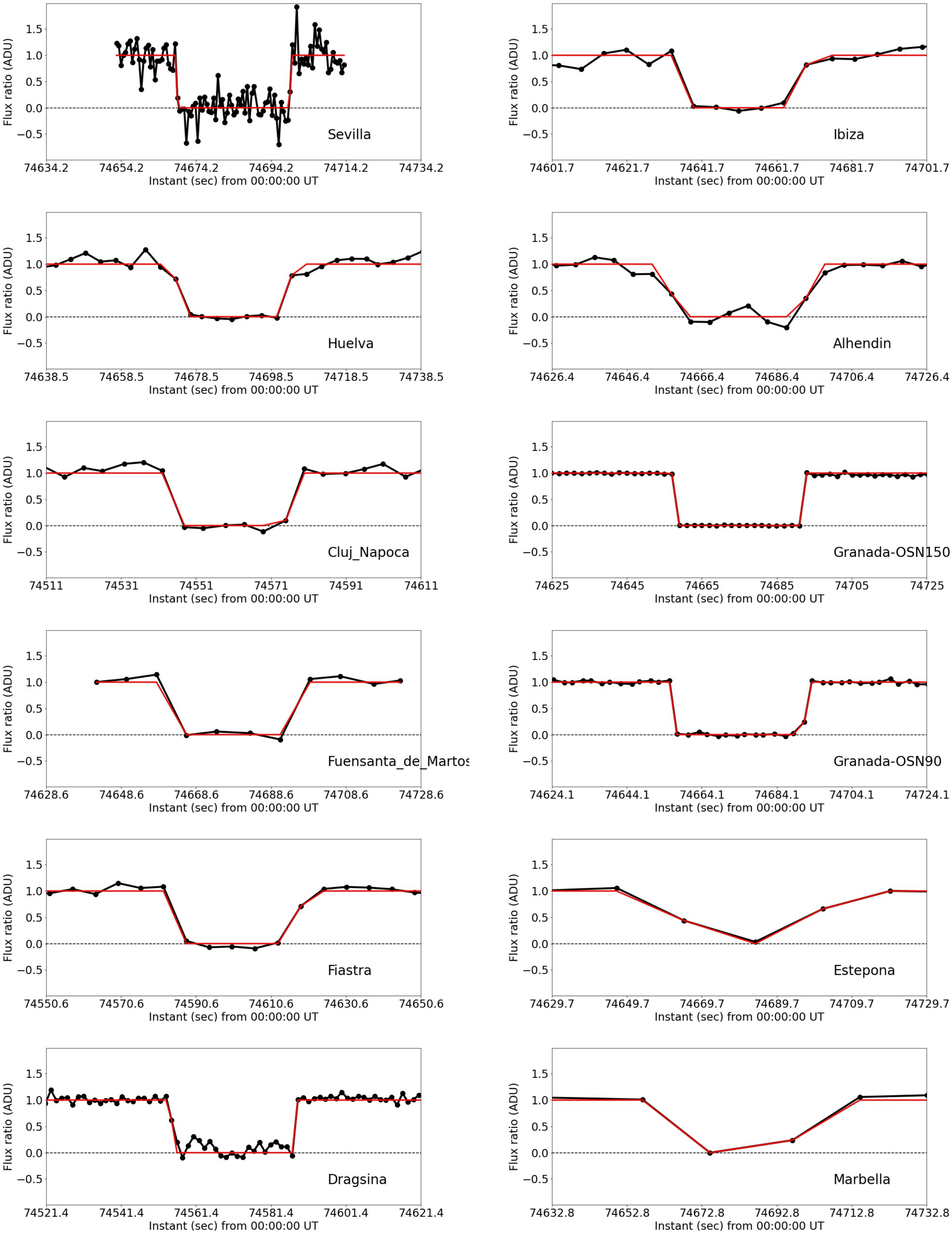

Figure B.3: continued.

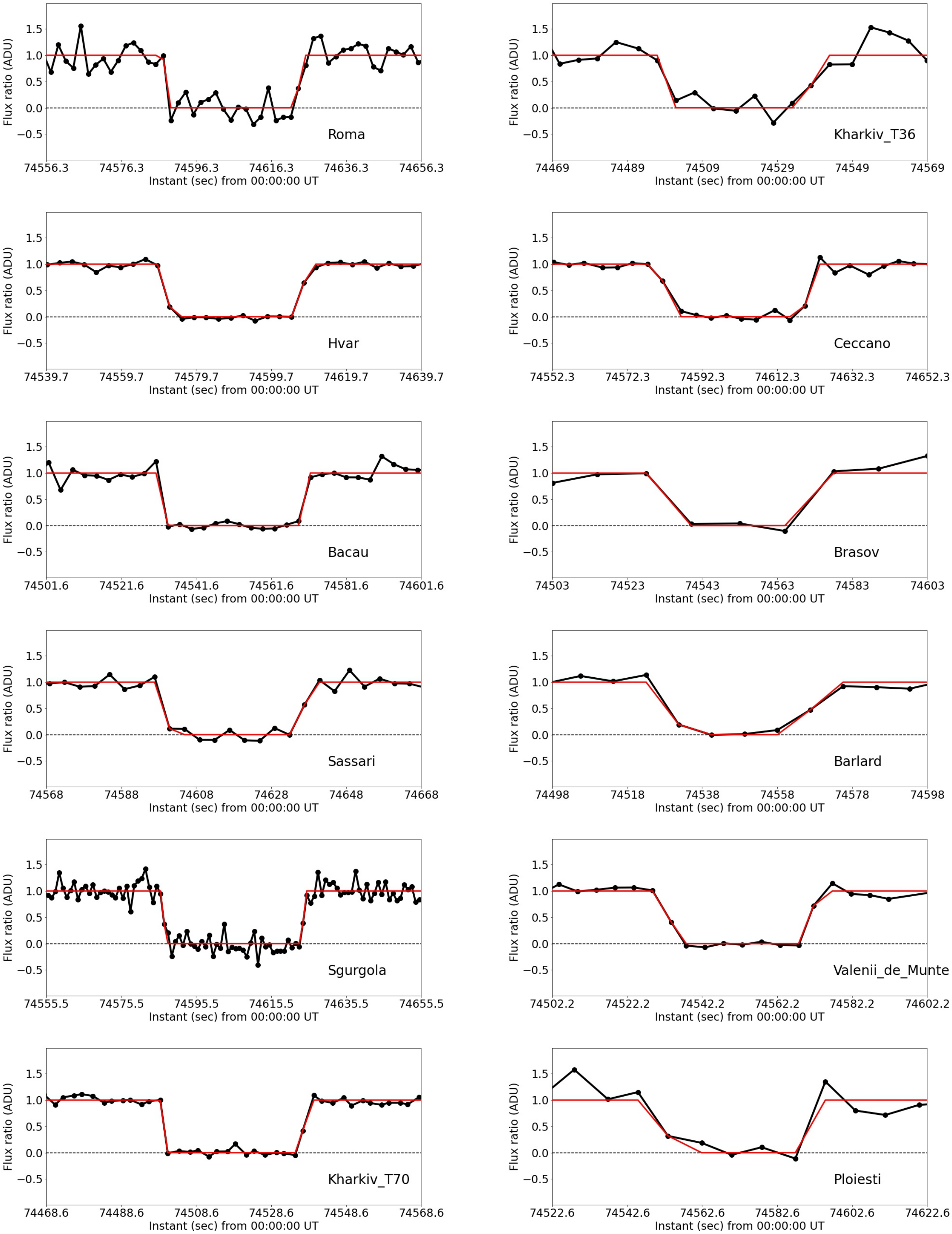

Figure B.4: continued.

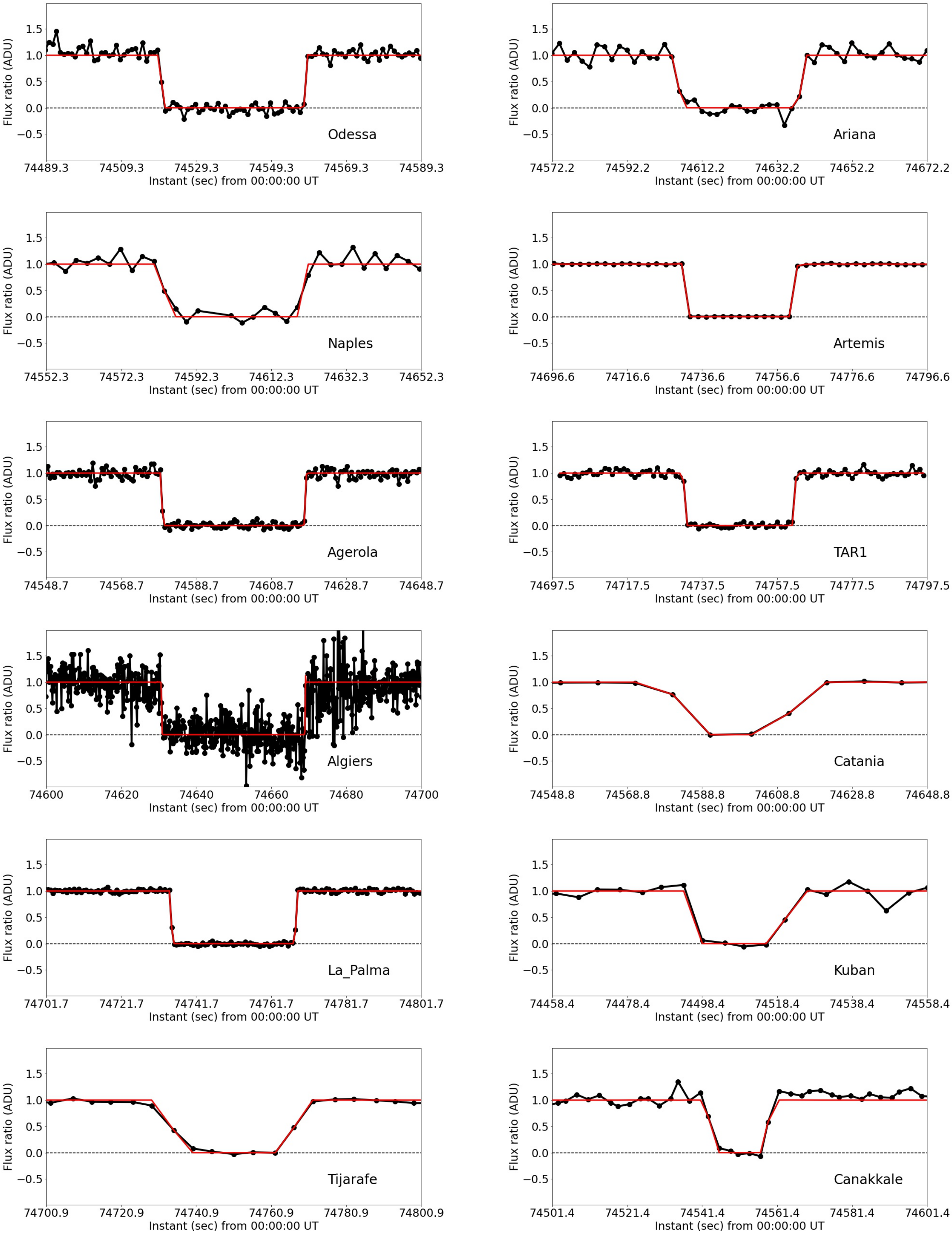

Figure B.5: continued.

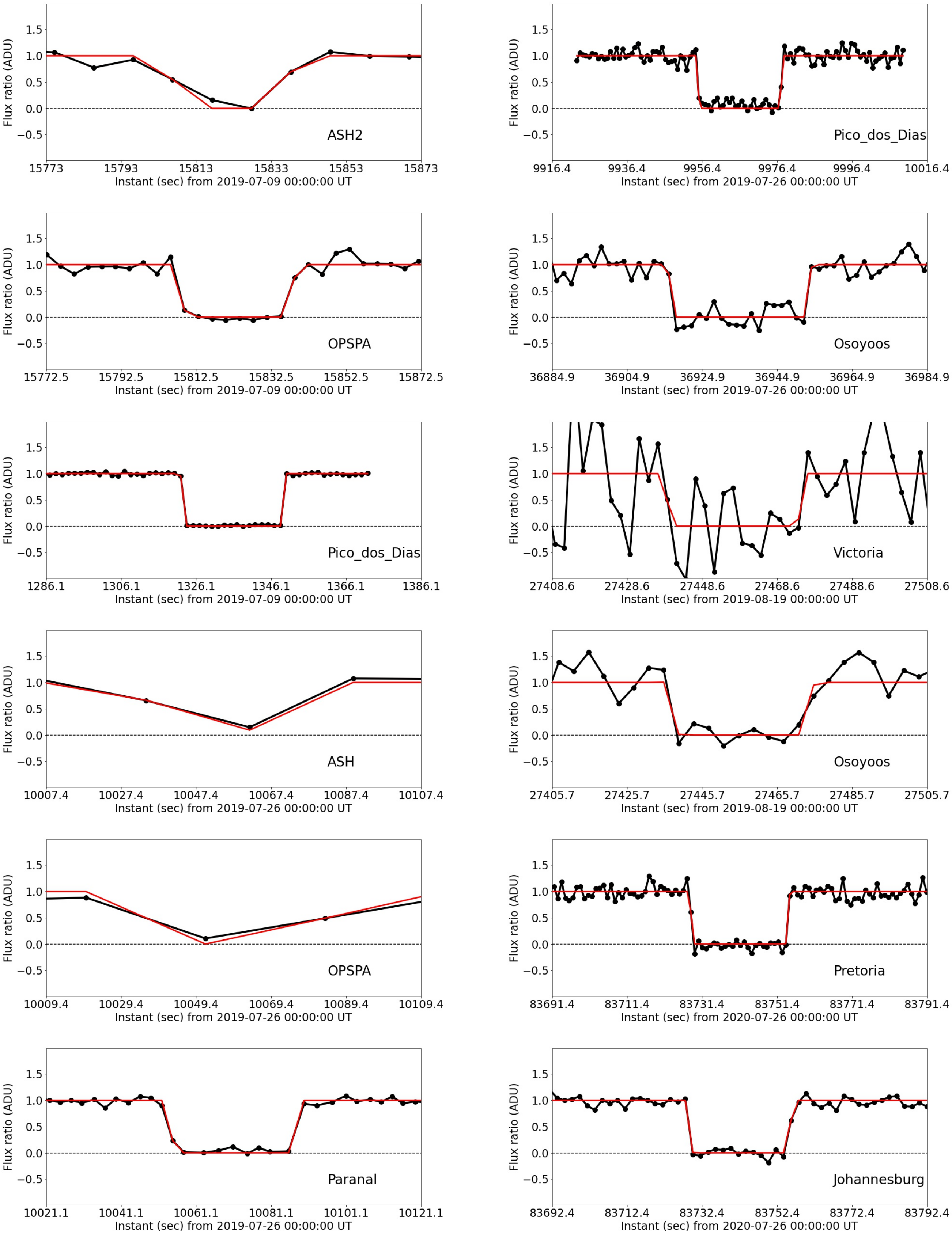

Figure B.6: Observed (black points) and calculated (red line) light curves for each site that observed a stellar occultation by 2002 MS_4, except the 8 August 2020 multi-chord event - see table A.4 for observational details.

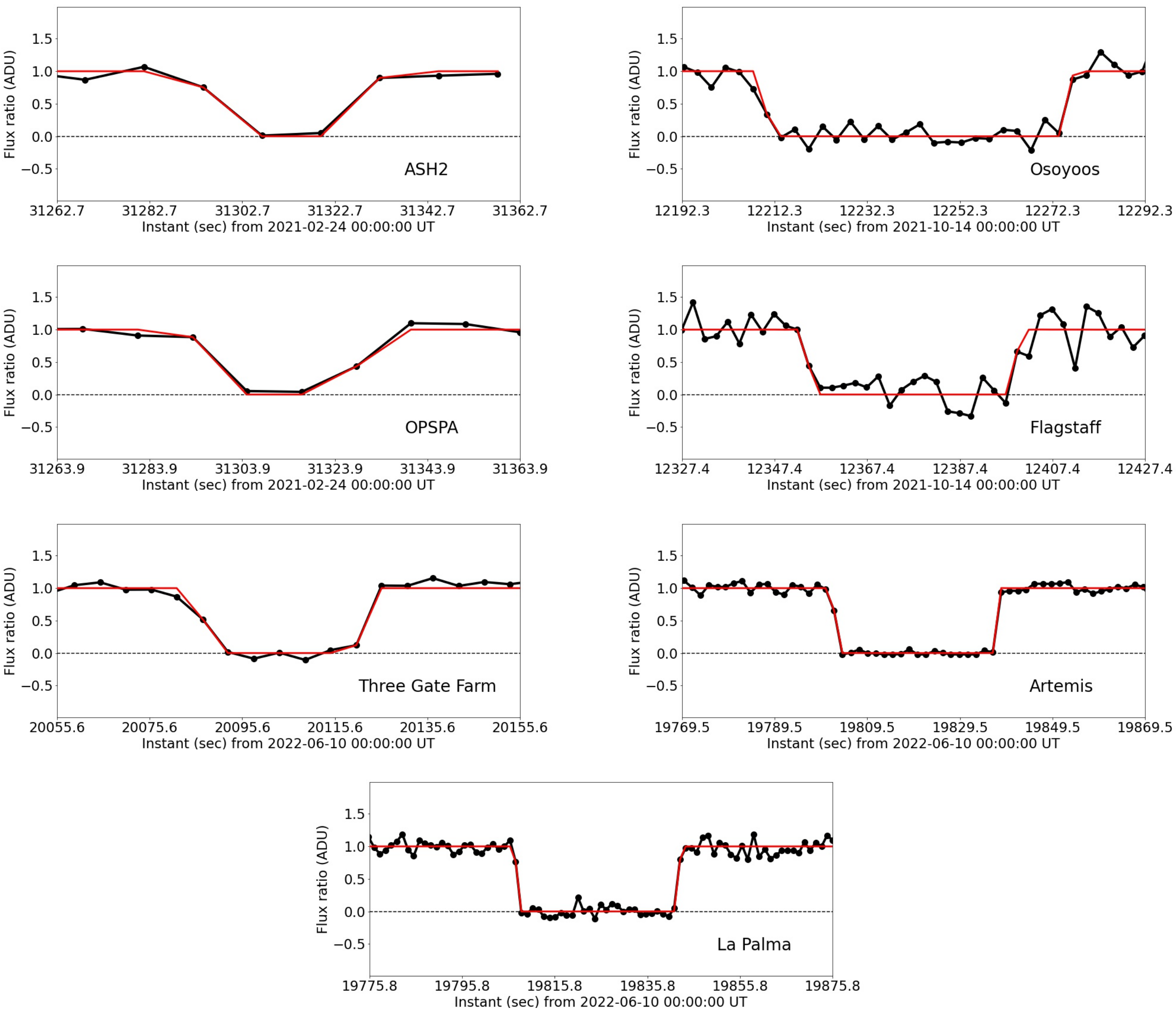

Figure B.7: Continue.

Appendix C

Stellar occultation instants

Table C.1: Star's dis- and re-appearance instants with 1σ error bars for 8 August 2020 positive chords.

Sites	**Immersion (hh:mm:ss.ss ± ss.ss)**	**Emersion (hh:mm:ss.ss ± ss.ss)**
Varages	20:43:44.871 ± 0.069	20:43:53.358 ± 0.032
Caussols	20:43:39.5 ± 2.0	20:43:51.5 ± 2.0
Grasse	20:43:39.477 ± 0.025	20:43:53.961 ± 0.028
Cannes 01	20:43:39.28 ± 0.14	20:43:54.17 ± 0.56
Budapest	20:42:49.58 ± 0.13	20:43:08.62 ± 0.21
Lleida	20:44:01.4 ± 6.6	20:44:19.6 ± 5.7
Nice	20:43:36.435 ± 0.068	20:43:52.83 ± 0.10
Cannes 02	20:43:37.21 ± 0.21	20:43:55.66 ± 0.40
Valbonne	20:43:37.384 ± 0.056	20:43:54.08 ± 0.13
Crni Vrh	20:43:09.75 ± 0.91	20:43:26.57 ± 0.34
Mátraszentistván	20:42:46.865 ± 0.023	20:43:04.735 ± 0.045
Ljubljana	20:43:06.783 ± 0.095	20:43:25.39 ± 0.42
Trieste	20:43:09.42 ± 0.67	20:43:27.30 ± 0.79
Catalonia	20:43:57.14 ± 0.20	20:44:17.83 ± 0.14
Bologna	20:43:17.40 ± 0.25	20:43:38.77 ± 0.67
Massa 01		
Massa 02	20:43:20.52 ± 0.39	20:43:43.84 ± 0.32
Castelvecchio Pascoli	20:43:18.037 ± 0.089	20:43:43.5 ± 1.4
Borgo a Mozzano	20:43:19.209 ± 0.077	20:43:42.83 ± 0.12
San Marcello Pistoiese	20:43:16.203 ± 0.072	20:43:42.6 ± 1.2
Sta. Maria a Monte	20:43:17.18 ± 0.13	20:43:42.31 ± 0.10
Signa	20:43:16.163 ± 0.078	20:43:40.33 ± 0.67

Table C.1 continued

Lastra a Signa	20:43:13.814 ± 0.083	20:43:41.9 ± 1.3
Khmelnytskyi	20:42:00.95 ± 0.012	20:42:49.7 ± 15.7
Sevilla	20:44:29.04 ± 0.13	20:44:59.40 ± 0.19
Huelva	20:44:32.71 ± 0.36	20:45:02.76 ± 0.28
Cluj-Napoca	20:42:25.0 ± 1.2	20:42:56.6 ± 0.30
Fuensanta de Martos	20:44:22.0 ± 3.0	20:44:55.0 ± 3.1
Fiastra	20:43:05.2 ± 1.8	20:43:37.87 ± 0.51
Dragsina	20:42:34.911 ± 0.092	20:43:07.83 ± 0.30
Ibiza	20:43:56.6 ± 1.8	20:44:28.54 ± 0.24
Alhendín	20:44:17.88 ± 0.57	20:44:54.84 ± 0.18
Sierra Nevada (150 cm)	20:44:17.569 ± 0.008	20:44:52.08 ± 0.52
Sierra Nevada (90 cm)	20:44:16.05 ± 0.47	20:44:51.769 ± 0.028
Estepona	20:44:24.15 ± 0.45	20:45:00.50 ± 2.0
Marbella	20:44:26.1 ± 4.3	20:45:59.64 ± 0.22
Roma	20:43:08.37 ± 0.37	20:43:43.79 ± 0.37
Hvar	20:42:51.69 ± 0.20	20:43:27.96 ± 0.35
Bacau	20:42:12.63 ± 0.35	20:42:50.48 ± 0.70
Sgurgola	20:43:03.86 ± 0.15	20:43:41.13 ± 0.15
Sassari	20:43:19.34 ± 0.36	20:43:56.60 ± 0.51
Kharkiv (70 cm)	20:41:40.00 ± 0.13	20:42:17.16 ± 0.12
Kharkiv (36 cm)	20:41:39.6 ± 1.9	20:42:18.3 ± 1.2
Ceccano	20:43:02.34 ± 0.41	20:43:40.86 ± 0.39
Brasov	20:42:14.2 ± 2.7	20:42:51.5 ± 1.6
Bârlad	20:42:09.21 ± 0.60	20:42:47.04 ± 0.49
Valenii de Munte	20:42:13.69 ± 0.24	20:42:51.08 ± 0.49
Ploiesti	20:42:14.24 ± 2.1	20:42:53.2 ± 1.5
Odessa	20:42:00.00 ± 0.14	20:42:38.49 ± 0.11
Naples	20:43:00.67 ± 0.30	20:43:37.7 ± 1.1
Agerola	20:42:59.607 ± 0.049	20:43:37.843 ± 0.093
Algiers	20:43:50.841 ± 0.021	20:44:29.115 ± 0.073
La Palma	20:45:35.037 ± 0.013	20:46:08.314 ± 0.019
Tijarafe	20:45:35.68 ± 0.19	20:46:08.10 ± 0.10
Ariana	20:43:23.85 ± 0.29	20:43:56.81 ± 0.25
Artemis	20:45:31.944 ± 0.035	20:46:01.295 ± 0.021
TAR 1	20:45:32.359 ± 0.057	20:46:01.592 ± 0.064
TAR 2		
Catania	20:43:04.60 ± 0.92	20:43:34.561 ± 0.072

Table C.1 continued

Kuban	20:41:36.2 ± 1.2	20:42:00.62 ± 0.30
Çanakkale	20:42:23.41 ± 0.54	20:42:38.815 ± 0.071

Table C.2: Star's dis- and re-appearance instants with 1σ error bars for the other eight stellar occultations events.

Date	**Sites**	**Immersion (hh:mm:ss.ss ± ss.ss)**	**Emersion (hh:mm:ss.ss ± ss.ss)**
09 July 2019	OPSPA	04:23:28.64 ± 0.19	04:23:58.26 ± 0.39
	ASH2	04:23:27.2 ± 1.1	04:23:56.75 ± 2.1
	Pico dos Dias	04:22:02.85 ± 0.69*	04:22:29.44 ± 0.67
26 July 2019	OPSPA	02:47:15.7 ± 7.8	02:48:04.1 ± 3.7
	ASH2	02:47:20.9 ± 4.1	02:47:54.8 ± 5.4
	Paranal	02:47:34.33 ± 0.12	02:48:07.9 ± 1.4*
	Pico dos Dias	02:45:55.315 ± 0.097	02:46:17.586 ± 0.092
26 July 2019	Osooyos	10:15:16.91 ± 0.48	10:15:52.65 ± 0.27
19 August 2019	Osooyos	07:37:17.54 ± 0.55	07:37:53.7 ± 2.0
	Victoria	07:37:19.2 ± 2.6	07:37:55.2 ± 1.3
26 July 2020	Pretoria	23:15:28.46 ± 0.12	23:15:54.27 ± 0.15
	Johannesburg	23:15:28.940 ± 0.093	23:15:55.89 ± 0.18
24 February 2021	ASH2	08:41:36.82 ± 0.98	08:42:08.45 ± 0.30
	OPSPA	08:41:37.00 ± 0.61	08:42:09.173 ± 0.089
14 October 2021	Osoyoos	03:23:30.13 ± 0.40	03:24:35.32 ± 0.68
	Flagstaff	03:25:54.60 ± 0.44	03:26:39.34 ± 0.73
10 June 2022	Three Gate Farm	05:34:47.18 ± 0.33	05:35:22.12 ± 0.28
	La Palma	05:30:08.475± 0.091	05:30:43.30 ± 0.13
	Artemis	05:30:02.427 ± 0.066	05:30:37.51 ± 0.49

Appendix D

Observing proposal submitted to SOAR

Here is the proposal to observe 2002 MS_4 from the SOAR in the second semester of 2020. It was approved in the 11th position among the 21 submitted projects with 45.54 points. The board granted 22 h of observations divided into four observational nights. We arranged the nights carefully to avoid background star contamination on the images. However, with the outbreak of the COVID-19 pandemic in 2020, the observatory was closed, and no observations were made. Therefore, we do not have images related to this proposal.

Proposal ID : ____________
Data Received : ___/___/______

SOAR TELESCOPE - Brazilian National Office

Observing Time Application Form (Ver. 2.4)

Semester: *2020B* (Aug/2020 - Jan/2021)

A.M.(<=)	Any	**Moon P.**	Bright
Image Quality	Seeing < 1.3 "		
Cloudy Cover	Photometric		

Title of Proposal: ***Rotational light curve for full shape characterization of 2002 MS4***

Observing Mode: Remote/Classical mode

Principal Investigator: Flavia Luane Rommel

PI Affiliation: ON

PI Email: flaviarommel@on.br

PI Phone: +55 46 99923 9822

Co-authors

Name	Affiliation	E-mail
Felipe Braga Ribas	*UTFPR / DAFIS*	*ribas@on.br*
Julio Ignacio Bueno de Camargo	*ON*	*camargo@on.br*
Roberto Vieira Martins	*ON*	*rvm@on.br*
Rodrigo Boufleur	*ON*	*rcboufleur@gmail.com*
Marcelo Assafin	*ObservatÃ³rio do Valongo / UFRJ*	*massaf@astro.ufrj.br*
Gustavo Benedetti Rossi	*Observatoire de Paris-Meudon*	*gugabrossi@gmail.com*
Bruno Eduardo Morgado	*Observatoire de Paris-Meudon*	*morgado.fis@gmail.com*
Altair Ramos Gomes Junior	*UNESP/Guaratingueta*	*altairgomesjr@gmail.com*
Bruno Sicardy	*Observatoire de Paris-Meudon*	*bruno.sicardy@obspm.fr*
Colin Snodgrass	*R.O. Edinburgh*	*csn@roe.ac.uk*

Is there a thesis or dissertation that will benefit from the data?: YES

Student	Degree
Flavia Luane Rommel	PhD student

Abstract:

We propose the observation of the Trans-Neptunian Object (TNO) 2002 MS4 to determine its rotational light curve to allow its full 3D shape characterization. Candidate to be a dwarf planet, 2002 MS4, is one of the biggest hot classical TNOs, and no rotational light curve has ever been published. We have detected four stellar occultations by this object in 2019 which allowed constraining its limb size and shape. We aim to obtain its rotation light curve a few days before the next two good stellar occultation events that will cross Europe on August 08th, and South America on September 03rd, allowing to link the rotation phase with the detected limb. With that, we will be able to derive the first three-dimensional figure for this big TNO. These objects are known as leftovers of the solar system formation, therefore understand their physical properties help the understand of a much broader picture of the formation of our planetary system.

Time requested: 28 hours.

Minimum time accepted: 22 hours.

Instruments:

Instrument	**Camera**

Goodman (Imaging)	Red Camera

Instrument	Filter	Grating	Slit
Goodman (Imaging)	R		

Optimal dates:

2020AUG05, 2020AUG09, 2020AUG11, 2020AUG12, 2020SEP04, 2020SEP07

Impossible dates:

Any other

Scientific category: *Solar System*

Previous missions of this proposal with the SOAR Telescope:

This proposal has not been submitted before.

Previous missions of other proposals with the SOAR Telescope:

- 2020A: No observations so far (and perhaps no observations at all due to a pandemic COVID-19).
- 2019B-008: Chariklo's rotation light curve for 3D shape characterization: Data acquired but high seeing and pointing limitations prevented to attain the proposal objective.
- 2019B - Occultation by (3793) Leonteus (large Jupiter Trojan). SOAR got a **positive detection**, giving a lower limit to the object's size, other sites did not observe (overcast). An event by Quaoar could not be observed due to bad weather and instrumental problems. A first event by (60558) Echeclus was lost by little as SOAR was at the southern border of the shadow. Such events are useful to impose upper limits in the dimensions of the body. A second event by Echeclus was **positive** at SOAR and from another site in the south. Analysis of data are on its way, which will provide size and ring detection limits.
- SO2019A-003: stellar occultation events by Quaoar, Phoebe and 2002 MS4 were observed. Quaoar observation was positive and is under analysis. The event by Phoebe was negative to SOAR. Predictions indicates a grazing event for Phoebe in 2019A within uncertainties. The observation however worth trying because a negative chord close to the body is very useful to set upper limits to its dimensions. 2002 MS4: SOAR, NTT, Pico dos Dias (OPD), San Pedro de Atacama, UNESP, UEPG, CASLEO, Córdoba, El catalejo and Cerro Burek tried to observe the event. Positive detections were obtained from San Pedro de Atacama and OPD, negative chords from UEPG, CASLEO, Cordoba, El Catalejo and Cerro Burek. SOAR were overcast (but SOAR was outside the shadow path anyway - see left side of figure 1).
- SO2018B-003: Two events successfully observed in June (Phoebe) and July (2010 EK_{139}). Very good light curves were obtained, using visitor instrument. A paper using Phoebe observations has been published [5].
- SO2015A-015: we got 5 hours as payback which were used to obtain a new Chariklo light curve (using SOI), in a different epoch from previous observations and is published [6].
- Observations related to the preparation for the flyby of the TNO (486958) 2014 MU69 by New Horizons (NOAO time at SOAR using the visitor instrument - Raptor camera). CONTROL ID: 2817945, submitted to the DPS - Division of Planetary Sciences, American Astronomical Society, 2017.
- Discovery of the first ring system around a small solar system object: "A ring system detected around the Centaur (10199) Chariklo", Braga-Ribas et al. (2014), Nature, DOI: 10.1038/nature13155 [8].

Previous results in the field by the Principal Investigator:

1. "The Trans-Neptunian Object (84922) 2003 VS_2 through Stellar Occultations", Benedetti-Rossi, G.; Santos-Sanz, P.; Ortiz, J. L.; Assafin, M.; Sicardy, B. et al. (2019), The Astronomical Journal, DOI: 10.3847/1538-3881/ab3b05

2. "Database on detected stellar occultations by small outer Solar System objects", Braga-Ribas, F.; Crispim, A.; Vieira-Martins, R.; Sicardy, B.; Ortiz, J. L.; Assafin, M. et al. (2019), Journal of Physics: Conference Series, Volume 1365, Issue 1, article id. 012024. DOI: 10.1088/1742-6596/1365/1/012024

3. "First stellar occultation by the Galilean moon Europa and upcoming events between 2019 and 2021", Morgado, B.; Benedetti-Rossi, G.; Gomes-Júnior, A. R.; Assafin, M.; Lainey, V. et al. (2019), Astronomy & Astrophysics, DOI: 10.1051/0004-6361/201935500

4. "The size, shape, density and ring of the dwarf planet Haumea from a stellar occultation", Ortiz, J.L., et al. (2017), Nature, DOI:10.1038/nature24051

Publications:

Not related to this proposal since it is its first submission. Nevertheless they are relevant for this proposal, as they use data obtained with SOAR, and have the PI or at least one of the co-authors participation.

5. "The first observed stellar occultations by the irregular satellite Phoebe (Saturn IX) and improved rotational period", Gomes-Júnior, A. R.; Assafin, M.; Braga-Ribas, F.; Benedetti-Rossi, G.; Morgado, B. E. et al. (2020), Monthly Notices of the Royal Astronomical Society, DOI: 10.1093/mnras/stz3463

6. "Size and shape of Chariklo from multi-epoch stellar occultation", Leiva, R., Sicardy, B., Camargo, J. I. B., et al. (2017), AJ, DOI:10.3847/1538-3881/aa8956

7. "The Centaur 10199 Chariklo: investigation into rotational period, absolute magnitude, and cometary activity", Fornasier et al. (2014), A&A, DOI:10.1051/0004-6361/201424439

8. "A ring system detected around the Centaur (10199) Chariklo", Braga-Ribas,et al. (2014), Nature, 508, 72.

Scientific Case

Trans-Neptunian Objects (TNOs) are a class of small Solar System bodies that orbit the Sun with semi-major axis larger than that of Neptune [9]. Due to the low spatial density of material in this orbital region and significant distance from the Sun, these bodies do not experience a high surface differentiation. They are thought to be remnants of the primordial disk and an invaluable source of information about the primitive solar nebula as well as about the Solar System history and evolution [10][11]. Besides that, the determination of the size-frequency distribution of TNOs allows constraining the Solar System formation models [12].

Dynamically classified as a hot classical, 2002 MS_4 has an equivalent diameter of 934 $\pm$ 47 km derived from thermal data [13] and is a dwarf planet candidate. Stellar occultations can provide precise measurements of the object's limb size and shape in the observed instant. On 2019 July 09, our collaboration in South America observed the first stellar occultation by 2002 MS_4, with two positive detections. Just a few days later, on July 26, in the same region, three positive chords were observed. The preliminary results (Figure 1) show a smaller object with an equivalent diameter of 773.5 $\pm$ 2.7 km, under the assumption of Maclaurin equilibrium figure. Other single and double-chord occultations were observed from Canada on July 26 and August 19, respectively. These four events were used to derive astrometric positions, and thus improving the accuracy of the forthcoming occultation events, especially those occurring on August, 8th 2020, observable from Europe, and September 03rd, from South America.

Up to this date, there is no rotational light curve published in the literature. If its rotation light-curve is caused only by albedo variegation, it will present an amplitude in the magnitude of just a few percents, which can be considered a lower limit. The knowledge of the light curve's amplitude and phase during the coming occultation events will impose significant constraints to derive its complete three-dimensional figure [1]. If the rotational light curve and the limb figure observed in 2020 is compatible with an oblate model, it will strengthen the assumption of a Maclaurin body as made for the observed occultation events. Thus its volume and density will be obtained.

Scientific Impact

The determination of the size-frequency distribution (SFD) of TNOs is important to constraint the Solar System models for dynamical evolution. The larger bodies originated from accretion processes, while the smaller ones are the result of collisional evolution [12]. Besides that, the Nice model can not fully explain the details about the distribution of hot and cold classical TNOs [12].

In this context, obtaining physical constraints of a hot classical TNO does help to improve our knowledge about this population. We already started this study using stellar occultation data from 2019, and some preliminary results are present in figure 1. Assuming a Maclaurin equilibrium shape to 2002 MS_4, we computed size and shape solutions. With an equivalent diameter of 773.5 $\pm$ 2.7 km and an apparent flattening of 0.155 $\pm$ 0.015, this object seems to be smaller than previous calculations from thermal data. With a rotational light curve, we most likely will be able to confirm, or dismiss, if this big TNO has a Maclauring equilibrium shape. Furthermore, if successful, this may become the first time that the rotational parameters of 2002 MS_4 will be published.

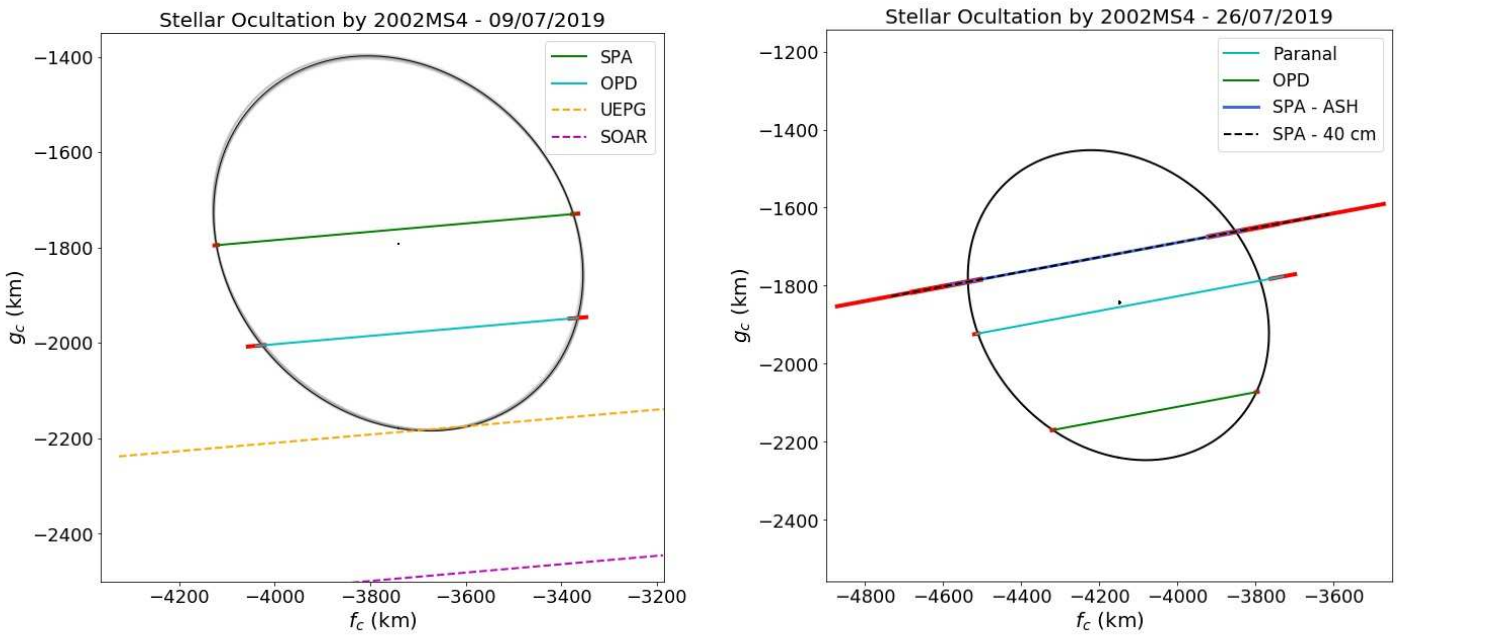

Figure 1: Ellipses fitted to both stellar occultations data sets acquired on 2019, in black the best fit to the chords; gray ellipses are the possible solutions considering all the available chords (positive and negative). Green, blue and cyan lines are the positive chords and the error bars are present in red. The dashed lines are negative chords, which helped to restrict the ellipse parameters.

References

9. Jewitt, D.; Morbidelli, A.; Rauer, H., 2008, in “Trans-Neptunian Objects and Comets”, Saas-Fee Advanced Course 35, 2008 XII.

10. Gladman, B.; Marsden, B. G.; Vanlaerhoven, C., 2008, in “The Solar System Beyound Neptune”, M. A. Barucci, H. Boehnhardt, D. P. Vruikshank, and A. Morbidelli, University of Arizona Press.

11. Morbidelli, A., Levison, H. F., Gomes, R., 2008, in “The Solar System Beyond Neptune”, ed. M. A. Barucci, H. Boehnhardt, D. P. Cruikshank, A. Morbidelli, 275.

12. Petit, J.-M., Kavelaars, J. J., Gladman, B., Loredo, T. 2008, in “The Solar System Beyond Neptune”, University of Arizona Press, Tucson, 71

13. Vilenius, E.; Kiss, C.; Mommert, M. et al. 2012, “A & A”, 541, A94.

14. Scargle, J. D. 1982, “ApJ”, 263, 835

15. Stellingwerf R. F., 1978, “ApJ”, 224, 953

Technical Justification

We request 28 observation hours (22 hours on target plus 6 hours of calibrating fields and overheads) with Goodman RED (imaging), to measure the rotational light curve of 2002 MS_4 on dates close to two stellar occultation events predicted to occur on August 08th and September 03rd, 2020. The times are essential to allow linking the rotational phase with the limb obtained from the occultation events. As the target is crossing the galactic plane, it is not rare that to find it blended to a background star. To avoid this issue, we adopt an observing window strategy. We searched for periods where the object's apparent sky path yields none (or minor) contamination from surrounding sources. Six different time intervals ranging from two to six hours, adding up 22 hours of on-target observation were selected (see object list), which is the minimum time needed to accomplish this project. We request six additional hours to obtain field calibration images to perform difference image analysis - DIA [7]. Considering ten images per field with exposures of 5 minutes each, we will need a bit over 5 hours, plus about 1 hour of overheads.

TNO's rotation period averages around 8 hours, and therefore the time would allow covering all rotational phase space. The strategy adopted will enable us to achieve high precision once it includes around 240 rotation cycles of a typical TNO during the period requested. Such a time coverage allows high accuracy on the period determination and, therefore, lower errors on the propagation of the TNOs observed phase during occultations. The target's apparent V magnitude between August and September 2020 will be around 20.4. Hence, we intend to use exposure times of at least 290 seconds (obtained with ETC for SOI instrument)[1] to achieve an $SNR > 120$ and therefore allowing precisions at the order of 0.01 mag. However, higher exposures might be needed. The R filter is chosen as it gives a good compromise between flux and image quality. The object list contains the target's position at the beginning of each observational interval, where the observable conditions are most favourable.

After traditional flat and dark calibrations, we will process the images for background subtraction using difference image analysis (DIA) as done in [7]. The DIA is the procedure where a master image of the field is generated to subtract background stars. The preferred way to obtain this image is to point the telescope to the same FOV (ideally with the same airmass) when the object is not present. Otherwise, it is possible to generate the master from the sum of all science images on the same night, knowing that the target object is a moving one.

To build the light curve and to measure the rotation period, we will use differential photometry to measure the fluxes once the technique already accounts for common variations that affect all objects on the image. Once the light curve is built, we will search for periodic signatures in the data using standard time series analysis techniques. Well tested methods available to analyze unevenly spaced data are the Lomb-Scargle periodogram [14] and the Phase Dispersion Minimization [15]. Parameter uncertainties will be approached with Monte Carlo techniques. Once we have the light curve properties such as period and rotation phase modulation, we will build a model using the phase folded data and propagate the rotation template to the instant of the occultations to aid in the derivation of its three-dimensional shape [1].

Special Instruments Requirements

No special requirements.

[1] Available on https://www.noao.edu/gateway/ccdtime/

Objects List.

Object	A.R.(h,m)	Dec.(deg)	Mag.	Band	Comments
2002MS4	18:47:39.944	-06:15:47.833	20.36	R	2020-Aug-06 (00:30 - 03:30 UT)
2002MS4	18:47:26.109	-06:16:49.052	20.37	R	2020-Aug-10 (00:00 - 04:00 UT)
2002MS4	18:47:19.465	-06:17:21.227	20.37	R	2020-Aug-12 (00:00 - 06:00 UT)
2002MS4	18:47:15.952	-06:17:39.031	20.38	R	2020-Aug-13 (02:00 - 05:00 UT)
2002MS4	18:46:19.473	-06:24:43.444	20.41	R	2020-Sep-05 (00:30 - 04:30 UT)
2002MS4	18:46:14.950	-06:25:42.897	20.42	R	2020-Sep-07 23:50 UT / 2020-Sep-08 02:20 UT
FOV_AUG06	18:47:39.944	-06:15:47.833	20.4	R	DIA Calibration
FOV_AUG10	18:47:26.109	-06:16:49.052	20.4	R	DIA Calibration
FOV_AUG12	18:47:19.465	-06:17:21.227	20.4	R	DIA Calibration
FOV_AUG13	18:47:15.952	-06:17:39.031	20.4	R	DIA Calibration
FOV_SEP05	18:46:19.473	-06:24:43.444	20.4	R	DIA Calibration
FOV_SEP07	18:46:14.950	-06:25:42.897	20.4	R	DIA Calibration

Appendix E

Paper in preparation

Here is the draft of the paper in preparation for 2002 MS_4. The results regarding the nine stellar occultation events, as described in this thesis, are compiled in the text. However, the rotational analysis described above is outside the scope of this publication and needs more data to be confirmed.

The size, shape, and topography of (307261) 2002 MS_4 from multiple stellar occultations

F. L. Rommel[1,2], F. Braga-Ribas[3,1,2], J. L. Ortiz[4], B. Sicardy[5], P. Santos-Sanz[4], J. Desmars[6,7], E. Fernández-Valenzuela[8], B. E. Morgado[9,2,1], R. C. Boufleur[1,2], G. Benedetti-Rossi[10,5,2], R. Vieira-Martins[1,2,9], M. Vara-Lubiano[4], J. I. B. Camargo[1,2], N. Morales[4], R. Duffard[4], A. R. Gomes-Júnior[11,10,2], M. Assafin[9,2], Y. Kilic[12,13], G. Margoti[3,2], C. L. Pereira[1,2], B. Holler[14], M. Rodríguez-Marco[15], E. Frappa[16], J. Marques-Oliveira[5], J. Lecacheux[5], E. Jehin[17], A. Maury[18], J. Fábrega-Polleri[19], P. Ceravolo[20], D. Albanese[21], R. Anghel[22], D. Baba-Aissa[23,24], P. Bacci[25], R. Bacci[26], M. Bachini[27], V. Baldini[28], R. Behem[29], M. Bertini[30], M. Bigi[31], J. M. Bosch-Ignés[32], A. Burdanov[33], J. F. Calvo-Fernández[34], D. Carosati[35], J. Carrillo-Gómez[36], A. J. Castro-Tirado[37], A. Catanzaro[38], O. Çakır[39], V. Chiorny[40], F. Ciabattari[41], A. Ciarnella[42], A. Cikota[43], S. Cikota[43], M. Collins[44], M. Conjat[21], I. Coretti[28], C. Costa[45], B. Csak[46], F. Cuevas[48], L. Curelaru[49], I. de la Cueva[50], C. A. Danescu[51], T. O. Dementiev[17], B. Dintinjana[17], R. Fafet[17], E. J. Fernández-García[37], S. Fişek[39], C. Foster[17], A. Frasca[38], R. M. Gherase[17], J. F. Gout[17], B. Gowe[17], M. D. Grazia[25], Z. Gringahcene[17], E. Guido[17], L. Hudin[17], G. Iafrate[28], G. Isopi[17], A. L. Ivanov[17], V. A. Ivanov[17], N. B. Ivanova[17], A. Juravle[17], S. Kamoun[17], V. Kashuba[24], A. Klotz[17], N. Koshkin[24], O. M. Kozhukhov[17], Y. Krugly[40], S. Lamina[17], G. Leto[38], J. Licandro[17], J. M. Madiedo[17], M. Maestripieri[25], M. Mannucci[17], P. D. Marcantonio[28], H. Mariey[16], G. Masi[17], H. Mikuž[28], N. Montigiani[17], M. Moreno-Yuste[50], L. Morrone[17], S. Özer[40,41], A. Pál[46], J. L. Plouvier[17], J. P. Prost[29], S. Renner[17], M. Rodríguez-Alarcón[15], N. Ruocco[17], D. Ruždjak[43], M. Sánchez-González[43], C. Schmitz[17], C. Schnabel[37,36], M. Schnabel[36], M. Serra-Ricart[17], F. Signoret[38], I. Slyusarev[40], L. Stoian[17], M. D. Sora[17], A. Sota[17], G. Succi[27], R. Szakáts[33], U. Tagliaferri[17], A. Valvasori[17], A. Vîntdevară[17], R. Zanchez[38], A. Zheleznyak[17], V. Zhukov[17], M. Emílio[44], D. Nardiello[29,30], T. Santana[17], M. N. Bagiran[17], M. Bento[17], M. Borkowski[17], M. Boutet[17], V. Burwitz[17], W. Burzynski[17], L. Buzzi[17], W. Bykowski[17], G. B. Casalnuovo[17], J. J. Castellani[17], C. A. Colazo[17], G. Dangl[17], P. Delincak[17], X. Delmonte[17], H. Er[17], O. Erece[17], S. Eryilmaz[17], J. Ferreira[17], M. Ferreira[17], B. Gährken[17], G. Gianni[17], R. Gonçalves[17], K. Guhl[17], K. Hornoch[22], M. Husárik[17], B. Klempt[17], O. Kloes[17], R. Komžík[25], J. Kubánek[17], E. F. Lajus[17], M. Lavayssiere[17], L. A. Mammana[17], A. Marciniak[26], S. Meister[17], Z. Moravec[17], T. Müller[17], W. Ogloza[17], A. Ossola[31], A. Pascal[17], L. Perez[17], J. Polak[17], T. Pribulla[17], M. Rottenborn[17], L. Rousselot[17], J. Sanchez[17], M. Schmidt[17], M. Serrau[17], E. Sonbas[17], J. Spagnotto[17], P. Sybilski[17], M. Tekeş[17], D. Tomko[17], M. Urbaník[17], C. Weber[17], N. Wuensche[17], and

(Affiliations can be found after the references)

Last version: November 26, 2022

ABSTRACT

Context. The physical properties of the trans-Neptunian Objects are essential for improving our understanding of the solar system's formation and evolution. Stellar occultations have become the most precise Earth-based technique to determine such properties.

Aims. The purpose of this work is to constrain the size, shape, and geometric albedo of the dwarf planet candidate (307261) 2002 MS_4 through the analysis of nine stellar occultation events. From the multichord detection, we also searched for topography in the object's limb.

Methods. We predicted and organized the observational campaigns for nine stellar occultations by 2002 MS_4 between 2019 and 2022 resulting in two single-chord events, four double-chord detections, and three events that have three or more positive chords. Using differential aperture photometry, we derived the light curves from which the star dis- and re-appearance instants were calculated. Using selected chords from the 8 August 2020 event, we determined the best elliptical fit to the limb of 2002 MS_4. Combined with its rotational information from the literature, the best-fitted ellipse constrains the object's size, shape, and albedo. Additionally, we investigated the detected topography and, for the first time, developed a method to characterize it.

Results. The best-fitting elliptical limb has a semi-major axis of $a' = 412 \pm 10$ km, a semi-minor axis of $b' = 385 \pm 17$ km, and the position angle of the minor axis is $121^\circ \pm 16^\circ$. From this instantaneous limb, we obtained 2002 MS_4's geometric albedo $p_V = 0.07 \pm 0.12$ using an $H_V = 4.0 \pm 0.6$ mag and a projected area-equivalent diameter of 796 ± 24 km. A topography detection was observed in the light curve one station , distant 11 km from the best-fitted ellipse (radial direction). Moreover, an elevation of 25^{+4}_{-5} km and a 45.1 ± 1.5 km depth depression are detected, from multiple sites, in the northernmost limb.

Conclusions. Our results present an object ≈ 138 km smaller in diameter than derived from thermal data. However, the geometric albedo in the V-band agrees with the results published in the literature. For the first time, the stellar occultation allowed for a multichord detection and measurement of topography in a TNO.

Key words. Kuiper belt: individual: 2002 MS4 – Methods: observational

1. Introduction

Trans-Neptunian Objects (TNOs) are small solar system bodies that orbit the Sun with a semi-major axis larger than Neptune's (Jewitt *et al.* 2008). Due to the low spatial density of material in this orbital region and significant distance from the Sun, their global physical-chemical composition has been largely unaffected since their formation. Therefore, they are considered remnants of the primordial disk, a valuable source of information about the primitive solar nebula and the evolution of our planetary system (Gladman *et al.* 2008; Morbidelli *et al.* 2008; Nesvorný & Morbidelli 2012). Besides that, the knowledge of the size-frequency distribution of TNOs allows for constraining the solar system formation models (Petit *et al.* 2008).

Mainly due to the faintness and small angular sizes seen from Earth, our knowledge of the fundamental physical properties of the TNO population is still scarce and fragmented (Stansberry *et al.* 2008; Lellouch *et al.* 2013; Lacerda *et al.* 2014). Since the discovery of (15760) Albion in 1992 (Jewitt & Luu, 1993), thousands of objects have been observed in this orbital region. However, the size and albedo of only 178 Centaurs and TNOs have been determined using thermal observations (Müller, Lellouch, and Fornasier 2020). On the other hand, spacecraft visits can fully characterize these objects, for instance, the NASA/New Horizons mission (Weaver and Stern 2008) visit to the Pluto system (Stern *et al.* 2015, 2020; Spencer *et al.* 2020 b) and (486958) Arrokoth (Stern *et al.* 2019; Benecchi et al. 2019; Buie *et al.* 2020 a; Spencer et al. 2020 a). Unfortunately, the abovementioned approaches require large investments and cannot be used to study hundreds of objects.

Stellar occultation is a ground-based and more approachable method to study these distant bodies. It consists of observing a background star while a small body passes in front of it, blocking the stellar flux for a few seconds. An updated list of stellar occultation detections - that we are aware of - can be found at the SOSB Database[1] (Braga-Ribas *et al.* 2019). Then, the limb derived from occultation data can be combined with information derived from other observational methods to characterize the object (Ortiz *et al.* 2020b).

In this work we predicted, observed, and analyzed nine stellar occultations by the large TNO (307261) 2002 MS_4 - MS4 hereafter. It was discovered by the Near-Earth Asteroid Tracking (NEAT)[2] program on 18 June 2002 and is classified as a hot classical TNO due to its high orbital inclination (Gladman *et al.* 2008; Van Laerhoven *et al.* 2019). Furthermore, MS4 is a candidate to be a dwarf planet due to its thermally derived equivalent diameter (Vilenius *et al.* 2012). Physical and orbital parameters taken from previously published works are listed in Table 1.

In 2019, we observed four stellar occultations by MS4 from Argentina, Brazil, Canada, and Chile (see Tables A.4 and A.5). On July 26, we obtained a multichord detection from three well-separated sites and, ≈ 8 hours later, a single-chord occultation of a different star from Canada. On July 9 and August 19, we detected two positive chords and a set of negatives. The astrometric results from 2019 data (Table 5) were used to calculate a new ephemeris and predict the subsequent events (Desmars *et al.* 2015).

The first observation in 2020 was a double chord from South Africa on July 26, which confirmed the accuracy of MS4's ephemeris at an eight-milliarcsec (mas) level. Next, we organized an extensive campaign and successfully observed, from 61 sites, an occultation of a bright star on August 8, 2020. As described in this work, we derived valuable physical information from this multichord event observed in North Africa, Europe, and Western Asia. Finally, in the last two years, observatories from Europe, South, and North America recorded single-, double- and triple-chord events, respectively.

Table 1: Orbital and physical properties of MS4 from the literature.

Orbital properties[a]		**Physical properties**	
a	41.9 au	D^b	934 ± 47 km
q	35.9 au	$p_V{}^b$	$0.051^{+0.036}_{-0.022}$
i	17.7°	$H_V{}^b$	4.0 ± 0.6
e	0.14	$Ap_{mag}{}^c$	20.39 mag

Notes. [(a)] Orbital elements from JPL Small-Boby Database Browser web page https://ssd.jpl.nasa.gov/tools/sbdb_lookup.html#/?sstr=2002MS4 . [(b)] Physical properties obtained by Vilenius *et al.* (2012): **D:** area-equivalent diameter and geometric albedo at V-band (**p_V**); **H_V:** average absolute visual magnitude at V-band; Stansberry *et al.* (2008) obtained D = 726.05 ± 123.05 km and $p_V = 0.084^{+0.038}_{-0.023}$ for a value of H_V = 4.0 using Spitzer data only. [(c)] **Ap_{mag}:** object's average apparent visual magnitude at the multichord stellar occultations' epoch, from JPL website https://ssd.jpl.nasa.gov/horizons/app.html#/.

2. Predictions and observations

We performed classical astrometric runs to refine MS4's ephemeris at the Pico dos Dias (Brazil), La Silla (Chile), Calar Alto (Spain), and Pic du Midi (France) observatories between 2009 and 2019. The updated ephemeris and the *Gaia* Data Release 1 catalog (Gaia Collaboration *et al.* 2016 a,b, 2018) significantly improved the prediction of the 9 July 2019 occultation resulting in our first occultation by MS4. Furthermore, the astrometry derived from this occultation data allowed improvements in the subsequent predictions.

The default procedure for all events was to update the prediction and send alerts to potential observers within or close to the predicted shadow path. However, an exception was made for the 8 August 2020 event, and we built a campaign web page with helpful information for the observers[3]. Table 2 shows the relevant information about the occulted stars from the *Gaia* Early Data Release 3 catalog (GEDR3, Gaia Collaboration *et al.*2021).

The data came from a wide range of telescopes, from small portable ones (apertures between 13 cm and 30 cm) to large facilities like the 4.1 m telescope at the Southern Astrophysical Research (SOAR, Chile), the 2 m Liverpool telescope at Roque de Los Muchachos (Spain), the 1.6 m telescope at Pico dos Dias (Brazil), and the 1.5 m telescope at Sierra Nevada (Spain) observatories. Most observers did not use filters to maximize photon fluxes on CCD and thus got a better signal-to-noise ratio (SNR). Even though some observers used Global Positioning System (GPS) to acquire the time, the most common time source was the computer clock synchronization with a Network Time Protocol (NTP). A compilation of all the participating observers and instruments is presented in Appendix A. All the predictions and observational efforts were developed inside the European Research Council (ERC) *Lucky Star* project[4].

[1] http://occultations.ct.utfpr.edu.br/results
[2] More information on https://sbn.psi.edu/pds/resource/neat.html
[3] The campaign web page is available in https://lesia.obspm.fr/lucky-star/campaigns/2020-08-08_2002MS4.html
[4] https://lesia.obspm.fr/lucky-star/

Table 2: Target star designation and geocentric star coordinates at closest approach instant (UT) sorted by occultation date (day-month-year). Also, the V and K magnitudes used to determine the star's diameter ($S_{\rm Diam}$) at the MS4's geocentric distance (Δ_{MS4}). It is important to mention that none of the stars have a duplicity flag in the *Gaia* DR3 catalog.

Date	Designation Gaia DR3	Propagated Right Ascension (hh mm ss.sssss)	Error (mas)	Propagated Declination (° ' ")	Error (mas)	V (mag)	K (mag)	$S_{\rm Diam}$ (km)	Δ_{MS4} (au)
09-07-2019	4253196402592965504	18 45 19.24565	0.15	-06 24 13.0031	0.12	15.00	14.15	0.19	45.62
26-07-2019	4253186506987951104	18 44 07.57274	0.54	-06 26 40.1240	0.46	17.78	16.27	0.08	45.67
	4253186477047835648	18 44 06.31756	0.13	-06 26 43.8948	0.11	15.45	11.66	0.98	45.68
19-08-2019	4253181804071259648	18 42 43.51905	0.24	-06 32 34.0868	0.19	16.51	16.59	0.05	45.88
26-07-2020	4253244201379441792	18 48 18.07372	0.12	-06 13 31.6134	0.12	14.76	12.61	0.47	45.60
08-08-2020	4253248324549054464	18 47 29.96384	0.12	-06 16 31.4727	0.10	14.62	11.13	1.19	45.70
24-02-2021	4253709191700784896	18 56 35.98731	0.25	-06 30 23.1569	0.23	16.51	12.96	0.53	47.05
14-10-2021	4252495635735083264	18 50 30.76176	0.31	-06 24 13.3375	0.27	15.83	13.44	0.34	46.52
10-06-2022	4253907305577009664	19 00 15.44628	0.23	-05 42 42.9960	0.21	15.1	13.00	0.39	45.48

3. Data reduction, analysis and results

The great diversity of telescopes and detectors was reflected in five data formats[5]: *avi*, *adv* (Pavlov *et al.* 2020), *ser*, *cpa*, and FITS. Most *avi*, *adv*, and *ser* video files were converted to FITS images using TANGRA[6] software. However, from some videos, the images were extracted using a PYTHON 3 script based on ASTROPY v4.0.1 (Astropy Collaboration *et al.* 2013). When calibration images were available, the raw images were corrected from bias, dark, and flat-field using standard procedures with Image Reduction and Analysis Facility (IRAF, Butcher & Stevens,1981).

We applied aperture photometry on the target and some comparison stars on all the FITS files using the Package for Automatic Reduction of Astronomical Images (PRAIA, Assafin et al. 2011). The chosen photometric apertures considered the maximization of the SNR. In addition, we used the flux of the comparison stars to correct for sky transparency variations. As the images of MS4 and the star were blended, the photometric aperture measured the sum of their fluxes. The highest MS4's flux contribution was only 1%, considering the observed occultation of the faintest star (Table 2).

The target's (MS4 + Star) light curve is normalized by dividing it by the light curve containing the averaged comparison stars' flux. Then the Stellar Occultation Reduction and Analysis package v0.2.1 (SORA, Gomes-Júnior *et al.* 2022) is used to perform a polynomial fit and normalize the total flux outside the occultation to unity. On the other hand, the bottom flux during occultation was normalized to the median value of all images where the target star completely disappeared. Immersion and emersion instants were derived using the standard chi-square method (χ^2 test) between the observed and synthetic light curves. The synthetic light curve considers a sharp-edge model convolved with Fresnel diffraction, finite exposure time, CCD bandwidth, and star diameter at MS4's distance (details about this procedure are available in Gomes-Júnior *et al.* 2022 and references therein). The star diameters projected at MS4 distance are listed in Table 2. They were calculated according to Kervella *et al.* (2004)'s formalism and used to determine the event instants. Organized by the event's date, Table 3 contains the ingress and egress UTC times with 1σ uncertainties for each station with a positive detection. Appendix B presents the original normalized and the synthetic light curves used to obtain the instants.

If homogeneous, large TNOs like MS4 may reach one of the hydrostatic equilibrium shapes: the Jacobi three-axial ellipsoid or the Maclaurin oblate spheroid (Chandrasekhar 1987; Tancredi and Favre 2008). The apparent global limb of the body is then an ellipse projected in the sky plane. This ellipse is defined by M = 5 free parameters: center relative to the ephemeris (f and g), the semi-major axis (a'), the semi-minor axis (b'), or equivalently, the oblateness ($\epsilon' = a' - b'/a'$), and the position angle (PA) of the semi-minor axis (b'). The PA counts positively starting from the celestial north and increasing to the east.

For each stellar occultation event, we converted the ingress and egress instants into a star position (f, g) with f and g increasing toward celestial east and north, respectively. At this point, we can fit a limb model to these points, which provides, among others, the position of MS4's center in the sky plane, and thus the ephemeris offset.

Among the nine stellar occultation events, only three allow for an elliptical fit to the chords: 9 July 2019, 8 August 2020, and 10 June 2022. We started our fitting procedure with the 61 chords acquired on 8 August 2020 (Sect. 3.1), and we then used the residuals of the elliptic limb fit to search for topographic features on MS4 (Sect. 3.2). We finally compared the resulting mean ellipse with the chords observed in the other events (Sect. 3.3).

3.1. 8 August 2020

Three circumstances triggered an extensive observational campaign: i) the bright target star (G = 14.6 mag from GEDR3 catalog), ii) a micro-arc second-level accuracy of MS4's ephemeris stemming from previously detected occultations , and iii) a shadow path crossing densely populated regions. Accordingly, the observational campaign motivated the participation of 116 telescopes from Europe, North Africa, and Western Asia. As a result, we received 61 positive and 40 negative data sets. Other 15 locations had bad weather conditions, and observers could not acquire images. The number of effective chords is smaller than the 61 positives due to the overlapping of observations from nearby observatories along the object's limb.

We then submitted all the images to the procedure described at the beginning of this Section. As absolute time acquisition is

[5] *avi* = Audio Video Interleave. For the *adv* (Astronomical Digital Video) more information can be found in https://www.iota-es.de/JOA/JOA2020_3.pdf. *ser* format is a simple image sequence format and the documentation can be found in http://www.grischa-hahn.homepage.t-online.de/astro/ser/. *cpa* is a compressed image file associated with PRISM (http://www.prism-astro.com/fr/index.html. FITS stands for Flexible Image Transport System, and the most recent documentation can be found in https://fits.gsfc.nasa.gov/fits_standard.html

[6] http://www.hristopavlov.net/Tangra3/

Table 3: Star's dis- and re-appearance instants with 1σ error bars from the nine stellar occultations events, sorted from northernmost to southernmost station.

Sites	**Immersion (hh:mm:ss.ss ± ss.ss)**	**Emersion (hh:mm:ss.ss ± ss.ss)**
	09 July 2019	
OPSPA	04:23:28.65 ± 0.19	04:23:58.26 ± 0.38
ASH2	04:23:27.2 ± 1.1	04:23:56.73 ± 2.1
Pico dos Dias	04:22:02.182 ± 0.006	04:22:29.44 ± 0.67
	26 July 2019 - South America	
OPSPA	02:47:15.6 ± 7.8	02:48:04.0 ± 3.7
ASH2	02:47:21.0 ± 3.8	02:47:54.8 ± 5.3
Paranal	02:47:34.33 ± 0.12	02:48:07.9 ± 1.2
Pico dos Dias	02:45:55.310 ± 0.099	02:46:17.581 ± 0.093
	26 July 2019 - North America	
Osooyos	10:15:16.65 ± 0.40	10:15:53.12 ± 0.33
	19 August 2019	
Victoria	07:37:19.2 ± 2.6	07:37:55.2 ± 1.3
Osooyos	07:37:17.55 ± 0.55	07:37:53.7 ± 2.0
	26 July 2020	
Pretoria	23:15:28.46 ± 0.12	23:15:54.27 ± 0.15
Johannesburg	23:15:28.940 ± 0.092	23:15:55.89 ± 0.18
	08 August 2020	
Varages	20:43:44.858 ± 0.058	20:43:53.359 ± 0.028
Caussols	20:43:39.5 ± 2.0	20:43:51.5 ± 2.0
Grasse	20:43:39.488 ± 0.021	20:43:53.960 ± 0.027
Cannes 01	20:43:39.27 ± 0.13	20:43:54.18 ± 0.56
Budapest	20:42:49.59 ± 0.13	20:43:08.61 ± 0.20
Lleida	20:44:01.4 ± 6.6	20:44:25.13 ± 0.12
Nice	20:43:36.444 ± 0.029	20:43:52.834 ± 0.071
Cannes 02	20:43:37.23 ± 0.21	20:43:55.64 ± 0.39
Valbonne	20:43:37.376 ± 0.055	20:43:54.07 ± 0.13
Črni Vrh	20:43:09.71 ± 0.94	20:43:26.58 ± 0.35
Mátraszentistván	20:42:46.866 ± 0.015	20:43:04.739 ± 0.045
Ljubljana	20:43:06.70 ± 0.20	20:43:25.20 ± 0.33
Trieste	20:43:07.7 ± 3.3	20:43:27.41 ± 0.85
Catalonia	20:43:57.15 ± 0.21	20:44:17.84 ± 0.14
Bologna	20:43:17.40 ± 0.26	20:43:38.77 ± 0.67
Massa 01	Photometry not done	Very long video
Massa 02	20:43:20.52 ± 0.39	20:43:43.83 ± 0.32
Castelvecchio Pascoli	20:43:18.742 ± 0.088	20:43:44.1 ± 1.4
Borgo a Mozzano	20:43:19.224 ± 0.078	20:43:42.80 ± 0.12
San Marcello Pistoiese	20:43:16.200 ± 0.072	20:43:42.6 ± 1.2
Sta. Maria a Monte	20:43:17.68 ± 0.12	20:43:42.80 ± 0.11
Signa	20:43:15.61 ± 0.57	20:43:40.38 ± 0.67
Lastra a Signa	20:43:13.815 ± 0.084	20:43:41.9 ± 1.2
Khmelnytskyi	20:42:01.81 ± 0.82	20:42:49.7 ± 15.7
Sevilla	20:44:29.03 ± 0.13	20:44:59.40 ± 0.19
Huelva	20:44:32.74 ± 0.37	20:45:02.72 ± 0.28
Cluj-Napoca	20:42:25.0 ± 1.2	20:42:56.61 ± 0.30
Fuensanta de Martos	20:44:22.0 ± 3.0	20:44:55.0 ± 3.1
Fiastra	20:43:05.1 ± 1.8	20:43:37.89 ± 0.52
Dragsina	20:42:32.938 ± 0.087	20:43:05.82 ± 0.32
Ibiza	20:43:56.6 ± 1.8	20:44:28.55 ± 0.24
Alhendín	20:44:17.89 ± 0.57	20:44:54.83 ± 0.18
Granada (150 cm)	20:44:17.571 ± 0.008	20:44:52.08 ± 0.51
Granada (90 cm)	20:44:16.53 ± 0.51	20:44:51.755 ± 0.026
Estepona	20:44:24.37 ± 0.45	20:45:00.4 ± 1.9
Marbella	20:44:26.1 ± 4.3	20:44:59.64 ± 0.22
Roma	20:43:08.37 ± 0.37	20:43:43.79 ± 0.37
Hvar	20:42:51.69 ± 0.21	20:43:27.96 ± 0.35
Bacau	20:42:12.60 ± 0.30	20:42:50.49 ± 0.72
Sgurgola	20:43:03.86 ± 0.15	20:43:41.13 ± 0.15
Sassari	20:43:19.35 ± 0.35	20:43:56.60 ± 0.50
Kharkiv (70 cm)	20:41:40.00 ± 0.13	20:42:17.16 ± 0.12
Kharkiv (36 cm)	20:41:39.6 ± 1.9	20:42:18.3 ± 1.2
Ceccano	20:43:02.39 ± 0.41	20:43:40.76 ± 0.37
Brasov	20:42:14.2 ± 2.7	20:42:51.5 ± 1.6
Bârlad	20:42:09.23 ± 0.55	20:42:47.00 ± 0.49
Valenii de Munte	20:42:15.14 ± 0.24	20:42:52.61 ± 0.50
Ploiesti	20:42:14.25 ± 2.1	20:42:53.2 ± 1.5
Odessa	20:42:00.00 ± 0.14	20:42:38.49 ± 0.11
Naples	20:43:00.66 ± 0.30	20:43:37.7 ± 1.1
Agerola	20:42:59.603 ± 0.050	20:43:37.842 ± 0.093
Algiers	20:43:50.844 ± 0.021	20:44:29.115 ± 0.075
La Palma	20:45:35.032 ± 0.014	20:46:08.313 ± 0.018
Tijarafe	20:45:35.68 ± 0.19	20:46:08.08 ± 0.11
Ariana	20:43:23.87 ± 0.29	20:43:56.80 ± 0.25
Artemis	20:45:31.938 ± 0.022	20:46:01.297 ± 0.024
TAR 1	20:45:32.360 ± 0.057	20:46:01.595 ± 0.063
Catania	20:43:04.59 ± 0.92	20:43:34.564 ± 0.085
Kuban	20:41:36.2 ± 1.2	20:42:00.63 ± 0.31
Çanakkale	20:42:23.39 ± 0.56	20:42:38.830 ± 0.072
	24 February 2021	
ASH2	08:41:36.82 ± 0.98	08:42:08.43 ± 0.30
OPSPA	08:41:37.00 ± 0.61	08:42:09.182 ± 0.082
	14 October 2021	
Osoyoos	03:23:30.14 ± 0.40	03:24:35.33 ± 0.67
Flagstaff	03:25:54.61 ± 0.44	03:26:39.33 ± 0.73
	10 June 2022	
La Palma	05:30:08.475 ± 0.091	05:30:43.30 ± 0.13
Artemis	05:30:02.427 ± 0.066	05:30:37.51 ± 0.49
Three Gate Farm	05:34:47.18 ± 0.33	05:35:22.12 ± 0.28

essential to achieve good results, we checked each data set and applied offsets when: i) the observer reported time issues during the acquisition, ii) the camera acquisition software is known to have a systematic offset, and iii) overlapped chords do not match each other. The time shifts applied to the original positive data are presented in Table A.1, and the corrected instants are in Table 3. Figure 1 shows all the positives (blue lines) and their uncertainties in the star dis- and re-appearance (red segments). Finally, data showed no clear detection of surrounding features like satellites, rings, or jets (green lines). The search for such features will be the subject of a future work.

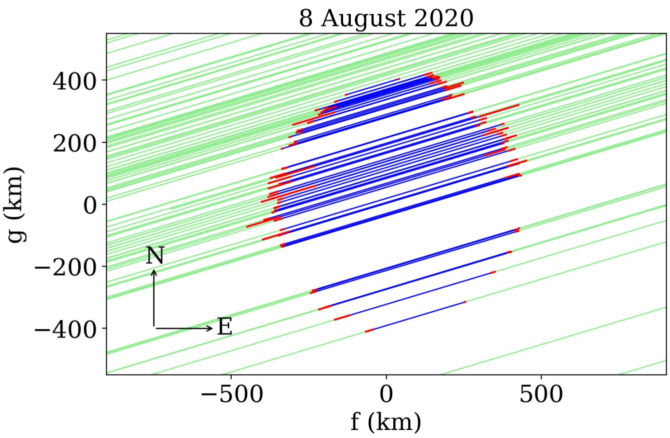

Fig. 1: The chords acquired on the 8 August 2020 event show the detection of MS4's limb in blue with 1σ error bars (red segments). For better visualization, six positive chords with large error bars were suppressed from this plot: TAROT, Lleida, Khmelnytskyi, Fuensanta de Martos, Kharkiv T36, and Marbella. The green lines are representing positions compatible with full target's flux, within the noise (i.e. no secondary occultation).

The plot of the chords at sky plane shows that an elliptical limb does not represent the observed profile (see discussion in Sect. 3.2). Thus, to derive MS4's global limb on this event, we excluded the chords that probed the northeast region and selected the following positive chords: Grasse (FRA), Valbonne (FRA), Mátraszentistván (HUN), Catalonia (ESP), Massa (ITA), Roma (ITA), Hvar (HRV), Sassari (ITA), Odessa (UKR), Agerola (ITA), Algiers (DZA), La Palma (ESP) and Çanakkale (TUR). The selection was based in a balance between time reliability, data SNR, and separation from other chords. Therefore, the selected chords provide N = 26 independent points at the sky plane to fit the five ellipse parameters.

The elliptical limb is determined by minimizing the classical χ^2 function. The quality of the result is given by the χ^2 per degree of freedom $\chi^2_{\text{pdf}} = \chi^2/(N-M) \approx 1$, where N is the number of points and M is the number of fitted parameters (Gomes-Júnior *et al.* 2022) . Following the theoretical approach proposed by Johnson and McGetchin (1973), the lower limit for topography in MS4 is 6-7 km (see Sect. 3.4). A set of empirical tests using topography values between 0 and 10 km, revealed that a good fit ($\chi^2_{\text{pdf}} = 0.92$) is obtained when we consider that topographic features up to 7 km are present on MS4's limb.

Among the elliptical solutions inside the 3σ region, we excluded those that crossed or approached the grazing negative chords to within the tolerance level of 7 km. Therefore, although the solutions cross the negative chord as seen from Montsec (Fig. 2), they are inside the 7 km assumed range. The center (f and

g) was calculated using the GEDR3 star position (Table 2) and MS4's ephemeris provided by the Numerical Integration of the Motion of an Asteroid (NIMA)[7] as described by Desmars (2015) and Desmars *et al.* 2015. The equivalent surface radius was determined using the relation $R_{\text{equiv}} = a'\sqrt{1-\epsilon'}$. Finally, the limb solution presented in Table 4 represents the best-fitted elliptical limb at the sky plane.

Table 4: The parameters (with 3σ error bars) of the best-fitted elliptical limb, derived from the 13 selected positive chords. The solutions admit topographic features up to 7 km and are limited at north by the negative chord from the Montsec station (orange segments in Fig. 2).

MS4's global elliptical limb			
f	43.4 ± 6.2 km	a'	411.8 ± 9.9 km
g	6.9 ± 9.3 km	ϵ'	0.066 ± 0.034
PA	121.3 ± 16.3°	R_{equiv}	398 ± 12 km

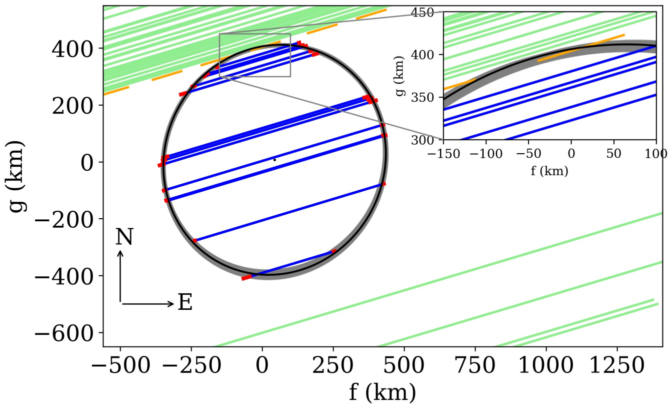

Fig. 2: Best elliptical limb (black ellipse) and the solutions within 3σ (gray region) plotted over the 13 selected chords (blue segments). The orange segments present each image acquired from the Montsec station, and the light green segments show other negative chords.

3.2. Topographic features

Determining topography limits for small bodies orbiting the Sun beyond Neptune is challenging. From an observational point of view, our target and most TNOs do not have in situ or high resolution images. However, we can use stellar occultation data to search for features on these objects' surfaces (Dias-Oliveira *et al.* 2017; Leiva *et al.* 2017). Johnson and McGetchin (1973) proposed a theoretical method to determine such limits for planetary satellites using the global density and composition. Using it for MS4 and assuming an icy body with a density between $\rho = 1.0-2.0$ g/cm^3, the lower limit for superficial features is 6-7 km. If we consider that material strength may increase toward the nucleus, the surface might support even more prominent features.

The advance in interplanetary spacecraft technology allowed to characterize the surface of a few objects using in situ images. For instance, using Voyager's images of Uranus's largest satellites Schenk and Moore (2020) found superficial features up to 11 km. Likewise, New Horizons' flyby over Pluto system (Moore *et al.* 2016; Nimmo et al. 2017) and (486958) Arrokoth (Spencer et al. 2020 a) revealed superficial structures on the same scale. Considering the sizes of the observed structures, the assumption of features up to 7 km on MS4's surface is reasonable.

A first evidence of topography on MS4 was detected on the Varages light curve. The data do not have dead time, and the exposure translates into a resolution of 1.97 km into the sky plane. The Fresnel diffraction and star diameter at MS4 geocentric distance are at the same level, 1.54 km and 1.19 km, respectively. It presents a sharp ingress and a gradual egress above the noise level as shown in Fig. 3. The feature did not appear in any of the other high SNR light curves, thus disbelieving the possibility of a secondary star. Thus, the most plausible explanation is a topographic feature where a portion of the star appeared during a few frames before egress, corresponding to a more than 20 km long feature in the chord's direction. The insert in Fig. 3 pictures the star position in each frame, represented by yellow circles, relative to a proposed limb in gray.

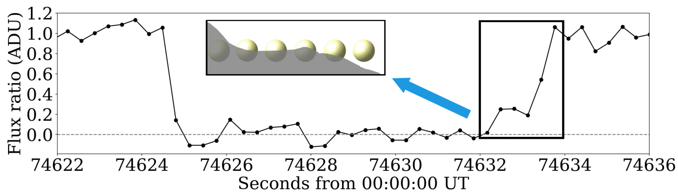

Fig. 3: Black dots represent the normalized star flux in each frame acquired in Varages station as a function of time. The insert selects the egress region, and illustrates a possible explanation for such a signal (see text).

As already stated, it is clear in Fig. 1 the presence of a group of chords showing a deviation from an elliptical limb. An elevation next to a large depression is seen in the northeast limb. To characterize these features, we first derived the radial difference (R_D) between the chords' extremities and the global best-fitted ellipse (Table 4). The points with R_D larger than their 1σ uncertainties were selected. In Fig. 4, we see groups of points with positive and negative R_D, meaning topographic elevation and depression with respect to the global elliptical limb. Most of these points are concentrated between position angles -5° and 75°, therefore, we restrict our analysis to this data set.

The simplest function that can reproduce the observed features is a parabola. Equations 1 and 2 provide the models used to fit the group of points with negative and positive R_D, respectively. A positive a coefficient indicates a depression. The b term accounts for the parabola's depth or height, while c accounts for the distance from the plot's origin. The $x = PA$ and $y = R_D$, where all y values outside the parabola are defined as zero.

$$Depression = \begin{cases} 0 & y \geq 0 \\ a(x-c)^2 - b & y < 0 \end{cases} \tag{1}$$

$$Elevation = \begin{cases} 0 & y \leq 0 \\ a(x-c)^2 + b & y > 0 \end{cases} \tag{2}$$

Despite a reasonable model for a single feature, one single parabola can not describe the observed R_D points distribution. Therefore, the fitted model comprises three parabolic functions,

$$Model = Depression + Elevation + Depression$$

[7] The NIMA-v9 ephemeris is publicly available and can be downloaded from https://lesia.obspm.fr/lucky-star/obj.php?p=692

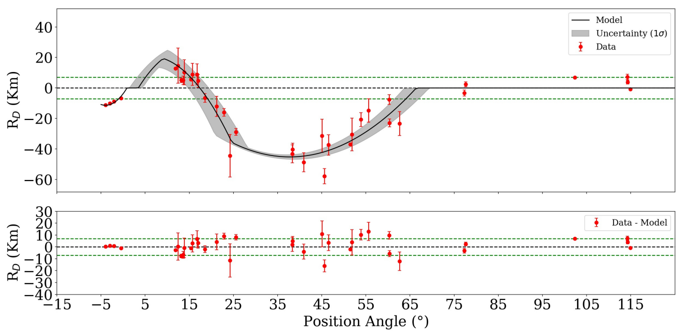

Fig. 4: The horizontal green lines mark the limits the assumed ± 7 km tolerance (see text), and the black dashed line is the best-fitted ellipse. **Upper panel:** red points are the R_D as a function of position angle, and the solid black line is the model with 1σ uncertainties represented in grey. **Lower panel:** the residuals after subtracting the model from the data.

where one depression corresponds to the Varages egress region (Here as negative position angles for better viewing).

The fitting was made using a high-level PYTHON interface for non-linear optimization and curve-fitting problems named LMFIT[8]. We used the Differential Evolution (DE) minimization method (Storn and Price 1997) to derive the first estimation of the model's parameters, which can explore large areas of candidate space without getting stuck in a local minimum. Then, to get a representative estimation of the model's uncertainties, we explored the parameters' space using the Maximum likelihood via Monte-Carlo Markov Chain sampler - *emcee*[9](Foreman-Mackey *et al.* 2013). Finally, the shaded region in Fig. 4 was derived by accounting for unknown uncertainties of ≈ 4.5 km.

After subtracting the model from the data set, residuals are inside the expected range (bottom box in Fig. 4). Therefore, according to the model at 1σ level, MS4's surface has an ≈ 11.0 km depth depression in the region detected by Varages station, followed by an elevation of 25^{+4}_{-5} km. However, the most impressive feature is the 45.1 ± 1.5 km depth depression with a length of 322 ± 39 km. Figure 5 presents a general view of the detected limb and summarizes the topography solutions. Also, because the depression was likely not in its middle position at the limb, it is likely larger and deeper than what it seems from this snapshot at a particular rotation phase.

3.3. Other occultation events

Object's three-dimensional shape strongly correlates with the body's rotational modulation (Chandrasekhar 1987; Tancredi and Favre 2008). Maclaurin objects usually have single-peaked rotational light curves with small peak-to-peak amplitudes caused by albedo features, while Jacobi shapes usually present double-peaked curves with more pronounced amplitudes (unless they are seen nearly pole-on). Therefore, a reasonable determination of MS4's rotational parameters is crucial to derive an accurate three-dimensional size, shape, albedo, and density.

However, since its discovery, MS4 has been crossing a highly dense field of stars, and it is complicated to obtain precise photometric measurements for rotational light curve determination.

[8] More about this library can be found in the https://lmfit.github.io/lmfit-py/

[9] Documentation available on https://emcee.readthedocs.io/en/stable/

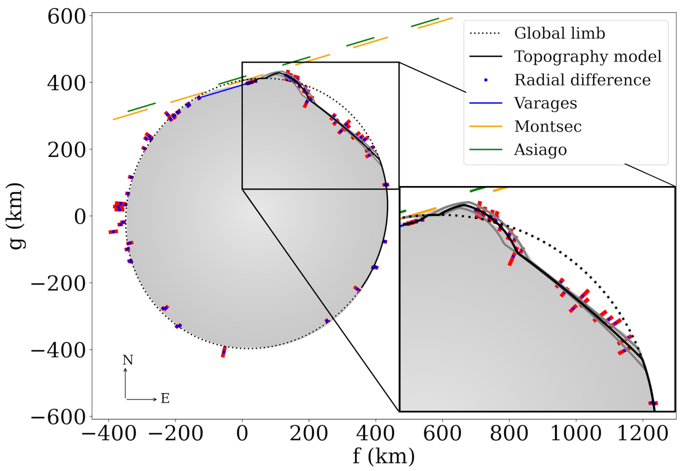

Fig. 5: The blue points present the R_D points projected at the sky plane with 1σ uncertainties in red. The blue segment is the positive detection from Varages station. Orange and green segments correspond to negative frames acquired in Montsec and Asiago stations, respectively. In black, the dotted line is the global limb described in Sect. 3.1 and the solid line is the model for local topography. The solid gray lines limit the model's 1σ-error bars. Finally, the proposed limb is shown by the gray color.

The only exception occurred in 2011 when MS4. At the time passed in front of a dark cloud on the galactic plane Thirouin, 2013 derived a single-peaked light curve with an amplitude of 0.05 ± 0.01 mag and two possibilities for the rotational period: 7.33 h or 10.44 h. Such a small amplitude may indicate that MS4 is a Maclaurin object, or a Jacobi ellipsoid/other shape that is being observed in pole-on orientation (an unlikely orientation in general). In both cases, the projected area on the sky plane should not change significantly in a short period (2019-2022) neither due to rotational variability or changes in the aspect angle. However, for the triaxial case the position angle of the projected ellipse would change significantly in different occultations due to changing in the rotational phase.

Due to its diameter and small rotational light curve amplitude, our preferred three-dimensional shape for MS4 is Maclaurin spheroid. Therefore we focused on it and tried to fit the same elliptical limb derived from the 8 August 2020 event (Table 4) on the chords obtained on the other occultation events. Using χ^2 minimization, the ellipse was fitted having only the center (f and g) set as a free parameter. When two center positions are equally possible (single chord cases), we present the center solution closer to the position predicted by the NIMA v9 ephemeris. The oblateness, equatorial radius, and position angle were free to vary inside the 3σ limits presented in Table 4. Figures 6 and 7 show the results of the limb fitting for the other eight events. The derived astrometric information is presented in Table 5.

3.4. MS_4's 3D shape and albedo

The small rotational light curve amplitude and the limb observed on the different occultation events being the same favors a Maclaurin spheroid. Therefore, we will consider that MS4 has a Maclaurin shape ($a = b > c$) with equatorial radius a, polar radius c, and true oblateness $\epsilon = (a - c)/a$. In addition, we will assume that it was observed with the same polar aspect angle θ during all the stellar occultations, where $\theta = 0°$ (resp. 90°) corresponds to a pole-on (resp. equator-on) viewing.

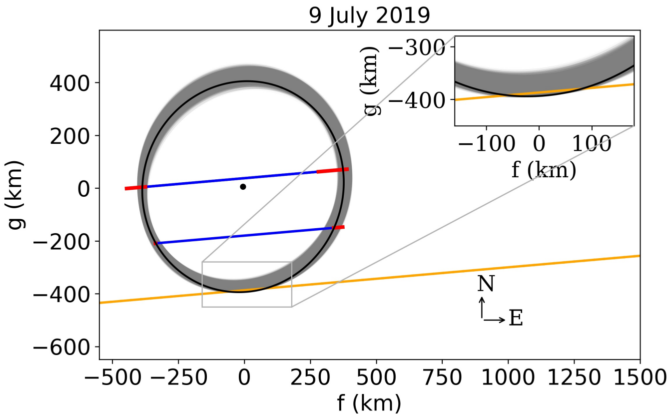

Fig. 6: The blue segments correspond to the positive data acquired from the stellar occultation on 9 July 2019. The 1σ uncertainties are in red, and the negative chord acquired from the Ponta Grossa station is in orange. The best-fitted ellipse is in black, and the solutions in the 3σ range are in gray. The fit considers topography of up to 7 km, thus the ellipses crossing the negative chord are in this range.

Table 5: Astrometric information (ICRS) for the geocentric closest approach instant (UT) obtained from the nine stellar occultation events observed between 2019 and 2022, sorted by date (day-month-year).

Date	Instant (UT) (hh:mm:ss.ss)	Right Ascension (hh mm ss.ss)	Error (mas)	Declination (° ' '')	Error (mas)
09-07-2019	04:23:49.08	18 45 19.245981	0.23	-06 24 13.05928	0.60
26-07-2019	02:47:08.52	18 44 07.573463	0.57	-06 26 40.17686	0.51
26-07-2019	10:18:43.02	18 44 06.315990	0.37	-06 26 43.7686	1.3
19-08-2019	07:41:52.28	18 42 43.51613	1.0	-06 32 33.9776	1.1
26-07-2020	23:17:56.04	18 48 18.075014	0.12	-06 13 31.70897	0.12
08-08-2020	20:44:27.26	18 47 29.961308	0.12	-06 16 31.34442	0.10
24-02-2021	08:45:52.82	18 56 35.9873	1.1	-06 30 23.1583	2.8
14-10-2021	03:26:05.50	18 50 30.768595	0.48	-06 24 13.20676	0.52
10-06-2022	05:32:47.30	19 00 15.446841	0.32	-05 42 42.8843	1.3

Using Eq. 3 and the semi-major axis as derived in this work ($a' = a$), we explored the relation between θ, ϵ, and c. A true oblateness of $\epsilon \leq 0.417$ for a Maclaurin body limited the calculation (Tancredi and Favre 2008). Which results in an interval to the true polar axis as $241.5 < c < b'$, where $b' = 385 \pm 17$ km is the apparent semi-minor axis.

$$\epsilon = 1 - \frac{\sqrt{(c/a)^2 - \cos^2(\theta)}}{\sin(\theta)} \quad (3)$$

Assuming that the true oblateness is the same as apparent oblateness derived from the stellar occultations and following the Maclaurin spheroid formalism (Braga-Ribas *et al.* 2013), a plot of the true oblateness against density for different rotational periods is presented in Fig. 8. The blue curve corresponds to a rotational period of P = 10.44 h, while the green one is for P = 7.33 h (Thirouin 2013). The density interval is delimited for each period by the oblateness interval (dotted gray lines). The black solid line presents the nominal apparent oblateness derived from the stellar occultation data. The red segments show the corresponding limits for MS4 global density: 2.62 - 7.98 g/cm^3 for P = 7.33 h and 1.3 - 3.93 g/cm^3 for P = 10.44 h. These values are rather high for objects in the trans-Neptunian region, so it is reasonable to infer that the true oblateness is higher than the apparent one. The geometric albedo in V-band can be obtained using the absolute magnitude as published by Vilenius *et al.* (2012) and the equivalent radius here derived, giving $p_V = 0.071 \pm 0.12$. The large uncertainty in the geometric albedo comes from the very large absolute magnitude uncertainty from Vilenius *et al.* (2012).

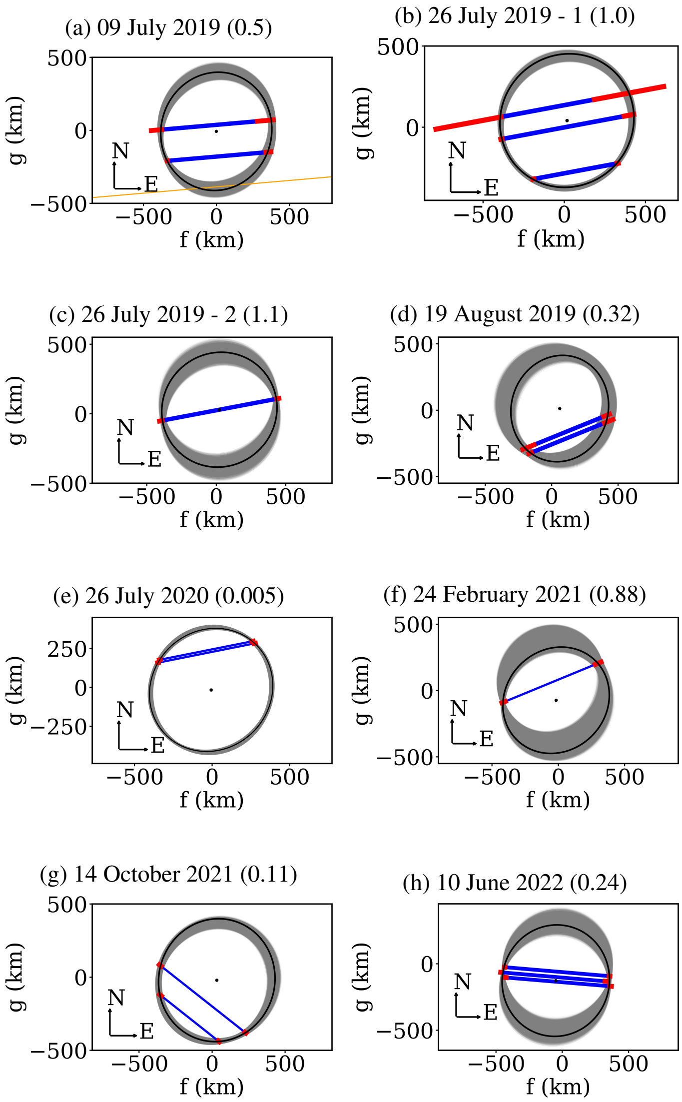

Fig. 7: These plots present the results for the additional eight stellar occultation events. Blue segments are the positive detections with 1σ uncertainties in red. The best elliptical limb is in black, with the center presented by the black dot. The gray region presents all the limb solutions inside 3σ. The $\chi^2_{\rm pdf}$ of each fit is presented between parenthesis in the individual labels. For the occultations presented in d), e), and f), the chosen center solution was the closest one to the predicted by NIMA v9 ephemeris.

4. Discussion and conclusions

This work presents physical and astrometric information derived from nine stellar occultations by the hot classical TNO (307261) 2002 MS_4 (MS4 for short), observed between 2019 and 2022 from sites in America, Africa, Europe, and Western Asia. The most successful campaign took place on 8 August 2020, with 116 telescopes involved and 61 positive chords. A record number of detections of a stellar occultation by a TNO up to date.

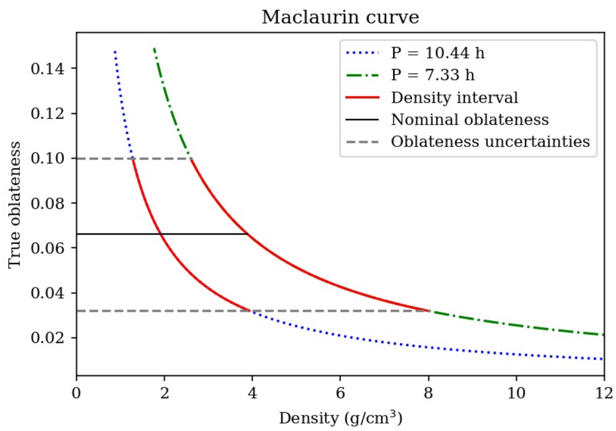

Fig. 8: Relation between the true oblateness and the density of a Maclaurin spheroid for the rotational periods of 10.44 h (blue dotted line) and 7.33 (green dashed line). The black solid line is the nominal oblateness value with uncertainties (gray dashed lines) derived from the multichord stellar occultation event. Red segments present the global density interval for each rotational period.

The projected elliptical limb of MS4 derived from the 8 August 2020 provides a semi-major axis of 411.8 ± 9.9 km, a semi-minor axis of 385 ± 17 km, and an area-equivalent radius of 398 ± 12 km. The obtained diameter is ≈138 km smaller than that derived with observations in thermal bands (Vilenius *et al.* 2012). It may indicate the presence of an unknown satellite as suggested for 2002 TC_{302} in similar circumstances Ortiz *et al.* (2020a) but the error bars from the thermal diameter are large and can accommodate the difference within 2 σ.

This is the first multichord detection of an extensive feature on the surface of a monolithic TNO. At the same time, we developed a mathematical model to describe the identified features. According to our measurements, MS4 has at least one depression with a depth of 45.1 ± 1.5 km and an extension of 322 ± 39 km, and a mountain of 25^{+4}_{-5} km high. Such large topography may indicate that MS4 has suffered a big impact during its history, but this topic is out of the scope of this work. Finally, despite the unprecedented coverage of a stellar occultation by a TNO, no clear secondary drops in the star flux caused by rings, jets, or satellites were identified. Upper limits for detecting such structures in the occultation light curves are also out of the scope of this work.

Despite not being conclusive, the shallow rotational light curve, the derived equivalent diameter, and the agreement between the limb obtained from the nine stellar occultations favor an oblate spheroid (Maclaurin). Furthermore, the density intervals mentioned above are higher than expected for TNOs. This might indicate that the object's true oblateness is higher than observed in the occultations. However, more data are needed to confirm MS4's three-dimensional shape and density.

Acknowledgements. This study was financed in part by the Coordenação de Aperfeiçoamento de Pessoal de Nível Superior – Brazil (CAPES) – Finance Code 001 and the National Institute of Science and Technology of the e-Universe project (INCT do e-Universo, CNPq grant 465376/2014-2). The following authors acknowledge the respective CNPq grants: F.B.-R. 309578/2017-5; R.V.-M. 307368/2021-1; J.I.B.C. 308150/2016-3; M.A. 427700/2018-3, 310683/2017-3, 473002/2013-2; O.C.W. 305210/2018-1. The following authors acknowledge the respective grants: B.E.M. thanks the CAPES/Cofecub-394/2016-05 grant; G.B-R. acknowledges CAPES- FAPERJ/PAPDRJ grant E26/203.173/2016; M.A. acknowledges FAPERJ grant E-26/111.488/2013; A.R.G.Jr acknowledges FAPESP grant 2018/11239-8; O.C.W. and R.S. acknowledge FAPESP grant 2016/24561-0. D.N. acknowledges support from the French Centre National d'Etudes Spatiales (CNES). K.H. and P.P. were supported by the project R.V.O.: 67985815. A.P. and R.S. received support from the K-125015 grant from the National Research, Development, and Innovation Office (NKFIH, Hungary). Partial funding for the computational infrastructure and database servers is received from the grant KEP-7/2018 of the Hungarian Academy of Sciences. Some of the results were based on observations taken at the 1.6 m telescope on the Pico dos Dias Observatory of the National Laboratory of Astrophysics (LNA/Brazil). Some data are based on observations collected at the Copernicus and Schmidt telescopes (Asiago, Italy) of the INAF-Astronomical Observatory of Padova. This work was carried out within the "Lucky Star" umbrella that agglomerates the efforts of the Paris, Granada and Rio teams, which is funded by the European Research Council under the European Community's H2020 (ERC Grant Agreement No. 669416). This work has made use of data from the European Space Agency (ESA) mission Gaia (https://www.cosmos.esa.int/gaia), processed by the Gaia Data Processing and Analysis Consortium (DPAC, https://www.cosmos.esa.int/web/gaia/dpac/consortium). Funding for the DPAC has been provided by national institutions, in particular the institu- tions participating in the Gaia Multilateral Agreement. TRAPPIST is a project funded by the Belgian FNRS under grant FRFC 2.5.594.09.F and the ARC grant for Concerted Research Actions, financed by the Wallonia-Brussels Federation. E.J. is a FNRS Senior Research Associate. We would like to acknowledge financial support by the Spanish grant AYA-RTI2018-098657-JI00 "LEO-SBNAF" (MCIU/AEI/FEDER, U.E.) and the financial support from the State Agency for Research of the Spanish MCIU through the "Center of Excellence Severo Ochoa" award for the Instituto de Astrofísica de Andalucía (SEV-2017-0709). Also, AYA2017-89637-R and FEDER funds are acknowledged. We are thankful to the following observers who participated and provided data for respective events as listed in Table B.1: Orlando A. Naranjo from Universidad de Los Andes, Mérida/VEN; Faustino Organero from La Hita Observatory – Toledo/ESP.

References

Assafin, M., Vieira Martins, R., Camargo, J. I. B., et al.: 2011, Gaia follow-up network for the solar system objects : Gaia FUN-SSO workshop proceedings, 85-88.

Astropy Collaboration, Robitaille, T. P., Tollerud, E. J., et al. 2013, A&A, 558, A33. doi:10.1051/0004-6361/201322068

Benecchi, S.D., Porter, S.B., Buie,et al: 2019, Icarus, 334, 11.

Braga-Ribas, F., Sicardy, B., Ortiz, J. L., Lellouch, E., Tancredi, G., et al.: 2013, *The Astrophysical Journal* **773**, 26.

Braga-Ribas, F., Crispim, A., Vieira-Martins, R., Sicardy, B., Ortiz, J.L., Assafin, M., and, ...: 2019, *Journal of Physics Conference Series* **1365**, 012024. doi:10.1088/1742-6596/1365/1/012024.

Buie, M. W., Porter, S. B., Tamblyn, P., et al. 2020, AJ, 159, 130. doi:10.3847/1538-3881/ab6ced.

Butcher, H., Stevens, R. 1981, Kitt Peak National Observatory Newsletter, 16, 6.

Chandrasekhar, S.: 1987, *New York : Dover, 1987.*

Desmars, J.: 2015, *Astronomy and Astrophysics* **575**, A53. doi:10.1051/0004-6361/201423685.

Desmars, J., Camargo, J.I.B., Braga-Ribas, F., Vieira-Martins, R., Assafin, M., Vachier, F., and, ...: 2015, *Astronomy and Astrophysics* **584**, A96. doi:10.1051/0004-6361/201526498.

Dias-Oliveira, A., Sicardy, B., Ortiz, J. L., Braga-Ribas, F., Leiva, R., et al.: 2017, *The Astronomical Journal* **154**, 22.

Foreman-Mackey, D., Hogg, D.W., Lang, D., and Goodman, J.: 2013, *Publications of the Astronomical Society of the Pacific* **125**, 306. doi:10.1086/670067.

Gaia Collaboration, Prust, T., de Bruijne, J. H. J., Brown, A. G. A., et al. 2016(a), A&A, 595, A1.

Gaia Collaboration; Brown, A. G. A.; Vallenari, A.; et al. 2016(b). A&A, 595, A2.

Gaia Collaboration; Brown, A. G. A.; Vallenari, A.; et al. 2018. A&A, 616, A1.

Gaia Collaboration, Brown, A.G.A., Vallenari, A.; et al. 2021, A&A, 649, A1. doi:10.1051/0004-6361/202039657.

Gladman, B., Marsden, B. G., and Vanlaerhoven, C.: 2008, *The Solar System Beyond Neptune*, 43.

Gomes-Júnior, A.R., Morgado, B.E., Benedetti-Rossi, G., Boufleur, R.C., Rommel, F.L., Banda-Huarca, M.V., and, ...: 2022, *Monthly Notices of the Royal Astronomical Society* **511**, 1167. doi:10.1093/mnras/stac032.

Jewitt, D., and Luu, J.: 1993, *Nature* **362**, 730.

Jewitt, D., Morbidelli, A., and Rauer, H.: 2008, *Saas-Fee Advanced Course 35: Trans-Neptunian Objects and Comets*.

Johnson, T.V. and McGetchin, T.R.: 1973, *Icarus* **18**, 612. doi:10.1016/0019-1035(73)90064-X.

Kervella, P., Thévenin, F., Di Folco, E., and Ségransan, D.: 2004, *Astronomy and Astrophysics* **426**, 297. doi:10.1051/0004-6361:20035930.

Lacerda, P., Fornasier, S., Lellouch, E., Kiss, C., Vilenius, E., Santos-Sanz, P., and, ...: 2014, *The Astrophysical Journal* **793**, L2. doi:10.1088/2041-8205/793/1/L2.

Leiva, R., Sicardy, B., Camargo, J.I.B., Ortiz, J.-L., Desmars, J., Bérard, D., and, ...: 2017, *The Astronomical Journal* **154**, 159. doi:10.3847/1538-3881/aa8956.

Lellouch, E., Santos-Sanz, P., Lacerda, P., et al.: 2013, *Astronomy and Astrophysics* **557**, A60.

Moore, J.M., McKinnon, W.B., Spencer, J.R., Howard, A.D., Schenk, P.M., Beyer, R.A., and, ...: 2016, *Science* **351**, 1284. doi:10.1126/science.aad7055.

Morbidelli, A., Levison, H. F., and Gomes, R.: 2008, *The Solar System Beyond Neptune*, 275.

Morgado, B.E., Sicardy, B., Braga-Ribas, F., Desmars, J., Gomes-Júnior, A.R., Bérard, D., and, ...: 2021, *Astronomy and Astrophysics* **652**, A141. doi:10.1051/0004-6361/202141543.

Müller, T., Lellouch, E., and Fornasier, S.: 2020, The Trans-Neptunian Solar System, 153.

Nesvorný, D., and Morbidelli, A.: 2012, *The Astronomical Journal* **144**, 117.

Nimmo, F., Umurhan, O., Lisse, C. M., et al. 2017, Icarus, 287, 12. doi:10.1016/j.icarus.2016.06.027

Ortiz, J.L., Santos-Sanz, P., Sicardy, B., Benedetti-Rossi, G., Duffard, R., Morales, N., and, ...: 2020, *Astronomy and Astrophysics* **639**, A134. doi:10.1051/0004-6361/202038046.

Ortiz, J.L., Sicardy, B., Camargo, J.I.B., Santos-Sanz, P., and Braga-Ribas, F.: 2020, *The Trans-Neptunian Solar System*, 413. doi:10.1016/B978-0-12-816490-7.00019-9.

Pavlov, H., Anderson, R., Barry, T., Gault, D., Glover, R., Meister, S., and, ...: 2020, *Journal for Occultation Astronomy* **10**, 8. doi:www.iota-es.de/JOA/JOA2020_3.pdf#page=8.

Petit, J.-M., Kavelaars, J. J., Gladman, B., and Loredo, T.: 2008, *The Solar System Beyond Neptune*, 71.

Schenk, P.M. and Moore, J.M.: 2020, *Philosophical Transactions of the Royal Society of London Series A* **378**, 20200102. doi:10.1098/rsta.2020.0102.

Spencer, J.R., Stern, S.A., Moore, J.M., et al.: 2020 (a), Science, 367, aay3999.

Spencer, J., Grundy, W.M., Nimmo, F., and Young, L.A.: 2020 (b), *The Trans-Neptunian Solar System*, 271. doi:10.1016/B978-0-12-816490-7.00012-6.

Stansberry, J., Grundy, W., Brown, M., et al.: 2008, *The Solar System Beyond Neptune*, 161.

Stern, S.A., Bagenal, F., Ennico, K., et al.: 2015, *Science* **350**, aad1815. doi:10.1126/science.aad1815.

Stern, S. A., Weaver, H. A., Spencer, J. R., et al.: 2019, *Science* **364**, aaw9771.

Storn, R., Price, K.: 1997, *Differential Evolution – A Simple and Efficient Heuristic for global Optimization over Continuous Spaces*, 11. doi.org/10.1023/A:1008202821328.

Stern, S.A., Spencer, J.R., Verbiscer, A., et al.: 2020, *The Trans-Neptunian Solar System*, 379. doi:10.1016/B978-0-12-816490-7.00017-5.

Tancredi, G. and Favre, S.: 2008, *Icarus* **195**, 851. doi:10.1016/j.icarus.2007.12.020.

Thirouin, A. 2013. Study of Trans-Neptunian Objects using photometric techniques and numerical simulations. *thesis*, ISBN: 978-84-9028-749-1.

Van Laerhoven, C., Gladman, B., Volk, K., Kavelaars, J.J., Petit, J.-M., Bannister, M.T., and, ...: 2019, *The Astronomical Journal* **158**, 49. doi:10.3847/1538-3881/ab24e1.

Vilenius, E., Kiss, C., Mommert, M., et al.: 2012, *Astronomy and Astrophysics* **541**, A94.

Weaver, H.A. and Stern, S.A.: 2008, *The Solar System Beyond Neptune*, 557.

[1] Observatório Nacional/MCTIC, R. General José Cristino 77, Bairro Imperial de São Cristóvão, Rio de Janeiro (RJ), Brazil
e-mail: flaviarommel@.on.br

[2] Laboratório Interinstitucional de e-Astronomia - LIneA & INCT do e-Universo, Rua Gal. José Cristino 77, Bairro Imperial de São Cristóvão, Rio de Janeiro (RJ), Brazil

[3] Federal University of Technology - Paraná (UTFPR / DAFIS), Rua Sete de Setembro, 3165, Curitiba (PR), Brazil

[4] Instituto de Astrofísica de Andalucía, IAA-CSIC, Glorieta de la Astronomía s/n, 18008 Granada, Spain

[5] LESIA, Observatoire de Paris, Université PSL, CNRS, Sorbonne Université, Univ. Paris Diderot, Sorbonne Paris Cité, 5 place Jules Janssen, 92195 Meudon, France

[6] Institut Polytechnique des Sciences Avancées IPSA, 63 boulevard de Brandebourg, F-94200 Ivry-sur-Seine, France

[7] Institut de Mécanique Céleste et de Calcul des Éphémérides, IMCCE, Observatoire de Paris, PSL Research University, CNRS,Sorbonne Universités, UPMC Univ Paris 06, Univ. Lille, 77, Av. Denfert-Rochereau, F-75014 Paris, France

[8] Florida Space Institute, University of Central Florida, 12354 Research Parkway, Partnership 1, Orlando, FL, USA

[9] Observatório do Valongo/UFRJ, Ladeira Pedro Antônio 43, Rio de Janeiro (RJ), Brazil

[10] UNESP - São Paulo State University, Grupo de Dinâmica Orbital e Planetologia, CEP 12516-410, Guaratinguetá, SP, Brazil

[11] Institute of Physics, Federal University of Uberlândia, Uberlândia, MG, Brazil

[12] Institute of science and technology, Akdeniz University, Antalya, Turkey

[13] Tübitak National Observatory, Bakirlitepe mountain, Antalya, Turkey

[14] Space Telescope Science Institute: Baltimore, MD, United States of America

[15] Syrma-GUA, Valladolid, Spain

[16] Euraster, 1 rue du tonnelier, 46100 Faycelles, France

[17] STAR Institute, Université de Liège, Allée du 6 août, 19C, 4000 Liège, Belgium

[18] San Pedro de Atacama Celestial Explorations - SPACE, Chile

[19] Panamanian Observatory in San Pedro de Atacama - OPSPA

[20] Anarchist Mt. Observatory, Osoyoos, Canada

[21] Côte d'Azur Observatory, Caussols, France

[22] Bacau Observatory, Romania

[23] The Fireball Recovery and InterPlanetary Observation Network (FRIPON), Algeria

[24] Observatory of Algiers, CRAAG, Route de l'Observatoire, Algiers, Algeria

[25] Osservatorio Astronomico Montagna Pistoiese GAMP, San Marcello Pistoiese, Italy

[26] G. Pascoli Observatory, Castelvecchio Pascoli, Italy

[27] Tavolaia Observatory, Santa Maria a Monte, Italy

[28] INAF – Osservatorio Astronomico di Trieste, Trieste, Italy

[29] Caussols Observatory, Cannes, France

[30] Spica Observatory, Signa, Italy

[31] Missing information, Massa, Italy

[32] Santa Maria de Montmagastrell, Lleida, Spain

[33] Department of Earth, Atmospheric and Planetary Science, Massachusetts Institute of Technology, Massachusetts, United States of America

[34] Cancelada Observatory, Estepona, Spain

[35] EPT Observatories, Tijarafe, La Palma, Spain

[36] OACM Observatory, Fuensanta de Martos, Jaen, Spain

[37] Missing information

[38] Istituto Nazionale di AstroFisica. INAF Osservatorio Astrofisico di Catania (OACt-INAF), Catania, Italy

[39] I.Ü.F.F Astronomy and Space Sciences Department, University of İstanbul, Turkey

[40] Kharkiv University, Kharkiv, Ukraine

[41] Osservatorio Astronomico di Monte Agliale, Via Cune Motrone, Borgo a Mozzano, Italy

[42] Grupo Astrofili Galileo Galilei - GrAG, Viterbo, Italy

[43] Hvar Observatory, Faculty of Geodesy, University of Zagreb, Zagreb, Croatia

[44] Lowell Observatory, Flagstaff, Arizona, United States of America

[45] Colle S. Agata observatory, Rome, Italy

[46] Konkoly Observatory, Research Centre for Astronomy and Earth Sciences, Budapest, Hungary

[47] Cosmos Observatory, Marbella, Spain

[48] Stardust Observatory, Brasov, Romania

[49] Cala D'Hort observatory, Ibiza, Spain

[50] St george Observatory, Ploiesti, Romania

[51]

[52] CARA Project, INAF—Osservatorio Astronomico, via Tiepolo 11, I-34143 Trieste, Italy

[53] Department of Physics, Faculty of Arts and Sciences, Çanakkale Onsekiz Mart University, 17100 Çanakkale, Turkey

[54] Astrophysics Research Center and Ulupınar Observatory, Çanakkale Onsekiz Mart University, 17100, Çanakkale, Turkey

[55] Canary Islands Institute of Astrophysics, Tenerife, Spain
[56] Missing information
[57] Physics Division, Lawrence Berkeley National Laboratory, 1 Cyclotron Road, Berkeley, CA 94720, USA
[58] University of Zagreb, Faculty of Electrical Engineering and Computing, Department of Applied Physics, Unska 3, 10000 Zagreb, Croatia
[59] Astronomical Institute, Academy of Sciences of the Czech Republic, Fričova 298, 251 65 Ondřejov, Czech Republic
[60] Astronomical Observatory of Odessa I.I. Mechnikov National University, 1v Marazlievska str., Odessa, 65014, Ukraine
[61] Astronomical Institute, Slovak Academy of Sciences, 059 60 Tatranská Lomnica, Slovakia
[62] Astronomical Observatory Institute, Faculty of Physics, Adam Mickiewicz University, Poznan, Poland
[63] University of Ljubljana, Faculty of Mathematics and Physics, Jadranska 19, 1000 Ljubljana, Slovenia
[64] Aix Marseille Univ, CNRS, CNES, LAM, Marseille, France
[65] INAF-Astronomical Observatory of Padova, Vicolo dell'Osservatorio 5, I-35122 Padova, Italy
[66] SOTAS - Stellar Occultation Timing Association Switzerland, Swiss Astronomical Society, Switzerland
[67] Eötvös Loránd University, Department of Astronomy, Pázmány Péter sétány 1/A, 1117 Budapest, Hungary
[68] ELTE Eötvös Loránd University, Institute of Physics, Pázmány Péter sétány 1/A, 1117 Budapest, Hungary
[69] Agrupación Astronómica de Sabadell, Carrer Prat de la Riba, s/n, 08206 Sabadell, Catalonia, Spain
[70] International Occultation Timing Association - European Section (IOTA-ES), Germany
[71] Leonard de Vinci Telescope, GAPRA, 2 rue Marcel Paul, 06160 Antibes, France
[72] Agrupación Astronómica de Eivissa, Ibiza, Spain
[73] Sociedad Astronomica Granadina, Granada, Spain
[74] Universidade Estadual de Ponta Grossa (UEPG), Ponta Grossa, Brazil
[75] Rothney Astrophysical Observatory, University of Calgary, Calgary, Canada
[76] Purdue University Northwest, Hammond Campus, Indiana, United States
[77] Department of Physics University of Idaho, Idaho, United States
[78] The University of Kansas, Kansas, United States
[79] Department of Physics and Astronomy, Calvin College, Grand Rapids, Michigan, USA
[80] Institute for Fundamental Science, University of Florida, United States

Appendix A: Observational circumstances

The following tables summarize the observational circumstances of each station of the nine stellar occultations presented in this work. For better visualization, the tables were divided into two groups i) the 8 August 2020 event and ii) the other eight stellar occultations. The positive, negative and overcast locations involved in the 8 August 2020 campaign are listed in the Tables A.1, A.2 and A.3, respectively. Positive and negative observations of the other eight events are present in the Tables A.4 and A.5, respectively.

Table A.1: Observational circumstances of all observatories that detected the stellar occultation by MS4 on 8 August 2020. The * symbol indicates that this data was taken in drift scan mode.

Observatory, nearest city, country	**Latitude (°), longitude (°), altitude (m)**	**Telescope, aperture (m), filter**	**Time source, instrument**	**Exposure (s), cycle (s), correction (s)**	**Observers**
Domaine de La Blaque, Varages, France	+43.61239 +05.96363 468.0	Ritchey-Chrétien 0.5 Clear	GPS WATEC 910HX	0.32 0.32 -	Jean Lecacheux, Jean-Luc Plouvier
TAROT Calern, Caussols, France	+43.752001 +06.923613 1268.0	TAROT North 0.25 Clear	GPS Andor DZ936N-BEX2-DD	90.0* 90.0* -	Eric Frappa, Alain Klotz
Méo Station, Grasse, France	+43.7546 +06.9216 1323.1	Ritchey-Chrétien 1.54 Clear	NTP ZWO ASI1600MM	1.0 1.0 -	Dominique Albanese, Hervé Mariey
Caussols, Cannes, France	+43.753055556 +6.921666667 1268.0	- 0.40 Clear	NTP ZWO 294 MC -	3.0 4.0 +0.4	Raymond Behem, Jean Pierre Prost
Sta Maria de Montmagastrell, Lleida, Spain	+41.720166 +01.105361 318.0	- 0.406 Clear	NTP SBIG STL-11000	7.0 18.0 -4.0	Josep M. Bosch Ignés
Saint-Paul-en-Forêt, Cannes, France	+43.560124 +06.692868 45.0	- 0.2 Clear	NTP ZWO ASI290MM	2.0 2.22 -	Romain Fafet
Nice, Nice, France	+43.725902 +07.299875 364.0	- 0.4 Clear	GPS Raptor Photonics	0.3 0.3 -3.7	Stéfan Renner, Matthieu Conjat
Valbonne, Valbonne, France	+43.619604 +07.039157 174.0	François Giraud (TFG) 0.4 Clear	GPS WATEC 910HX	1.0688 1.5163 -0.5339	Florian Signoret
Crni Vrh, Crni Vrh, Slovenia	+45.94586111 +14.07122222 726.0	Cichocki Sky Survey 0.6 W (clear)	NTP Apogee Alta U16M	1.5984 3.1095 -	Herman Mikuz
Piszkéstető Mountain Station, Mátraszentistván, Hungary	+47.917833 +19.8955833 960.0	Ritchey-Chrétien-Coudé 1.0 Clear	NTP Andor iXon - 888	0.56115 0.56791 -	Róbert Szakáts
University of Ljubljana, Ljubljana, Slovenia	+46.043806 +14.5274444 400.0	- 0.25 Clear	NTP QHY 5III-178M	2.0 2.0 -	Bojan Dintinjana
Konkoly, Budapest, Hungary	+47.4999553 +18.9620488 470.0	- 0.3 Clear	NTP ASI178MM	1.0 1.0385 -	Andras Pal, Balazs Csak
Trieste, Trieste, Italy	+45.642721 +13.875383 400.0	Schmidt-Cassegrain 0.355 Luminance	NTP Apogee U Alta KAF-8300	4.0 5.0 +2.0	Paolo Di Marcantonio, Igor Coretti, Giulia Iafrate, Veronica Baldini
Sant Esteve Sesrovires, Catalonia, Spain	+41.494867 +01.8738 180.0	Newtonian 0.4 Clear	GPS Mintron 12V6HC-EX	1.28 1.28 - 1.28	Carles Schnabel, Martí Schnabel
ALMO Observatory, Bologna (Padulle), Italy	+44.627 +11.2805 19.0	Schmidt-Cassegrain 0.235 Clear	NTP ZWO ASI120mm	3.0 3.0 +1.0	Adriano Valvasori, Ernesto Guido
- Massa, Italy	+44.026083333 +10.138611111 41.0	Schmidt-Cassegrain 0.2 Clear	GPS WATEC 910BD	2.56 2.60 -2.56	Michele Bigi
G. Pascoli, Castelvecchio Pascoli, Italy	+44.0603 +10.4625 257.0	Newtonian 0.41 Clear	NTP Sony QHY22	1.5 4.0 +2.2	Roberto Bacci

Table A.1 continued

Mount Agliale, Borgo a Mozzano, Italy	+43.99530 +10.51494 750.0	Newtonian 0.50 Clear	NTP FLI - Proline 4710	4.0 5.35 -	Fabrizio Ciabattari
Pistoiese Mountain, San Marcello Pistoiese, Italy	+44.063055 +10.804166 990.0	Newtonian 0.6 Clear	NTP (GPS-PPS) Apogee U6 Alta	1.0 3.13 -	Paolo Bacci, Martina Maestripieri, Marta Di Grazia
Tavolaia, Sta. Maria a Monte, Italy	+43.736833 +10.673445 34.0	Newtonian 0.4 Clear	NTP ASI 174 MM	2.0 2.0 -2.0	Mauro Bachini, Giacomo Succi
Spica, Signa, Italy	+43.789336 +11.089922 50.0	- 0.3 Clear	NTP SBIG ST-402 XME	3.0 4.0 -	Mauro Bertini
Margherita Hack, Lastra a Signa, Italy	+43.742280556 +11.1030305556 216.0	- 0.356 Clear	NTP SBIG ST10XME	2.0 4.45 -	Nico Montigiani, Massimiliano Mannucci
Zalistci, Khmelnytskyi, Ukraine	+48.84778 +26.72139 100.0	- 0.5 V	GPS FLI 16070	2.0 33.2 -	T.O. Dementiev, O. M. Kozhukhov
- Sevilla, Spain	+37.346111 -5.980556 28.0	- 0.28 Clear	GPS QHY 174M	0.6 0.6 -	Jose Maria Madiedo
El Arenosillo, Huelva, Spain	+37.103889 -06.7338889 54.0	BOOTES-1B 0.3 Clear	NTP Andor Ixon	2.0 4.0 -0.7	Emilio Jesus Fernández García, Alberto J. Castro Tirado
ROASTERR-1, Cluj-Napoca, Romania	+46.820954 +23.596400 390.0	- 0.3 Clear	NTP atik 383L+	4.0 5.0 -	Lucian Hudin
Fuensanta de Martos, Fuensanta de Martos, Spain	+37.646389 -03.917468 710.0	Newtonian 0.36 Luminance	atom time SBIG ST-10xme	2.0 8.0 -	Jose Carrillo Gomez
- Fiastra, Italy	+43.057093 +13.173074 700.0	- 0.254 Clear	NTP SBIG ST8-XME	3.0 6.1 -	Alessio Ciarnella
- Dragsina, Romania	+45.703344 +21.436879 97.0	- 0.4 Clear	NTP ZWO ASI 1600MM-Pro	0.9 1.47 -2.0	Liviu Stoian, Andrei Juravle
Cala D'Hort, Ibiza, Spain	+38.89111111 -1.24083333 130.0	- 0.5 Luminance	NTP Sbig STL11000	3.0 6.0 -	Ignacio de la Cueva Torregrosa, Marco Moreno Yuste
Alhendín, Granada, Spain	+37.1110313 -03.6394227 740.0	Newtonian 0.2 Clear	NTP ZWO ASI 178MM	5.0 5.125 -	Miguel Sánchez González
Sierra Nevada, Granada, Spain	+37.0641667 -03.384722 2896.0	T150 1.5 Clear	NTP Andor Ikon-L	1.0 2.0 -	Alfredo Sota, Pablo Santos Sanz, José Luis Ortiz, Nicolás Morales
Sierra Nevada, Granada, Spain	+37.0641667 -03.384722 2896.0	T90 0.9 Clear	NTP Roper VersArray	1.0 3.0 -	
Cancelada, Estepona, Spain	+36.461111111 -05.05444444 25.0	- 0.254 Luminance	Mount Sync MaxIm DL 6 ATIK - 460 ex	10.0 18.0 -	Juan Francisco Calvo Fernández
Cosmos, Marbella, Spain	+36.516229 -04.857376 70.0	- 0.355 Luminance	NTP ATIK 460ex	10.0 21.0 -	Fran Cuevas
Colle S. Agata, Rome, Italy	+41.94955555 +12.42855555 124.0	Schmidt-Cassegrain 0.28 Clear	GPS QHY174M	2.0 2.0 -	Claudio Costa
Hvar, Hvar, Croatia	+43.178944 +16.447748 190.0	- 1.06 Clear	NTP ASI294MC Pro	3.0 3.2 -	Stefan Cikota, Domagoj Ruždjak, Aleksandar Cikota
- Bacau, Romania	+46.50779 +26.80007 555.0	Newtonian 0.254 IR Cut	NTP ZWO ASI 178 MM	3.0 3.18 -	Radu Anghel

Table A.1 continued

Agrustos, Sassari, Italy	+40.7278448 +09.6948317 20.0	SC 0.13 Clear	GPS QHY174 M	4.0 4.0 -	Salvatore Lamina
Campo Catino, Sgurgola, Italy	+41.821115 +13.3292867 1485.0	- 0.8 Clear	GPS QHY 174C	1.0 1.0 -3.0	Ugo Tagliaferri, Mario Di Sora, Giovanni Isopi
Kharkiv University, Kharkiv, Ukraine	+49.64083 +36.93389 156.0	Reflector AZT - 8 0.7 Luminance	NTP FLI ML4710	2.0 3.0 -	Y. Krugly, I. Slyusarev, V. Chiorny
Kharkiv University, Kharkiv, Ukraine	+49.64083 +36.93389 156.0	Baker-Schmidt 0.36 R	NTP FLI PL1001E	4.0 5.0 -	Y. Krugly, A.Zheleznyak
Ceccano, Ceccano, Italy	+41.567717 +13.333301 178.0	- 0.432 Clear	NTP SBIG STL-6303E	3.5 4.0 -	Gianluca Masi
Stardust, Brasov, Romania	+45.641611 +25.621889 597.0	CPC800 0.2 Clear	NTP Atik 383L+	10.0 13.0 -	Lucian Curelaru
- Bârlad, Romania	+46.2313888 +27.6694444 70.0	EQMOD ASCOM 0.2 Luminance	NTP ASI 1600	8.0 8.8 -	Dumitru Ciprian Vîntdevară
Stardreams, Valenii de Munte, Romania	+45.203642 +26.045526 380.0	- 0.203 Clear	NTP ATIK 460ex	4.0 5.0 +1.5	Radu Mihai Gherase
St. George, Ploiesti, Romania	+45.007213 +25.978711 243.0	- 0.19 Luminance	NTP ATIK 460EX mono	7.0 8.0 -18.0	Cristian Adrian Danescu
Odessa-Mayaki, Odessa, Ukraine	+46.39696195 +30.27127709 19.0	- 0.80 Clear	GPS QHY174M	1.0 1.0 -	V. Kashuba, N. Koshkin, V. Zhukov
Nastro Verde, Naples, Italy	+40.618714 +14.357628 275.0	SC Meade LX200 0.3556 Clear	NTP ASI 120 MM-S	2.5264 2.96 -3.2	Nello Ruocco
- Agerola, Italy	+40.6260833 +14.571555 708.0	SC C14 EDGE HD 0.355 Clear	NTP ASI 178 mono	0.6 0.6 -	Luigi Morrone
Algiers-Bouzareah, Algiers, Algeria	+36.79787333 +03.032248333 348.3	Ritchey-Chrétien 0.81 Clear	GPS WATEC 910 HX/RC	0.08 0.08 -0.04	D. Baba Aissa, Z. Gringahcene
Roque de Los Muchachos, La Palma, Spain	+28.7624 -17.8792 2363.0	Liverpool 2.0 V+R	NTP Andor DW485 (RISE)	0.6 0.6324 -	Pablo Santos-Sanz Nicolás Morales, José Luis Ortiz
EPTOs, Tijarafe, Spain	+28.741667 -17.92972223 1079.0	Marcon RC 0.40 Clear	NTP FLI PL4240	4.0 5.0 +1.0	Daniele Carosati
Astronomic Society of Tunisia, Ariana, Tunisia	+36.8842 +10.1949 5.0	- 0.203 Clear	GPS ZWO ASI 120 MM	2.0 2.0 -1.894	Sofien Kamoun
Teide, Spain	+28.3000 -16.5097 2390.0	Artemis 1.0 Clear	GPS Andor IKONL BEX2 DD	1.5 2.0 -	Artem Burdanov, Emmanuel Jehin
Teide, Spain	+28.3000 -16.5097 2390.0	TAR1 0.46 Clear	NTP FLI KL 400	1.0 1.0 -0.5	Miquel Serra-Ricart, Miguel R. Alarcón, Javier Licandro
- Catania, Italy	+37.69291 +14.97355 1727.0	- 0.91 Clear	NTP Developed at observatory	6.0 10.0 +2.0	A. Frasca, G. Catanzaro, R. Zanchez, Giuseppe Leto
Kuban State University, Kuban, Russia	+45.01667 +39.0333 76.0	Paramount ME 0.508 Luminance	GPS FLI PL1001E	3.0 5.0 -	A.L. Ivanov, V.A. Ivanov, N.B. Ivanova
Istanbul University, Çanakkale, Turkey	+40.09899 +26.47449 410.0	Ritchey-Chrétien 0.6 Clear	GPS Andor iXon Ultra 888	2.0 3.0 -	Süleyman Fişek, Oğuzhan Çakır, Simge Özer

Table A.2: Observational circumstances of all the stations that acquired data of the 8 August 2020 event but did not detect the occultation. * This information is from http://www.ieec.cat/en/content/210/telescope-and-dome.

Observatory, nearest city, country	Latitude (°), longitude (°), altitude (m)	Telescope, aperture (m), filter	Time source, instrument	Exposure (s), cycle (s), correction (s)	Observers
Sternwarte Comthurey, Neustrelitz, Germany	+53.26608 +13.1901666 74.0	- 0.18 Clear	GPS QHY174	2.964 2.964	Konrad Guhl
Breitenweg, Herkenrath, Germany	+50.993310 +07.183794 200.0	RC 0.304 Clear	GPS Watec 120N+	2.56 2.56	Bernd Klemt
Biesenthal, Biesenthal, Germany	+52.759278 +13.663 263.0	Newtonian 0.3 Clear	GPS QHY174	? ?	Nikolai Wuensche
- Berlin, Germany	+52.516111 +13.427778 40.0	Newtonian 0.254 Clear	GPS DVTI	3.0 3.0	Christian Weber
Eppstein-Bremthal, Wiesbaden, Germany	+50.13816667 +08.364 256.0	Schmidt-Cassegrain 0.254 Clear	GPS QHY-174M	3.0 3.0	Oliver Kloes
Vierzon, Vierzon, France	+47.223258 +02.052731 100.0	- 0.25 Clear	Time Box ZWO 1600 M	1.5 ?	Lionel Rousselot
Borowiec, Poznan, Poland	+52.276896 +17.075216 123.0	- 0.4 Clear	NTP SBIG ST7	3.0 (S) 5.0	Anna Marciniak
Teplice, Teplice, Czech Republic	+50.63833 +13.84675 275.0	Planewave CDK17 0.43 Clear	TimeBox Apogee Aspen CG9000	0.5 0.58	Zdenek Moravec
Plzen, Plzen, Czech Republic	+49.69475 +13.321 339.0	- 0.303 Clear	GPS QHY 174	1.0 ?	Jiri Polak
Plzen, Plzen, Czech Republic	+49.7073333 +13.3321667 326.0	- 0.303 Clear	GPS QHY 174	1.0 ?	Michal Rottenborn
Ksiezyno, Bialystok, Poland	+53.075944 +23.102194 145.0	Newtonian 0.3 Clear	GPS QHY174	2.0 ?	Wojciech Burzynski, Maciej Borkowski
Ondrejov, Ondrejov, Czech Republic	+49.91056 +14.78364 528.0	- 0.65 Clear	NTP Moravian G2-3200	6.0 ?	Kamil Hornoch
Allariz, Orense, Spain	+42.2 -07.77 490.0	- 0.254 Clear	NTP QHY6	8.0 ~10.0	Luis Perez
Buelach, Buelach, Switzerland	+47.51956 +08.57064 550.0	- 0.50 Clear	GPS DVTI	? ?	Stefan Meister
Max Planck Institut, Garching, Germany	+48.261388889 +11.671111111 480.0	- 0.61 Clear	GPS SBIG STX-16803	3.0 12.9	Vadim Burwitz, Piotr Sybilski, Wienczyslaw Bykowski, Thomas Müller
Giesing, Munich, Germany	+48.12194 +11.6072 500.0	Cassegrain 0.80 Orange	Computer Atik 3141	1.355 1.355	Bernd Gährken
Český Rudolec - Matějovec, Strmilov, Czechia	+49.08277778 +15.22841667 707.0	- 0.203 Clear	GPS QHY 174M	2.5 ?	Jiří Kubánek
Wendelstein, Brannenburg, Germany	+47.703638889 +12.012055556 1836.0	- 2.1 SDSS r + SDSS i	GPS 3kk	1.0 13.0	Michael Schmidt
Nonndorf, Waidhofen an der Thaya, Austria	+48.78695667 +15.23565667 549.0	- 0.254 Clear	GPS WAT-610BD	1.28 ?	Gerhard Dangl
Cannet, Riscle, France	+43.62093 -0.044685 180.0	- 0.40 Clear	GPS Watec 120N+	1.28 ?	Jean Jaques Castellani
Saint-Caprais, Rabastens, France	+43.874044 +01.718749 193.0	- 0.94 Clear	GPS WATEC 910HX	0.64 ?	Eric Frappa, Alain Klotz, Maylis Lavayssiere
PDlink, Cadca, Slovakia	+49.4042222 +18.7026306 680.2	- 0.4 Clear	NTP or GPS? QHY 5 III 290M	0.9945 0.9945 -	Peter Delincak
- Muzzano-Lugano, Switzerland	+45.9862778 +08.91958333 350.0	Schmidt-Cassegrain 0.23 Clear	GPS Watec 910/HX-RC	1.28 ?	Alberto Ossola

Table A.2 continued

Schiaparelli, Varese, Italy	+45.86778 +08.77083 1230.0	Reflector 0.84 Clear	NTP SBIG STX-16803	4.0 7.0	Luca Buzzi
- Kysucké Nové Mesto, Slovakia	+49.307305556 +18.765388889 469.0	- 0.252 Clear	GPS QHY174	380 380	Marian Urbaník
Belesta, Toulouse, France	+43.438391949 +01.83152549 234.0	- 0.20 Clear	GPS WATEC 910HX	0.64 ?	Andre Pascal
Latrape, Toulouse, France	+43.243969 +01.290111 350.0	- 0.305 UV-IR block	GPS Watec 910 HX/RC	5.12 ?	Michel Boutet, Jacques Sanchez
Suhora, Poreba Wielka, Poland	+49.5691728579 +20.06728579 1000.0	- 0.6 Clear	GPS Apogee Aspen-47	2.0 3.0 -	Waldemar Ogloza
Filzi School, Bolzano, Italy	+46.42278 +11.33833 280.0	RC Refractor 0.355 Clear	NTP ASI 294 pro	1.0 1.0 -	G. B. Casalnuovo
GiaGa, Pogliano Milanese, Italy	+45.54145833 +08.9954750 172.0	Schmidt-Cassegrain 0.356 Clear	NTP Moravian G2-3200 Mark II	4.0 12.33 -	Galli Gianni
Skalnaté Pleso, Tatranská Lomnica, Slovakia	+49.189355 +20.233816 1786.0	- 0.61 Clear	NTP SBIG ST-10XME	4.0 6.8 -	Marek Husárik
Skalnaté Pleso, Poprad, Slovakia	+49.1894 +20.2341 1786.0	- 1.3 Clear	NTP ZWO ASI 1600MM pro	1.0 1.0	Richard Komzik, Theodor Pribulla, Dusan Tomko
Chante-Perdrix, Dauban, France	+43.99972222 +05.6475 630.0	SC 0.275 Clear	NTP SBIG ST8-XME	2.0 4.1	Marc Serrau, X. Delmotte
Centro de Ciência Viva, Constância, Portugal	+39.49489 -08.32367 147.0	RC 0.508 Clear	GPS WATEC 910HX-RC	0.64 (E) ?	Rui Gonçalves, João Ferreira, Maximo Ferreira, Miguel Bento
Cima Ekar, Asiago, Italy	+45.8494453 +11.5688257 1369.9	- 0.67 Clear	NTP Moravian G4-16000	4.0 ?	Domenico Nardiello
Montsec, Catalonia, Spain	+42.051666 +0.7297222 1570	Joan Oró 0.8 V	NTP+GPS* MEIA3	5.0 ~8.85	Toni Santana
TURKSAT, Ankara, Turkey	+39.636632 +32.804157 950.0	TURKSAT 0.5 Clear	GPS FLI PL4240	3.0 5.0	Mehmed Naim Bagiran
TUBITAK National, Antalya, Turkey	+36.825271 +30.3333 2538.725	ACE T100 1.0 Clear	GPS SI 1100 Cryo	3.0 6.45	Yucel Kilic, Orhan Erece, Sila Eryilmaz
Çukurova University, Adana, Turkey	+37.059684 +35.3554 130.0	Pro RC 500 LK7 0.50 Clear	NTP Apogee Aspen CG6	5.0 5.0	Mahmut Tekeş
Adiyaman University, Adiyaman, Turkey	+37.751667 +38.225278 675.0	ADYU60 0.61 Clear	GPS Andor iKon-M 934	3.0 3.0	Eda Sonbas, Huseyin ER

Table A.3: Observational circumstances of all the sites that tried to observe the 8 August 2020 event but had bad weather or technical issues and did not acquired data. The symbol * indicates that the information is from Google Earth.

Observatory, Nnearest city, country	**Latitude (°), longitude (°), altitude (m)**	**Telescope aperture (m) filter**	**Time source, instrument**	**Observers**
Pinsoro, Pinsoro, Spain	+42.19916666 -01.3388888 365.0	- 0.28 Clear	GPS Mintron MTV-12V6HC-EX	Oscar Canales Moreno
Montseny, Sant Celoni, Spain	+41.7214 +02.5206 300.0	- 0.254 Clear	NTP ST8	Josep M. Trigo-Rodríguez
Sabadell, Sabadell, Spain	+41.55002777 +2.08333333 224.0	- 0.5 Clear	GPS Watec 910HX-RC	Carlos Perelló
Calar Alto, Almería, Spain	+37.22083245 -2.540997836 2168.0	- 1.23 Clear	NTP PlanetCam	Ricardo Hueso
Urseanu, Bucharest, Romania	+44.448611 +26.093056 100.0	- 0.405 Clear	NTP ZWO ASI 224 MC color	Dascalu Mihai
Traian - Ialomița, Slobozia, Romania	+44.761488 +27.341830 30.0	- 0.2 UV/IR Cut	NTP QHY 163 M	Daniel Nicolae Bertesteanu
TRAPPIST-North, Oukaimeden, Morroco	+31.2061 -7.8664 2751	- 0.6 Clear	NTP Andor IKONL BEX2 DD	Emmanuel Jehin
AGM, Marrakech, Morroco	+31.173411 -8.077456 400.0	- 0.355 Clear	NTP DMK 31AU03.AS	Mohammed Sabil
Specca, Ioannina, Greece	+39.60175 +20.87014 480.0	- 0.2 Clear	GPS Canon Eos 1200D	Georgios Lekkas
Empesos, Agrinion, Greece	+39.02570544 +21.31730396 334.0	- 0.25 Clear	Occult Flash Tag ZWO ASI 224 MC	Vagelis Tsamis, Kyriaki Tigani
- Amfiloxia, Greece	+38.805170 +21.173370 218.0	- 0.25 Clear	NTP ATIK 460exm	Nick Sioulas
Istanbul Univ., Istanbul, Turkey	+41.011749 +28.965718 60.0	İST40 0.4 Clear	NTP Moravian G2 8300	Süleyman Fişek, Oğuzhan Çakır
Athens University, Zografos, Greece	+37.968561 +23.783368 250.0	- 0.4 Clear	NTP ZWO ASI 290MM	Kosmas Gazeas
Eskisehir Univ., Eskisehir, Turkey	+39.885472 +30.460689 1005.0	- 0.4 Clear	GPS FLI	Metin Altan
Ondokuz Mayıs Univ. Samsun, Turkey	+41.367727 +36.201576 150.0	- 0.37 Clear	GPS SBIG STL-4020M	Selami Kalkan

Table A.4: Observational circumstances of all stations that detected 2002 MS4 in a stellar occultation on the other eight events.

Date	Site/country (detection)	Latitude (° ' '') Longitude (° ' '') Altitude (m)	Telescope aperture (m) filter	Time source instrument	Exposure (s) cycle (s) correction (s)	Observers
09 July 2019	San Pedro de Atacama/CHL	22 57 11.4 S 68 10 47.6 W 2,396.9	OPSPA 0.4 ?	? Proline PL1680	2.0 ≈ 3.67	Alain Maury, Joaquín Fábrega Polleri
		22 57 12.1 S 68 10 46.8 W 2,398.5	ASH2 0.407 ?	NTP SBIG STL11000	8.0 ≈ 10.5	Nicolás Morales
	Pico dos Dias/BRA	22 32 07.8 S 45 34 57.5 W 1,810.7	Perkin-Elmer 1.60 ?	GPS Andor Ixon 4269	0.3 ∼1.65	Flavia L. Rommel, Rodrigo Boufleur
26 July 2019	San Pedro de Atacama/CHL	22 57 11.4 S 68 10 47.6 W 2,396.9	OPSPA 0.4 ?	? Proline PL16803	30.0 ≈ 31.9	Alain Maury, Joaquín Fábrega Polleri
		22 57 12.1 S 68 10 46.8 W 2,398.5	ASH2 0.407 ?	NTP SBIG STL11000	25.0 ≈ 27.6 +3.0	Nícolás Morales
	Paranal/CHL	24 36 57.9 S 70 23 26.0 W 2,479.2	SPECULOOS 1.0 ?	? Andor Tech	2.0 ≈ 4.0	Emmanuel Jehin
	Pico dos Dias/BRA	22 32 07.78 S 45 34 57.5 W 1,810.7	Perkin-Elmer 1.60 ?	GPS Andor Ixon 4269	0.8 ≈ 0.813	Gustavo Benedetti Rossi
26 July 2019	Osoyoos/CAN	49 00 31.8 N 119 21 46.7 W 1,088.0	? ? ?	GPS QHY174M	2.0 2.0	Peter Ceravolo
19 August 2019	Victoria/CAN	49 32 02.0 N 119 33 27.0 W 0.0	Meade SCT 0.4 ?	GPS QHY174M	2.5 2.5	Bruce Gowe
	Osoyoos/CAN	49 00 31.8 N 119 21 46.7 W 1,088.0	? ? ?	GPS QHY174M	4.0 4.0	Peter Ceravolo
26 July 2020	Pretoria/ZAF	25 53 00.0 S 28 09 00.0 E 1,489.0	Celestron SCT 0.356 ?	NTP ZWOASI290MM	1.0 1.015	Clyde Foster
	Johannesburg/ZAF	26 06 20.0 S 27 57 03.0 E 1,547.0	- 0.305 ?	NTP ZWOASI290MM	2.0 2.015	Cory Schmitz
24 February 2021	San Pedro de Atacama/CHL	22 57 11.4 S 68 10 47.6 W 2,396.9	OPSPA 0.4 ?	? ZWO ASI6200MM Pro	10.0 ≈11.7	Alain Maury, Joaquín Fábrega Polleri
		22 57 12.1 S 68 10 46.8 W 2,398.5	ASH2 0.407 ?	NTP SBIG STL11000	10.0 ≈12.8	Nicolás Morales
14 October 2021	Osoyoos/CAN	49 00 32.1906 N 119 21 46.268 W 0.0	? ? ?	GPS QHY174M	3.0 3.0	Peter Ceravolo
	Flagstaff/USA	35 12 10.4508 N 111 40 01.416 W 2216.0	Ritchey–Chrétien 0.318 ?	GPS CMOS	2.498 2.4996	Michael Collins
10 June 2022	La Palma/ESP	28 45 45.0576 N 17 52 45.12 W 2,387.63	Liverpool 2.0 ?	NTP Andor DW485 (RISE)	1.183 1.2226	René Duffard, Jose Luis Ortiz, Nicolás Morales
	Teide/ESP	28 18 00.00 N 16 30 34.92 W 2,390.0	Artemis 1.0 ?	GPS Andor IKONL BEX2 DD	1.0 1.81 +0.5	Emmanuel Jehin
	Three Gate Farm/USA	33 20 51.5376 N 88 43 58.3114 W 93.05	Schmidt–Cassegrain 0.2 ?	NTP Atik 414ex via Ekos	5.0 5.4518 -0.8	Jean-Francois Gout

Table A.5: Observational circumstances of all the stations that did not detect 2002 MS4 or had bad weather during the other eight stellar occultations.

Date	**Site/country (detection)**	**Latitude (° ’ ") longitude (° ’ ") altitude (m)**	**Telescope aperture (m) instrument**	**Exposure (s) cycle (s) time source**	**Observers**
09 July 2019	Guaratinguetá/BRA (technical problems)	22 48 10.02 S 45 11 30.5 W 573.0	Meade LX200 0.4 SBIG ST7XME	- - -	Rafael Sfair, Thamiris Santana
	Ponta Grossa/BRA (negative)	25 05 22.2 S 50 05 56.4 W 909.0	Meade RC400 0.406 Merlin Raptor	1.5 1.5 GPS	Chrystian L. Pereira, Marcelo Emílio
	La Silla/CHL (bad weather)	29 15 32.1 S 70 44 01.5 W 2,375.0	NTT 3.58 SOFI	- - -	Emmanuel Jehin
	Cerro Pachón/CHL (bad weather)	30 14 16.41 S 70 44 01.11 W 2,713.0	SOAR 4.0 Merlin Raptor	- - -	Julio I. B. Camargo
	San Juan/ARG (negative)	31 47 54.7 S 69 17 44.1 W 2,552.0	CASLEO 2.15 PI-2040B	? ? ?	Luis A. Mammana, Eduardo F. Lajus
	Córdoba/ARG (negative)	31 21 24.58 S 64 35 34.41 W 864.0	? ? ?	? ? ?	Carlos A. Colazo
	Santa Rosa/ARG (negative)	36 38 16.0 S 64 19 28.0 W 182.0	- 0.3 ?	5.0 ? ?	Julio Spagnotto
26 July 2020	Sutherland/ZAF (bad weather)	32 22 32.0 S 20 48 38.9 E 1,750.6	? ? ?	? ? ?	Amanda Sickafoose
	La Reunion Island/FRA (bad weather)	? ? ?	? ? ?	? ? ?	Jean Paul, Piere Thierry
	Santa Rosa/ARG (bad weather)	36 38 16.0 S 64 19 28.0 W 182.0	? ? ?	? ? ?	Julio Spagnotto
		? ? ?	? ? ?	? ? ?	Aldo Javier Wilberger
24 February 2021	Cerro Pachón/CHL (negative)	30 14 16.41 S 70 44 01.11 W 2,713	SOAR 4.0 Merlin Raptor	1.0 1.0 GPS	Altair Gomes Júnior, Flavia L. Rommel, Julio I. B. Camargo
14 October 2021	North Carolina/USA (Negative ????????)	? ? ?	? ? ?	? ? ?	David Wake
	North Carolina/USA (Technical Problems)	35 13 32.1 N 82 09 17.6 W 320.0	? ? ?	? ? ?	Randy L. Flynn
	Alberta/USA (Cloudy)	? ? ?	? ? ?	? ? ?	Phil Langill
	North Dakota/USA (Cloudy)	? ? ?	? ? ?	? ? ?	Sherry Fieber-Beyer
	Indiana/USA (Cloudy)	? ? ?	? ? ?	? ? ?	Adam W. Rengstor
	Illinois/USA (Cloudy)	? ? ?	? ? ?	? ? ?	Aart Olsen
	Idaho/USA (Cloudy)	? ? ?	? ? ?	? ? ?	Jason W. Barnes
	Kansas/USA (Cloudy)	? ? ?	? ? ?	? ? ?	Greg Rudnick
	New Mexico/USA (Cloudy)	? ? ?	? ? ?	? ? ?	Larry Molnar
	Ohio/USA (Cloudy)	? ? ?	? ? ?	? ? ?	Rush Swaney
	Oregon/USA (Cloudy)	? ? ?	? ? ?	? ? ?	Scott Fisher
	Montana/USA (Cloudy)	? ? ?	? ? ?	? ? ?	Bill Hanne

Appendix B: Light curves

Here we provide the plots of the 80 positive occultation light curves acquired during the nine events observed between 2019 and 2022. They are normalized to the unity and the time is given in seconds counting from 00:00:00 (UTC) of the event date. Figures B.1, B.2, B.3, B.4 and B.5 present the plots from the 8 August 2020 stellar occultation, listed from the northernmost to the southernmost stations. Figures B.6 and B.7 shows the light curves from the other eight events. The black dots present the observational data and the red line is the fitted model. Note to be deleted later: they are missing the light curves from TAROT, Massa 01 e TAR 02.

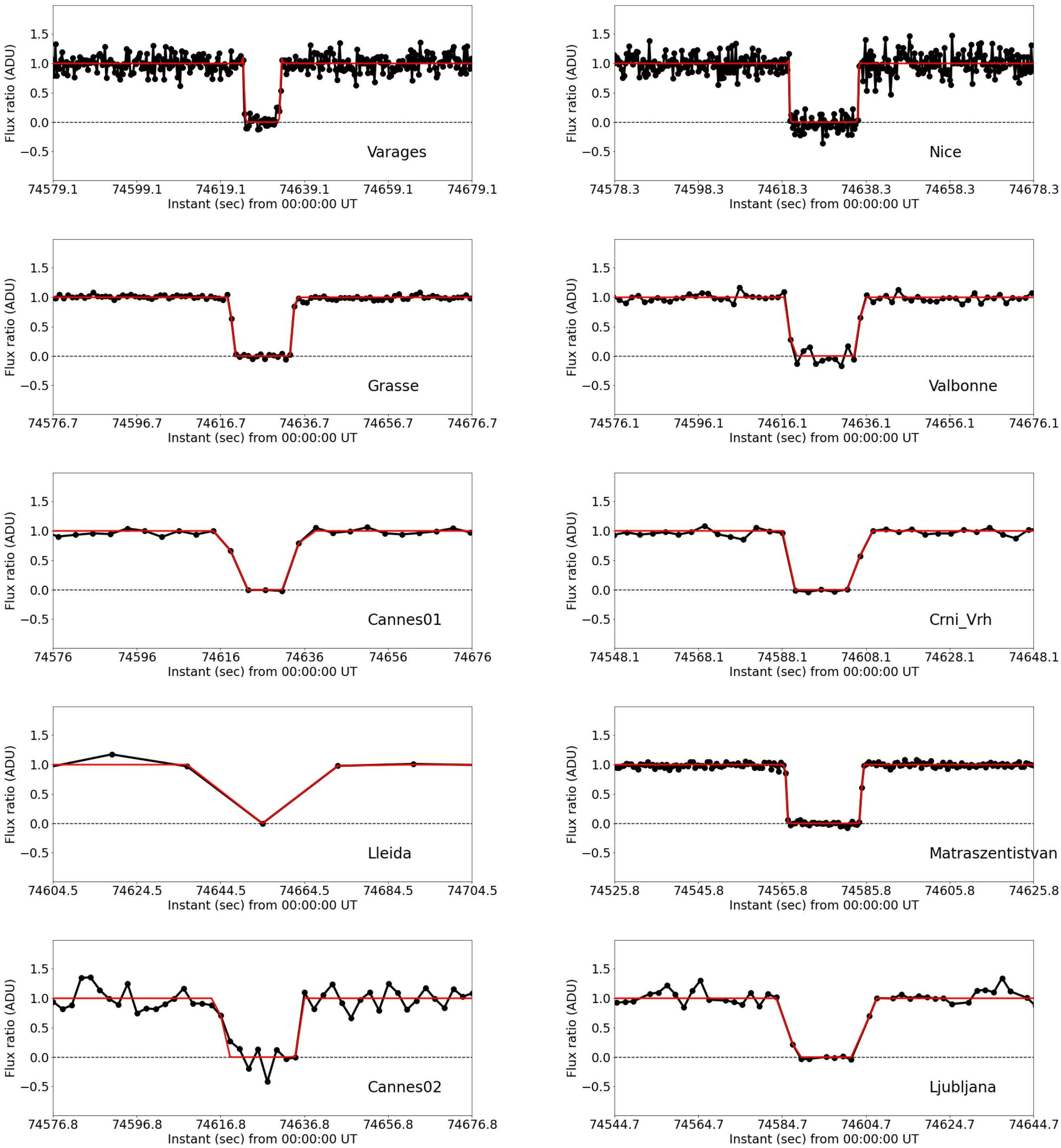

Fig. B.1: The 61 normalized light curves, centered in the occultation instant, obtained on the 8 August 2020 campaign. The station that acquired the light curve is mentioned in each plot. The black points and the red line present the observed data and the fitted model, respectively.

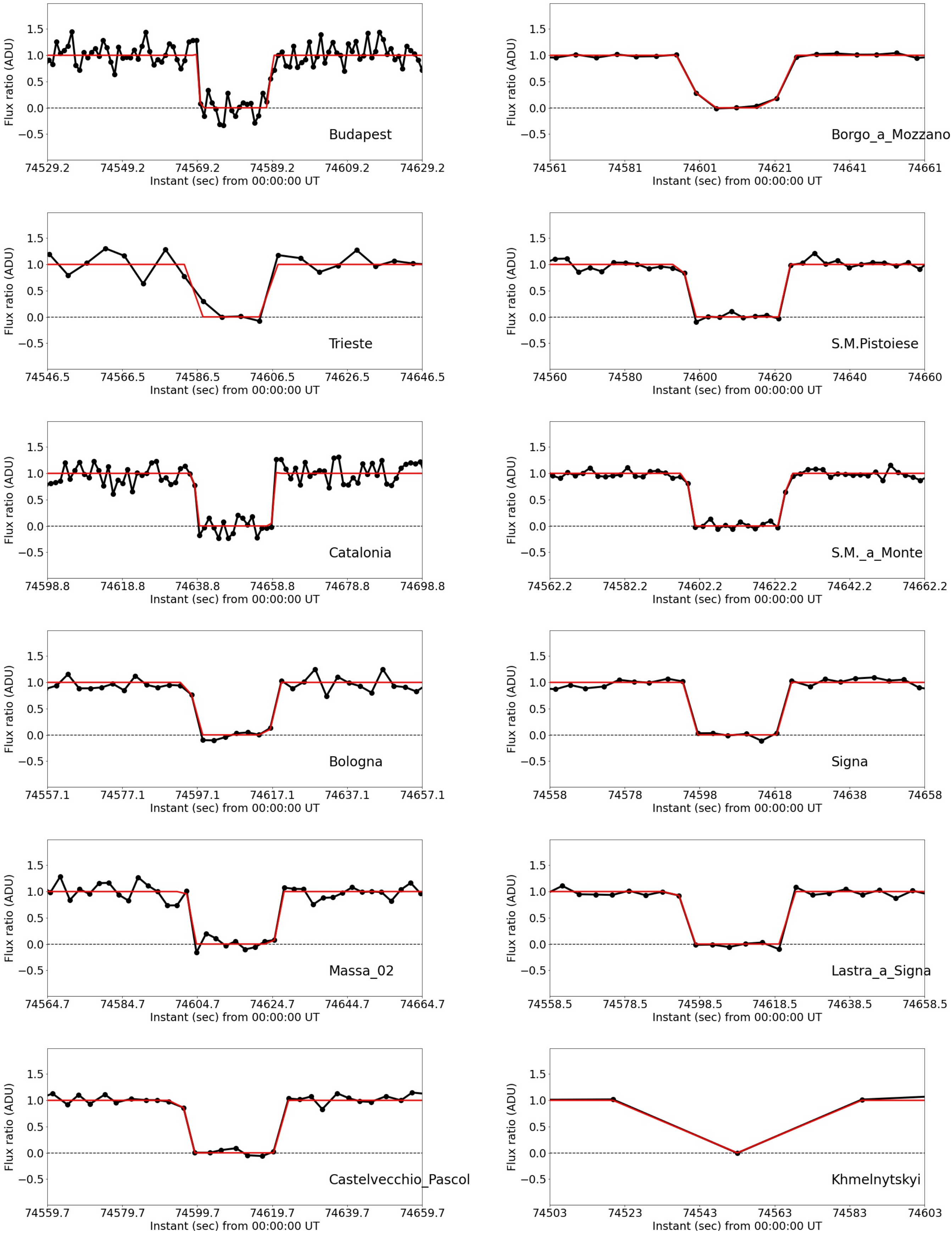

Fig. B.2: Continue.

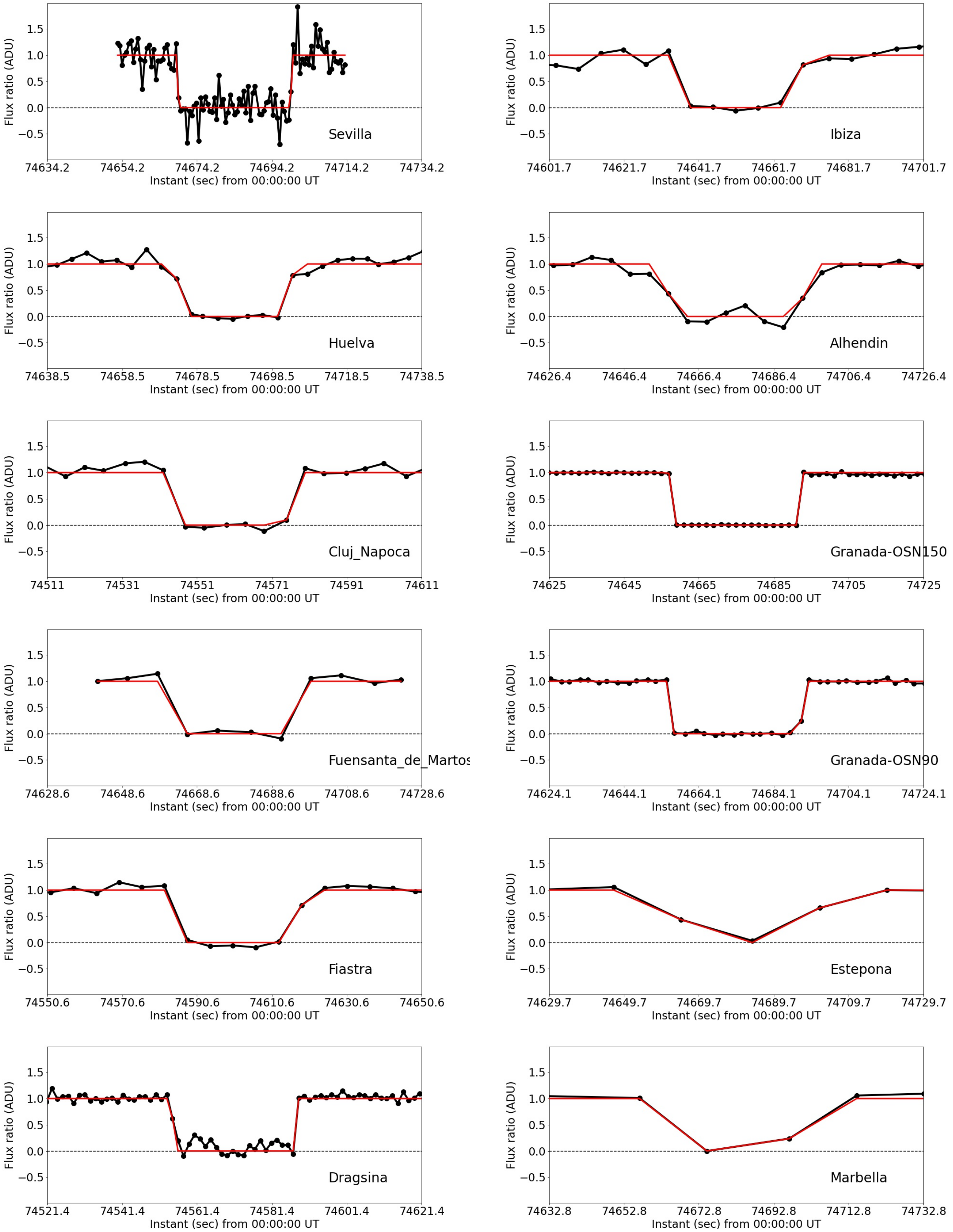

Fig. B.3: continued.

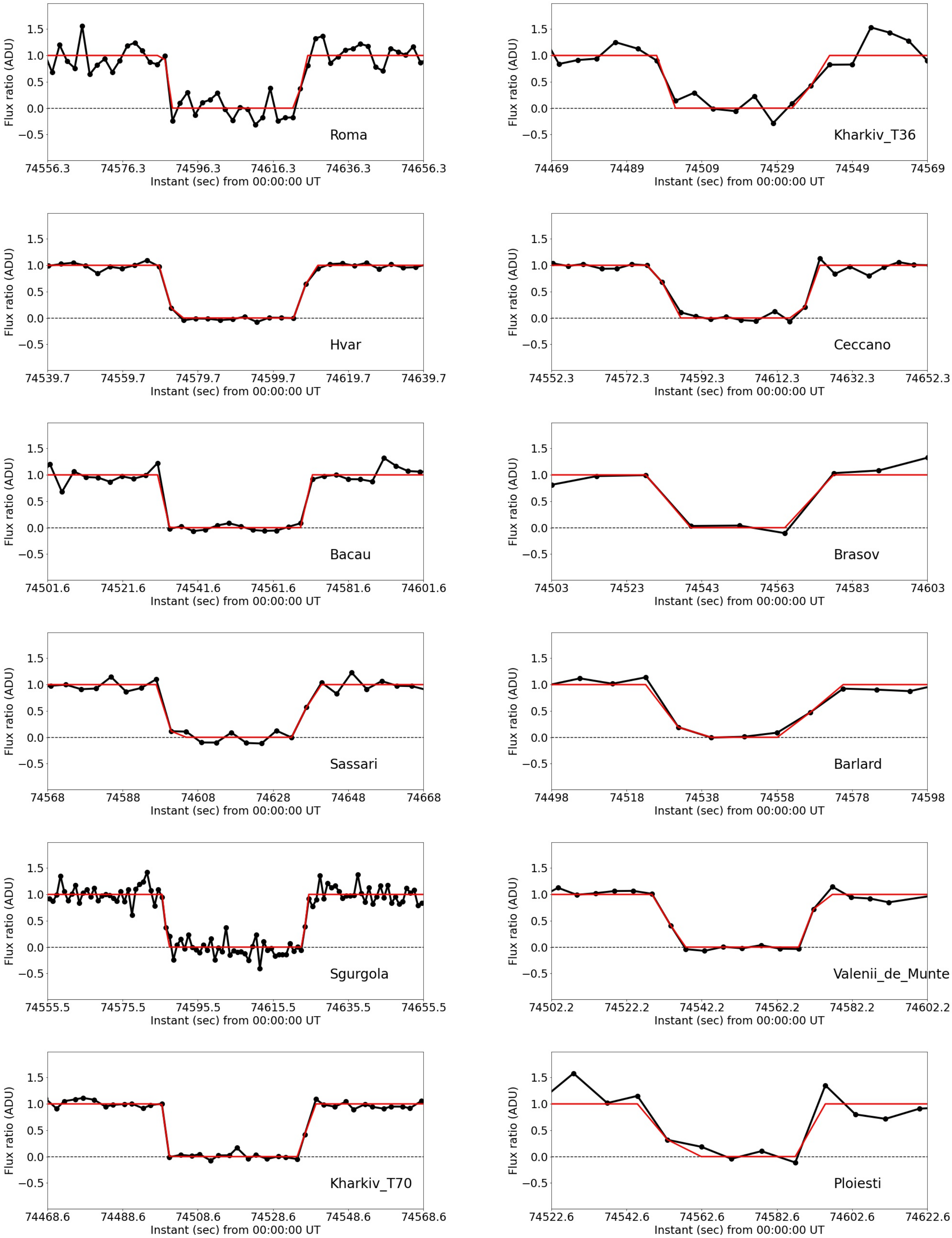

Fig. B.4: continued.

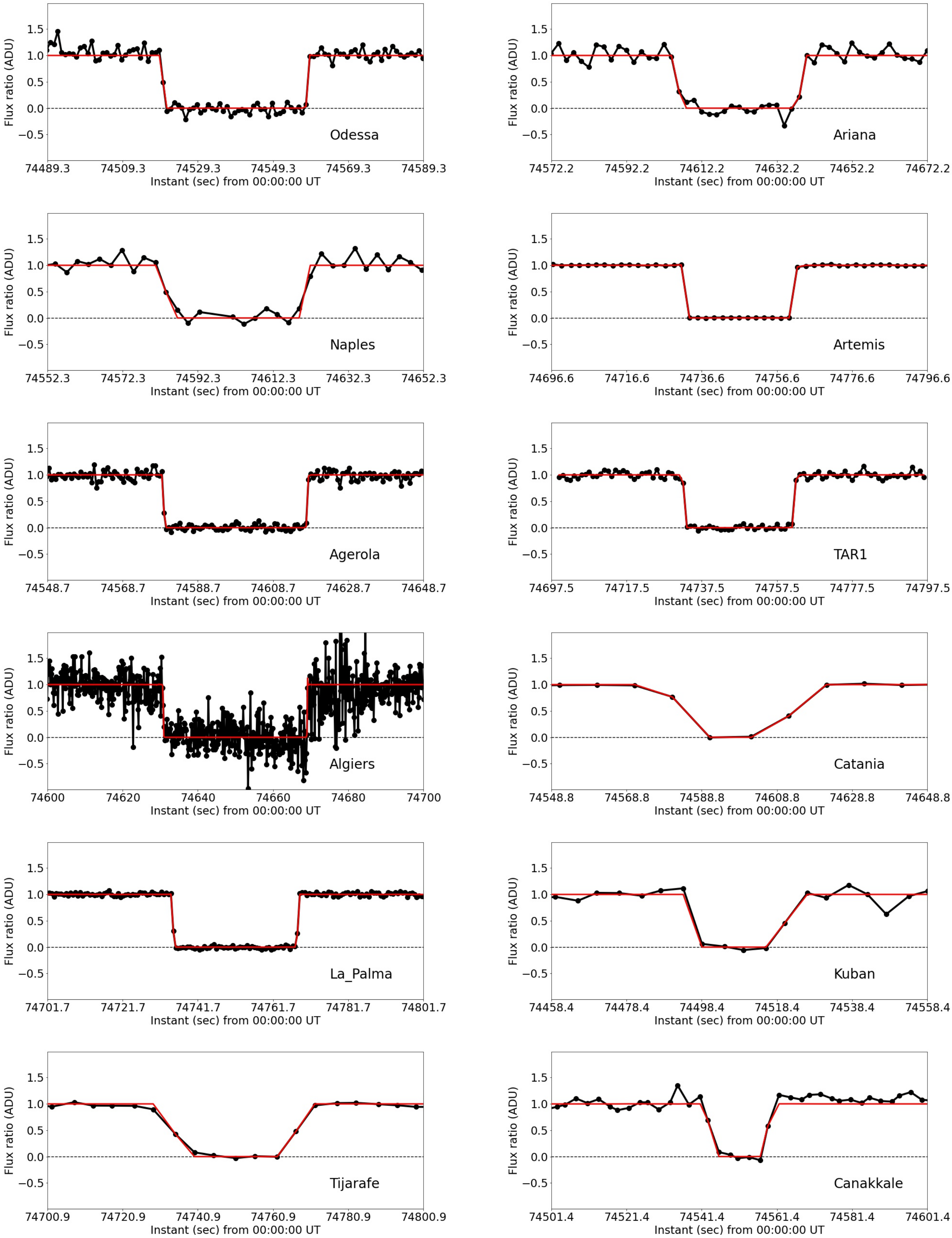

Fig. B.5: continued.

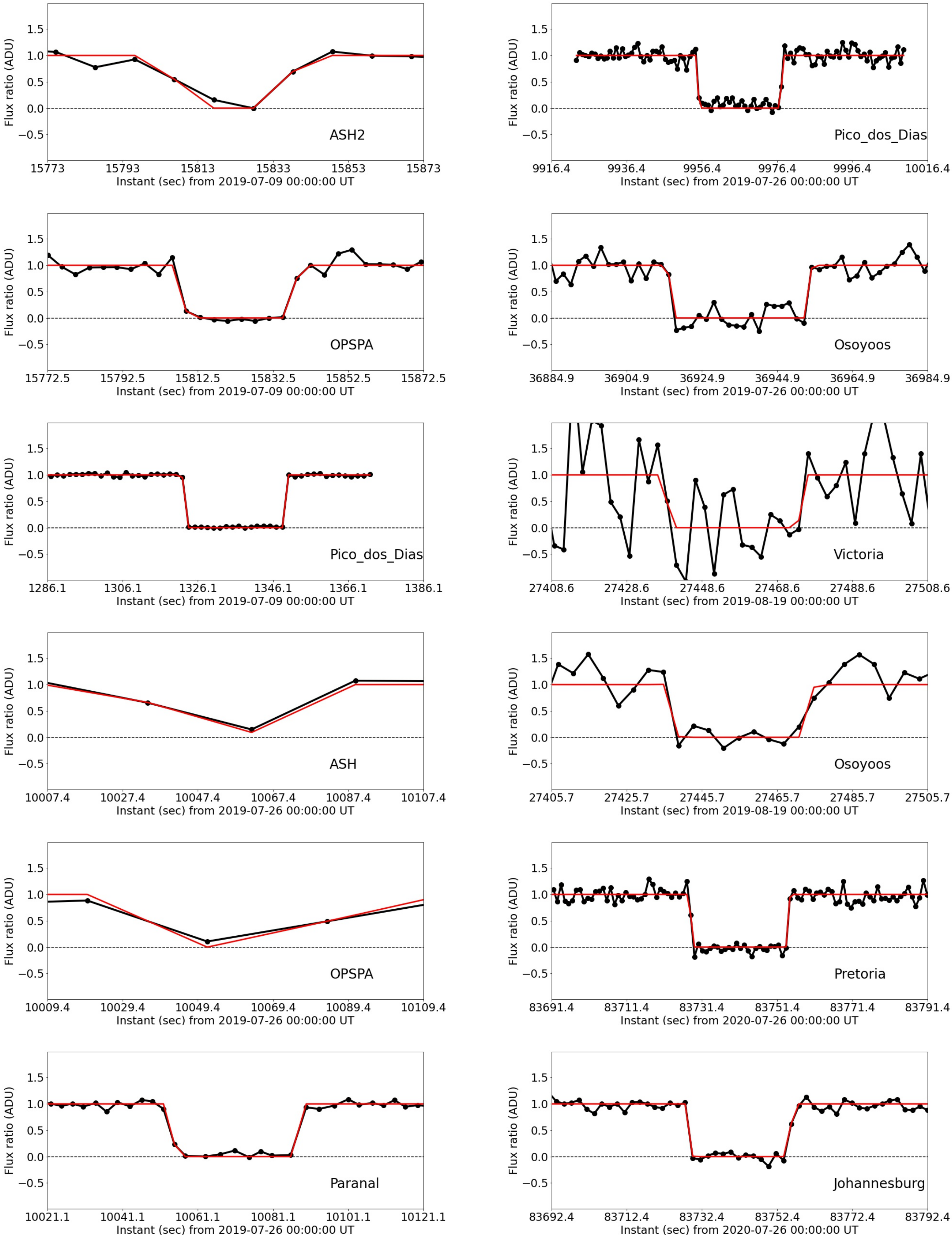

Fig. B.6: Observed (black points) and calculated (red line) light curves for each site that observed a stellar occultation by 2002 MS_4, except the 8 August 2020 multichord event - see table A.4 for observational details.

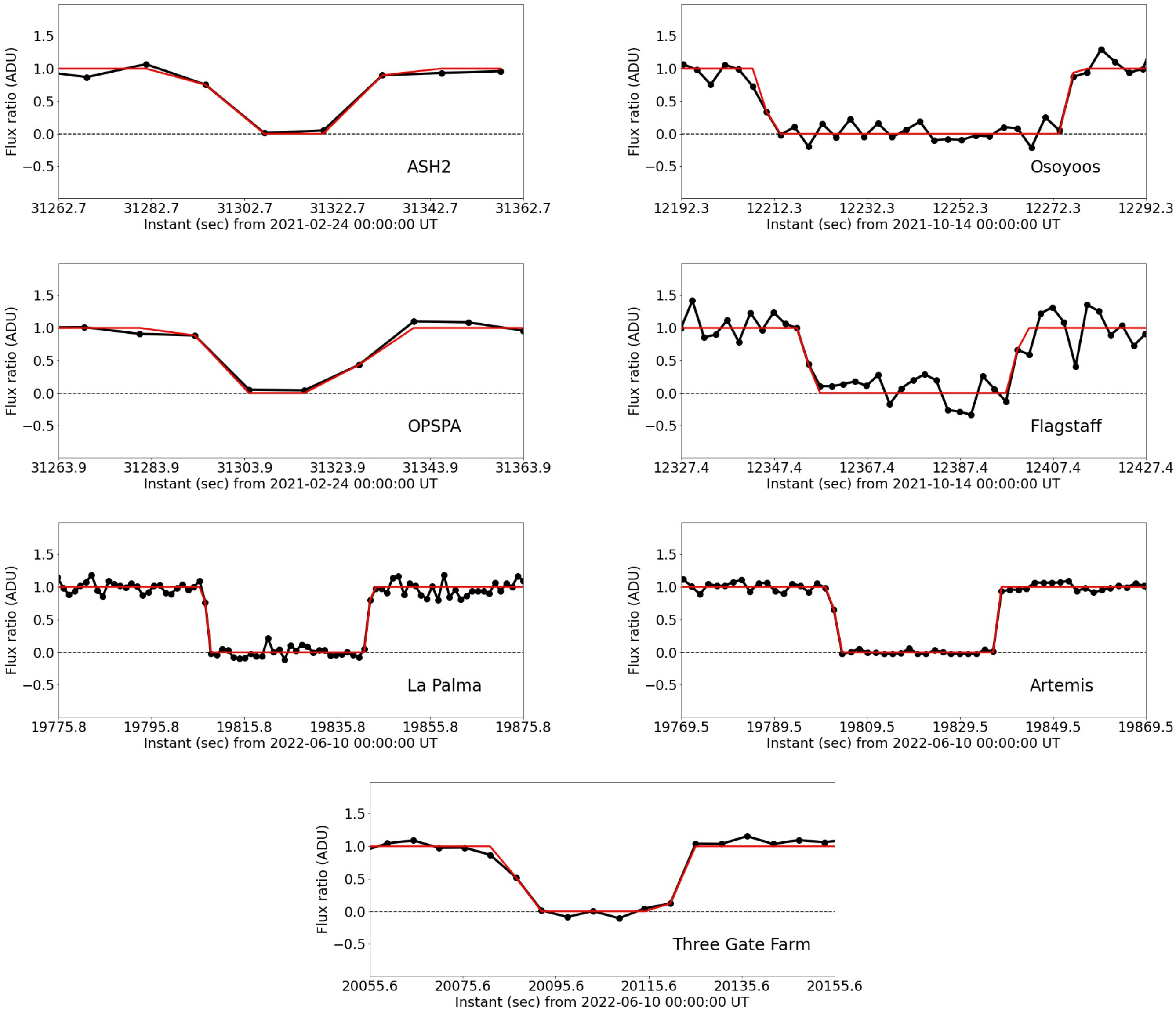

Fig. B.7: Continue.